Université du Québec
Institut National de la Recherche Scientifique
Centre Énergie, Matériaux et Télécommunications

Integrated multifunctional nanoplatforms with bioimaging and therapeutic modalities in the biological window

Par
Fan Yang

Thèse présentée pour l'obtention du grade de Philosophiæ doctor (Ph.D.)
en sciences de l'énergie et des matériaux

Jury d'évaluation

Président du jury et examinateur interne	Jinyang Liang INRS-EMT
Examinateur externe	Antonella Badia Université de Montréal
Examinateur interne	Hendrick W. de Haan University of Ontario Institute of Technology
Directeur de recherche	Dongling Ma INRS-EMT
Codirecteur de recherche	Fiorenzo Vetrone INRS-EMT
Codirecteur de recherche	Xinyu Liu University of Toronto

ABSTRACT

Nowadays, with the rapid development of nanotechnology towards personalized and nano-medicine, engineering multifunctional nanoplatforms for the purpose of concurrent therapeutic and diagnostic (theranostic) modalities is critical for addressing challenging issues associated with cancers. Multifunctional nanoparticles (NPs), which integrate superparamagnetic and photoluminescent nanocomponents into a single particle, as an emerging class of nanomaterials, are extremely important for realizing this ultimate goal. Owing to their unique superparamagnetism, superparamagnetic NPs can be used to magnetically confine various biological species (DNAs, proteins, bacteria, cancer cells, *etc.*), thus allowing for ultra-sensitive biological detection. They can also serve as: i) magnetic resonance (MR) imaging contrast agents for the diagnosis of malignant tissues, ii) vehicles for carrying therapeutic payloads (anticancer drugs, small inhibitory RNA) to desired tumor sites in a target-specific manner, and iii) hyperthermia agents for cancer therapy under an alternating magnetic field. On the other hand, photoluminescent nanomaterials as contrast agents are widely used for the purposed of photoluminescence bioimaging, mainly for cells and tissues, thus allowing to acquire information of biological species and events. Therefore, multifunctional (superparamagnetic and photoluminescent) NPs which simultaneously possess both diagnostic and therapeutic functions, are expected to lead to a combined range of potential applications, such as bimodal imaging, photoluminescence monitored magnetic-driven drug delivery and simultaneous *in vivo* imaging and targeted hyperthermia therapy. However, the photoluminescent component in most studies regarding multifunctional NPs has so far been based on visible-emitting organic dyes, quantum dots (QDs) and upconverting nanoparticles (UCNPs). These multifunctional NPs exhibit low tissue penetration of excitation and emission light as a result of the considerable tissue absorption and low signal-to-noise ratio due to strong background autofluorescence from biological tissues, which restrict their use as contrast agents for *in vivo* imaging. To overcome this issue, the alternative contrast agents, whose absorption and emission wavelength are both in the so-called biological windows situated in the near-infrared (NIR) range (denoted as NIR-I: 700–950 nm; NIR-II: 1000–1350 nm) in which tissues are optically transparent, should be used. In this thesis, our work is mainly focused on the development of multifunctional magnetic and photoluminescent nanoplatforms in the NIR-I/II range with modalities for bioimaging and therapeutics.

In the first part, we developed a multifunctional core/shell/shell nanoplatform (Fe_3O_4@SiO_2@$NaYF_4$:Nd^{3+}), which consists of a superparamagnetic Fe_3O_4 core surrounded by an intermediate SiO_2 shell and further coated by an outer photoluminescent shell of $NaYF_4$:Nd^{3+}. Recently, Nd^{3+}-doped NPs became one of the most rapidly growing research areas because of their high absorption cross section and low phototoxicity

compared with commonly used Yb^{3+}-doped UCNPs. Most importantly, Nd^{3+}-doped NPs can be efficiently excited by laser at *ca.* 800 nm (NIR-I) and present three emission peaks at 900 (NIR-I), 1060 (NIR-II), and 1340 nm (NIR-II), respectively. Both excitation and emission wavelengths of Nd^{3+}-doped NPs are located within the optically transparent biological windows in the NIR. Owing to this unique NIR-to-NIR photoluminescence feature, the prepared Fe_3O_4@SiO_2@$NaYF_4$:Nd^{3+} NPs exhibit deep-tissue penetrated optical properties with a high signal-to-noise ratio. Our NIR imaging experiment has demonstrated that the NIR photoluminescence signal of Fe_3O_4@SiO_2@$NaYF_4$:Nd^{3+} NPs can be transmitted across a tissue as thick as 13 mm, about three times thicker than that can be achieved by similar core/shell/shell NPs containing the upconverting shell of Fe_3O_4@SiO_2@$NaYF_4$:Er^{3+},Yb^{3+} NPs. Meanwhile, these multifunctional NPs possess excellent superparamagnetic properties due to Fe_3O_4 core inside, which result in rapid magnetic response to an external magnetic field, making them suitable for magnetic-driven biological applications. Another important bio-medical application of Fe_3O_4@SiO_2@$NaYF_4$:Nd^{3+} NPs, arising from superparamagnetic propriety, is their exploitation as T_2 contrast agents for MR imaging. *In vivo* MR imaging exhibits the significant darkening effect in T_2-weighted images with the use of Fe_3O_4@SiO_2@$NaYF_4$:Nd^{3+} NPs as contrast agents. Moreover, by designing this nanoplatform, the potential toxicity of highly photoluminescent optical probes, such as QDs that usually contain Pb and/or Cd can be largely avoided, as demonstrated through cytotoxicity assay using HeLa cancer cells and human embryonic kidney (HEK 293T) cells. Therefore, this multifunctional nanoplatform is a promising candidate for high-resolution and deep-tissue bimodal (optical and MR) imaging *in vivo*.

The multifunctional nanoplatform in Part I shows low magnetization due to their single magnetic core feature, which is not suitable for magnetic-driven bioapplications and magnetothermal therapy. Engineering multifunctional nanoplatform containing multiple magnetic NPs is beneficial for realizing fast confinement bioapplications and achieving more effective magnetothermal therapy. Part II is thus focused on the development of novel multifunctional theranostic NPs that exploit multiple superparamagnetic Fe_3O_4 NPs and interesting NIR-emitting PbS/CdS QDs, and their integration into a single nanoplatform. Self-assembly, as a powerful tool to design and fabricate functional nanomaterials for the purpose of rational control of the optical, electronic and magnetic pairing between distinct NPs, has attracted increasing research attention for their applications in biomedical diagnosis, plasmonics, and energy conversion. Self-assembled supernanoparticles (SPs) involving different types of NPs can possess not only the intrinsic physical and chemical characteristics of their individual NPs but also the collective properties of these NPs due to the coupling effect. In this part, the nanoplatform was specifically prepared by the self-assembling of superparamagnetic Fe_3O_4 NPs and photoluminescent PbS/CdS QDs with their emission in NIR-II and its self-assembly formation mechanism was systematically studied. Due to their unique NIR photoluminescence feature, the self-assembled Fe_3O_4 and PbS/CdS (NIR-II) supernanoparticles [SASNs

(NIR-II)] exhibit outstanding deep-tissue penetration property as an optical imaging probe, allowing the NIR photoluminescence signal to be detected through a tissue as thick as 14 mm, about three times thicker than that can be achieved by their counterpart operating within the first biological window [SASNs (NIR-I)]. At the same time, clustered Fe_3O_4 NPs constituting SASNs (NIR-II) largely increase the magnetic field inhomogeneity by the synergistic effect, resulting in a significantly enhanced T_2 relaxivity (282 $mM^{-1}s^{-1}$, *ca.* 4 times higher than that of free Fe_3O_4 NPs), as demonstrated by the remarkable darkening effect on *in vivo* MR imaging. Regarding the potential nanomedicine-related therapeutic modalities, magnetothermal therapy suffers from the low heat conversion efficiency of currently studied magnetic NPs, while photothermal therapy is not suitable for deep-lying subcutaneous cancer cells due to the limitation of light penetration. More interestingly, the prepared SASNs (NIR-II) in our work possess the dual capacity to act as both magnetothermal and photothermal agents, overcoming the main drawbacks of each type of heating separately. When SASNs (NIR-II) were exposed to the dual-mode (magnetothermal and photothermal) heating set-up, the thermal energy transfer efficiency (specific loss power, SLP) was amplified 7-fold compared with magnetic heating alone. These results, in hand with the excellent photo and colloidal stability, and negligible cytotoxicity, demonstrate the potential use of SASNs (NIR-II) for deep-tissue bimodal (optical and MR) imaging *in vivo*, while simultaneously enabling SASNs (NIR-II) mediated dual-mode heating treatment for cancer therapy.

Although SASNs (NIR-II) possess excellent dual-mode heating therapeutic modality, polyvinylpyrrolidone (PVP) coating served as NPs surface stabilizer shows fair biocompatibility and difficulty of further versatile functionalization. In addition, we propose to explore drug delivery modality with our multifunctional nanoplatform. Previously published work has indicated mesoporous materials are extremely suitable for drug delivery. With this consideration, mesoporous silica ($mSiO_2$) appears as a promising drug carrier because it generally possesses a rigid mesostructured framework with high stability and ease of surface functionalization for linking drug molecules. In the third part, we specifically designed another type of multifunctional theranostic nanoplatform based on the large-pore $mSiO_2$. To date, the work regarding the preparation of uniform $mSiO_2$ with large pore size (> 5 nm) is very limited. In this part, relatively-large-pore (>10 nm) $mSiO_2$ as matrix was deliberately synthesized by a biphase stratification continuous growth approach, followed by a simple silane coupling reaction to form thiol-modified $mSiO_2$. Owing to its unique relatively-large-pore structure with high loading capacity, the nanoplatform ($mSiO_2$@PbS/CdS-Fe_3O_4) was then fabricated by coordination-driven embedding of superparamagnetic Fe_3O_4 NPs and PbS/CdS QDs of suitable size into the mesoporous channels of $mSiO_2$. In particular, the QDs were selected in such a way that they could be excited by the light in NIR-I as well as emit in NIR-II. The excellent NIR deep-tissue optical and superparamagnetic behavior of $mSiO_2$@PbS/CdS-Fe_3O_4 particles enables their use as bimodal imaging (optical and MR) contrast agents, thus increasing the reliability and accuracy of diagnosis. On the

other hand, when the $mSiO_2$@PbS/CdS-Fe_3O_4 nanoplatform was exposed to external physical stimuli of magnetic field (MF) and/or a NIR laser, this nanoplatform produced strong local heating as a highly efficient magnetic hyperthermia therapy (MHT)/photothermal therapy (PTT) agent. At last, this nanoplatform also demonstrate great potential as a drug delivery carrier due to large-pore characteristics. Doxorubicin (DOX), a widely used clinical anticancer drug, was chosen as a model to study their drug release behavior. After being loaded with DOX, the release rate of DOX under multi-stimuli (pH/MF/NIR) was significantly enhanced at lower pH and higher temperatures, caused by magnethermal/photothermal effects. This nanoplatform thus yielded a synergistic effect from the integrated heating mode and multi-stimuli responsive drug release to achieve a high therapeutic efficacy.

ACKNOWLEDGEMENTS

Foremost I would like to express my deepest and sincere gratitude to my supervisor Prof. Dongling Ma, for accepting me in her group and giving me the chance to pursue my PhD degree. It has been a pleasure working with her who created a warm and stimulating research environment for us. The frequent and useful discussions with her at different stages of my research work largely contributed to the success of my research. I am forever and extremely grateful for her continual and dedicated guidance and constant encouragements. Her attitude towards academic research has greatly motivated me to be a good researcher.

Meanwhile, I would like to acknowledge my co-supervisor Prof. Fiorenzo Vetrone. His endless effort in improving the quality of my research project by giving me some novel ideas makes me explore a fascinating scientific filed. He has always been a strong supporter when I need help throughout the duration of my PhD study.

Beside my supervisors in INRS, I would like to express my sincere thanks to another co-supervisor Prof. Xinyu Liu, from University of Toronto, for giving me invaluable suggestions and inspirations make me find the right direction of my research.

I am also grateful to Prof. John Oh from Concordia University for the collaboration of cytotoxicity assay in his group, and Prof. Sylvain Martel from Polytechnique Montréal for allowing me to carry out hyperthermia experiment in his lab. Their important comments have largely improved the quality of the articles I wrote for publication.

I would like to thank Dr. Fuqiang Ren who has contributed to my research work by carrying out some experiments involved in my project and discussing about the experiments and results with me. I also acknowledge Artiom Skripka, who gave me invaluable help and comments on my research and articles writing. I gratefully acknowledge the contribution to this work made by my collaborators, Dr. Antonio Benayas, Dr. Yue Huang, Xianke Dong, Sung Hwa Hong and Maryam Sadat Tabatabaei.

I am also grateful to all the group members for their help throughout the work. These people include: Dr. Hongyang Liang, Dr. Jianming Zhang, Dr. Mee Rahn Kim, Dr. Belete Atomsa Gonfa, Dr. Zhenghe Xu, Dr. Long Tan, Yanlong Liu, T. G. Deepak, Pandeng Li, Qingzhe Zhang, Shengyun Huang, Dr. Yannan Liu, Yong Wang and Ting Yu.

I would like to thank Jean-Philippe Masse for carrying out TEM measurements for me. I also thank departmental and technical staff at INRS-EMT, particularly Christophe Chabanier, for giving me training and technical help in using some equipment.

A massive thanks to all my friends: Chao Wang, Xin Chai, Xin Tong, Daling Cui, Wei Huang, Qiliang Wei, Xin Jin, Xiaohua Yang, *et al*.; without you I cannot have such wonderful memories these years.

I am eternally grateful to my parents, for their constant support and encouragement throughout all of my studies. I would like to thank my wife, Peijun Huang, who loves me deeply and supports me selflessly.

Finally, I wish to acknowledge the following organizations for their financial support: The Natural Sciences and Engineering Research Council of Canada and Fonds de recherche du Québec-Nature et technologies for PhD Program.

CONTENTS

LIST OF FIGURES

Figure 1.6 (a) TEM images of CdSe plain core nanocrystals and the corresponding core/shell nanocrystals with different shell thickness from the same SILAR reaction. (b) Scheme of synthesis of PbSe/CdSe QDs by cation exchange method. (c) PL spectra from a series of aliquots during CdSe shell formation, corresponding to 15 min, 2 h, and 24 h of reaction time proceeding from red to blue. Each spectrum is corrected for variation in optical density as well as grating and detector efficiencies to reflect relative QY. Shown in black is the original PbSe core, magnified 10-fold so its shape is discernible. The inset lists the calculated core diameter (column "PbSe") and shell thickness ("CdSe") from elemental analysis. Also included is the approximate effective core size predicted by the PL peak position ("PL"). Figure 1.6a was obtained from reference[32] and Figure 1.6b~c was obtained from reference[33].

Figure 1.7 (a) Energy diagrams for Ln^{3+} in a $LaCl_3$ lattice. (b) UC processes for lanthanide-doped crystals: ESA and ETU. (c) Schematic illustration of UC nanoparticles composed of a crystalline host and lanthanide dopant ions (activator and sensitizer) embedded in the host lattice. Figure 1.7a was obtained from reference[35].

Figure 2.1 (a) Synthetic procedure of Fe_3O_4@SiO_2(F)@meso-SiO_2(P)-Folate nanoparticles. (b) Labeling of g-Fe_2O_3-SiO_2-AP and g-Fe_2O_3-SiO_2-AP-CMCS nanoparticles with FITC. Figure 2.1a was taken from reference[50] and Figure 2.1b was taken from reference[61].

Figure 2.2 (a) Schematic illustration of the formation of $NaYF_4$:Yb, Er/Tm@SiO_2@Fe_3O_4 NPs. (b) Bright-field TEM image and (c~e) EDX elemental mappings of $NaYF_4$:Yb, Er/Tm@SiO_2@Fe_3O_4, (f) HRTEM image of $NaYF_4$:Yb, Er/Tm@SiO_2@Fe_3O_4 (inset: SAED image of $NaYF_4$:Yb, Er) and (g) HRTEM image of Fe_3O_4 (inset: FFT image of Fe_3O_4). (h) Schematic of fabrication of ($CdTe$/Fe_3O_4)@SiO_2 FMNS with different magnetic potentials: weak (WFMNS), moderate (M-FMNS), and strong (S-FMNS), Respectively. TEM images of ($CdTe$/Fe_3O_4)@SiO_2 FMNS: (i) W-FMNS, (j) M-FMNS, and (k) S-FMNS. Figure 2.2a~g was taken from reference[66] and Figure 2.3h~k was taken from reference[65].

Figure 2.3 (a) Synthetic procedure for the drug-loaded Fe_3O_4@SiO_2@α-NaYF/Yb, Er nanorattles (DOX-MUC-F-NR). (b) TEM and SEM (the inset in (b)) images of Fe_3O_4@SiO_2 nanospheres. (c) TEM image of magnetic upconversion oxide nanospheres (MUC-O-NS); inset in (c) is a HRTEM image after growing the outer Y_2O_3/Yb, Er layer. (d) TEM image of the MUC-F-NR; insets are higher-magnification TEM image of one (upper left) and the SAED image recorded on part of the α-$NaYF_4$/Yb, Er shell (lower left). (e) TEM image of Fe_3O_4@SiO_2@α-NaYF/Yb, Er with SiO_2 fully etched; inset is a higher-magnification TEM image of a single hollow nanosphere. (f) Illustration of the preparation of multifunctional mesoporous Fe_3O_4/SiO_2/CdTe nanoprobe. (g) TEM images of oleic acid-stabilized Fe_3O_4 nanoparticles and (h) their particle size statistics. (i) TEM images of mesoporous Fe_3O_4@SiO_2 particles and (j) mesoporous

Fe_3O_4/SiO_2/CdTe nanoprobes. Figure 2.3a~e was taken from reference[72] and Figure 2.3f~j was taken from reference[73].

Figure 2.4 (a) Schematic diagram of the conjugation of amine-functionalized quantum dots (QDs) to the surface of carboxylate-functionalized MNSs using conventional NHS/EDC coupling method; (b) Scheme of PTX loading using a thin PLGA coat on the surface of QD-MNSs. (c) Schematic illustration of the facile fabrication of MR/NIR multimodal imaging nanoprobes based on magnetofluorescent polyelectrolyte nanocomposites (MagFL-PEN) *via* electrostatic assembly between polyelectrolytes and functional colloidal nanoparticles. (d) SEM and TEM (inset) images of MagFL-PEN after adsorption of QD800(COOH). (e) EDX analysis of MagFL-PEN. Figure 2.4a~b was taken from reference[81] and Figure 2.4c~e was taken from reference[85].

Figure 2.5 (a) The two-step hybrid formation. Step I: A) iron oxide nanocrystals (native ligands not shown), B) iron oxide nanoparticles with the first polystyrene shell, C) nanohybrid after the deposition of QDQRs. Step II: D) nanohybrid after synthesizing a thin PS shell, E) nanohybrid after second emulsion polymerization, when dyads cluster owing to high styrene concentration. (b, c) Representative TEM images of the different hybrids achieved using different amounts of monomer during the second emulsion polymerization. The inset shows a three-dimensional histogram of the number of QDQRs n (QDQR) and the number of iron oxide n (Fe_3O_4) within one hybrid. Amounts used of each monomer: (b) 4 nmol and (c) 8 nmol. (d) Scheme for synthesis of MUCNBs; TEM images of 23 nm UCNPs (e), 15 nm IONPs (f), 6 nm UCNPs (g), and MUCNBs with 15 nm IONPs and 23 nm UCNPs (h) or 6 nm UCNPs (i). Figure 2.5a~c was taken from reference[89] and Figure 2.6d~i was taken from reference[94].

Figure 2.6 (a) Schematic representation of the synthetic routine of the water-soluble $NaYF_4:Yb^{3+}$, $Tm^{3+}@Fe_xO_y$ nanocrystals. (b) TEM image of $NaYF_4:Yb^{3+}$, Tm^{3+} nanocrystals and (c) $NaYF_4:Yb^{3+}$, $Tm^{3+}@Fe_3O_4$ nanocrystals. (d) EDX spectrum of the $NaYF_4:Yb^{3+}$, $Tm^{3+}@Fe_3O_4$ nanocrystals. (e) Illustration of the multistep sequential synthesis producing the magneto-fluorescent hybrid structures. (f) TEM images of CdSe@CdS@hollow-Fe_2O_3 nanostructure. (g) Enlarged TEM image of f. Figure 2.6a~d was taken from reference[101] and Figure 2.6e~g was taken from reference[102].

Figure 2.7 (a) Architecture of water-dispersible shell-doped mQDs (NAC-CdTe/30%Fe:ZnS) (A) and core-doped mQDs (NAC-30%Fe-CdTe/ZnS (B). (b) Representative TEM image of shell-doped mQDs and the corresponding diffraction pattern (inset), indicating that the mQDs are crystalline. (c) The corresponding size distribution, where the average particle diameter was determined to be 2.9 ± 0.3 nm. Figure 2.7a~c was taken from reference[104].

Figure 2.8 Dual-modal UCL/MR *in vivo* imaging. (a) The bright field, (b) UCL, and (c) merged images of a KB tumor-bearing mouse one hour after intravenous injection of PEG–MFNP. Strong UCL signals were observed from the liver and tumor sites (arrow) of the mouse. (d) *Ex vivo* UCL imaging showing accumulation of MNFPs in the liver, spleen, tumor, bone, and lung of the injected mouse at 24 h post injection. UCL signals from other organs were barely detectable. T_2-weighted images of KB-tumor bearing nude mice with (e) and without (f) injection of MFNPs. Obvious darkening contrast was shown in the mouse liver and tumor. (g) Multimodal UCL and (h) MR imaging for *in vivo* lymphangiography mapping using MFNPs. MR images were taken before (left) and after (right) injection of MFNPs. Figure 2.8a~h was taken from reference[117].

Figure 2.9 (a) Schematic illustration of targeting of DOX loaded multifunctional drug carrier to tumor cells assisted by an externally applied magnetic field (MF). (b) Tumor location as defined by MUC-F-NR intensity increases with 1 h magnetic field treatment. Mice bearing H22 xenograft tumor were injected with DOX loaded MUC-F-NR (1 mg/kg) and subjected (+MF) or not subjected (-MF) to the magnetic field for 1 h. At 24 h postinjection, mice were imaged *in vivo*. (c) The luminescence signal was measured from the whole tumor *in vivo* and *ex vivo*. (Excitation was provided by the CW infrared laser at 980 nm and upconversion luminescence signals were collected at 650 ± 10 nm. Fluence rates for 980 nm excitation light were 80 mW/cm^2.) (d) Tumor volume changes of saline-treated mice compared to mice treated with MUC-F-NR, DOX, and DOX loaded MUC-F-NR over 21 d in the absence and presence of magnetic field. Data show mean ± SD ($n = 5$, $^*p \leq 0.05$). Figure 2.9a~d was taken from reference[72].

Figure 2.10 (a) Schematic illustration of the preparation of the acetylated hyaluronic acid–pheophorbide-a coated Fe_3O_4 magnetic nanoparticles (AHP@MNPs); amphiphilic and negatively charged AHP can interact with positively charged MNP through multibinding interactions. (b) Schematic representation of multifunctional AHP@MNPs for tumor-targeted bimodal imaging and photodynamic/hyperthermia treatment when AHP@MNPs were irradiated with magnetic and near infrared lasers. Figure 2.10a~b was taken from reference[120].

Figure 3.1 Schematic illustration of the setup for synthesis of (a) Fe_3O_4 NPs, (b) PbS QDs, (c) PbS/CdS QDs and (d) $Fe_3O_4/SiO_2/NaYF_4:Nd^{3+}$ NPs.

LIST OF CHEMICAL COMPOUNDS, ABBREVIATIONS AND SYMBOLS

Chemical compounds

$FeCl_3 \cdot 6H_2O$	iron chloride hexahydrate
$NH_3 \cdot H_2O$	ammonium hydroxide solution
TEOS	tetraethyl orthosilicate
$Y(NO_3)_3 \cdot 6H_2O$	yttrium nitrate hexahydrate
$Yb(NO_3)_3 \cdot 5H_2O$	ytterbium nitrate pentahydrate
$Er(NO_3)_3 \cdot 5H_2O$	erbium nitrate pentahydrate
$Nd(NO_3)3 \cdot 6H_2O$	neodymium nitrate hexahydrate
$PbCl_2$	lead chloride
$Pb(OAc)_2$	lead acetate trihydrate
CdO	cadmium oxide
S	sulfur
N_2	nitrogen
PbS	lead sulfide
CdS	cadmium sulfide
NH_4NO_3	ammonium nitrate

Abbreviations

OA	oleic acid
TDE	1-tetradecene
ODE	1-octadecene
OLA	oleylamine
$(TMS)_2S$	bis(trimethylsilyl) sulfide
TEA	triethanolamine
THF	tetrahydrofuran

TOP	trioctylphosphine
PEI	polyethylenimine
PBS	phosphate buffered saline
PVP	polyvinylpyrrolidone
EG	ethylene glycol
DMSO	dimethyl sulfoxide
CTAC	cetyltrimethylammonium chloride
DTAB	dodecyltrimethylammonium bromide
DOX	doxorubicin hydrochloride
FBS	fetal bovine serum
DMEM	dulbecco's modified Eagle's medium
MTT	3-(4,5-dimethylthiazol-2-yl)-2,5-diphenyltetrazolium bromide
NPs	nanoparticles
UCNPs	upconverting nanoparticles
UV	ultraviolet
NIR	near-infrared
PL	photoluminescence
QDs	quantum dots
TEM	transmission electron microscopy
SAED	selected area electron diffraction
EDX	energy dispersive x-ray spectroscopy
XRD	x-ray diffraction
XPS	x-ray photoelectron spectrometry
DLS	dynamic light scattering
ICP-OES	inductively coupled plasma-optical emission spectrometry
FTIR	fourier-transform infrared spectroscopy

VSM	vibrating sample magnetometer
MR	magnetic resonance
BET	Brunauer-Emmett-Teller
FC	field-cooled magnetization
ZFC	zero-field-cooled magnetization

Symbols

T_b	blocking temperature
Oe	Oersted (magnetic field strength unit)
M	magnetization
emu/g	mass magnetization
r	relaxivity coefficient
H	magnetic field strength
I	applied current
V	the volume of sample
m	the mass of sample

LIST OF PUBLICATIONS AND CONFERENCE CONTRIBUTIONS

Journal Publications

1. **Fan Yang**, Artiom Skripka, Antonio Benayas, Xianke Dong, Sung Hwa Hong, Fuqiang Ren, Jung Kwon Oh, Xinyu Liu, Fiorenzo Vetrone, and Dongling Ma, An Integrated Multifunctional Nanoplatform for Deep-tissue Dual-Mode Imaging. *Adv. Funct. Mater.,* 28 (2018) 1706235.

2. **Fan Yang**, Artiom Skripka, Maryam Sadat Tabatabaei, Sung Hwa Hong, Fuqiang Ren, Antonio Benayas, Jung Kwon Oh, Sylvain Martel, Xinyu Liu, Fiorenzo Vetrone, and Dongling Ma, Multifunctional self-assembled supernanoparticles for deep-tissue bimodal imaging and amplified dual-mode heating treatment. *ACS Nano,* 13 (2019) 408-420.

3. **Fan Yang**, Artiom Skripka, Maryam Sadat Tabatabaei, Sung Hwa Hong, Fuqiang Ren, Yue Huang, Jung Kwon Oh, Sylvain Martel, Xinyu Liu, Fiorenzo Vetrone, and Dongling Ma, Magnetic-Photoluminescent Nanoplatform Built from Large-Pore Mesoporous Silica. *Chem. Mater.,* 31 (2019) 3201-3210.

4. Qingzhe Zhang, **Fan Yang**, Zhenhe Xu, Mohamed Chaker, and Dongling Ma, Are lanthanide-doped upconversion materials good candidates for photocatalysis? *Nanoscale Horiz.,* 4 (2019) 579-591.

5. Fuqiang Ren, Shengyun Huang, **Fan Yang**, Aycan Yurtsever, Dongling Ma, Diameter dependent transparency changes of nanorod-based large-area flexible smart window devices. *J. Mater. Chem. A*, 6 (2018) 24157-24165.

6. Long Tan, **Fan Yang**, Mee Rahn Kim, Pandeng Li, Deepak Thrithamarassery Gangadharan, Joëlle Margot, Ricardo Izquierdo, Mohamed Chaker, and Dongling Ma, Enhanced Long-term and Thermal Stability of Polymer Solar Cells in Air at High Humidity with the Formation of Unusual Quantum Dot Networks. *ACS Appl. Mater. Interfaces,* 9 (2017) 26257-26267.

7. Fuqiang Ren, Blanca del Rosal, So Young An, **Fan Yang**, Elisa Carrasco, Antonio Benayas, Jung Kwon Oh, Daniel Jaque, Ángeles Juarranz de la Fuente, Fiorenzo Vetrone, and Dongling Ma, Development and Investigation of Ultrastable PbS/CdS/ZnS Quantum Dots for Near-Infrared Tumor Imaging. *Part. Part. Syst. Charact.,* 34 *(*2017) 1600242.

8. Long Tan, Yufeng Zhou, Fuqiang Ren, Daniele Benetti, **Fan Yang**, Haiguang Zhao, Federico Rosei, Mohamed Chaker and Dongling Ma, Ultrasmall PbS quantum dots: a facile and greener synthetic route and their high performance in luminescent solar concentrators. *J. Mater. Chem. A,* 5 (2017) 10250-10260.

9. Fuqiang Ren, Sarah A. Lindley, Haiguang Zhao, Long Tan, Belete Atomsa Gonfa, Ying-Chih Pu, **Fan Yang**, Xinyu Liu, François Vidal, Jin Z. Zhang, Fiorenzo Vetronead and Dongling Ma, Towards understanding the unusual photoluminescence intensity variation of ultrasmall colloidal PbS quantum dots with the formation of a thin CdS shell. *Phys. Chem. Chem. Phys.,* 18 (2016) 31828-31835.

10. Zhenhe Xu, Yanlong Liu, Fuqiang Ren, **Fan Yang**, Dongling Ma, Development of functional nanostructures and their applications in catalysis and solar cells. *Coord. Chem. Rev.*, 320-321 (2016) 153-180. Invited

Conference Presentations

1. **Fan Yang**, Xinyu Liu, Fiorenzo Vetrone, Dongling Ma. Fluorescent-magnetic nanoparticles for bioapplications. International Conference on Energy, Materials and Photonics (EMP19). July 14-16, 2019, Shanghai, China (*Oral presentation*)
2. **Fan Yang**, Artiom Skripka, Antonio Benayas, Xianke Dong, Sung Hwa Hong, Fuqiang Ren, Jung Kwon Oh, Xinyu Liu, Fiorenzo Vetrone, Dongling Ma. An Integrated Multifunctional Nanoplatform Based on Superparamagnetism and Near-Infrared to Near-Infrared Photoluminescence for Deep-tissue Dual-mode Imaging. 256th ACS Fall National Meeting, August 19-23, 2018, Boston, USA (*Oral presentation*)
3. **Fan Yang**, Artiom Skripka, Antonio Benayas, Xianke Dong, Sung Hwa Hong, Fuqiang Ren, Jung Kwon Oh, Xinyu Liu, Fiorenzo Vetrone, Dongling Ma. A Dual-mode Nanoparticle Probe for Deep-tissue Optical and Magnetic Resonance Imaging. International Conference on Energy, Materials and Photonics (EMP18). Montreal, July 8-11, 2018 (*Poster presentation*)
4. **Fan Yang**, Artiom Skripka, Antonio Benayas, Xianke Dong, Sung Hwa Hong, Fuqiang Ren, Jung Kwon Oh, Xinyu Liu, Fiorenzo Vetrone, Dongling Ma. An Integrated Multifunctional Nanoplatform Based on Superparamagnetism and Near-Infrared to Near-Infrared Photoluminescent Nd^{3+}-doped $NaYF_4$ Nanoparticles for Deep-tissue Dual-mode Imaging. 2nd annual meeting of Quebec Center for Advanced Materials (QCAM), Montreal, May 3-4, 2018 (*Oral presentation*)
5. **Fan Yang**, Fuqiang Ren, Xinyu Liu, Fiorenzo Vetrone, Dongling Ma. Multifunctional (superparamagnetic and upconversion) core/shell/shell nanoparticles for biomedical applications. 9e Colloque annuel du CQMF, Montreal, November 24 and 25, 2016 (*Oral presentation*)
6. **Fan Yang**, Fuqiang Ren, Xinyu Liu, Fiorenzo Vetrone, Dongling Ma. Synthesis and characterization of multifunctional (superparamagnetic and upconversion) core/shell/shell nanoparticles for biomedical applications. Materials Science & Technology, October 23-27, 2016 Salt Lake City, Utah USA (*Oral presentation*)

CHAPTER 1 INTRODUCTION

1.1 Superparamagnetic nanoparticles

Magnetic nanoparticles (NPs) exhibit unique magnetic property, which is totally different from their bulk counterparts. The bulk ferromagnetic materials usually consist of a large number of magnetic domains and each domain contains parallel magnetic moments that are separated by domain walls. The formation of domain walls is driven by the balance between the magnetostatic energy and domain-wall energy. The magnetostatic energy increases with the volume of materials proportionally while the domain-wall energy is responsible for the increased interfacial area between domains. If the size of ferromagnetic materials is reduced to the nanometer regime, there is a critical value below which a stable single domain NP can be formed since energy for creating domain walls is much higher than that of magnetostatic energy for the single domain state. When magnetostatic energy

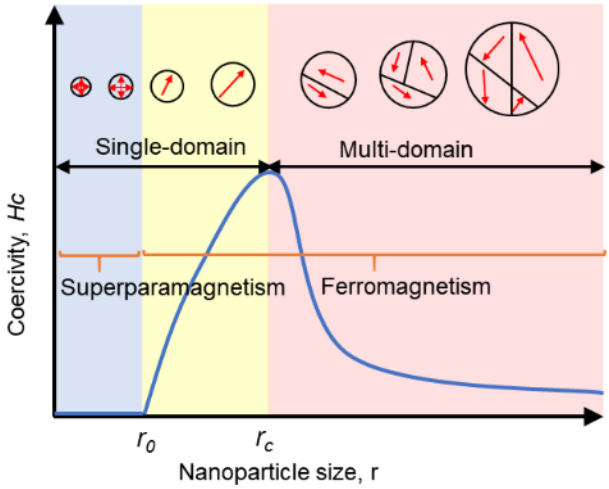

Figure 1.1 Schematic illustration of magnetic coercivity (H_c, magnetic field required to reduce the magnetization to zero) behavior of a magnetic NP as a function of its size. When the size of NP gradually decreases to critical size (r_c), the H_c shows an increase as the domain wall in NP disappears. If the size is further decreased to r_0 in which the thermal agitation energy is higher than magnetic anisotropy energy and the magnetic moment of NP fluctuates freely, the NP enters the superparamagnetic regime and shows zero coercivity.

is equal to domain-wall energy, with NP transferring from multiple domains to the single-domain state, as shown in Figure 1.1, the critical size (r_c) of NP for can be expressed as the equation (1):[1]

$$r_c = 18.\frac{\sqrt{A.K_{eff}}}{\mu_0 M^2} \quad (1)$$

where A is the exchange constant, K_{eff} is the anisotropy constant, μ_0 is the vacuum permeability and M is the saturation magnetization. For the majority of magnetic NPs, the critical diameter typically lies in the range of 10~100 nm.

As mentioned above, the magnetic spins in a single domain of ferromagnetic NPs are coupled and parallel-aligned. The magnetic anisotropy energy (ΔE) in single domain of ferromagnetic NPs can keep the magnetic moments along a certain direction, which is given by the equation (2):

$$\Delta E = K_{eff}.V \qquad (2)$$

where V is the volume of the NP, as exemplified in Figure 1.2a.

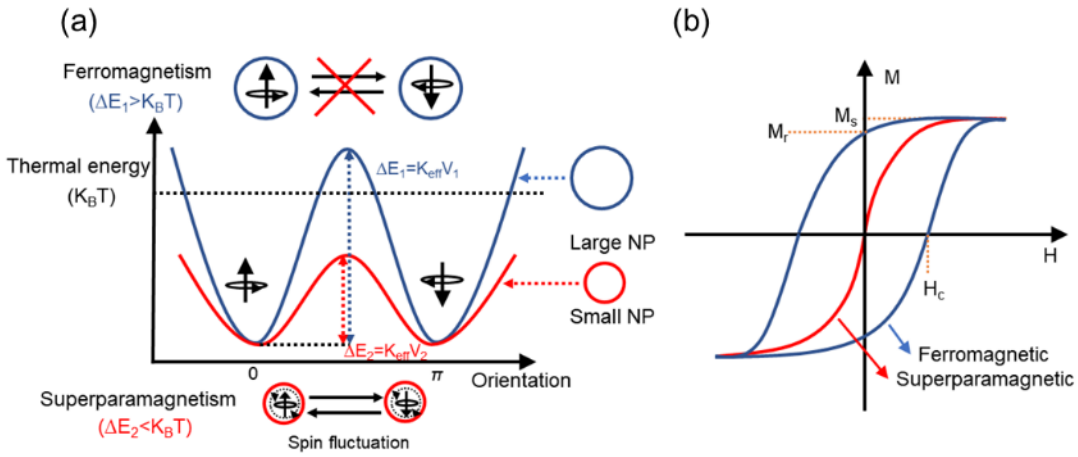

Figure 1.2 (a) Energy diagram of magnetic NPs with different magnetic spin alignment. Thermal energy (K_BT) represents the energy barrier to the rotation of the magnetization. The large NP shows the ferromagnetism on the top and the small NP shows the superparamagnetism on the bottom. (b) The comparison of typical magnetic curves for ferromagnetic and superparamagnetic materials. Saturation magnetization (M_S) is the maximum value of magnetic field; the remanence magnetization (M_r) stands for the residual magnetization after removing external magnetic field; and the coercivity (H_c) is the external field required to reduce the magnetization to zero.

The relatively large single-domain ferromagnetic NPs have much larger magnetic anisotropy energy than the thermal energy ($\Delta E > K_BT$, where K_B is the Boltzmann constant and T is the temperature) (blue line in Figure 1.2a). The thermal energy is not high enough to invert the magnetic spin-spin direction. When the size of single-domain ferromagnetic NPs is further decreased from r_c to r_0 (Figure 1.2a), the thermal energy can overcome the magnetic anisotropy barrier ($\Delta E < K_BT$) (red line in Figure 1.2a), which results in the magnetic fluctuation of moment in the domain of NPs. Such magnetic fluctuation will no longer be stable and further leads to a zero net-magnetization, and this behavior is said to be superparamagnetism.[2-3] The comparison of typical magnetic curves for ferromagnetic and superparamagnetic NPs is shown in the Figure 1.2b. It can be seen that the superparamagnetic NPs are easily saturated under an external magnetic field and show similar saturation magnetization value (M_S, maximum value of magnetic field) as that of

ferromagnetic NPs. Once the magnetic field is removed, the superparamagnetic NPs give a zero remanence (Mr, residual magnetization) and coercivity, which is different from ferromagnetic NPs.

Owing to their unique superparamagnetic properties, along with excellent biocompatibility and biodegradability, superparamagnetic NPs have great potential for use as inherent contrast agents for MR imaging. Additionally, after conjugation with additional functional targeting groups and therapeutic moieties, superparamagnetic NPs can be extended to other bioapplications beyond MR imaging contrast enhancer, including, but not limited to, cell separation and targeting, nanocarriers of therapeutic payloads (drugs, nucleic acids and proteins) and hyperthermia agents for treating cancers under an alternating magnetic field.

1.2 Fluorescent nanoparticles

The general definition of fluorescent NPs is nano-sized structure that can produce fluorescence light emission under suitable optical excitation. Their fluorescence feature makes them suitable for various biomedical applications. In the case of bioimaging, fluorescent NPs are frequently introduced to the portions of biological samples *in vitro* (cell/tissue level) and *in vivo* (the whole animal) being imaged in order to acquire better understanding of the cellular and physiological information. Over the past several decades different types of fluorescent NPs, including organic dye-doped silica NPs,[4] organic polymer NPs,[5] metallic NPs,[6] carbon-based NPs (nanotubes and nanodots),[7-8] quantum dots (QDs) and lanthanide-doped upconverting nanoparticles (UCNPs),[9-10] have emerged for bioimaging. Regarding the constituent of fluorescent NPs used for bioimaging, they can be mainly classified into two groups: organic and inorganic NPs. As the general criteria for the selection of fluorescent probes for imaging, ideal fluorescent NPs should fulfill the following requirements: i) good stability under physiological conditions, ii) high brightness, iii) minimal cytotoxicity and minimal distortion of cellular functions, iv) large strokes shifts to avoid self-quenching and vi) high signal to background ratio.[11] Although the organic-based NPs are the earliest and classic contrast agents used for bioimaging, they suffer from several inherent drawbacks, such as low photostability (susceptible photobleaching), small Stokes shifts (difficulty in separating the excitation and emission signals). In addition, in general they have short fluorescence lifetime *ca.* 10^{-9} s, which is too short for efficient discrimination of short-lived fluorescence interference from scattered excitation light.[12] Nowadays inorganic-based NPs are attracting the interest of the largest scientific community, so in this chapter we mainly focus on inorganic-based QDs and lanthanide-doped UCNPs, which are also the luminescent nanomaterials explored in this thesis.

1.2.1 Biological windows

As we described above, in biological and preclinical studies, fluorescent NPs are utilized to localize biospecies, to elucidate the cellular and tissue structures or to monitor the internal dynamic processes of interaction with the biological media in cells or living organisms. For *in vitro* imaging experiments, the medium between cells and the microscope objectives is only composed of water-based phosphate-buffered saline or cell growth medium, which has a thickness of several hundred micrometers or less. Therefore, even the emission of fluorescent NPs is partially absorbed by the cell medium, they still can be appropriate for *in vitro* imaging, as the reduced thickness of cell medium has negligible effect on the attenuation of fluorescence intensity.

However, regarding *in vivo* experiments, the situation becomes more complicated as the medium between fluorescent NPs and the microscope imaging system is a highly inhomogeneous tissue containing different absorbing and scattering components, unlike the thin water-like layer in *in vitro* imaging study. Both the excited/emitted photons can interact with tissues, depending on their optical properties. The sum of the light absorption and scattering by tissues is termed as optical extinction (attenuation), which can be expressed as the equation (3):[13]

$$\alpha_{ext} = \alpha_{abs} + \alpha_{sct} \qquad (3)$$

The overall value of extinction determines the penetration depth of light (both excitation and emission) in living tissue and the relevant extinction coefficient of given tissue strongly depends on wavelengths.

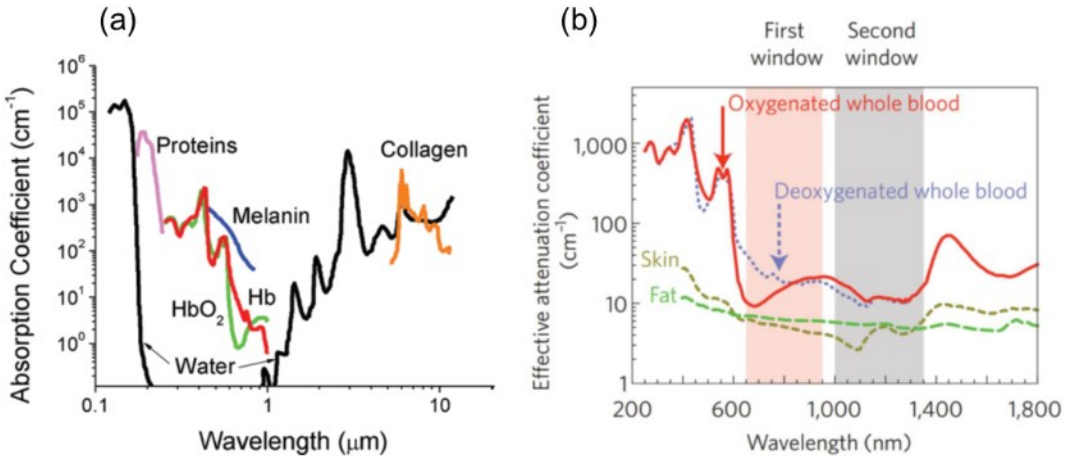

Figure 1.3 (a) Absorbance of various tissue and blood components from 200 nm to 10 μm. (b) Optical windows in biological tissues. These plots of effective attenuation coefficient (on a log scale) versus wavelength show that absorption and scattering from oxygenated blood, deoxygenated blood, skin and fatty tissue is lowest in either the first (pink shaded area) or second (grey) near-infrared window. Figure 1.3a was taken from reference[14] and Figure 1.3b was taken from reference[7].

Normally, the absorbance of the blood component (water, proteins, melanin and hemoglobin-Hb) is quite high in the range of 200~650 nm, which almost covers the whole visible range, as can be seen in Figure 1.3a.[14] In this wavelength range study of tissue by fluorescence techniques can only be roughly assessed as the light has a small penetration depth due to the heavy tissue absorbance. This is a major barrier for *in vivo* imaging. In order to overcome this issue, it is highly desired to perform fluorescence imaging with the wavelength region above 650 nm. Figure 1.3b shows the extinction coefficient of main components in tissue. In the visible range tissue extinction shows the similar trend as absorbance of the blood component, mainly from the oxygenated and deoxygenated blood.[7] For wavelength larger than 1400 nm in the NIR range, the oxygenated/deoxygenated blood-induced extinction remains at a high level. Thus, the overall extinction coefficient can be minimized in the two wavelength ranges (650-950 nm and 1000-1350 nm), the so-called first and second biological windows (NIR-I and NIR-II), as shown in Figure 1.3b. In addition, autofluorescence, which comes from the natural light emission by biological tissues and cells under the excitation light, is reduced since light absorbed by tissue is negligible in NIR-I/II. Initially most of the *in vivo* imaging studies are performed in the visible range, however, with the objective of deep-tissue *in vivo* imaging, researchers have shown great interest in moving into the NIR-I/II.[15]

1.2.2 Quantum dots

QDs are tiny semiconductor nanocrystals with their diameters varying from 1 nm to about 20 nm, normally composed of II-VI, III-V, and IV-VI elements of the periodic table.[16] Unlike their bulk semiconductors, the most striking characteristic of QDs is the unique size-dependent optical property which arises from the so-called quantum confinement effect. When the size of the semiconductor material is smaller than the Bohr exciton radius (known as the distance in an electron-hole pair), the exciton is spatially confined and the electrons of QDs are quantized to certain energies presented as discrete energy levels, rather than "bands" of energies in the bulk material (Figure 1.4a).[17] The band energy gap of QDs can be regarded as the sum of the energy gap of the bulk material, the confinement energy of exciton and the Coulomb attraction energy between the electron and hole in a spherical QD, as described in the equation (4):

$$E_{g(QDs)} = E_{g(bulk)} + \frac{h^2}{8R^2}\left(\frac{1}{m_e^*} + \frac{1}{m_h^*}\right) - \frac{1.8e^2}{4\pi\varepsilon\varepsilon_0 R} \quad (4)$$

where $E_{g(bulk)}$ is the band gap energy of the bulk material, h is the Plank constant, R is the radius of QDs, m_e^* and m_h^* are the effective mass of electron and hole, ε_0 and ε are the vacuum permittivity and permittivity of QDs. The second term and the third term are the confinement and Coulomb attraction energy of exciton, respectively.

From the equation (4) above, it can be concluded that the QDs show size-dependent band gap when the dimension of semiconductor nanocrystal is smaller than the exciton Bohr radius. That is to say that the

bandgap of QDs decreases as the size of QDs increases because more and more atoms are bound together which makes the discrete energy levels gradually merge into energy bands, as shown in Figure 1.4b.[18] Meanwhile, the optical properties of the QDs become size-dependent, which allows their absorption and photoluminescence (PL) tuned through a wide spectral range by varying their size. For example, the PL emission wavelength of CdSe QDs (Eg = 1.76 eV for the bulk, Bohr radius = 9.6 nm) can be tuned within the visible range from 450 nm to 750 nm by controlling their size, as shown in Figure 1.4c[17]. The unique size-dependent optical properties of QDs make them extremely useful for bioimaging, diagnostics and various types of optoelectronic devices.

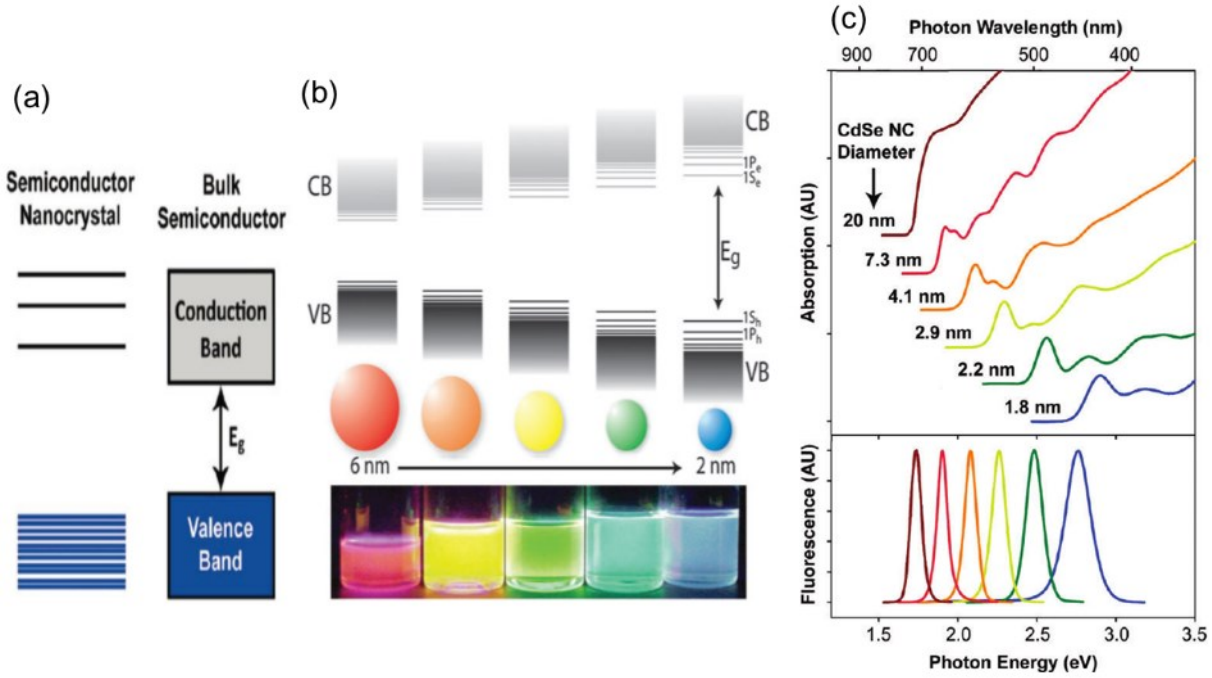

Figure 1.4 (a) Electronic energy states of a semiconductor in the transition from nanosized crystals to bulk crystals. Blue shading denotes ground state electron occupation. (b) Schematic representation of the quantum confinement effect on the energy level structure of a semiconductor material. The lower panel shows colloidal suspensions of CdSe nanocrystals of different sizes under UV excitation. (c) Absorption (upper) and fluorescence (lower) spectra of CdSe semiconductor nanocrystals showing quantum confinement and size tunability. Figure 1.4a and c was taken from reference[17] and Figure 1.4b was taken from reference[18].

1.2.2.1 PbS quantum dots

NIR-emitting QDs, with their wavelengths tuned from 750~3700 nm, are of great interest in the past two decades due to their potential applications in the field of solar cells, telecommunications, quantum computing and biomedicine.[19] Of all these applications, NIR QDs appear as a very powerful and crucial tool for *in vivo* bioimaging, diagnostics and possible therapeutics since they exhibit deep-tissue penetration of excitation and emission light through thick tissue and reduced autofluorescence background in the NIR-

I/II, as we mentioned in the chapter 1.2.1. A variety of NIR QDs including, InX (X= As, P, III-V),[20-21] PbX (X= S, Se, Te, IV-VI),[22-24] Ag_2X (X=S, Se, I-VI) [25-26] and $CuInX_2$ (X= S, Se, I-III-VI2),[27-28] have been reported for bio-related applications.

Among these NIR QDs, PbS QDs with a direct band gap of 0.41 eV at room temperature and large exciton

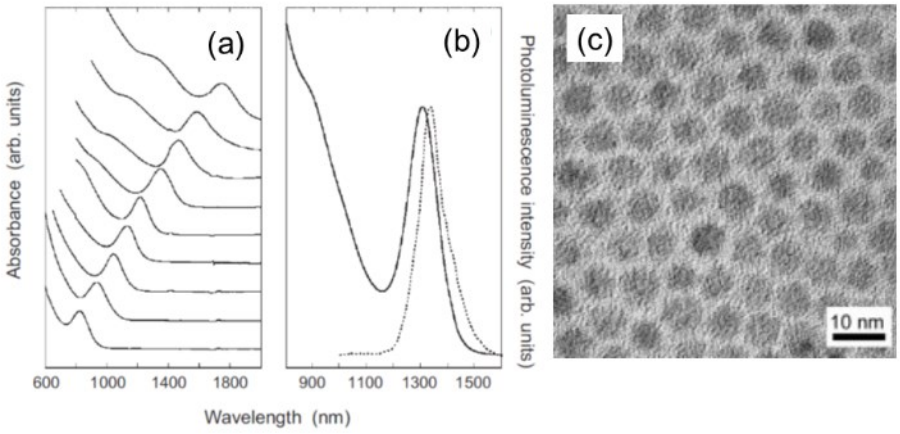

Figure 1.5 (a) Absorption spectra spanning the range of tuneable sizes of PbS QDs. (b) Band-edge absorption and photoluminescence peaks for PbS QDs 6.5 nm in diameter. (c) TEM image of colloidal PbS nanocrystals with an exciton absorption at 1440 nm. Figure 1.5 a~ c was obtained from reference[29].

Bohr radius of 18 nm, providing tunable fluorescence emission in the NIR regions (825-1750 nm), have gained increasing attention for bioimaging application. There are various synthetic routes for the synthesis of PbS QDs, including gas phase, solid-state synthesis and wet chemistry.[29] However, the gas phase and solid-state synthesis are limited as both are difficult to achieve tunable yet highly uniform particle size. The wet chemistry method, normally based on hot-injection of sulfur source to lead organometallic precursors, can solve this problem as an efficient low-cost approach to obtain high-quality PbS QDs because the nucleation and growth stages of PbS QDs are effectively separated by precisely controlling temperature during the hot-injection process. The initial well-known hot-injection synthesis for the production of monodisperse PbS QDs using lead oxide and bis(trimethylsilyl) sulfide [$(TMS)_2S$] was reported by Hines and Scholes.[29] The PbS QDs show first-excitonic absorption peaks tuned from 800 nm to 1800 nm (Figure 1.5a) and narrow size dispersion (15-20%, Figure 1.5c) with full width at half maximum (FWHM) of PL peak about 100 meV without any post-synthesis size-selective precipitation (Figure 1.5b). Currently, most of the studies regarding synthesis of PbS QDs follow this or slightly modified method. However, toxic chemical $(TMS)_2S$ was involved as the sulfur source in the QDs synthesis and the obligatory manipulation of air and moisture-sensitive $(TMS)_2S$ in a glove box made this synthesis complicated and inconvenient for large-scale industrial production. Another route, green hot-injection, in which $(TMS)_2S$ was replaced with elemental sulfur, has been subsequently developed for synthesizing PbS QDs by Ozin's group.[30] The high-

quality PbS QDs (with FWHM of PL peak *ca.* 52 meV) could be produced in multigram-scale quantities. However, the synthetic reaction was achieved in viscous solution with high concentration of lead precursors and molar ratio of (Pb/S), which could not easily operate under certain circumstances. Recently, Owen *et al.*[31] reported a fast and reproducible method of preparing PbS QDs with comparatively small sizes (first-excitonic absorption peak tuned down to 850 nm) and narrow size distribution using thiourea derivatives as sulfur source, which could be produced at industrially relevant reaction scales. Although other sulfur source can be used, complicated procedure was required to synthesize the thiourea precursors. Among these previously reported studies, Ozin's method is considered as relatively green and less costly due to the use of elemental sulfur. In our work, we made our effort to synthesize PbS QDs in a simpler and greener "non-viscous" oleylamine (OLA) system.

1.2.2.2 Core/shell quantum dots

Normally, QDs synthesized by the wet chemistry method are capped by organic ligands, which are sensitive to the surface state due to the large surface-to-volume ratio. The introduction of trap states on the surface of QDs increases the probability of nonradiative decay, thus decreasing the fluorescence quantum yield (QY). They also make QDs unstable during manipulation. It is thus essential to eliminate the surface trap by surface engineering to obtain more stable QDs with higher QY. To this end, a few groups have tried to grow an inorganic shell of larger band gap over the QDs to form a core/shell structure.[32-33] After coating with a robust inorganic shell, the core QDs are not only protected by shell against the surrounding environment, but also passivated with reduced surface trap sites. Therefore, the stability and fluorescence QY of core/shell QDs can be largely enhanced compared to the initial core QDs. For example, the cadmium-based QDs have been passivated by growing a CdS or ZnS shell using classical epitaxial growth. Peng *et al.*[32] firstly applied an extremely efficient technique named successive ion layer adsorption and reaction (SILAR) to grow a passivating shell of CdS over CdSe core (Figure 1.6a), in which the increase of QDs' size observed by TEM correlates well with the numbers of CdS monolayers estimated from the injected amount of Cd or S precursors. The synthesis of core/shell CdSe/CdS QDs with PLQY of 20~40% can be readily performed on a multigram scale and their size distribution was maintained even after five monolayers of CdS shell were grown onto the core CdSe QDs. The SILAR method is based on the formation of monolayer of shell at one time by alternating injections of cationic and anionic precursors into the reaction mixture of core QDs. The most attractive feature of SILAR technique is the precise thickness control without homogeneous nucleation of the shell QDs. This technique has been extended to NIR core/shell QDs, such as PbSe/PbS QDs.[34]

Recently, another less used approach, named cation exchange, has been reported to synthesize high-quality core/shell QDs. In this approach, the cationic precursor of shell materials is introduced during the reaction

and the shell growth proceeds at the expense of core cations; they are replaced by newly introduced cations and the anion sublattice remains basically undisturbed. Hollingsworth *et al.*[33] firstly demonstrated the controllable synthesis of PbSe/CdSe core/shell QDs *via* partially cation exchange method [Figure 1.6b and c]. The observed PL peak shifts to shorter wavelength as the effective size of PbSe core decreases resulting from sacrificial replacement of Pb with Cd during cation exchange. In addition, the PbSe/CdSe QDs exhibit enhanced PLQY compared to bare PbSe QDs due to the surface passivation of CdSe shell. Although a large number of visible-emitting core/shell QDs have been studied, relevant publications regarding NIR-emitting lead chalcogenide-based core/shell QDs, especially PbS-based core/shell QDs, are limited.

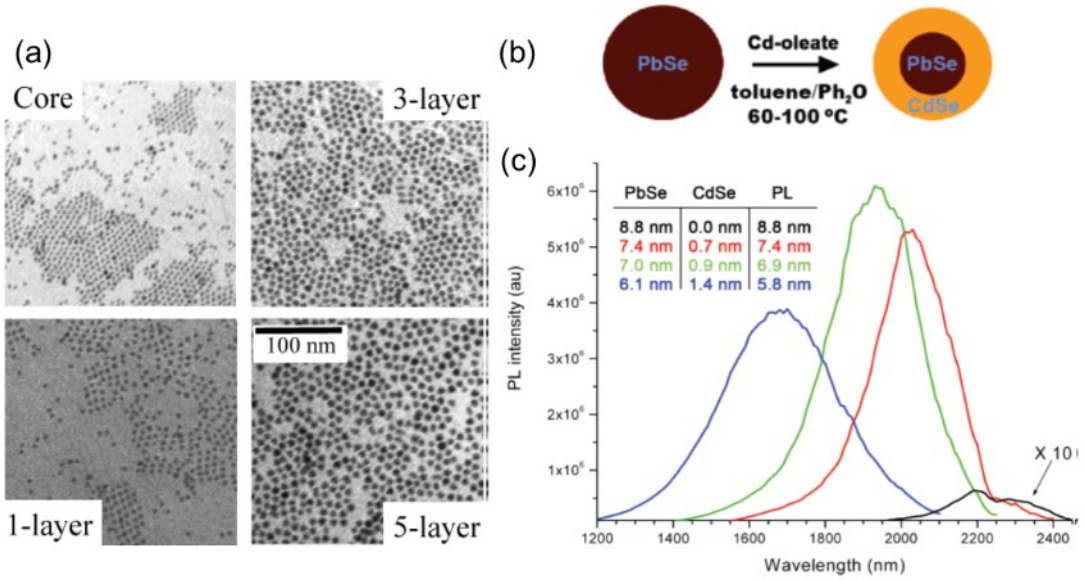

Figure 1.6 (a) TEM images of CdSe plain core nanocrystals and the corresponding core/shell nanocrystals with different shell thickness from the same SILAR reaction. (b) Scheme of synthesis of PbSe/CdSe QDs by cation exchange method. (c) PL spectra from a series of aliquots during CdSe shell formation, corresponding to 15 min, 2 h, and 24 h of reaction time proceeding from red to blue. Each spectrum is corrected for variation in optical density as well as grating and detector efficiencies to reflect relative QY. Shown in black is the original PbSe core, magnified 10-fold so its shape is discernible. The inset lists the calculated core diameter (column "PbSe") and shell thickness ("CdSe") from elemental analysis. Also included is the approximate effective core size predicted by the PL peak position ("PL"). Figure 1.6a was obtained from reference[32] and Figure 1.6b~c was obtained from reference[33].

1.2.3 Lanthanide-doped upconverting nanoparticles

Lanthanides (Ln) refer to the series of metallic chemical elements with atomic numbers 57 through 71 from lanthanum (La) to lutetium (Lu). Owing to their similar electron configuration $[Ln]4f^n5d^{0-1}6s^2$, Ln exhibits similar physical properties. Ln ions, normally exist in their most stable oxidation state as trivalent ions (Ln^{3+}), which are characterized by their unique $4f^n$ ($0<n<14$) electron configuration. Because of the diverse arrangements of electrons within the $4f^n$ configuration, Ln^{3+} ions offer abundant energy levels, mostly

originating from the Coulombic interaction and the spin-orbit coupling between f electrons,[35] as shown in Figure 1.7a. These arrangements endow Ln^{3+} capability of emitting photons in the UV-visible-NIR range through 4f-4f intra-configurational transitions. The radiative transition between the energy levels depends on the selected Ln^{3+} ions. It is obvious that a less radiative process occurs if the transition happens between a larger energy gap. For example, the radiation of Gd^{3+} locates at shorter wavelength in the UV region due to lack of adequate intermediate states while the transition of Sm^{3+} ($4f^5$), Eu^{3+} ($4f^6$), Tb^{3+} ($4f^8$), Dy^{3+} ($4f^9$) and Ho^{3+} ($4f^{10}$) can give out strong emission in the visible resulting from their adequate energy gaps. In addition, compared with those five ions mentioned above, Nd^{3+} ($4f^3$), Er^{3+} ($4f^{11}$) and Tm^{3+} ($4f^{12}$) possess smaller energy gaps, which usually leads to the NIR emission. With the rapid developments on lanthanide luminescence and related materials, especially on upconversion luminescence, the versatile lanthanide-doped UCNPs have gained tremendous attraction for bioimaging, diagnostics and therapeutics.

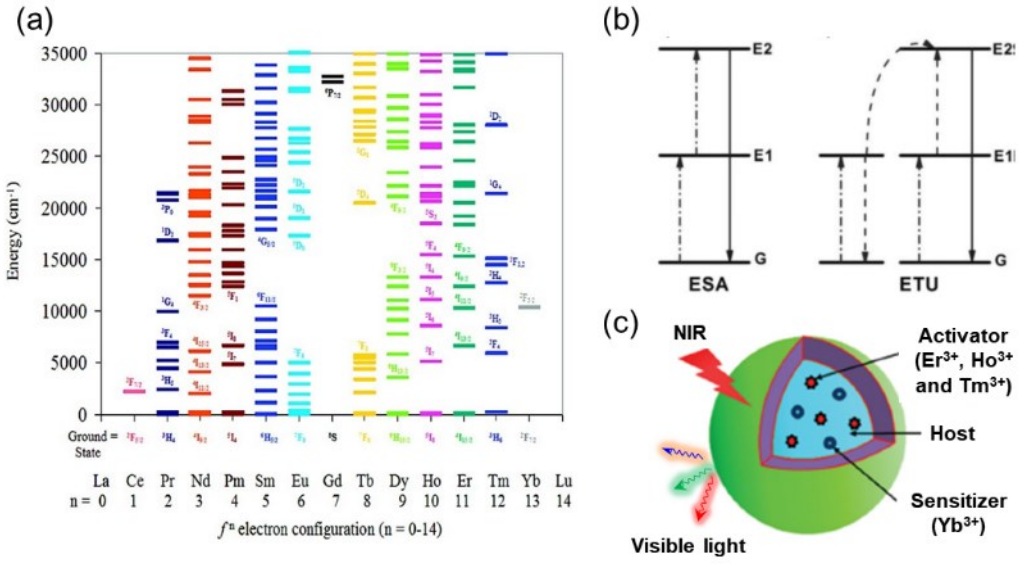

Figure 1.7 (a) Energy diagrams for Ln^{3+} in a $LaCl_3$ lattice. (b) UC processes for lanthanide-doped crystals: ESA and ETU. (c) Schematic illustration of UC nanoparticles composed of a crystalline host and lanthanide dopant ions (activator and sensitizer) embedded in the host lattice. Figure 1.7a was obtained from reference[35].

Upconversion is a phenomenon by the conversion of low energy of long-wavelength radiation (NIR excitation), to higher energy short-wavelength emission, usually in the UV and visible range *via* the anti-Stokes optical process. In this process, upconversion is achieved by absorbing two or more excitation photons to generate one emission photon, which can be explained by two main mechanisms: excited state absorption (ESA) and energy transfer upconversion (ETU), as shown in Figure 1.7b. In a typical ESA process, the emitting ions in the ground state sequentially absorb at least two photons of suitable energy to promote to the higher excited state. The UC emission occurs when the electron returns back to the ground state in a radiative manner. The requirements for ESA are rigorous as the adequate population of the

intermediate state is required to capture the second photon. Unlike ESA, ETU process usually involves two types of luminescent centers (sensitizer and activator). In ETU, one photon of energy is absorbed by the activator, but the absorbed sequential photon energy transferred from the neighboring ions (sensitizer) result in the population of higher excited states of emitting ions. Radiative emission could be observed as the activator drops back to the ground state. ETU is the most frequently observed in the lanthanide-doped UCNPs since it is easier to achieve compared to ESA. The UC process benefits from the long lifetime of intermediate excited states of excited Ln^{3+} ions, typically in the μs to ms range. These long lifetimes allow Ln^{3+} ions to be promoted to higher energy states by step-wise absorption of photons before returning to the ground state, followed by the generation of higher energy photon.

Basically, the lanthanide-doped UCNPs consist of inorganic crystalline host and doped ions (Ln^{3+} ions) acting as activators/sensitizers (Figure 1.7c). In addition to acting as a host matrix, the lattice has a strong influence on the UC of doped ions because it determines the distance between the doped ions, their coordination numbers and the anions surrounding the dopant. In order to achieve efficient UC, the optimal host should have low lattice phonon energy in order to reduce nonradiative losses, as well as high chemical stability. Of the available host materials for UC Ln^{3+} ions pairs, fluoride materials can fulfill these requirements, which possess low phonon energies (*ca.* 350 cm^{-1}) of the crystal lattice accompanied with the long lifetimes of the excited states of Ln^{3+} ions.[36] Among fluoride hosts, hexagonal (β-) phase $NaYF_4$ and $NaGdF_4$ are extensively studied as the most efficient UC host materials to date. It is believed that the high emission intensity of Ln^{3+} ions in β-phase $NaYF_4$/$NaGdF_4$ results from the interaction of doped ions located at two different lattice sites.[37] Regarding doped ions (Figure 1.7c), Yb^{3+} is normally selected as the sensitizer in the ETU system due to its unique and simple energy level with only one excited level of $^2F_{5/2}$ (Figure 1.7a), which is in resonance with the energy of excited 980 nm photons; While Er^{3+}, Tm^{3+} and Ho^{3+} are typically employed as activators in UC system owing to the long lifetime of excited states and excellent resonance energy transfer with transition ($^2F_{7/2}$-2F5/2) of Yb^{3+}.

1.3 Research Objectives and Organization

1.3.1 Our objectives

This thesis is divided into two parts with two highly related objectives. Specifically, two different main types of multifunctional nanoplatforms will be designed based on magnetic core. The first type is a core/shell structure with a fluorescence shell around a single magnetic core while the other multifunctional nanoplatform contains randomly distributed hundreds of magnetic and fluorescent NPs.

Part I: Multifunctional (superparamagnetic and NIR-to-NIR photoluminescent) nanocomposites with single magnetic core for dual-mode bioimaging.

So far, multifunctional (superparamagnetic and photoluminescent) NPs have been shown as extremely useful tools for bioapplications. One of the most interesting bioapplications is dual-mode imaging. It is well known that optical imaging shows great potential to translate into the clinic due to its high sensitivity at the subcellular level and the relatively low cost of imaging facilities; whereas MR imaging is considered as a superior technique for obtaining anatomical, physiological and functional images with high 3D spatial resolution. The integration of optical and MR imaging for dual-mode imaging is clearly advantageous as it will allow retrieving both macroscopic and subcellular information of biological species, thus leading to improved diagnostic accuracy. Thus, it is of great importance to engineer new, high-sensitivity multifunctional (superparamagnetic and photoluminescent) NPs for dual-mode imaging. However, multifunctional (superparamagnetic and photoluminescent) NPs in most cases are based on visible emitting organic dyes, QDs and UCNPs, which show low tissue penetration and severe autofluorescence from biological tissue, thereby limiting their use as bioprobe for *in vivo* imaging. To address this issue, the ideal photoluminescent components with their absorption and emission wavelengths in the optically transparent biological windows (NIR-I/II) are highly desired. This can ensure that both the excitation and emission signals are less attenuated for acquiring deep-tissue imaging with higher signal-to-noise ratio.

Therefore, the objectives for this part are as follows:

1. Preparing and characterizing novel multifunctional (superparamagnetic and photoluminescent) core/shell/shell $Fe_3O_4/SiO_2/NaYF_4:Nd^{3+}$ NPs.
2. Investigating the NIR-to-NIR photoluminescence properties of $Fe_3O_4/SiO_2/NaYF_4:Nd^{3+}$ NPs.
3. Comparing the deep-tissue penetration properties of NIR-to-NIR $Fe_3O_4/SiO_2/NaYF_4:Nd^{3+}$ NPs with visible-emitting upconverting $Fe_3O_4/SiO_2/NaYF_4:Er^{3+}$, Yb^{3+} NPs by *ex vivo* optical imaging.
4. Exploiting $Fe_3O_4/SiO_2/NaYF_4:Nd^{3+}$ NPs as T_2 contrast agents for MR imaging

Part II: Multifunctional nanoplatforms based on multiple magnetic NPs and NIR QDs with therapeutic modality

The development of advanced multifunctional theranostic nanoplatforms is critical for addressing the challenges with cancers treatment, aiming to realize the ultimate goals of personalized medicine. These systems are expected to simultaneously carry both diagnostic and therapeutic functions to get high-quality images identifying the tumor site/morphology and to achieve the enhanced cure rate of cancers through specific therapeutic strategies. The survival rate can be largely increased using these multifunctional theranostic nanoplatforms. Specifically, compared with optical imaging and MR imaging alone, as individual diagnostic tools, bimodal imaging has shown to be particularly attractive because they can provide complementary information, as we mentioned above. Regarding the nanoplatform-related therapeutic modalities, magnetothermal therapy is hindered by poor thermal energy transfer efficiency of currently reported magnetic NPs, while photothermal therapy is not suitable for cancer cells in distant organs due to the limited penetration depth of light into the tissue. Thus, the integration of magnetothermal and photothermal therapy into a single nanoplatform may provide a dual-mode therapeutic approach to achieve high-efficiency and deep-tissue cancer treatment. In addition, conventional chemotherapy against cancers often suffers from the low therapeutic efficacy (since the mono-therapy approach cannot cure cancer in a synergistic or an additive manner) and severe side effects due to uncontrollable drug release characteristics. Multifunctional (superparamagnetic and photoluminescent) nanoplatform with drug-delivery modality can improve the performance of chemotherapeutic agents and reduce the overall toxicity by enhancing the specificity of the drug delivery through tumor targeting in the presence of an applied magnetic field. Furthermore, designing external stimulus-responsive nanoplatform for remotely controlled cancer treatment can potentially avoid drug overdose and reduce side effects.

Therefore, the objectives for this part are as follows:

1. Preparing and characterizing self-assembled Fe_3O_4 and PbS/CdS (NIR-II) supernanoparticles [SASNs (NIR-II)], and studying their self-assembly formation mechanism.
2. Investigating the application of SASNs (NIR-II) for deep-tissue bimodal (optical and MR) imaging.
3. Studying the dual-mode (magnetothermal and photothermal therapy) heating treatment using SASNs (NIR-II).
4. Synthesizing and characterizing large-pore $mSiO_2$ and $mSiO_2$ based multifunctional (superparamagnetic and photoluminescent) nanoplatform ($mSiO_2$@PbS/CdS-Fe_3O_4).
5. Monitoring the multi-stimuli (pH/MF/NIR) responsive drug release behavior of $mSiO_2$@PbS/CdS-Fe_3O_4 after being loaded with anticancer drug.

6. Studying the synergistic effect from the integrated heating mode and multi-stimuli responsive drug release of $mSiO_2$@PbS/CdS-Fe_3O_4.

1.3.2 Thesis organization

This thesis is divided into four chapters and organized as follows:

Chapter 1 Introduction: This chapter briefly introduces the basic knowledge of the background and objectives of this thesis.

Chapter 2 Literature review on multifunctional magnetic-fluorescent hybrid nanoparticles for bioapplication

Chapter 3 Experimental and characterization: This chapter describes the experimental details of synthesis of Fe_3O_4 NPs, PbS QDs, PbS/CdS QDs, $mSiO_2$ and other related hybrid (superparamagnetic and photoluminescent) nanocomposites. The main characterization techniques for obtained NPs are also presented.

Chapter 4 Results and discussion:

Part I: Multifunctional (superparamagnetic and NIR-to-NIR photoluminescent) nanocomposites for dual-mode (optical and MR) bioimaging, and the publication related to this chapter is

Fan Yang, Artiom Skripka, Antonio Benayas, Xianke Dong, Sung Hwa Hong, Fuqiang Ren, Jung Kwon Oh, Xinyu Liu, Fiorenzo Vetrone, and Dongling Ma, An Integrated Multifunctional Nanoplatform for Deep-tissue Dual-Mode Imaging. *Adv. Funct. Mater.,* 28 (2018) 1706235.

Part II: Self-assembled iron oxide and NIR PbS/CdS QDs for deep-tissue bimodal imaging and amplified dual-mode (magnetothermal and photothermal therapy) heating treatment, and the publication related to this chapter is

Fan Yang, Artiom Skripka, Maryam Sadat Tabatabaei, Sung Hwa Hong, Fuqiang Ren, Antonio Benayas, Jung Kwon Oh, Sylvain Martel, Xinyu Liu, Fiorenzo Vetrone, and Dongling Ma, Multifunctional self-assembled supernanoparticles for deep-tissue bimodal imaging and amplified dual-mode heating treatment. *ACS Nano,* 13 (2019) 408-420.

Part III: Multifunctional large-pore $mSiO_2$ based multifunctional nanoplatforms used for bioimaging and multi-stimuli responsive drug delivery, and the publication related to this chapter is

Fan Yang, Artiom Skripka, Maryam Sadat Tabatabaei, Sung Hwa Hong, Fuqiang Ren, Yue Huang, Jung Kwon Oh, Sylvain Martel, Xinyu Liu, Fiorenzo Vetrone, and Dongling Ma, Magnetic-Photoluminescent Nanoplatform Built from Large-Pore Mesoporous Silica. *Chem. Mater.,* 31 (2019) 3201-3210.

Chapter 5 Conclusions and Perspectives: Main conclusions are presented based on the results and analysis, and some potential work in the future is proposed.

In this thesis, most of the work was completed by Fan Yang, however, some parts were conducted through collaboration. More specifically, cell culture and viability assays were performed by Sung Hwa Hong working in our collaborator Prof. John Oh's group at Concordia University. The hyperthermia experiment was conducted by Maryam Sadat Tabatabaei in Prof. Sylvain Martel's group at Polytechnique Montréal. The TEM measurements were carried out by Jean-Philippe Masse at Polytechnique Montréal. Artiom Skripka and Dr. Antonio Benayas assisted me with the deep-tissue photoluminescence imaging experiments.

CHAPTER 2 LITERATURE REVIEW ON MUTIFUNCTIONAL FLUORESCENT-MAGNETIC HYBIRD NANOPARTICLES FOR BIOAPPLICATION

In this chapter a literature survey on synthesis of multifunctional fluorescent-magnetic hybrid NPs and their bioapplications is presented. In particular, various synthetic strategies and approaches for the preparation of multifunctional fluorescent-magnetic hybrid NPs are described and discussed. The main bioapplications of multifunctional fluorescent-magnetic NPs, including multimodal imaging, magnetic targeted drug delivery and cancer therapy, are discussed.

2.1 Introduction

Over the last two decades, the rapid development in nanotechnology has allowed researchers to engineer various functional nanomaterials with distinct chemical and physical properties. Up to now, a large variety of NPs with different shapes, such as nanospheres, nanocubes and nanocages made of different materials, mainly including metals, semiconductors, carbon and oxide-based materials, have been fabricated and explored for their application in many scientific fields, such as plasmonics, energy conversion, catalysis and biomedicine.[38-42] Amongst these NPs, unlike the properties of the corresponding bulk materials, magnetic NPs (*e.g.* superparamagnetic iron oxide NPs) and fluorescent nanocomponents (*e.g.* QDs and lanthanide-doped UCNPs) represent nowadays extremely hot research fields due to their intrinsic physicochemical properties and potential bioapplications.[41-43]

Magnetic iron oxide NPs, such as magnetite (Fe_3O_4), maghemite (γ-Fe_2O_3) and MFe_2O_4 (M= Ni, Co, or Mn), belong to the spinel-structured ferrite family. They have been widely used for biomedical applications over the past few decades. The main reason is that iron oxide NPs are biocompatible as iron is a naturally essential element in the human body and can be utilized by the body in metabolic processes. When the size of magnetic NPs decreases to a critical size (of the order of 10 nm), each NP becomes a single magnetic domain, which results in superparamagnetic behavior since the thermal energy can overcome the anisotropy energy barrier of a single NP. The superparamagnetic NPs are easily saturated under an external magnetic field and show near-zero residual magnetization and coercivity upon removal of external magnetic field. Therefore, the superparamagnetic NPs can be easily manipulated by an external magnetic field and well dispersed again in solution in the absence of external magnetic field, distinctly different from the behavior of classic ferromagnetic NPs that form nonseparable agglomerates after initial magnetic confinement. This unique superparamagnetic property endows them tremendous advantages for bioapplications. For example, superparamagnetic NPs can be used to magnetically confine, label and separate various biological species

(DNAs/mRNA, proteins, bacteria, cancer cells, *etc.*) and thus allow for ultrasensitive biodetection. They can also serve as magnetic resonance (MR) imaging contrast agents for the diagnosis of malignant tissues, nanoscale vehicles for carrying therapeutic payloads (anticancer drugs, small inhibitory RNA) and delivering them to desired tumor sites in a target-specific manner, as well as hyperthermia agents for treating cancers under an alternating magnetic field.

The other attractive possibility of magnetic NPs is the fact that they can be integrated with fluorescent nanocomponents to form new types of multifunctional fluorescent-magnetic hybrid NPs. These fluorescent nanocomponents include organic dyes, QDs and lanthanide-doped UCNPs as mentioned above, which are very promising probes for bioimaging application. In the last decade, the research field of combined magnetic and fluorescent NPs has become a fast-evolving branch of science with increasing number of developments every year. The combination of magnetic and fluorescent entities provides new two-in-one multi-functional nanomaterials to act as multi-dimensional (imaging, confining and treatment) tools with a broad range of bioapplications. Firstly, multifunctional fluorescent-magnetic hybrid NPs are capable of separation, detection and tracking of different cells by the application of external magnetic field. After operation by magnetic field, the fluorescent component can be beneficial for distinguishing the normal cells and cancer cells *via* a fluorescent microscope, which in principle could achieve the cancer cells diagnosis at an early stage. Secondly, these nanocomposites can serve as diagnostic imaging tools based on bimodal (optical and MR) imaging, which allow retrieving macroscopic (MR imaging) and subcellular information (optical imaging) of biological species, thereby leading to improved diagnostic accuracy. Furthermore, another important bioapplication of these NPs is their use as effective carriers to deliver anticancer drugs and biomolecules to specific sites under an external magnetic field, and thus largely reducing the side effects to other normal tissues compared with conventional chemotherapy. The fluorescence signal can simultaneously provide the visual imaging of cancer treatment for the purpose of realizing two-in-one theranostic (*i.e.*, therapeutic and diagnostic) tool. Finally, multifunctional fluorescent-magnetic NPs can be potentially exploited for both magnetothermal and photothermal heating therapy, overcoming the main drawbacks of each type of heating separately and realizing high-efficiency and deep-tissue cancer treatment. The dual-mode (magnetothermal and photothermal) heating can be provided as an adjuvant therapy tool in targeted-drug delivery therapy with multifunctional NPs for cancer treatment.

As we can see, the integration of fluorescent and magnetic nanocomponents into single nanocomposite leads to fascinating multifunctional properties, which hold great potential to open up the prospects in the field of nanobiotechnology. Therefore, the multifunctional fluorescent-magnetic hybrid NPs have attracted increasing research interest and been the subject of several interesting review articles.[44-48] In this review, we will only focus on the recent developments of multifunctional fluorescent-magnetic hybrid NPs since

2010 and describe the classifications and synthetic routes that used to prepare such hybrid NPs in detail. In addition, the potential applications of these fluorescent-magnetic multifunctional NPs in multimodal bioimaging, magnetic targeted drug delivery and cancer therapy will be introduced.

2.2 Types and synthetic routes of multifunctional fluorescent-magnetic hybrid nanoparticles

The integration of magnetic and fluorescent components into a desired multifunctional nanoplatform is of great importance for biomedical applications. Up to date, although several strategies were attempted to fabricate highly stable and monodispersed multifunctional NPs with both fluorescent and magnetic properties, the area is still in its developing stage and synthesis could be quite complicated. In the following text, we describe the four major types of multifunctional fluorescent-magnetic NPs based on the synthetic strategies and their structure.

2.2.1 Silica-based fluorescent-magnetic nanoparticles

Silica coating has been a widely used technique for surface modification of NPs since silica has remarkable stability, optical transparency, high biocompatibility and ease of surface modification.[49] Moreover, the silica coating enables the transfer of functional NPs from an organic phase to aqueous solution and protects the NPs against the physicochemical influence from aqueous media, thus enhancing their colloidal stability.[49] With all these advantages, silica-based method is considered to be one of the most effective routes to prepare fluorescent-magnetic NPs.

2.2.1.1 Fluorescent silica shell coated magnetic nanoparticles

Many fluorescent-magnetic NPs based on fluorescent silica shell have been reported in the last few years. In most cases, dyes are physically incorporated into a silica shell in the hydrolysis process of tetraethyl orthosilicate (TEOS) during the formation of the silica shell around magnetic cores. The others immobilize dyes on the surface of silica coated magnetic NPs through a stable covalent linkage.

Zheng *et al.*[50] fabricated novel multifunctional core/shell mesoporous silica NPs for dual-mode (MR and fluorescence) imaging, cell targeting and photosensitization treatment (Figure 2.1a). To incorporate fluorescein isothiocyanate (FITC) into the multifunctional NPs, FITC was treated with 3-aminopropyltriethoxysilane (APTES) and then co-hydrolyzed with TEOS during the reverse micelle encapsulation process to yield Fe_3O_4@fluorescent-SiO_2-shell NPs. The encapsulation of superparamagnetic NPs and dyes into mesoporous silica matrix endowed the multifunctional NPs with MR and fluorescence imaging capabilities, allowing non-invasive tracking and monitoring of NPs within cells. The same method has also been reported to prepare other similar multifunctional fluorescent-magnetic NPs, including β-cyclodextrin conjugated fluorescein-doped magnetic silica NPs [Fe_3O_4@SiO_2(FITC)-FA/CMCD NPs,[51] Janus fluorescent-magnetic mesoporous silica NPs,[52] chlorotoxin-conjugated magnetic and fluorescent

NPs,[53] multilayer fluorescent-magnetic FA-conjugated Fe_3O_4@SiO_2@P(HEMA)@P(NIPAAM-*co*-AA) NPs,[54] multifunctional fluorescent-magnetic eccentric-(concentric-Fe_3O_4@SiO_2)@polyacrylic acid core-shell nanocomposites.[55] With the same isothiocyanate moiety as FITC, rhodamine B isothiocyanate (RITC) is another commonly used fluorescent dye that has been embedded within silica matrix to fabricate the fluorescent-magnetic NPs. For example, Li *et al.* [56] reported a facile and reproducible route to prepare monodisperse and highly uniform branched polyethyleneimine (PEI) coated fluorescent mesoporous SiO_2 ($fmSiO_2$) shells and Fe_3O_4 cores (denoted as PEI-Fe_3O_4@$fmSiO_2$ yolk–shell NPs), in which RITC as fluorescent component was entrapped in silica shell during the hydrolysis process of TEOS. Chang and co-workers presented the incorporation of iron oxide NPs and RITC into a silica coating of NPs with further conjugation with cetuximab for targeting and imaging of cancer cells.[57] In addition, highly versatile nanocomposites were synthesized by decorating the surface of mesoporous FITC/RITC-incorporated silica NPs with multiple magnetic NPs, for the purpose of achieving simultaneous enhanced MR and fluorescence imaging and drug delivery.[58] By utilizing this method, other dyes, such as Tris(2,2'-bipyridyl)dichlororuthenium(II) hexahydrate (Rubpy) [59] and 7-hydroxycoumarin,[60] were also encapsulated into the silica shell to form fluorescent-magnetic NPs.

Another strategy to obtain fluorescent silica shell coated magnetic NPs is to link the dye on the surface of the silica shell through covalent interaction. Sykova *et al.*[61] reported the preparation of multifunctional fluorescent-magnetic FITC-labeled γ-Fe_2O_3 NPs for MR and fluorescent imaging of a rat brain (Figure 2.1b). The synthesis of these hybrid NPs involved the reaction of the isothiocyanate groups of FITC with the primary amino groups of APTES on the silica surface, resulting in the formation of a stable thiourea linkage between FITC and APTES on the NPs surface.[62] Following the same method, cyanine dyes, including Cy5[63] and Cy5.5[64], were immobilized on the silica shell *via* covalent linking to fabricated multifunctional fluorescent-magnetic core/shell NPs for bioimaging.

Considering the small size of organic dye molecules, these multifunctional fluorescent-magnetic NPs can retain relatively small size while with reasonable brightness. The silica surface makes it suitable for further functionalization with other biomolecules (proteins, DNA, antibodies, peptides, drugs). Nonetheless, these NPs usually suffer from intrinsically poor photostability arise from organic dyes and easy to agglomerated in solution due to the lack of appropriate surface modification. The potential fluorescence quenching due to the close distance between magnetic core and incorporated dye in silica shell is another concern.

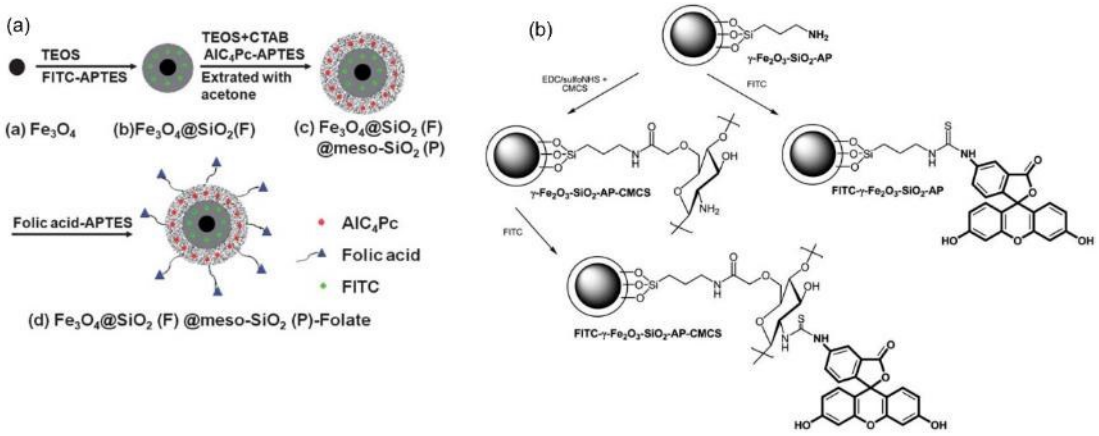

Figure 2.1 (a) Synthetic procedure of Fe_3O_4@SiO_2(F)@meso-SiO_2(P)-Folate nanoparticles. (b) Labeling of γ-Fe_2O_3-SiO_2-AP and γ-Fe_2O_3-SiO_2-AP-CMCS nanoparticles with FITC. Figure 2.1a was taken from reference[50] and Figure 2.1b was taken from reference[61].

2.2.1.2 Magnetic and fluorescent nanoparticles co-embedded into silica matrix

The co-embedment of magnetic and fluorescent NPs into silica matrix is a simple strategy to prepare multifunctional NPs, which has been reported by several groups.[65-67] This approach involves the encapsulation of mixed fluorescent and magnetic NPs in a silica matrix in a random way by hydrolysis and condensation of TEOS under ammonia catalysis based on the Stöber or reverse microemulsion method, which are known as two common strategies for silica particle synthesis and silica coating.[68] The Stöber synthesis is generally applied to the NPs that are dispersed in polar media while the reverse microemulsion synthesis is an excellent approach for silica coating of hydrophobic NPs.[69] As a simple one-step synthesis protocol to prepare silica coating, the Stöber synthesis can be adopted to prepare silica encapsulated magnetic and fluorescent NPs in the mixture of ethanol and water under alkaline condition. For example, Wu *et al.*[66] presented the fabrication of core-shell-structured $NaYF_4$:Yb, Er/Tm@SiO_2@Fe_3O_4 NPs for bioimaging (Figure 2.2a~g) using the Stöber method. In their process, the EDTA-capped $NaYF_4$:Yb, Er/Tm NPs were mixed with oleic acid (OA)-modified magnetic Fe_3O_4 NPs in isopropyl alcohol, followed by the addition of TEOS, APTES and ammonium hydroxide. Similarly, Alveroglu *et al.* reported ZnS@Fe_3O_4 fluorescent/magnetic bifunctional nanospheres in which the QDs and Fe_3O_4 NPs were located inside a SiO_2 network.[67]

In addition to the Stöber synthesis, reverse microemulsions, also termed water-in-oil microemulsions, which requires the addition of surfactant (such as Triton-X 100, Igepal CO-520, *etc.*) to the organic phase, have been found favorable as nanoreactors for the synthesis of multifunctional fluorescent-magnetic NPs with diverse sizes and functions.[69] For example, Tan *et al.*[65] reported magnetic-encoded fluorescent (CdTe/Fe_3O_4)@SiO_2 multifunctional nanospheres (FMNS) by adjusting the initial ratio of Fe_3O_4 to CdTe

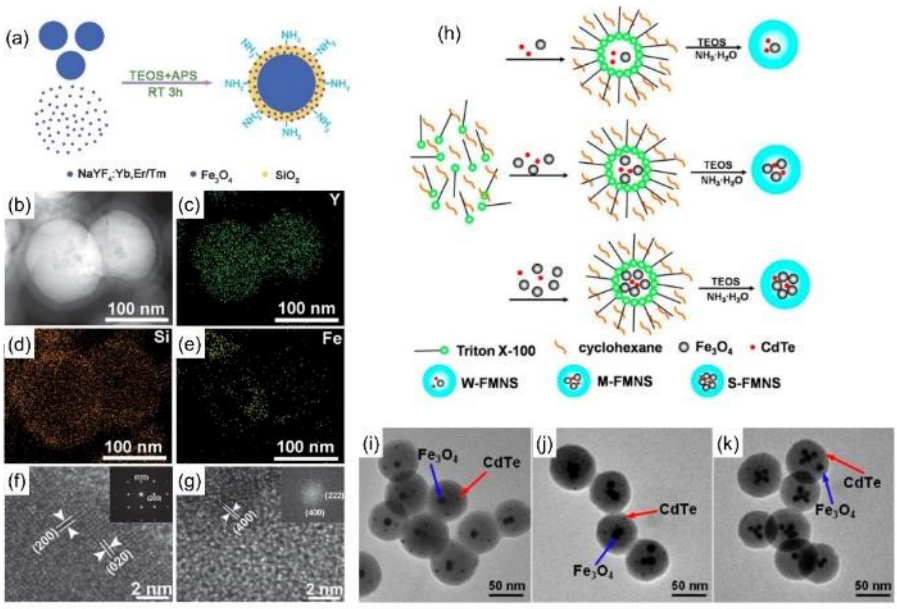

Figure 2.2 (a) Schematic illustration of the formation of $NaYF_4$:Yb, Er/Tm@SiO_2@Fe_3O_4 NPs. (b) Bright-field TEM image and (c~e) EDX elemental mappings of $NaYF_4$:Yb, Er/Tm@SiO_2@Fe_3O_4, (f) HRTEM image of $NaYF_4$:Yb, Er/Tm@SiO_2@Fe_3O_4 (inset: SAED image of $NaYF_4$:Yb, Er) and (g) HRTEM image of Fe_3O_4 (inset: FFT image of Fe_3O_4). (h) Schematic of fabrication of (CdTe/Fe_3O_4)@SiO_2 FMNS with different magnetic potentials: weak (WFMNS), moderate (M-FMNS), and strong (S-FMNS), Respectively. TEM images of (CdTe/Fe_3O_4)@SiO_2 FMNS: (i) W-FMNS, (j) M-FMNS, and (k) S-FMNS. Figure 2.2a~g was taken from reference[66] and Figure 2.3h~k was taken from reference[65].

in the synthesis process based on reverse microemulsion method, as demonstrated in Figure 2.2h~k. The same method was also used by Su and co-workers to fabricate CdTe-Fe_3O_4-SiO_2 microspheres, which further covalently bonded to graphene oxide (GO) *via* a facile amidation process between the carboxyl groups on GO and the amino groups on SiO_2 microspheres.[70] The reverse microemulsion method was also chosen for the synthesis of BRCAA1 monoclonal antibody-conjugated fluorescent magnetic nanoprobes, which consist of silica encapsulated CdTe QDs and Fe_3O_4 NPs.[71]

Unlike other strategies requiring complicated multi-step reactions to prepare multifunctional fluorescent and magnetic NPs, co-embedment of fluorescent and magnetic NPs into silica matrix is based on a simple one-step synthetic approach. Moreover, as the fluorescent and magnetic NPs are co-encapsulated by the robust silica shell, these multifunctional NPs are relatively stable in biological environment and the toxicity of the NPs can be effectively suppressed.

2.2.1.3 Magnetic nanoparticles linked to fluorescent entity via silica spacer

Direct linking of magnetic NPs to fluorescent entity, such as lanthanide-doped NPs and QDs, usually requires the use of silica shell as a spacer in order to minimize the lattice mismatch between magnetic NPs and fluorescent entity and bypass any possible fluorescent quenching by the superparamagnetic core.

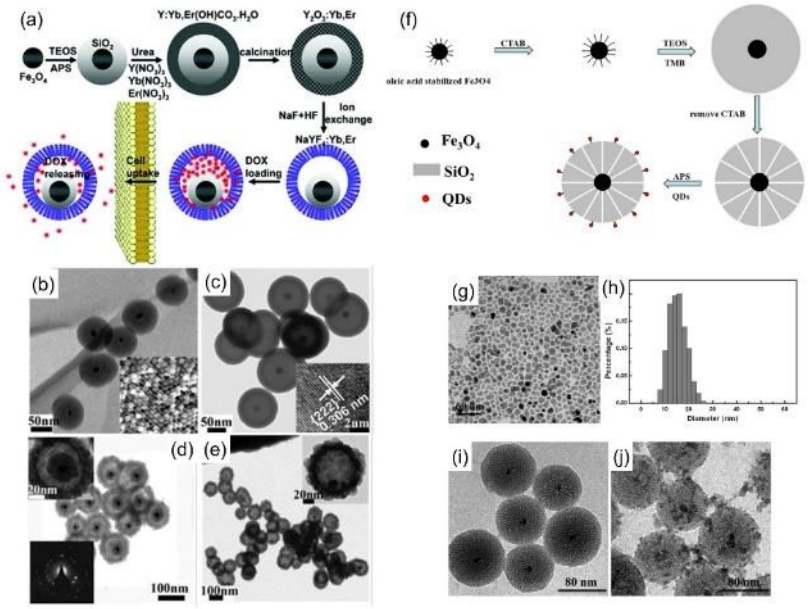

Figure 2.3 (a) Synthetic procedure for the drug-loaded Fe_3O_4@SiO_2@α-NaYF/Yb, Er nanorattles (DOX-MUC-F-NR). (b) TEM and SEM (the inset in (b)) images of Fe_3O_4@SiO_2 nanospheres. (c) TEM image of magnetic upconversion oxide nanospheres (MUC-O-NS); inset in (c) is a HRTEM image after growing the outer Y_2O_3/Yb, Er layer. (d) TEM image of the MUC-F-NR; insets are higher-magnification TEM image of one (upper left) and the SAED image recorded on part of the α-$NaYF_4$/Yb, Er shell (lower left). (e) TEM image of Fe_3O_4@SiO_2@α-NaYF/Yb, Er with SiO_2 fully etched; inset is a higher-magnification TEM image of a single hollow nanosphere. (f) Illustration of the preparation of multifunctional mesoporous Fe_3O_4/SiO_2/CdTe nanoprobe. (g) TEM images of oleic acid-stabilized Fe_3O_4 nanoparticles and (h) their particle size statistics. (i) TEM images of mesoporous Fe_3O_4@SiO_2 particles and (j) mesoporous Fe_3O_4/SiO_2/CdTe nanoprobes. Figures 2.3a~e was taken from reference[72] and Figure 2.3f~j was taken from reference[73].

Recently, Zhang *et al.*[72] prepared mesoporous multifunctional fluorescent and magnetic nanorattles, in which each hydrophilic rare earth-doped $NaYF_4$ shell contained loose magnetic NPs inside (Figure 2.3a~e). The magnetic upconversion fluoride nanorattles (MUC-F-NR) were synthesized by a multistep method. Specifically, the Fe_3O_4@SiO_2 NPs with diameters of ~90 nm (Figure 2.3b) were prepared using the reverse-microemulsion method, followed by coating a layer of Y/Yb, Er(OH)CO_3.H_2O *via* a homogeneous precipitation method. The thermal treatment then transformed the amorphous Y/Yb, Er(OH)CO_3.H_2O into the cubic phase of Y_2O_3:Yb, Er (Figure 2.3c). The final product of magnetic upconversion fluoride nanorattles (MUC-F-NR) Fe_3O_4@SiO_2@α-$NaYF_4$/Yb,Er NPs was formed *via* an ion-exchange process of magnetic upconversion oxide nanospheres (MUC-O-NS) in the presence of HF and NaF solution (Figure 2.3d,e). In their synthesis, the SiO_2 layer can not only reduce the lattice mismatch between the Fe_3O_4 core and UCNPs shell and fluorescence quenching by the Fe_3O_4 NPs, but also avoid iron leaching in acidic biological environments. Following the similar synthesis routine, other multifunctional particles based on rare earth-doped NPs *via* silica spacer, such as superparamagnetic iron oxide yolk-shell nanocapsules

(SPIO@Y_2O_3:Eu)[74], multifunctional monodispersed magnetic radioluminescent NPs (γ-Fe_2O_3@SiO_2@Gd_2O_3:Eu)[75], core-shell Fe_3O_4@$NaLuF_4$:Yb,Er/Tm nanostructure[76], multifunctional (magnetic, mesoporous, and upconversion luminescent) Fe_3O_4@nSiO_2@mSiO_2@$NaYF_4$:Yb^{3+}, Er^{3+} nanocomposites[77] have been reported. The rare earth precursors of all these multifunctional NPs are deposited on the silica shell by the homogeneous precipitation method. Interestingly, the calcination treatment at high temperature (> 400 ℃) required to transform amorphous lanthanide precursors to crystalline lanthanide-doped shells results in the shrink of silica, thus generating the yolk-shell structure. Such structure is extremely suitable for drug loading and delivery.

Alternatively, QDs as another fluorescent entity can be linked to magnetic NPs *via* silica spacer. For example, Cheng and co-works[73] reported multifunctional mesoporous Fe_3O_4/SiO_2/CdTe magnetic-fluorescent composite nanoprobes (Figure 2.3f~j). The synthetic procedure involves two steps: 1) the controlled growth of mesoporous silica layer on the surface of Fe_3O_4 NPs (Figure 2.3i); 2) layer-by-layer assembly of APTES and fluorescent CdTe QDs on the surface of mesoporous Fe_3O_4/SiO_2 NPs (Figure 2.3j). The coupling of QDs to mesoporous silica shell is mainly due to the electrostatic interaction between negative-charged carboxyl groups on QDs and positive-charged amino groups on SiO_2 NPs. Following the same synthesis, Zhu *et al.* [78] proposed a novel type of multi-shell structured multi-functional nanoprobe (Fe_3O_4/SiO_2/CdSeTe@ZnS-SiO_2/polydopamine), which is favored for its high fluorescent intensity and rapid magnetic separation. In another study, owing to strong coordination interaction between thiol-modified Fe_3O_4/SiO_2 NPs and water-soluble mercaptopropionic acid (MPA)-capped CdSe-ZnS QDs, a multifunctional magnetic-fluorescent nanocomposite (Fe_3O_4/SiO_2-QDs) was fabricated for radio frequency (RF) nanohyperthermia of cancer cells[79]. The same method was used by Dong *et al.*[80] in the development of hydrangea-like magneto-fluorescent Fe_3O_4-SH@CdSe/CdS/ZnS NPs.

Although these multifunctional NPs prepared with the use of silica spacer can maintain high fluorescence due to the effective separation of fluorescent and magnetic components, the multi-step synthetic method could increase the complexity for preparing NPs and have a reproducibility issue.

2.2.2 Polymer based fluorescent-magnetic nanoparticles

The polymerization coating method is another common routine to prepare multifunctional NPs. Normally, the polymer-based fluorescent-magnetic NPs can be achieved by polymer assisted coupling method and co-embedment method, similar to that of the silica method (2.2.1) in basic principle.

2.2.2.1 Polymer assisted fluorescent-magnetic nanoparticles via coupling method

Magnetic NPs or fluorescent NPs synthesized by chemical or physical method may not be directly integrated, depending on their surface chemistry. With the use of a polymer, the combination of

magnetic/fluorescent NPs becomes versatile and can proceed through coupling interactions (covalent linking or electrostatic adsorption) between the functional groups of polymer and ligands on the surface of magnetic/fluorescent NPs.

Covalent linking method is a commonly used method to bind different functional NPs together. With regard to the preparation of multifunctional NPs, the polymer bearing functional groups, such as -SH, -NH_2 and -COOH, is required to coat either magnetic or fluorescent NPs, which subsequently reacts with each other to form an irreversible bonding and produces multifunctional nanocomposites. By employing this approach, Shi *et al.*[81] prepared multifunctional nanospheres for cancer diagnosis and treatment (Figure 2.4a). The synthesis of these multifunctional nanospheres included two steps:1) covalent conjugation of amine-functionalized fluorescent QDs in the NIR range (~800 nm) to the surface of carboxylate-functionalized polyethylene oxide modified magnetic NPs through conventional 1-Ethyl-3-(3-dimethylaminopropyl)carbodiimide hydrochloride/N-hydroxysuccinimide (EDC/NHS) coupling; 2) loading of chemotherapeutic agent paclitaxel (PTX) onto the surface of these QDs-conjugated magnetic NPs using a layer of biodegradable poly(lactic-*co*-glycolic acid) (PLGA). The same method was used by Pham *et al.*[82] to prepare hybrid imaging nanoprobes for multimodal bioimaging, in which the superparamagnetic Fe_3O_4 NPs were conjugated with the visible emitting (~600 nm) fluorescent CdTe/CdS QDs *via* covalent linking between the oxidized dextran shell of magnetic NPs and the glutathione ligands of QDs. In addition, magnetic NPs coated by polymer with sticking-out functional groups are easily linked to the dyes with different functional groups (-COOH, -CHO, -NH_2) *via* covalent bonding. For example, fluorescent-magnetic NPs were obtained by covalently bonding FITC to the NH_2 group of poly(poly(ethylene glycol)monomethacrylate)-grafted Fe_3O_4[83]; O-carboxymethyl chitosan stabilized magnetic NPs with amine groups on the surface allowed for the covalent attachment of RITC.[84]

Alternatively, electrostatic adsorption can also be used to form multifunctional NPs. In this scenario, the charged polymers are coated on the magnetic (or fluorescent) NPs and then coupled with oppositely charged fluorescent (or magnetic) NPs *via* electrostatic interaction. In some cases, differently charged polymer or polyelectrolyte layers are applied layer by layer (LBL). This method has several advantages, including the flexibility to have either positively or negatively charged NPs simply by changing the last deposition layer and relatively easy and accurate tuning of polymer coating's thickness by controlling the number of deposition cycles of polymers. For example, Lim *et al.*[85] presented a robust chemical strategy to synthesize high-performance MR/NIR multimodal imaging nanoprobes (Figure 2.4 c-e). In their synthesis, poly-(γ-glutamic acid), as a negatively charged polyelectrolyte, was first used to transfer $MnFe_2O_4$ NPs from an organic solvent into aqueous solution and further facilitated ionic gelation with cationic polymer poly(L-lysine); the positive charged outer layer could be assembled with negatively charged carboxyl-

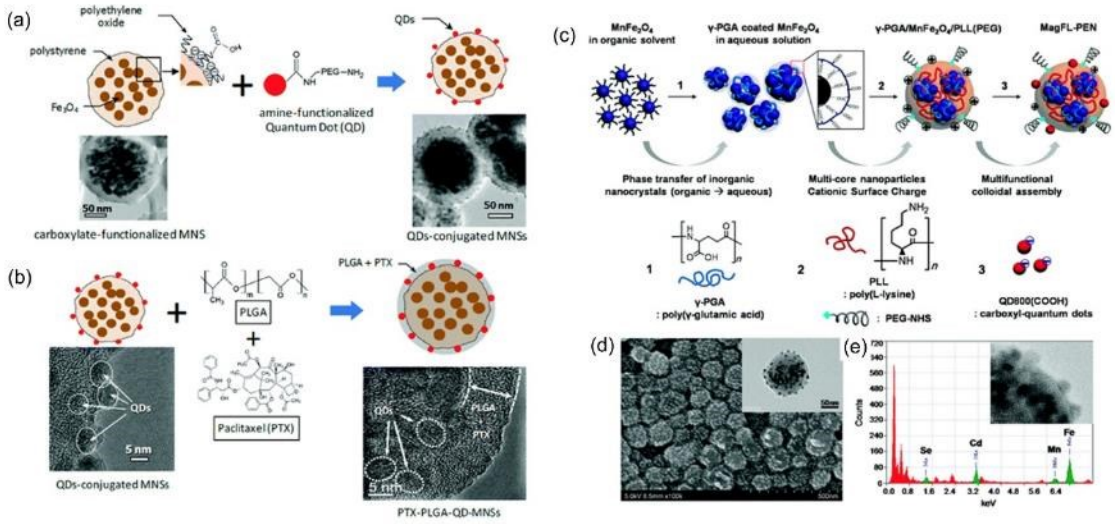

Figure 2.4 (a) Schematic diagram of the conjugation of amine-functionalized quantum dots (QDs) to the surface of carboxylate-functionalized MNSs using conventional NHS/EDC coupling method; (b) Scheme of PTX loading using a thin PLGA coat on the surface of QD-MNSs. (c) Schematic illustration of the facile fabrication of MR/NIR multimodal imaging nanoprobes based on magnetofluorescent polyelectrolyte nanocomposites (MagFL-PEN) via electrostatic assembly between polyelectrolytes and functional colloidal nanoparticles. (d) SEM and TEM (inset) images of MagFL-PEN after adsorption of QD800(COOH). (e) EDX analysis of MagFL-PEN. Figure 2.4a~b was taken from reference[81] and Figure 2.4c~e was taken from reference[85].

functionalized NIR emitting QDs. Ding and co-workers[86] reported a new class of magnetic-fluorescent nanoprobe, in which cationic PEI capped CdSe/ZnS QDs were firmly grafted with negatively charged magnetic nanorings *via* electrostatic interaction. Following the same synthetic strategy, Yu *et al.*[87] also synthesized water-soluble hybrid NPs based on the PEI coated magnetic NPs and trioctylphosphine oxide (TOPO)-capped CdSe/ZnS QDs. Similarly, Dong *et al.*[88] prepared hydrophilic magnetofluorescent nanobowls consisting of positively charged PEI-coated CdSe/CdS/ZnS QDs anchoring on the polyelectrolyte polyepoxysuccinic acid (PESA) modified magnetic NPs through electrostatic interaction.

Compared with other methods, polymer assisted coupling method has been widely adopted for preparation of multifunctional NPs due to its simplicity. The multifunctional NPs synthesized through this method might remain relatively small size, and can be easily separated from the solution under external magnetic field. But the poor stability under certain conditions may result in the agglomeration of NPs, which can restrict their bioapplications.

2.2.2.2 Magnetic and fluorescent nanoparticles co-embedded into polymer matrix

Same as the co-embedment of magnetic and fluorescent NPs into the silica matrix, the co-encapsulation of magnetic and fluorescent NPs can also be achieved in a polymer matrix. Generally, this approach uses amphiphilic copolymers to form a microemulsion solution and then coat both magnetic and fluorescent NPs

to form the multifunctional fluorescent-magnetic NPs, which not only possess the magnetic/fluorescent properties of embedded NPs, but also have the excellent biocompatibility of the polymer.

Weller *et al.*[89] reported co-encapsulation of iron oxide and elongated quantum dots-in-quantum rods (QDQRs) in a polystyrene (PS) matrix *via* consecutive emulsion polymerization (Figure 2.5a). The composition of the as-synthesized hybrid nanocomposites can be tuned from dyads to clusters containing 30~40 NPs with diameters ranging from 50 nm to 150 nm (Figure 2.5b-c). In another study, Pan and co-workers[90] prepared fluorescent-magnetic-biotargeting multifunctional nanobioprobes consisting of poly-(styrene/acrylamide) copolymer nanospheres and encapsulated CdSe/ZnS QDs and γ-Fe_2O_3 NPs. After coupling with monoclonal antibody (mAb), these multifunctional NPs can be used to detect and extract two different types of tumor cells (leukemia cells and prostate cancer cells) from complex samples containing both normal cells and the target cancer cells. The same encapsulation method was used by Pellegrino *et al.*[91] in the development of multifunctional nanobeads (MFNBs), which was made by embedding both superparamagnetic iron oxide NPs and core-shell CdSe/ZnS QDs into [poly(maleic anhydride-alt-1-octadecene), PMAO] matrix. Interestingly, since the addition of the destabilizing solvent could induce controlled aggregation of the components, a careful choice of destabilizing solvent allowed tuning both the total bead size and the distributions of iron oxide NPs and QDs within the polymer. Winter *et al.*[92] also reported amphiphilic block copolymers encapsulated superparamagnetic iron oxide NPs and QDs, in which the number of QDs and iron oxide NPs was controlled by the molecular structure of the polymer and the quantities of polymer, iron oxide NPs and QDs used. In addition to co-encapsulation with visible emitting QDs, Rodríguez *et al.*[93] demonstrated the encapsulation of nontoxic iron oxide superparamagnetic NPs and PbS QDs emitting in the second biological window (NIR-II) into a biocompatible and FDA-approved polymeric matrix [poly(lactic-co-glycolic-acid), PLGA], which hold great potential for simultaneous deep-tissue fluorescence and MR imaging, overcoming the tissue penetration limits of classical visible emitting based optical imaging in living mice.

The encapsulation method was also chosen for the preparation of multifunctional NPs consisting of lanthanide-doped NPs and iron oxide NPs. For example, Pellegrino *et al.*[94] presented the fabrication of aqueous multimodal imaging nanocomposites based on superparamagnetic NPs and two different sizes of lanthanide-doped UCNPs (Figure 2.5d-i). The simultaneous incorporation of both NPs was implemented by the amphiphilic PMAO polymer and the size of the resultant nanocomposites can be tuned in the range of 80 ~ 130 nm mainly depending on the NPs and polymer concentrations. Liu and co-workers[95] encapsulated hydrophobic UCNPs with iron oxide NPs using amphiphilic block copolymer [poly (styrene-block-allyl alcohol) (PS_{16}-b-PAA_{10})] to obtain multifunctional nanocomposites for multimodal imaging and magnetic targeted drug delivery. Similarly, Ortgies *et al.* prepared hybrid nanostructures by joint

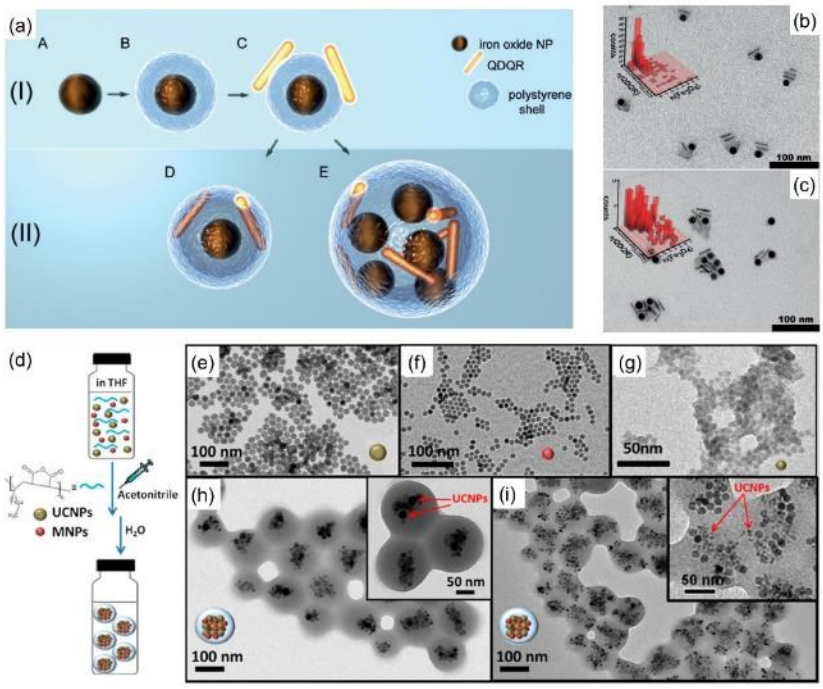

Figure 2.5 (a) The two-step hybrid formation. Step I: A) iron oxide nanocrystals (native ligands not shown), B) iron oxide nanoparticles with the first polystyrene shell, C) nanohybrid after the deposition of QDQRs. Step II: D) nanohybrid after synthesizing a thin PS shell, E) nanohybrid after second emulsion polymerization, when dyads cluster owing to high styrene concentration. (b, c) Representative TEM images of the different hybrids achieved using different amounts of monomer during the second emulsion polymerization. The inset shows a three-dimensional histogram of the number of QDQRs n (QDQR) and the number of iron oxide n (Fe_3O_4) within one hybrid. Amounts used of each monomer: (b) 4 nmol and (c) 8 nmol. (d) Scheme for synthesis of MUCNBs; TEM images of 23 nm UCNPs (e), 15 nm IONPs (f), 6 nm UCNPs (g), and MUCNBs with 15 nm IONPs and 23 nm UCNPs (h) or 6 nm UCNPs (i). Figure 2.5a~c was taken from reference[89] and Figure 2.6d~i was taken from reference[94].

encapsulation of both magnetic NPs and neodymium-doped NPs within the biocompatible polymer PLGA.

The co-encapsulation of fluorescent and magnetic NPs by polymer holds great potential for bioapplications compared with multifunctional NPs prepared by other methods since the toxicity of the NPs, like heavy metal toxicity of (Pb, Cd)-based QDs, can be significantly decreased due to the polymer coating. In addition, the polymer coating can be nontoxic, biocompatible and biodegradable in biological environments and can be easily coupled with other bioconjugators, such as DNA, peptides and antibodies.

2.2.3 Fluorescent-magnetic nanoparticles by seed-mediated growth method

The formation of NPs in solution phase are generally divided into two different stages: nucleation and growth. Based on the temporal and spatial differences of these two stages, the synthesis of crystal NPs can be classified into categories: homogeneous nucleation and heterogeneous nucleation. In the case of homogeneous nucleation, the decomposition or the redox reaction of relative precursors leads to the

formation of crystal nuclei during the nucleation stage, further serving as seeds *in situ* for the subsequent growth of NPs. Regarding the heterogeneous nucleation, the seed NPs are pre-synthesized and added into the growth solution to further grow into crystal NPs. In order to form high-quality and narrow sized NPs, the distinct temporal separation of nucleation and growth stages is required. On this regard, the seed-mediated growth method can definitely fulfill the requirement and becomes one of the most versatile methods for realizing crystallographic (shape, size and composition) control of NPs. In a typical seed-mediated growth of fluorescent-magnetic NPs, the fluorescent (or magnetic) NPs are firstly synthesized as seeds, followed by heterogeneous nucleation onto the seeds in a second solution containing magnetic (or fluorescent) precursors.

Li *et al.*[96] prepared bifunctional magnetic and upconversion NIR-to-NIR core-shell structured $NaYF_4:Yb^{3+}$, $Tm^{3+}@Fe_xO_y$ NPs (Figure 2.6a~d). Firstly, 20 nm of $NaYF_4:Yb^{3+}$, Tm^{3+} NPs (Figure 2.6b) were synthesized by thermal decomposition strategy, subsequently adding into iron precursor to from a 5 nm of Fe_3O_4 outer shell by the similar thermolysis process (Figure 2.6c). At last, ligand exchange with dopamine was carried out to transfer multifunctional NPs into water phase. Similarly, Lin and co-works[97] reported core-shell monodisperse bifunctional (magnetic and upconverting luminescent) NPs (Fe_3O_4@$NaGdF_4$:Yb/Er@$NaGdF_4$:Yb/Er) using the seed-mediated growth method, in which OA-capped Fe_3O_4 cores were obtained from the thermal decomposition of the iron-oleate precursor and then served as seeds for the outer shell growth of $NaGdF_4$:Yb/Er in the lanthanide precursor solution. Each of the components in the nanocomposites presents a unique function. Fe_3O_4 core endows NPs with magnetic property and the outer $NaGdF_4$:Yb/Er shell is to improve the luminescence efficiency of the intermediate upconverting shell. Blower *et al.*[98] designed two types of core-shell $Co_{0.16}Fe_{2.84}O4$@$NaYF_4$(Yb, Er) and Fe_3O_4@$NaYF_4$(Yb, Tm) NPs for trimodal [MR, positron emission tomography/single photon emission commuted tomography (PET/SPECT), and optical] imaging. In another study, multifunctional magnetic/upconversion luminescent $Fe_3O_4@LaF_3:Yb^{3+}$, Er^{3+} NPs have been developed for dual-modal bioimaging.[99] Yan *et al.*[100] also demonstrated superparamagnetic and upconversion emitting $Fe_3O_4/NaYF_4$: Yb, Er hetero-NPs by a modified seed-mediated growth method. These NPs were prepared by two steps: 1) high-quality β-$NaYF_4$:Yb, Er NPs were obtained *via* a thermal decomposition route; 2) as-obtained UCNPs were re-dispersed in the mixture of iron precursor and ODE-OA-OLA. In the second step, a crucial crosslinker, 1,10-decanedicarboxylic acid (DDA) or 11-mercaptoundecanoic acid (MUA), was introduced for anchoring Fe_3O_4 NPs onto the surface of UCNPs. More interestingly, resulting from the ligand spacing between Fe_3O_4 and $NaYF_4$:Yb, Er, the hetero-NPs preserve the superparamagnetic and UC emission properties simultaneously, which enables both effective optical detection and magnetic trapping.

In addition to forming UCNP-based fluorescent-magnetic NPs by seed-mediated growth method, Lilac *et*

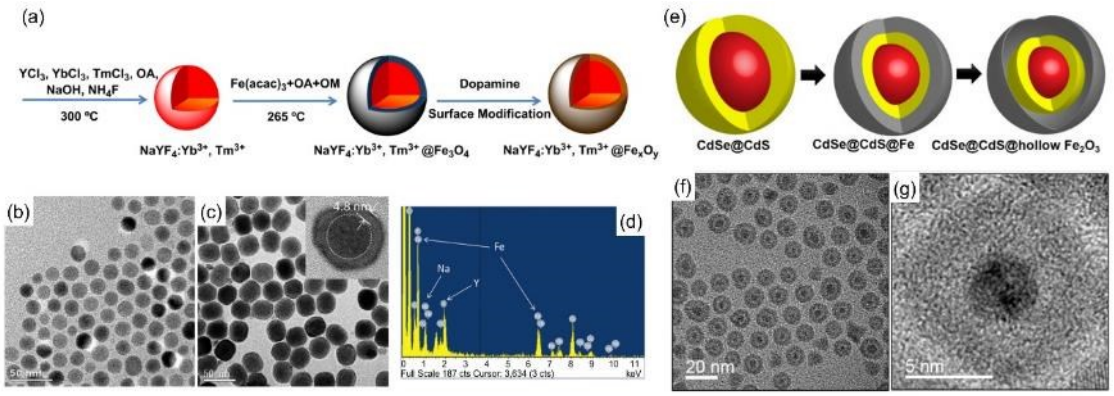

Figure 2.6 (a) Schematic representation of the synthetic routine of the water-soluble $NaYF_4$:Yb^{3+}, Tm^{3+}@Fe_xO_y nanocrystals. (b) TEM image of $NaYF_4$:Yb^{3+}, Tm^{3+} nanocrystals and (c) $NaYF_4$:Yb^{3+}, Tm^{3+}@Fe_3O_4 nanocrystals. (d) EDX spectrum of the $NaYF_4$:Yb^{3+}, Tm^{3+}@Fe_3O_4 nanocrystals. (e) Illustration of the multistep sequential synthesis producing the magneto-fluorescent hybrid structures. (f) TEM images of CdSe@CdS@hollow-Fe_2O_3 nanostructure. (g) Enlarged TEM image of f. Figure 2.6a~d was taken from reference[101] and Figure 2.6e~g was taken from reference[102].

al.[102] introduced a modified strategy for the fabrication of ultrasmall (hydrodynamic size: 15 nm in diameter) QDs-based magneto-fluorescent NPs (Figure 2.6e~g). The production of hybrid structures includes the successive procedure of CdSe@CdS QD synthesis, metallic iron deposition on the surface of CdSe@CdS QDs and controlled oxidation of the iron to form hollow iron oxide shell, as illustrated in Figure 2.6e. The yolk-shell morphology of CdSe@CdS@hollow-Fe_2O_3 (Figure 2.6f-g) avoids the direct contact between semiconductor and magnetic domains, which typically results in undesirable fluorescence quenching. Similarly, a one-pot facile synthesis of hydrophilic colloidal bimodal nanoprobe (FePt-CdS) was prepared through a seed-mediated nucleation and growth technique for efficient bimodal imaging application.[103]

Since fluorescent-magnetic NPs synthesized by seed-mediated growth method are required to grow the fluorescent/magnetic shell in their relevant precursors, it offers high tunability with respect to the composition, size and surface functionalization. However, the direct growth of second fluorescent/magnetic shell may result in fluorescence quenching of UCNPs/QDs by magnetic components due to the close distance between each other during shell growth process. It is also challenging as homogenous nucleation can compete with heterogeneous nucleation.

2.2.4 Magnetically doped quantum dots

Doping is a versatile strategy in material science to yield promising materials with desired properties and functions. The underlying mechanism of doping is based on the introduction of atoms/ions of appropriate elements into host lattices. Regarding crystalline NPs, doping is of great importance to modify electronic properties,[16, 104] tune emission properties[105-106] and modulate magnetism.[107] Magnetic ion doping into QDs offers the unique possibility to integrate fluorescent and magnetic properties in a single material. The

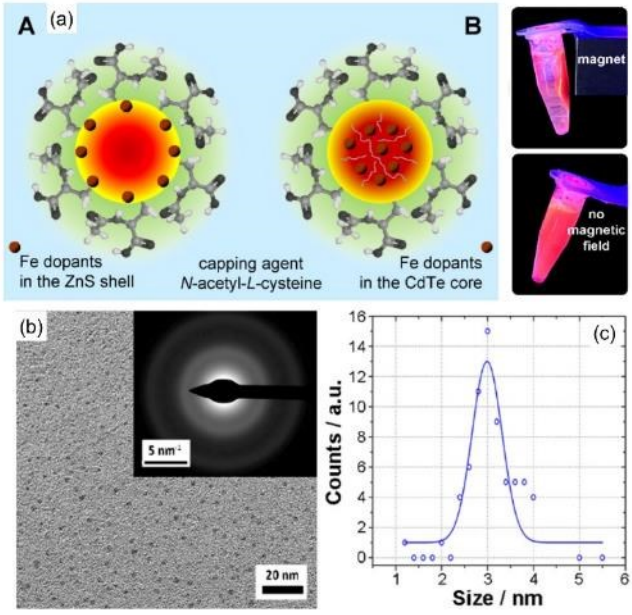

Figure 2.7 (a) Architecture of water-dispersible shell-doped mQDs (NAC-CdTe/30%Fe:ZnS) (A) and core-doped mQDs (NAC-30%Fe-CdTe/ZnS (B). (b) Representative TEM image of shell-doped mQDs and the corresponding diffraction pattern (inset), indicating that the mQDs are crystalline. (c) The corresponding size distribution, where the average particle diameter was determined to be 2.9 ± 0.3 nm. Figure 2.7a~c was taken from reference[108].

obtained magnetic QDs can serve as probes for multimodal bioimaging and labels for various applications in nanomedicine.

Ehmoser *et al.*[108] prepared water-dispersible magnetic CdTe/ZnS QDs *via* a facile aqueous synthesis route, in which ferrous ions were selectively doped in either their cores or shells (Figure 2.7a-c). The magnetic QDs show spherical shapes with diameter of 2.9 ± 0.3 nm (Figure 2.7b-c). The presented N-acetyl-L-cysteine (NAC)-capped magnetic QDs possess high water dispersibility and colloidal stability, which could be potentially used for multimodal (optical and MR) imaging. In addition to Fe^{2+} doping, paramagnetic ions (Mn^{2+} and Gd^{3+}) doped QDs, such as Gd-doped $CuInS_2$/ZnS,[109] Gd-Zn-Cu-In-S/ZnS,[110] Gd-Cu-In-S/ZnS,[111] Gd-doped CdTe QDs,[112] Gd-doped $CuInS_2$,[113] $Zn_{1-x}Gd_xS$ (x=0.1, 0.2 and 0.3),[114] Mn-doped ZnSe,[115] and Mn-doped NIR emitting QDs,[116] were reported and presented great potential as bimodal (fluorescence and MR) imaging contrast agents.

These magnetically doped QDs have demonstrated both fluorescent and magnetic properties and can be further functionalized with DNA, antibodies and proteins of particular interest for bioapplications. However, Mn^{2+} and Gd^{3+} doped QDs might suffer from the decreased fluorescence due to the introduction of paramagnetic ions. It is still challenging to engineer magnetically doped QDs without compromising

fluorescent/magnetic properties of each component for fluorescence or MR imaging. In addition, paramagnetic ions (Mn^{2+} and Gd^{3+}) doped QDs exhibit lower magnetization with respect to superparamagnetic NPs, which may limit their actual use for high-efficiency, magnetic manipulation-related bioapplications.

2.3 Bioapplication of multifunctional fluorescent-magnetic hybrid nanoparticles

Since fluorescent NPs have been widely used for fluorescence biosensing as well as bioimaging, while the magnetic NPs are of interest for various bioapplications, especially in the field of MR imaging and drug delivery, these fluorescent-magnetic hybrid NPs are naturally expected to be extremely attractive in various bioapplications, including, but not limited to, multimodal bioimaging, magnetic targeted drug delivery and cancer therapy.

2.3.1 Multimodal bioimaging

Fluorescent and MR imaging are two important imaging techniques for studying the biological processes at cellular/organic level, which have a tremendous impact on biomedical science. MR imaging involves proton alignment of water molecules in the soft tissues of human body under varying magnetic field, which is mainly used for *in vivo* imaging. Fluorescent imaging depending on the optical fluorescence signal is not only widely used for *in vitro* studies of fixed samples, such as cell labeling, monitoring and tracking under fluorescent microscope, but also allows for the imaging of live and intact organisms *in vivo*. However, MR imaging cannot provide high sensitivity and spatial resolution for *in vitro* cellular level study and fluorescent imaging are limited by the shallow tissue penetration of light and fair to work for deep-tissue imaging in distant organs. Obviously, these two imaging techniques are complementary to each other and can be integrated for more effective detection both *in vivo* and *in vitro*, which is promising for more accurate diagnosis of cancers and other diseases. In this case, multifunctional fluorescent-magnetic NPs can serve as dual mode contrast agents, which can be simultaneously used in fluorescent and MR imaging. In addition, they allow us to perform optical tracking of biological species with magnetic manipulation.

Several interesting advances have been achieved on the utilization of multifunctional NPs for dual mode imaging in recent years. For example, Liu *et al.*[117] reported multifunctional nanoprobes *via* LBL self-assembly of iron oxide NPs on the surface of $NaYF_4$-based UCNPs (Figure 2.8a-h). The capability of these nanocomposites as multimodal imaging probes was demonstrated *in vivo*. Specifically, female nude mice bearing tumors exhibited strong UCL signals in the liver and tumor sites after one-hour intravenous injection of these nanocomposites (Figure 2.8a-c). The high accumulation of these NPs in the tumor and reticuloendothelial systems (RES), including liver, spleen, lung, and bone marrow, was found after 24h

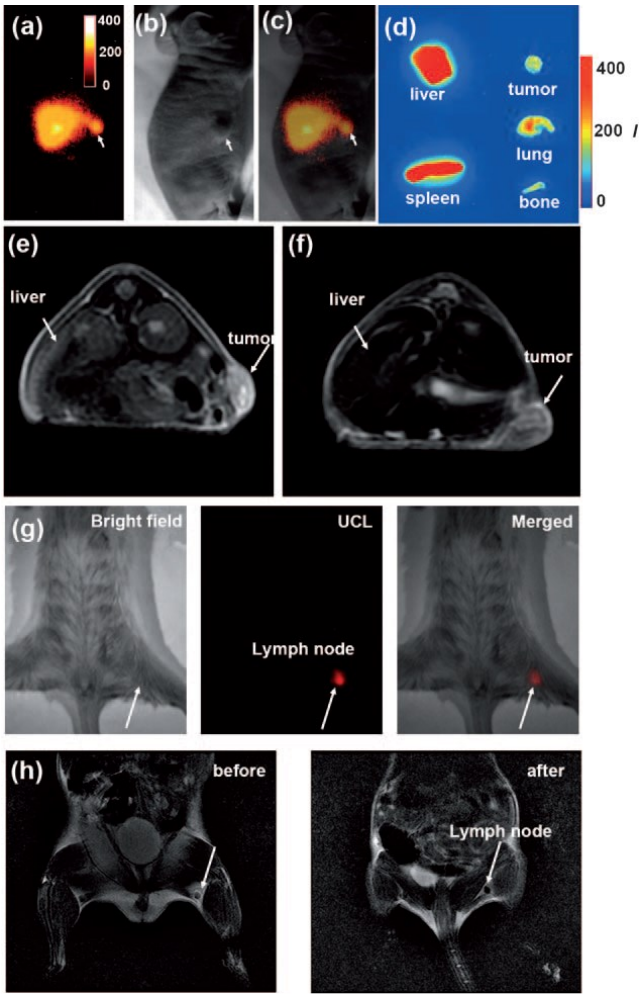

Figure 2.8 Dual-modal UCL/MR *in vivo* imaging. (a) The bright field, (b) UCL, and (c) merged images of a KB tumor-bearing mouse one hour after intravenous injection of PEG–MFNP. Strong UCL signals were observed from the liver and tumor sites (arrow) of the mouse. (d) *Ex vivo* UCL imaging showing accumulation of MNFPs in the liver, spleen, tumor, bone, and lung of the injected mouse at 24 h post injection. UCL signals from other organs were barely detectable. T_2-weighted images of KB-tumor bearing nude mice with (e) and without (f) injection of MFNPs. Obvious darkening contrast was shown in the mouse liver and tumor. (g) Multimodal UCL and (h) MR imaging for *in vivo* lymphangiography mapping using MFNPs. MR images were taken before (left) and after (right) injection of MFNPs. Figure 2.8a~h was taken from reference[117].

post-injection (Figure 2.8d). Meanwhile, the darkening effects (from 45.4 to 38.6%) in the liver and tumor area were observed in the T_2-weighted MR imaging (Figure 2.8e-f). Furthermore, multifunctional nanocomposites were also used for multimodal mapping of lymph nodes in mice after intracutaneous injection (Figure 2.8g-h). Similarly, Li *et al.*[101] also designed core/shell structured $NaYF_4$:Yb^{3+}, Tm^{3+}@Fe_xO_y NPs for dual model T_2-enhanced MR and NIR-to-NIR UCL imaging for small-animal of lymphatic node. In addition to dual model imaging *in vivo*, Zhang *et al.*[118] prepared fluorescent mesoporous

silica coated magnetic NPs with high MR sensitivity and excellent cell labelling efficiency. In their experiments, the labeled cells could be tracked migrating to the lesion sites by MR and fluorescent imaging.

2.3.2 Drug delivery

Conventional chemotherapy is commonly used for the clinic cancer treatment. However, the chemotherapeutic drugs are highly toxic and often cause severe side effects to the normal tissue and organs due to non-specific drug uptake. Ideally, the drugs should intelligently accumulate in the tumor sites, subsequently following controllable release. Multifunctional nanoplatforms can serve as vehicles for carrying drugs to desired tumor sites in a target-specific manner. The chemotherapy-related side effects could thus be eliminated since the administration of drug dosage is reduced while maintain the high concentration of drugs in the tumor site without affecting other normal tissue. In addition, these nanoplatforms can monitor the pharmacokinetics and biodistribution of NPs during the delivery process of therapeutic drugs to tumor site, which can largely enhance the sensitivity and efficiency of cancer therapy.

Regarding drug delivery using fluorescent-magnetic NPs, this process can be achieved by at least two different ways. First, these NPs can passively act as drug carriers for delivering drugs to tumor sites *via* the enhanced permeation and retention (EPR) effect, which arises from extravasation into leaky vascular endothelial cells around tumors. Most of the NPs related drug delivery system are based on passive targeting of NPs to tumors. For example, Hyeon *et al.*[58] reported a highly versatile nanocomposite which was prepared by decorating the surface of mesoporous dye-doped silica NPs with magnetic NPs. To examine drug delivery, DOX was loaded into the pores of nanocomposite and intravenously injected into nude mice bearing a tumor. The accumulation of NPs in the tumor sites *via* passive targeting was confirmed by the MR and fluorescence imaging. After treating with DOX loaded nanocomposite, apoptotic cells in tumor tissue were clearly detected, demonstrating that DOX was successfully delivered to the tumor sites and its anticancer activity was maintained. Drug delivery through passive targeting is directly related to the circulation time which means that the longer circulation time can promote more NPs to accumulate in the tumor sites. This is usually achieved by coating NPs with some sorts of hydrophilic, biocompatible polymer, such as PEG. But still, it cannot be completely avoided that some drugs will be released to normal tissues in the passive targeting, thus causing some relative side effects. The other route for drug delivery using fluorescent-magnetic NPs is realized by active targeting. The success of active targeting of NPs strongly depends on the targeting moiety that has specific affinity of binding to the receptors on the cell surface. For example, Shi *et al.*[119] reported a fluorescent-magnetic nanocarrier, in which the chemotherapeutic agent paclitaxel (PTX) was loaded by using a biodegradable PLGA layer. In order to realize active targeting, PTX-loaded nanocarrier was conjugated with anti-prostate specific membrane antigen (anti-PSMA). The anti-PSMA-conjugated nanocarrier was successfully targeted at LNCaP prostate cancer cells *in vitro*. The

in vivo experiments also observed the different fluorescent signals between tumor regions with targeted nanocarrier and non-targeted nanocarrier system, indicating the active targeting effect.

Owing to their unique magnetic property, in some cases, fluorescent-magnetic NPs can realize magnetically-guided drug delivery under external magnetic field, thus allowing remote drug manipulation. For example, Zhang *et al.*[72] reported mesoporous multifunctional fluorescent and magnetic nanocarriers for delivering drugs to tumor by an externally applied magnetic field (Figure 2.9a). To demonstrate their potential use for drug delivery, nanocarriers were loaded with DOX and injected into mice bearing a tumor. The significant increase of fluorescence (Figure 2.9b-c) in the tumor site by applying an external magnetic field demonstrated the accumulation of nanocarriers in the tumor. In addition, compared with free DOX and DOX-loaded nanocarrier without magnetic field, the DOX-loaded nanocarrier with magnetic field (Figure 2.9d) exhibited great inhibition of tumor growth. Similarly, Liu and coworkers[95] prepared polymer encapsulated UCNPs/iron oxide/DOX nanocomposites for multimodal imaging and imaging-guided magnetic targeted drug delivery.

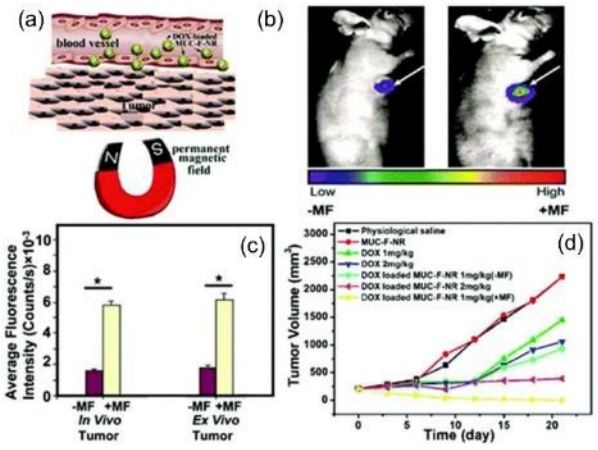

Figure 2.9 (a) Schematic illustration of targeting of DOX loaded multifunctional drug carrier to tumor cells assisted by an externally applied magnetic field (MF). (b) Tumor location as defined by MUC-F-NR intensity increases with 1 h magnetic field treatment. Mice bearing H22 xenograft tumor were injected with DOX loaded MUC-F-NR (1 mg/kg) and subjected (+MF) or not subjected (-MF) to the magnetic field for 1 h. At 24 h postinjection, mice were imaged *in vivo*. (c) The luminescence signal was measured from the whole tumor *in vivo* and *ex vivo*. (Excitation was provided by the CW infrared laser at 980 nm and upconversion luminescence signals were collected at 650 ± 10 nm. Fluence rates for 980 nm excitation light were 80 mW/cm^2.) (d) Tumor volume changes of saline-treated mice compared to mice treated with MUC-F-NR, DOX, and DOX loaded MUC-F-NR over 21 d in the absence and presence of magnetic field. Data show mean ± SD (n = 5, *p ≤ 0.05). Figure 2.9a~d was taken from reference[72].

2.3.3 Cancer therapy

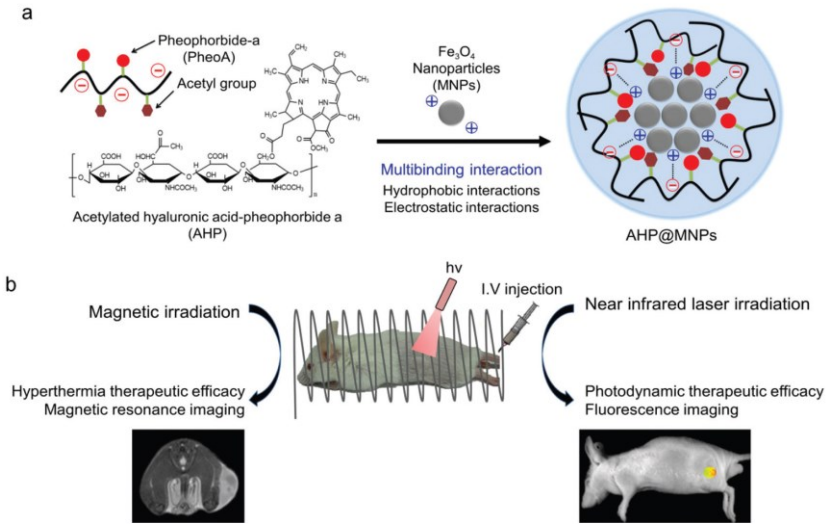

Figure 2.10 (a) Schematic illustration of the preparation of the acetylated hyaluronic acid–pheophorbide-a coated Fe_3O_4 magnetic nanoparticles (AHP@MNPs); amphiphilic and negatively charged AHP can interact with positively charged MNP through multibinding interactions. (b) Schematic representation of multifunctional AHP@MNPs for tumor-targeted bimodal imaging and photodynamic/hyperthermia treatment when AHP@MNPs were irradiated with magnetic and near infrared lasers. Figure 2.10a~b was taken from reference[120].

Magnetic hyperthermia (MHT) is a well-known thermal treatment for cancer, which was initially described by Gilchrist *et al.* in 1957.[121] The magnetic hyperthermia is based on the heating of magnetic NPs placed in a targeted tissue by applying an alternative magnetic field. Consequently, the cancer tissue is destroyed if the temperature in the cancer site can be held over 41 °C for several hours while the normal tissue is not affected.[122] Numerous researches emerged to optimize magnetic hyperthermia through studying different types of magnetic materials, surface modification and magnetic field strengths and frequencies, which paves the way for translating NanoTherm™ Therapy (MagForce AG) into commercial clinical setting for the treatment of cancers.[123] The main drawback of magnetic hyperthermia is the necessity of large amounts of magnetic NPs in tumor site to efficiently convert magnetic energy. Another thermal therapy modality, photothermal therapy (PTT), employing NIR photoabsorbing agents to generate heat from NIR laser irradiation to burn cancer cells, has received considerable attention. It has many advantages, such as non-invasion, high specificity and precise spatial-temporal selectivity. However, PTT is not applicable for cancer cells in distant organs due to the limited penetration depth of NIR light into the tissue.

In recently years, photodynamic therapy (PDT) has been one of the most rapidly growing scientific areas due to its low cost, non-invasion and repeatable treatment at the same site if needed. PDT involves the administration of a photosensitizing drug, followed by the irradiation of targeted tissue with light to trigger the generation of highly reactive singlet oxygen to kill cancer cells. The photosensitizer only becomes active

under light, so PDT also has the similar problem as PTT, which is not suitable for cancers grown deeply into the skin or other organs. In addition, it cannot be used to treat cancers that have spread to many places in the body.

Generally, multifunctional fluorescent-magnetic NPs can be utilized for MHT or PTT due to their magnetic and NIR absorbing properties. For example, Biris *et al.*[79] reported water-soluble magnetic-fluorescent nanocomposites, which acted as high-efficiency radio frequency absorber for nanohyperthermia of cancer cells. Later, Ortgies *et al.*[124] reported optomagnetic hybrid nanostructures comprising of iron oxide and Nd-doped NPs. These nanostructures not only show great potential for MHT under alternating magnetic field, but also for PTT by using NIR irradiation as external stimulus. In addition, the developed nanostructures can be capable of monitor subtissue thermal feedback while preserving their heating efficiency in biological tissues.

On the other hand, MHT and PDT can be combined using fluorescent-magnetic NPs, if appropriate photosensitizers are incorporated into the hybrid nanocomposites. It is expected that MHT and PDT could be complementary method in the cancer treatment. For example, Na *et al.*[120] prepared multifunctional fluorescent-magnetic nanocomposites, which is composed of acetylated hyaluronic acid coated Fe_3O_4 NPs and photosensitizer (Pheophorbide-a) (Figure 2.10a-b). These nanocomposites were allowed for cancer treatments by three therapeutic modes: MHT alone, PDT alone and integrated MHT/PDT. The final results demonstrated that each of single treatments slightly inhibited tumor growth, while their combination showed significant tumor growth inhibition, through the synergistic potential of combination therapy. Besides, the authors have used these multifunctional nanocomposites for *in vivo* detection of tumors by MR and optical imaging. In another study, the synergistic effect can also be observed by the combination of MHT/PDT for the treatment of glioblastoma.[125]

CHAPTER 3 EXPERIMENTS AND CHARACTERIZATIONS

In this chapter, experimental details for the synthesis and characterization of three kinds of multifunctional nanoplatforms using superparamagnetic Fe_3O_4 NPs, and NIR photoluminescent NPs are described. The first section mainly introduces the synthesis of Fe_3O_4 NPs with different morphology and size, and PbS and PbS/CdS QDs in the NIR-I and NIR-II windows. Subsequently, a nanoplatform based on Fe_3O_4 NPs and NIR-to-NIR photoluminescent $NaYF_4:Nd^{3+}$ was synthesized by a multistep procedure and their use for deep-tissue dual-mode (optical and magnetic resonance) imaging was investigated. Moreover, we prepared supernanoparticles consisting of Fe_3O_4 NPs and PbS/CdS QDs by self-assembly method and studied their amplified dual-mode (magnetothermal and photothermal) heating properties for therapeutics. The last section focuses on the synthesis and surface modification of large-pore dendritic mesoporous silica ($mSiO_2$), followed by embedding with Fe_3O_4 NPs and PbS/CdS QDs in NIR-II; DOX was further loaded into them and the drug release was evaluated under multi-stimuli (pH/MF/NIR).

3.1 Materials

Iron chloride hexahydrate ($FeCl_3 \cdot 6H_2O$), sodium oleate, ammonium hydroxide solution ($NH_3 \cdot H_2O$, 28.0~30.0% ammonia content), lead chloride ($PbCl_2$, 98%), lead acetate trihydrate ($Pb(OAc)_2.3H_2O$, 99.9%), cadmium oxide (CdO, 99%), sulfur (S, 100%), bis(trimethylsilyl) sulfide ($(TMS)_2S$, synthesis grade), Triton X-100, tetraethyl orthosilicate (TEOS, 99.999%), (3-mercaptopropyl)trimethoxysilane (MPTS, 95%), 1-hexanol (99%), rare earth nitrate [$Y(NO)_3 \cdot 6H_2O$, $Yb(NO)_3 \cdot 5H_2O$, $Er(NO)_3 \cdot 5H_2O$ $Nd(NO_3) \cdot 6H_2O$, 99.9%], urea (99.0%), oleic acid (OA, technical grade 90%), oleylamine (OLA, technical grade, 70%),1-Tetradecene (TDE, technical grade 92%), 1-Octadecene (ODE, technical grade 90%), branched polyethylenimine (PEI, $M_w \approx 25\,000$), polyvinylpyrrolidone (PVP, MW~55000), triethanolamine (TEA), cetyltrimethylammonium chloride solution (CTAC, 25 wt% in H_2O), ethylene glycol (EG, 99.8%), dimethyl sulfoxide (DMSO, ≥ 99.9%), dodecyltrimethylammonium bromide (DTAB, 99%), ammonium nitrate (NH_4NO_3), phosphate buffered saline (PBS) and doxorubicin hydrochloride (DOX) were purchased from Sigma-Aldrich Inc. Hexane, toluene, chloroform, cyclohexane, methanol and ethanol were purchased from Fisher Scientific Company. All chemicals were used as purchased.

3.2 Reaction setup

The schematic illustration of the typical reaction setup for synthesis of Fe_3O_4 NPs, PbS QDs, PbS/CdS QDs and $Fe_3O_4/SiO_2/NaYF_4:Nd^{3+}$ NPs is shown in Figure 2. Fe_3O_4 NPs were synthesized by a modified thermal decomposition method using the setup shown in Figure 2.1a. In this reaction, a heating mantle was adopted for a higher temperature (> 290 °C). Both smaller and larger PbS QDs were synthesized by a hot-injection

method using the oil bath with lower temperature (100~120 ℃) shown in Figure 2.1b. PbS/CdS QDs were synthesized by a microwave reactor, as shown in Figure 2.1c. $Fe_3O_4/SiO_2/NaYF_4:Nd^{3+}$ NPs were prepared by hydrothermal method and Teflon lined autoclave is shown in Figure 2.1d.

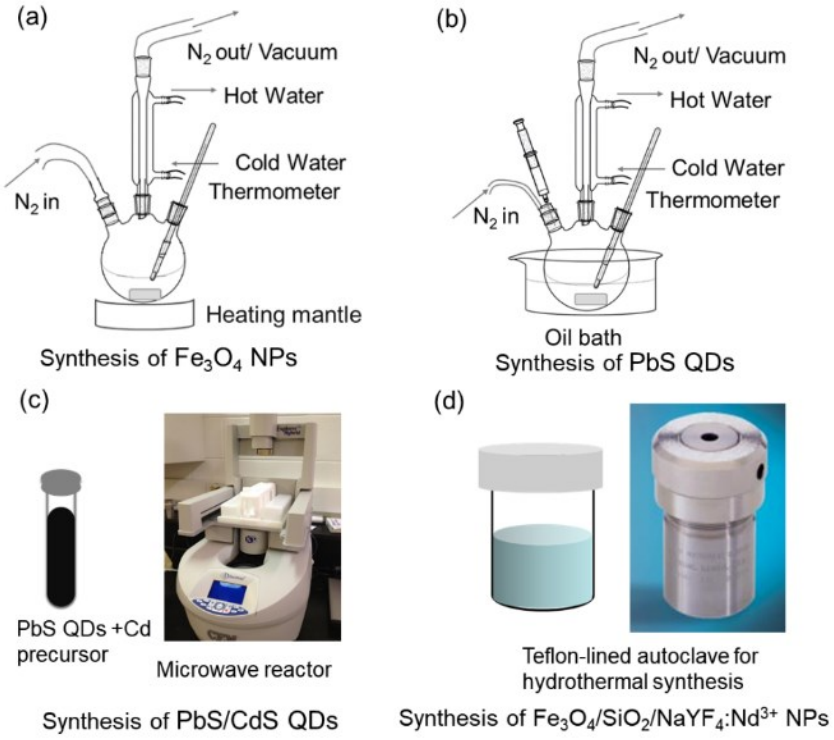

Figure 3.1 Schematic illustration of the setup for synthesis of (a) Fe_3O_4 NPs, (b) PbS QDs, (c) PbS/CdS QDs and (d) $Fe_3O_4/SiO_2/NaYF_4:Nd^{3+}$ NPs.

3.3 Synthesis of Fe_3O_4 nanoparticles, PbS and PbS/CdS quantum dots

3.3.1 Synthesis of Fe_3O_4 nanoparticles

Fe_3O_4 NPs were synthesized by a modified thermal decomposition method.

Firstly, the $Fe(oleate)_3$ complex precursor was prepared by reacting iron chloride and sodium oleate. In a typical synthesis of $Fe(oleate)_3$ precursor, 1.08 g (4 mmol) of $FeCl_3 \cdot 6H_2O$ and 4.87 g (16 mmol) of sodium oleate in a mixed solution of 8 mL of ethanol, 6 mL of distilled water and 14 mL of hexane was refluxed at 70 °C for 6 h. Then the formed $Fe(oleate)_3$ was washed several times by hot water to remove the unreacted iron chloride. After washing, the $Fe(oleate)_3$ was kept in a vacuum oven at 70 °C for 12 h in order to remove excess hexane.

Secondly, Fe_3O_4 NPs were synthesized by thermal decomposition of $Fe(oleate)_3$ precursor. 0.9 g (1 mmol) of $Fe(oleate)_3$, 142 mg (0.5 mmol) of OA and 10 mL of ODE were added to a three-neck round bottom flask and heated to 320 °C under N_2 protection for 1h. After cooling to room temperature, the Fe_3O_4 NPs

were washed several times with ethanol and hexane. Finally, the prepared Fe_3O_4 NPs were separated by centrifugation and dispersed in organic solvent such as hexane, chloroform or toluene.

Fe_3O_4 NPs synthesized by above method are usually larger than 10 nm in diameter. In order to obtain ultrasmall Fe_3O_4 NPs, the ODE (boiling point: 320 ℃) solvent was replaced by a mixture of TDE/ODE (boiling point: 290 ℃) to get a lower boiling solvent. Simply, 0.9 g (1 mmol) of $Fe(oleate)_3$, 142 mg (0.5 mmol) of OA, 5 mL of TDE and 10 mL of ODE were added to a three-neck round bottom flask and heated to 290 °C under N_2 protection for 1h.

In addition, Fe_3O_4 NPs synthesized by above method are usually spherical. Their morphology can be tuned from sphere to cube by adding sodium oleate in the decomposition step. Typically, 0.30g (1 mmol) sodium oleate, 0.9 g (1 mmol) of $Fe(oleate)_3$, 142 mg (0.5 mmol) of OA and 10 mL of ODE were added to a three-neck round bottom flask and heated to 320 °C under N_2 protection for 1h.

3.3.2 Synthesis of larger PbS quantum dots

The large size of PbS QDs (3.4 to 6 nm in diameter) were synthesized by a hot-injection method using OLA as capping ligands. Briefly, 10 g of $PbCl_2$ and 24 mL of OLA were added into a 50 mL flask and heated to 160 °C under N_2 protection for 1 h. The $PbCl_2$-OLA mixture was then cooled to 120 °C and degassed under vacuum for 30 min. Subsequently, 4 mL of OLA containing 115 mg of sulfur in syringe was quickly injected into the $PbCl_2$-OLA mixture under N_2 flow. The growth reaction of PbS QDs was conducted at 100 °C for several min. Once the PbS QDs reached the desired size (3.4 ~ 6 nm), the reaction was quenched by cold water. The purification of PbS QDs was performed by adding ethanol and toluene, followed by centrifugation to separate the PbS QDs. At last, the PbS QDs were dispersed in toluene for the further growth of CdS shell.

3.3.3 Synthesis of smaller PbS quantum dots

The smaller PbS QDs (less than 3 nm in diameter) were also synthesized by hot-injection method. The setup for synthesis of smaller PbS QDs is the same as that of synthesis of larger PbS QDs. Typically, 760 mg of $Pb(OAc)_2 \cdot 3H_2O$, 2.4 mL of OA and 15 mL of ODE were added into a 25 mL flask and heated to 150 °C under N_2 protection for 1 h. The mixture was then cooled to 130 °C and degassed under vacuum for 30 min. Then 2 mL mixture of $(TMS)_2S$ and TOP (1:10 ratio by volume) in the syringe was quickly injected into the flask. The temperature of the mixture was decreased and kept at 100 °C for 5 min under N_2 flow. Finally, the reaction was quenched by cold water. The smaller PbS QDs were purified by adding methanol and separated by centrifugation. The purification was repeated one more time and dispersed in toluene for the further growth of CdS shell.

3.3.4 Synthesis of PbS/CdS core/shell quantum dots

The PbS/CdS core/shell QDs were synthesized by a microwave-assisted cation exchange method. In a typical reaction of Cd oleate solution, 3 g of CdO, 15 mL of OA and 20 mL of ODE were heated to 230 °C to form a colorless solution. The Cd oleate solution was then cooled to 100 °C and degassed under vacuum for 30 min. Subsequently, 12 mL of PbS QDs and 8 mL of Cd oleate solution were added into a 35 mL microwave reaction tube and heated to 100 °C under microwave radiation for several min. At last, PbS/CdS QDs were purified by adding ethanol/toluene and separated by centrifugation. The purification procedure was repeated twice and dispersed in toluene/chloroform as stock solution.

3.4 Synthesis of Fe_3O_4/SiO_2 and $Fe_3O_4/SiO_2/NaYF_4:Nd^{3+}$ nanoparticles

3.4.1 Synthesis of Fe_3O_4/SiO_2 core/shell nanoparticles

The $Fe_3O_4@SiO_2$ core/shell NPs were synthesized by a simple microemulsion method. Briefly, 5 mL of Triton X-100, 4 mL of 1-hexanol, 0.5 mL of distilled water, 15 mL of cyclohexane and 125 μL of $NH_3 \cdot H_2O$ were mixed in a flask under gentle stirring to form a microemulsion solution. 200 μL of Fe_3O_4 cyclohexane dispersion was then added into the above solution. Subsequently, 40 μL of TEOS was added and stirred for 24 h at room temperature. Finally, the $Fe_3O_4@SiO_2$ NPs were precipitated by adding methanol and separated by centrifuge.

3.4.2 Synthesis of core/shell/shell $Fe_3O_4/SiO_2/NaYF_4:Nd^{3+}$ nanoparticles

Firstly, a $Y(OH)CO_3:Nd^{3+}$ precursor layer was synthesized by a urea-assisted homogeneous precipitation method. Typically, 0.364 g (0.95 mmol) of $Y(NO_3)_3 \cdot 6H_2O$, 0.0219 g (0.05 mmol) of $Nd(NO_3)_3 \cdot 6H_2O$ and 2 g of urea were added into 25 mL of distilled water. Then 20 mg of $Fe_3O_4@SiO_2$ NPs were added into the above solution and kept at 90 °C for 2 h. At last, $Fe_3O_4/SiO_2/Y(OH)CO_3:Nd^{3+}$ NPs were collected by centrifugation and washed with distilled water twice.

In the second step for synthesis of $Fe_3O_4/SiO_2/NaYF_4:Nd^{3+}$, the outer shell of $Y(OH)CO_3:Nd^{3+}$ was transformed into $NaYF_4:Nd^{3+}$ by a hydrothermal method. Briefly, 0.042 g (1 mmol) of NaF, 0.111 g (3 mmol) of NH_4F and 0.025 g (1 mmol) of PEI were dissolved in 10 mL of distilled water and transferred to a 25 ml Teflon lined autoclave at 110 °C for 3.5 h. The final $Fe_3O_4/SiO_2/NaYF_4:Nd^{3+}$ NPs were separated by centrifugation and washed with distilled water several times.

3.5 Synthesis of self-assembled Fe_3O_4 and PbS/CdS supernanoparticles

In a typical synthesis of SASNs, 1 mL of Fe_3O_4 (4 mg/mL) NPs and 1mL of PbS/CdS (NIR-II) QDs (6 mg/mL) chloroform dispersion were added into 1 mL of DTAB (20 mg/mL) aqueous solution and thoroughly mixed by vortex. After evaporating the chloroform by N_2 flow, the mixed aqueous solution was

swiftly injected into a PVP-in- EG solution (20 mg/mL) under vigorous stirring for 4 h. The resulting SASNs were separated by centrifugation and washed with ethanol several times. Finally, SASNs were dispersed in water as stock solution.

3.6 Synthesis of Fe_3O_4 and PbS/CdS loaded mesoporous silica nanospheres

3.6.1 Synthesis of large-pore mesoporous silica nanospheres

The large-pore $mSiO_2$ nanospheres were synthesized by a one-pot biphase stratification method. Typically, 12 mL of CTAC solution (25 wt%) and 0.09 g of TEA were dissolved in 18 mL of distilled water at 60 ℃ for 1 h. Subsequently, 0.5 mL of TEOS and 9.5 mL of cyclohexane were added to the above solution. The reaction was kept at 60 ℃ for 60 h. The $mSiO_2$ were collected by centrifugation and washed with ethanol several times. At last, the $mSiO_2$ nanospheres were refluxed with 0.6 wt% NH_4NO_3 ethanol solution at 60 ℃ for 6 h to remove the CTAC template completely.

3.6.2 Synthesis of thiol-modified mesoporous silica nanospheres

300 mg of $mSiO_2$ nanospheres dispersed in 15 mL of ethanol were added with 150 μL of MPTS and 375 μL of $NH_3.H_2O$ and gently stirred for 12 h at room temperature. Finally, the $mSiO_2$-SH were collected by centrifugation and washed with ethanol twice, and dispersed in chloroform.

3.6.3 Synthesis of Fe_3O_4 and PbS/CdS mesoporous silica nanospheres

Briefly, 1mL of Fe_3O_4 and PbS/CdS (4 mg/mL) chloroform solution were added into 4 mL of $mSiO_2$-SH chloroform solution (2 mg/mL) and stirred for 30 min at room temperature. Then $mSiO_2$@PbS/CdS-Fe_3O_4 were isolated by centrifugation and washed with chloroform twice to remove free Fe_3O_4 NPs and PbS/CdS QDs. Subsequently, 1 mL of $mSiO_2$@PbS/CdS-Fe_3O_4 in chloroform dispersion (5 mg/mL) was mixed with 20 mg of PEI and stirred for 2 h to transfer the $mSiO_2$@PbS/CdS-Fe_3O_4 into water by forming a PEI coating. Finally, the PEI-coated $mSiO_2$@PbS/CdS-Fe_3O_4 were precipitated by adding cyclohexane and re-dispersed in water.

3.7 Characterization

3.7.1 Transmission electron microscopy and energy dispersive X-ray spectroscopy

Transmission electron microscopy (TEM) is a major analysis tool for directly observing the morphology and size of nanostructures by using a beam of electrons to transmit through a specimen to form an image. In my experiment, NPs dispersed in water or organic solvent were deposited onto copper TEM grids coated with a thin (5-50 nm in thickness) carbon film. The grid was then dried in the air before TEM measurements. Low and High-resolution TEM images were obtained by using a JEOL-2100F microscope at 200 kV equipped with a charge-coupled device (CCD) camera. Meanwhile, energy dispersive X-ray spectroscopy

(EDX) was used to determine the elemental composition of prepared NPs at different areas on the sample during TEM measurement.

3.7.2 X-ray diffraction

X-ray diffraction (XRD) is an analytical technique used for identifying the crystalline structure of materials. The sample for XRD measurement was simply prepared by depositing the NPs solution on glass substrate and dried in fume hood to form a thin film. The XRD study for all samples was carried out with XRD diffractometer (Bruker D8 Advance) using Cu *K*α radiation source (λ = 0.1540598 nm) at a 40 kV tube voltage and 40 mA tube current. Diffraction patterns were collected in the 2θ range of 5-80°, by using the step of 0.1° and counting time of 0.02 s.

3.7.3 Absorption spectroscopy

The absorption spectra of all samples were measured by a UV-visible-NIR spectrophotometer (Cary 5000) with scan speed of 600 nm/min. All experiments were done in a transmission mode on NPs solution filled in a quartz cuvette. A reference was used to obtain a baseline before each experiment.

3.7.4 Photoluminescence spectroscopy

The upconverting and NIR photoluminescence spectra of lanthanide-doped NPs were acquired under continuous laser excitation of 980 and 806 nm, respectively. The upconverting emission signal focused by a lens in 90^o configuration was collected by an Avaspec-ULS2048L spectrometer (Avantes) through an optical fiber. By keeping the same optical path configuration, the NIR emission spectra was detected by a Shamrock 500i monochromator (Andor) equipped with an iDus InGaAs 1.7 NIR detector (Andor).

Photoluminescence spectra of QDs were taken with a Fluorolog®-3 system (Horiba Jobin Yvon) using a CCD or photomultiplier tube detector which depends on the emission wavelength of QDs. A Xenon lamp was used as excitation source.

3.7.5 Inductively coupled plasma optical emission spectroscopy

Inductively coupled plasma optical emission spectroscopy (ICP-OES) is an analytical technique for the detection of trace chemical elements, which is based on characteristic electromagnetic emission of particular elements when using inductively coupled plasma to produce excited atoms and ions. The concentration of the elements within the sample can be determined by the emission intensity in comparison with the standard sample. In our experiments, the content of Pb, Cd and Fe elements was assessed by ICP-OES (Agilent Technologies, 5100).

3.7.6 Fourier-transform infrared spectroscopy

Fourier-transform infrared (FTIR) Spectroscopy is an effective analytical method for detecting functional groups through characteristic IR absorption of chemical bonds in organic molecules. In my experiments, the FTIR spectra were collected in the range of 4000-500 cm^{-1} by a ThermoFisher Scientific Nicolet 6700 FTIR spectrometer using KBr as a reference.

3.7.7 Magnetic characterization

The magnetic hysteresis loop was taken by a vibrating sample magnetometer (VSM, Model 4 HF-VSM, ADE USA) at working temperature of 300 K with magnetic field up to 3 T. Temperature-dependent zero-field-cooled (ZFC) and field-cooled (FC) magnetization curves of the samples were measured by the same magnetometer under an applied field of 100 Oe between 5 K and 300 K.

3.7.8 Viability assay

In order to apply the as-prepared NPs for bioapplications, the cytotoxicity of NPs was studied firstly by using HeLa cancer cells and human embryonic kidney (HEK 293T) cells. They were plated into a 96-well plate with a density of 5×10^5 cells/well and incubated in 100 μL of Dulbecco's modified Eagle's medium (DMEM) for 24 h, followed by adding various concentrations of NPs dispersion. Blank controls without NPs dispersion (*i.e.*, cells only) were run simultaneously. Cell viability was measured using CellTiter 96 Non-Radioactive Cell Proliferation Assay kit (MTT, Promega) according to the manufacturer's protocol. Briefly, 3-(4,5-dimethylthiazol-2-yl)-2,5-diphenyltetrazolium bromide (MTT) solution (15 μL) was added into each well. After 24 h incubation, the medium containing unreacted MTT was carefully removed and the formed formazan blue crystals were dissolved by adding 100 μL of DMSO. The absorbance at $\lambda = 570$ nm was then measured using Powerwave HT Microplate Reader (Bio-Tek). Each concentration was replicated by 6 times. Cell viability was calculated as the ratio of absorbance of mixtures containing NPs to control cells.

3.7.9 NIR and visible imaging *ex vivo*

A homemade setup was designed to acquire the NIR and visible imaging *ex vivo* and estimate the photoluminescence penetration depth. Specifically, aqueous dispersion of NPs was filled in a microchannel underneath pieces of chicken tissue with various thickness and a NIR or visible camera was fixed on the top to take images.

The NIR images of samples were recorded by an Xeva-1.7 infrared camera (Xenics Corp), in which the InGaAs array is used to detect the emitting signal ranging from 900 nm to 1700 nm. The laser diode of 806 nm with power density of 10 W/cm^2 was used as excitation source. Appropriate long-pass optical filters

(830 nm, 980 nm and 1200 nm) were used to take the images in the specific spectral range and block the scattered excitation light of the 806 nm laser.

The visible images of samples were taken by a silicon chip camera (Point Grey) equipped with a 980 nm short-pass filter to remove the emission wavelengths beyond 980 nm. The laser diode of 980 nm with power density of 300 W/cm^2 was used as excitation source.

3.7.10 T_2 relaxivity measurements *in vitro* and MR imaging *in vivo*

T_2-weighted MR images were acquired by a 3T clinic MRI scanner (Bruker Biospin Corporation, Billerica, MA, USA) at room temperature. Briefly, NPs in PBS buffer with various concentrations were placed in a series of tubes for T_2-weighted MR imaging. The relaxivity value (r_2) was calculated based on the fitting curve of $1/T_2$ relaxation time (s^{-1}) *vs* the concentration of Fe (mM).

Mouse bearing one 4T1 tumor was injected with 200 μL of PBS buffer containing NPs (2 mg/mL, dose=10 mg/kg). The MR imaging of the mouse was conducted on the same MR imaging scanner equipped with a special coil designed for small animal imaging. The mouse was scanned before and after injection of the NPs.

CHAPTER 4 RESULTS

This chapter is divided into three different parts, each corresponding to published (or accepted) articles. The first part is about synthesis of novel multifunctional (superparamagnetic and NIR-to-NIR photoluminescent) nanocomposite and its application for dual-mode (optical and MR) imaging. However, the aforementioned multifunctional nanocomposite exhibits slow confinement due to the single magnetic core character, which restricts its use for magnetic-driven bioapplications and magnetothermal therapy. In the second part we develop another multifunctional nanoplatform containing multiple magnetic NPs and NIR PbS/CdS QDs by self-assembly. This nanoplatform constituted by multiple magnetic NPs can be not only used for deep-tissue bimodal imaging but also for amplified dual-mode (magnetothermal and photothermal therapy) heating treatment. Inspired by the promising drug delivery modality and ease of surface functionalization of large-pore $mSiO_2$, we engineer a new sort of multifunctional nanoplatform integrating magnetic NPs and PbS/CdS QDs based on large-pore $mSiO_2$ in the last part. By using this multifunctional nanoplatform, the bimodal imaging and synergistic effect from the dual-mode heating mode and multi-stimuli responsive drug release behavior are systematically studied.

4.1 An Integrated Multifunctional Nanoplatform for Deep-tissue Dual-mode Imaging

Fan Yang, Artiom Skripka, Antonio Benayas, Xianke Dong, Sung Hwa Hong, Fuqiang Ren, Jung Kwon Oh, Xinyu Liu, Fiorenzo Vetrone, and Dongling Ma

Adv. Funct. Mater. 28 (2018) 1706235.

As introduced in Chapter 1, multifunctional (superparamagnetic and photoluminescent) NPs, as an emerging class of highly functional nanomaterials, have drawn considerable attention for dual-mode imaging. However, because most of the photoluminescent components in these hybrid NPs are operated in the visible range, they show shallow tissue penetration and ambiguous signal contrast in optical imaging due to the tissue-induced optical extinction and autofluorescence. To address this issue, it is highly desirable but also challenging to develop new multifunctional (superparamagnetic and photoluminescent) NPs, with both of their excitation and emission in the optically transparent biological windows situated in the NIR range (NIR-I: 700–950 nm; NIR-II: 1000–1350 nm), for *in vivo*, deep-tissue dual-mode imaging. Recent studies have revealed that Nd^{3+} doped NPs as photoluminescent component possess both excitation and emission wavelength within the biological windows, which results in excellent deep-tissue *in vivo* bioimaging.

In this paper, we specifically designed a multifunctional nanoplatform that exploits unique superparamagnetic and NIR-to-NIR photoluminescence properties. This core/shell/shell nanoplatform (Fe_3O_4@SiO_2@$NaYF_4$:Nd^{3+}) is composed of superparamagnetic Fe_3O_4 core, intermediate silica shell and outer NIR-to-NIR photoluminescent shell of $NaYF_4$:Nd^{3+}. Due to their unique NIR-to-NIR photoluminescence properties, this nanoplatform exhibits three emission at 900 (NIR-I), 1060 (NIR-II), and 1340 nm (NIR-II) under excitation by by laser at ≈ 800 nm (NIR-I), allowing the NIR photoluminescence signal to be detected through a tissue as thick as 13 mm, superior to similar visible-emitting nanoplatform containing upconverting shell (Fe_3O_4@SiO_2@$NaYF_4$:Er^{3+},Yb^{3+}). On the other hand, Fe_3O_4@SiO_2@$NaYF_4$:Nd^{3+} can serve as a T_2 negative contrast agent for MR imaging, as demonstrated by the remarkable darkening effect in *in vivo* MR imaging experiment. These results suggest that Fe_3O_4@SiO_2@$NaYF_4$:Nd^{3+} NPs are highly promising candidates for high-resolution and deep-tissue dual-mode (optical and MR) *in vivo* imaging.

An Integrated Multifunctional Nanoplatform for Deep-Tissue Dual-Mode Imaging

Fan Yang, Artiom Skripka, Antonio Benayas, Xianke Dong, Sung Hwa Hong, Fuqiang Ren, Jung Kwon Oh, Xinyu Liu, Fiorenzo Vetrone, and Dongling Ma**

The combination of biocompatible superparamagnetic and photoluminescent nanoparticles (NPs) is intensively studied as highly promising multifunctional (magnetic confinement and targeting, imaging, etc.) tools in biomedical applications. However, most of these hybrid NPs exhibit low signal contrast and shallow tissue penetration for optical imaging due to tissue-induced optical extinction and autofluorescence, since in many cases, their photoluminescent components emit in the visible spectral range. Yet, the search for multifunctional NPs suitable for high photoluminescence signal-to-noise ratio, deep-tissue imaging is still ongoing. Herein, a biocompatible core/shell/shell sandwich structured Fe_3O_4@SiO_2@$NaYF_4$:Nd^{3+} nanoplatform possessing excellent superparamagnetic and near-infrared (excitation) to near-infrared (emission), i.e., NIR-to-NIR photoluminescence properties is developed. They can be rapidly magnetically confined, allowing the NIR photoluminescence signal to be detected through a tissue as thick as 13 mm, accompanied by high T_2 relaxivity in magnetic resonance imaging. The fact that both the excitation and emission wavelengths of these NPs are in the optically transparent biological windows, along with excellent photostability, fast magnetic response, significant T_2-contrast enhancement, and negligible cytotoxicity, makes them extremely promising for use in high-resolution, deep-tissue dual-mode (optical and magnetic resonance) in vivo imaging and magnetic-driven applications.

1. Introduction

In the past decades, multifunctional nanoparticles (NPs) with more than single functionality have been one of the most rapidly growing scientific areas.[1] Thanks to their unique superparamagnetism, superparamagnetic NPs can be used to magnetically confine, label, and separate various biological species (DNAs, proteins, bacteria, cancer cells, etc.) and thus allow for ultrasensitive biodetection.[2] They can also serve as magnetic resonance (MR) imaging contrast agents for the diagnosis of malignant tissues, nanoscale vehicles for carrying therapeutic payloads (anticancer drugs, small inhibitory RNA) and delivering them to desired tumor sites in a target-specific manner, as well as hyperthermia agents for treating cancers under an alternating magnetic field.[3] Optical imaging using photoluminescent materials as contrast agents is regarded as the most versatile visualization tool for biomedical research such as cell imaging and evaluation of drug effects.[4] In view of the above mentioned important applications of superparamagnetism and optical imaging in biomedicine, combing superparamagnetic and photoluminescent components into a single nanoplatform will undoubtedly lead to a new range of potential applications in the biomedical field. In particular, such multifunctional nanoplatform will enable dual-modal imaging, fluorescence monitored magnetic-driven drug delivery, and simultaneous in vivo imaging and targeted hyperthermia therapy, just to name a few.[5]

Among these biomedical applications, dual-mode imaging has been shown to be particularly attractive. Optical imaging shows great potential to translate into the clinic due to its high sensitivity at the subcellular level and the low cost of related imaging facilities; while MR imaging is regarded as a superior technique for acquiring anatomical, physiological, and functional images with high 3D spatial resolution.[6] Their combination for realizing powerful dual-mode

F. Yang, A. Skripka, Dr. A. Benayas, Dr. F. Ren, Prof. F. Vetrone, Prof. D. Ma
Institut National de la Recherche Scientifique – Énergie Matériaux et Télécommunications
Université du Québec
1650 Boul. Lionel-Boulet, Varennes, Québec J3X 1S2, Canada
E-mail: vetrone@emt.inrs.ca; ma@emt.inrs.ca
Dr. A. Benayas
Department of Physics and CICECO – Aveiro Institute of Materials
University of Aveiro
3810-193 Aveiro, Portugal
The ORCID identification number(s) for the author(s) of this article can be found under https://doi.org/10.1002/adfm.201706235.
X. Dong, Prof. X. Liu
Department of Mechanical and Industrial Engineering
University of Toronto
5 King's College Road, Toronto, Ontario M5S 3G8, Canada
S. H. Hong, Prof. J. K. Oh
Department of Chemistry and Biochemistry
Concordia University
Montreal, Quebec H4B 1R6, Canada

DOI: 10.1002/adfm.201706235

imaging is clearly advantageous because it will allow retrieving both macroscopic and subcellular information of biological species and events, and thus leading to improved diagnostic accuracy.[7] Therefore, it bears unmeasurable societal and biomedical importance. For instance, cancer as a major public health problem has caused millions of deaths worldwide. Despite considerable research efforts that have been devoted to cancer research over the past few decades, the cancer death rate has not been yet considerably decreased. It is largely because, in many cases, the cancer could only be diagnosed at an advanced stage, by then, however, the tumor is already metastasized to other parts of the body and the best time for surgical intervention has been missed. From the therapeutic viewpoint, the survival rate can be greatly increased by realizing early detection of the cancer. In addition to saving lives, early detection and treatment of the cancer can also reduce cancer treatment costs and medical care expenditure and thereby decrease the burden of patients, their families and the society in general. Considering all these factors, it is urgent to develop new, high-sensitivity probes for cancer detection at an early stage. Moreover, during the cancer therapy, these high-sensitivity diagnostic probes can also help monitor the response to cancer treatment and assess its effectiveness.

Inspired by their unprecedented capability and potentially huge impacts on our health and society, a variety of multifunctional (superparamagnetic and photoluminescent) NPs have been specifically engineered for dual-mode imaging. For example, Cheon and co-workers demonstrated "core-satellite" hybrid nanoparticle probes (involving rhodamine-doped silica and Fe_3O_4), which can provide highly improved fluorescence and MR imaging for the detection of neuroblastoma cells.[7] The study presented by Liu and co-workers showed that the unique multifunctional NPs with both upconversion luminescence (UCL) and superparamagnetic properties can realize in vivo multimodal imaging (UCL and MR imaging) of wounds under magnetic targeting.[5a] Recently, Bawendi and co-workers reported colloidal magnetofluorescent supernanoparticles based on magnetic Fe_3O_4 NPs and CdSe-CdS quantum dots (QDs) for dual-modal imaging (in vivo multiphoton and MR imaging) of mice bearing brain metastasis of a murine mammary carcinoma.[8]

However, in most of these studies the photoluminescent component is based on visible emitting organic dyes, upconversion nanoparticles (UCNPs) and QDs.[5a–c,7–9] The tissue-induced optical extinction and autofluorescence in the visible range will result in limited penetration depth and ambiguous photoluminescence signal, respectively, which restricts their use as in vivo optical probes.[10] To address this issue, the photoluminescent component, with absorption and emission wavelengths operating in the biological windows situated in the near-infrared (NIR) range (denoted as NIR-I: 700–950 nm; NIR-II: 1000–1350 nm; NIR-III: 1550–1870 nm) in which tissues are optically transparent, are highly desired.[11] In other words, ideal photoluminescent bioprobes for in vivo optical imaging should have both of their excitation and generated emission wavelengths lying within these three biological windows. This can ensure that both the excitation and emission signals are less attenuated. In addition, it is believed that the autofluorescence background can be minimized since the excitation radiation in the NIR biological windows absorbed by tissue is negligible.[12] This will lead to a higher signal-to-noise ratio. Taking all these into consideration, bioprobes with their excitation source and photoluminescence signal in the biological windows are expected to lead to deeper tissue imaging. It is even more attractive to develop new multifunctional (superparamagnetic and photoluminescent) NPs, containing NIR-to-NIR bioprobes, for in vivo, deep-tissue dual-mode imaging. Our group has worked on ultrastable NIR-to-NIR PbS/CdS/ZnS QDs, which demonstrate several interesting applications, such as deep-tissue fluorescence imaging and highly sensitive nanothermometry.[13] Nonetheless, in the field of biomedicine, the toxicity of heavy metals (Pb and Cd) remains a strong concern.

Recently, neodymium (Nd^{3+}) ions, as sensitizers for other visible emitting rare earth ions, have aroused growing interest due to their higher absorption cross section and thereby higher quantum yield of upconverted emission when compared with the most commonly used Yb^{3+} sensitizer ions.[11a,14] As a matter of fact, Nd^{3+} doped NPs can be efficiently excited by laser radiation at ≈800 nm (NIR-I) and present three emission bands located at about 900 (NIR-I), 1060 (NIR-II), and 1340 nm (NIR-II). That is, Nd^{3+} doped NPs can have both excitation and emission situated within the biological windows.[10] In view of this important feature, combined with their lower toxicity in comparison with Pb and Cd-based QDs, using Nd^{3+} ion doped materials directly as photoluminescent bioprobes, will be highly beneficial for optical imaging. Moreover, autofluorescence arising from endogenous fluorescent molecules of complex biological tissues in the NIR-II region is minimal, thus allowing for high contrast imaging.[15] Furthermore, it is known that the water absorption at 800 nm is much lower than that at 980 nm, which is commonly used to excite Yb^{3+} sensitized rare earth doped NPs. This can help to reduce the photodamage to biological tissues due to the decreased overheating effect.[11a] Therefore, in terms of excitation wavelength for photoluminescence imaging, circa 800 nm is superior to the conventionally used 980 nm wavelength. All these advantages make Nd^{3+}-doped materials very promising candidates for NIR-to-NIR deep-tissue optical imaging. Very recently, a few studies have shown that Nd^{3+}-doped NPs as photoluminescent bioprobes result in excellent deep-tissue in vivo bioimaging.[10,14c,16] However, work regarding hybrid multifunctional (superparamagnetic and photoluminescent) NPs, which combine superparamagnetic and NIR-to-NIR photoluminescent Nd^{3+}-doped components, has not been reported thus far.

In this paper, we have designed a hybrid nanoplatform that exploits unique superparamagnetic and NIR-to-NIR photoluminescence properties. The multifunctional NPs consist of a superparamagnetic Fe_3O_4 core surrounded by an intermediate SiO_2 shell and further coated by an outer NIR-to-NIR photoluminescent shell of $NaYF_4$:Nd^{3+}. They exhibit strong and stable emission at desired wavelengths within NIR-I and NIR-II biological windows coupled with rapid magnetic response. Deep-tissue imaging experiment shows that NIR photoluminescence can still be detected when the thickness of chicken breast samples reaches 13 mm, about three times thicker than what can be achieved by similar core/shell/shell NPs where the shell instead contains the Er^{3+}/Yb^{3+} upconverting pair, namely Fe_3O_4@SiO_2@$NaYF_4$:Er^{3+}, Yb^{3+} NPs. Meanwhile, in vivo MR imaging

exhibits a significant darkening effect in T_2-weighted images with the use of $Fe_3O_4@SiO_2@NaYF_4:Nd^{3+}$ NPs as the contrast agent. To the best of our knowledge, this is the first report on the development of multifunctional (superparamagnetic and photoluminescent) NPs involving the NIR-to-NIR photoluminescent component ($NaYF_4:Nd^{3+}$). With excellent NIR-to-NIR photoluminescence and superparamagnetic properties, they are expected to be suitable not only for deep-tissue dual-mode (optical and MR) bioimaging as demonstrated herein but also for a variety of other applications, including, but not limited to, high sensitivity detection of cancer cells enabled by magnetic confinement and dual-mode imaging, and magnetic-driven drug delivery in a target-specific manner.

2. Results and Discussion

The overall synthetic procedure for the $Fe_3O_4@SiO_2@NaYF_4:Nd^{3+}$ NPs is illustrated in **Figure 1**a. First, oleic acid stabilized Fe_3O_4 NPs with an average diameter of 11.5 ± 0.4 nm (Figure 1b; Figure S1, Supporting Information) were synthesized by a modified thermal decomposition method.[17] The well-resolved lattice fringes in the high-resolution transmission electron microscopy (HRTEM) image and clear diffraction rings (Figure S2, Supporting Information) reveal the highly crystalline nature of the synthesized NPs. Both the high-resolution X-ray photoelectron spectroscopy (XPS) spectrum of Fe 2p (Figure S3, Supporting Information) and X-ray diffraction (XRD) pattern (Figure S4, Supporting Information) confirmed that the NPs were magnetite (Fe_3O_4). Subsequently, a silica (SiO_2) layer with a thickness of about 11–12 nm (Figure 1c) was grown around the magnetic Fe_3O_4 core before the final deposition of the photoluminescent shell in order to minimize the lattice mismatch between the Fe_3O_4 core and $NaYF_4:Nd^{3+}$ shell, as well as the possible photoluminescence quenching by the superparamagnetic core.[18] Another benefit of this intermediate, robust SiO_2 shell is that it can help to prevent Fe_3O_4 NP dissolution and iron leaching in complicated biological environments, such as in highly acidic media.[19] Subsequently, prior to growing the final photoluminescent shell $NaYF_4:Nd^{3+}$, a stoichiometric lanthanide carbonate layer $Y(OH)CO_3:Nd^{3+}$ was first deposited on the SiO_2 shell using a urea-based homogenous precipitation process.[20] Finally, the outer precursor shell, $Y(OH)CO_3:Nd^{3+}$, was transformed into $NaYF_4:Nd^{3+}$ by a hydrothermal method.[20] Figure 1d shows the TEM image of $Fe_3O_4@SiO_2@Y(OH)CO_3:Nd^{3+}$ NPs. These sandwich structured NPs were ≈48–52 nm in diameter with a $Y(OH)CO_3:Nd^{3+}$ shell of 7–8 nm in thickness. After hydrothermal treatment, the $NaYF_4:Nd^{3+}$ shell was formed and the same sandwich-like morphology and overall size were retained (Figure 1e). The phase transition from amorphous [$Y(OH)CO_3:Nd^{3+}$] to crystalline ($NaYF_4:Nd^{3+}$) structure was confirmed by clearly observable lattice fringes with distance of 0.29 nm, assigned to the (110) plane of hexagonal β-$NaYF_4:Nd^{3+}$ in the HRTEM image (Figure 1f). It was further confirmed by the XRD pattern of $Fe_3O_4@SiO_2@NaYF_4:Nd^{3+}$ (Figure S4, Supporting Information). The Fourier

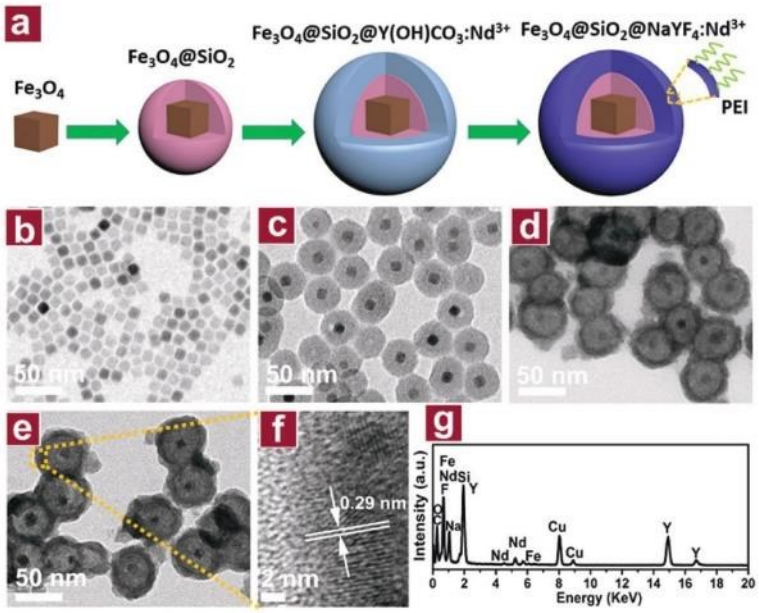

Figure 1. a) Schematic illustration of synthetic procedure of $Fe_3O_4@SiO_2@NaYF_4:Nd^{3+}$ NPs. TEM images of b) Fe_3O_4, c) $Fe_3O_4@SiO_2$, d) $Fe_3O_4@SiO_2@Y(OH)CO_3:Nd^{3+}$, $Fe_3O_4@SiO_2@NaYF_4:Nd^{3+}$. HRTEM image of f) $NaYF_4:Nd^{3+}$ shell shows lattice fringes with distance of 0.29 nm. g) Elemental analysis of the $Fe_3O_4@SiO_2@NaYF_4:Nd^{3+}$ NPs by EDX.

transform infrared (FTIR) spectrum indicates that polyethylenimine (PEI) was coated on Fe_3O_4@SiO_2@$NaYF_4$:Nd^{3+} NPs, endowing these NPs with water dispersity for potential biomedical application (Figure S5, Supporting Information). It should be noted that the overall size (≈50 nm in diameter) of Fe_3O_4@SiO_2@$NaYF_4$:Nd^{3+} NPs can well fit into the suitable size range (10–200 nm) of NPs for long circulation in blood, which is a merit for biorelated applications.[21] In order to detect the elemental composition of this multilayered nanoarchitecture, energy dispersive X-ray spectroscopy (EDX) analysis was carried out on the Fe_3O_4@SiO_2@$NaYF_4$:Nd^{3+} NPs (Figure 1g). The EDX spectrum shows all the expected constituent elements (Fe, O, Si, Na, Y, Nd, and F) of Fe_3O_4@SiO_2@$NaYF_4$:Nd^{3+} NPs, further supporting that Nd^{3+} was successfully integrated into the $NaYF_4$ crystal structure.

The NIR-to-NIR photoluminescence spectrum of Fe_3O_4@SiO_2@$NaYF_4$:Nd^{3+} NPs under 806 nm laser excitation shown in **Figure 2**a. Three well-resolved bands can be observed at around 900, 1060, and 1340 nm, corresponding to the $^4F_{3/2} \rightarrow {}^4I_{9/2}$, $^4F_{3/2} \rightarrow {}^4I_{11/2}$ and $^4F_{3/2} \rightarrow {}^4I_{13/2}$ transitions of Nd^{3+} ions, respectively.[16,21] The NIR-to-NIR photoluminescence generation mechanism is based on a single-photon process, as depicted in Figure 2b. Upon 806 nm laser irradiation, the Nd^{3+} ions are directly excited from the ground sate ($^4I_{9/2}$) to the excited state

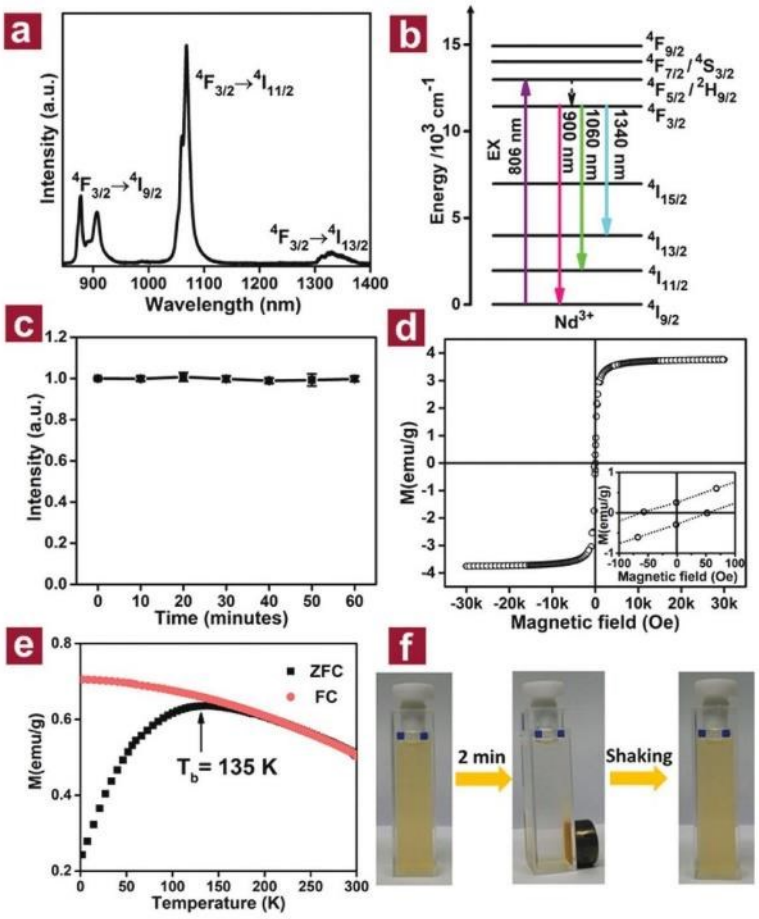

Figure 2. a) Photoluminescence spectrum of Fe_3O_4@SiO_2@$NaYF_4$:Nd^{3+} following excitation with an 806 nm laser. b) Energy level diagrams of Nd^{3+} and mechanism of NIR-to-NIR photoluminescence. c) Photostability of Fe_3O_4@SiO_2@$NaYF_4$:Nd^{3+} as a function of radiation time with the 806 nm laser. d) Magnetic hysteresis loop of Fe_3O_4@SiO_2@$NaYF_4$:Nd^{3+} NPs at 300 K. The inset shows the magnified view of hysteresis loop under low magnetic field. e) Temperature-dependent ZFC and FC magnetization curves at 100 Oe for Fe_3O_4@SiO_2@$NaYF_4$:Nd^{3+} NPs. f) Photographs of an aqueous dispersion of Fe_3O_4@SiO_2@$NaYF_4$:Nd^{3+} NPs before applying a magnet (left), after confinement by the magnet (middle), and after removing the magnet and shaking for redispersion (right).

($^4F_{5/2}$/$^2H_{9/2}$). The excited electrons then nonradiatively relax to the lower energy $^4F_{3/2}$ emitting state, and finally decay radiatively to the ^4I_J (J = 9/2, 11/2, and 13/2) states, generating the corresponding NIR photoluminescence emissions.[22] As mentioned above, the excitation wavelength at 806 nm and NIR emission bands at 900, 1060, and 1340 nm are all within the biological windows, which make these NPs ideal for biological imaging.

The photostability of Fe_3O_4@SiO_2@$NaYF_4$:Nd^{3+} NPs was examined first before deep-tissue imaging experiments. The photoluminescence intensity as a function of irradiation time under the 806 nm laser is plotted in Figure 2c. The integrated intensity of all three bands remained the same in aqueous solution for 1 h under continuous laser irradiation, indicating that these NPs possess excellent photostability. The magnetic properties of Fe_3O_4@SiO_2@$NaYF_4$:Nd^{3+} NPs were characterized by a hysteresis loop, as shown in Figure 2d. It can be seen that Fe_3O_4@SiO_2@$NaYF_4$:Nd^{3+} NPs exhibit a negligible hysteresis (near-zero coercivity and remanence), which reveals their superparamagnetic properties. The saturation magnetization of such NPs is 3.7 emu g^{-1} at 300 K. This value is lower than those reported in the literature for Fe_3O_4, which can be easily understood since the hybrid NPs contain nonmagnetic components of SiO_2 and $NaYF_4$:Nd^{3+}. The temperature-dependent zero-field-cooled (ZFC) and field-cooled (FC) magnetization measurements were obtained under an applied field of 100 Oe between 5 and 300 K. The ZFC and FC curves can coincide at relatively high temperature while separate with gradually decreasing temperature due to the progressive blocking of differently sized particles in the same sample as the temperature is decreased.[23] The blocking temperature (T_b) (≈135 K), which is much lower than room temperature, confirms the superparamagnetic properties of these NPs at room temperature and further ensures their easy manipulation by an external magnetic field at room temperature, as described below. The benefit of the superparamagnetic property of Fe_3O_4@SiO_2@$NaYF_4$:Nd^{3+} NPs is clearly demonstrated in Figure 2f. All of the Fe_3O_4@SiO_2@$NaYF_4$:Nd^{3+} NPs dispersed in water could be confined by a magnet in about two minutes. After shaking, Fe_3O_4@SiO_2@$NaYF_4$:Nd^{3+} NPs could be easily redispersed back into water, distinctly different from the behavior of classic magnetic NPs that can form nonseparable agglomerates after initial magnetic confinement.[24] The NIR images of Fe_3O_4@SiO_2@$NaYF_4$:Nd^{3+} NPs in aqueous solution confined by the magnet were also taken to further substantiate the observed superparamagnetism (Figure S6a, Supporting Information). The NIR images clearly show the variation of emission intensity distribution of such NPs in the excitation light path with time and quick accumulation of NPs toward the wall of the cuvette in two minutes after applying a magnet, resulting in a much brighter spot at the wall. The emission intensity on that spot saturates at around two minutes (Figure S6b, Supporting Information), indicating the fast response of Fe_3O_4@SiO_2@$NaYF_4$:Nd^{3+} NPs to the external magnetic field. All together, these results suggest that the Fe_3O_4@SiO_2@$NaYF_4$:Nd^{3+} NPs possess both excellent NIR-to-NIR photoluminescent and superparamagnetic properties, which render them simultaneously suitable for dual-mode (optical and MR) bioimaging and magnetic-driven applications.

To demonstrate the feasibility of the Fe_3O_4@SiO_2@$NaYF_4$:Nd^{3+} NPs for deep-tissue imaging and magnetic confinement, an ex vivo experiment was designed, as illustrated in **Figure 3**a. Briefly, a chicken breast sample was placed on the top of a microchannel filled with aqueous solution containing Fe_3O_4@SiO_2@$NaYF_4$:Nd^{3+} NPs. Then, an NIR camera equipped with different optical filters was fixed on the top of the microchannel in order to acquire images when the Fe_3O_4@SiO_2@$NaYF_4$:Nd^{3+} NPs were confined by a magnet located underneath. The 806 nm laser was used as an excitation source. Figure 3b shows the ex vivo imaging through chicken breast samples with different thickness (0, 2, 4, 6, 8, and 10 mm) using a series of long-pass filters (830, 980, and 1200 nm). We observed that all the NIR photoluminescence images show quite high contrast and consisted of a bright spot with a completely dark background. The bright spot was situated right above where the magnet was located and no other photoluminescence signal was detected in the rest of the microchannel, suggesting almost complete confinement of all the NPs by the magnet. The relative photoluminescence intensity of Fe_3O_4@SiO_2@$NaYF_4$:Nd^{3+} NPs as a function of penetration depth of the chicken breast is shown in Figure 3c. Importantly, when the thickness of the chicken breast reached 13 mm, the NIR photoluminescence signal longer than 830 and 980 nm could still be easily detected. It should be noted that the thin $NaYF_4$:Nd^{3+} shell only constitutes a small part of the Fe_3O_4@SiO_2@$NaYF_4$:Nd^{3+} NP, unlike a solid sphere of $NaYF_4$:Nd^{3+} of the same overall size, which would be expected to have a much higher emission intensity. However, even in this situation, the NIR photoluminescence signal of these NPs can already be transmitted across such a considerable depth of tissue, indicating the high quality of the formed shell and its excellent luminescence property. This deep penetration capability guarantees their potential application for deep-tissue bioimaging.

Meanwhile, in order to compare the deep-tissue penetration of NIR with visible light, we used the same synthetic strategy to prepare upconverting visible emitting Fe_3O_4@SiO_2@$NaYF_4$:Er^{3+}, Yb^{3+} UCNPs. The TEM image (Figure S7a, Supporting Information) shows that the Fe_3O_4@SiO_2@$NaYF_4$:Er^{3+}, Yb^{3+} UCNPs have similar morphology and size as that of Fe_3O_4@SiO_2@$NaYF_4$:Nd^{3+} NPs. The presence of the doping elements (Er, Yb) is evidenced in their EDX pattern (Figure S7b, Supporting Information). Under excitation with a 980 nm laser, the upconverted photoluminescence spectrum of Fe_3O_4@SiO_2@$NaYF_4$:Er^{3+}, Yb^{3+} UCNPs (Figure S8, Supporting Information) exhibits four peaks located at 409, 521, 542, and 654 nm ascribed to the $^2H_{9/2}\rightarrow{}^4I_{15/2}$, $^2H_{11/2}\rightarrow{}^4I_{15/2}$, $^4S_{3/2}\rightarrow{}^4I_{15/2}$, and $^4F_{9/2}\rightarrow{}^4I_{15/2}$ transitions of Er^{3+}, respectively. Based on these upconverted visible emissions of the Fe_3O_4@SiO_2@$NaYF_4$:Er^{3+}, Yb^{3+} UCNPs, we adopted the aforementioned experimental setup to acquire images by using a visible camera (Figure S9a, Supporting Information) and also further plotted their relative upconverted emission intensity as a function of the penetration depth of the chicken breast samples in Figure S9b (Supporting Information). The visible image without any chicken tissue shows a bright spot in the center. After placing chicken breast samples of increasing thicknesses, the emission intensity of that spot gradually decreases. When

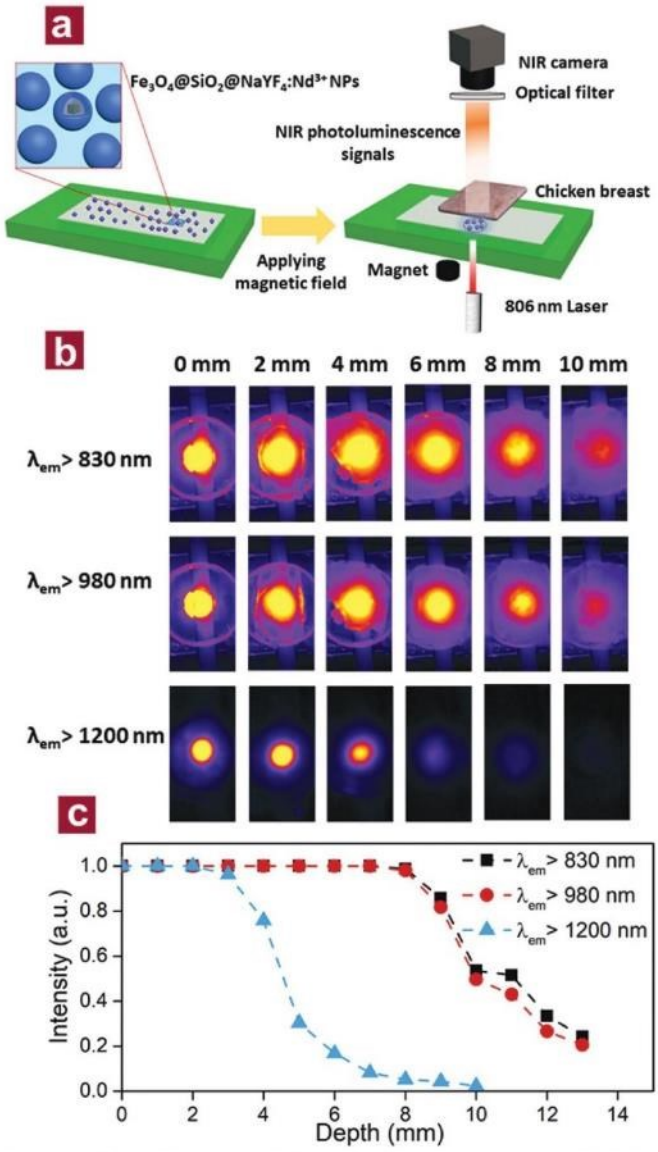

Figure 3. a) Scheme of the experimental setup used to demonstrate ex vivo imaging of a chicken breast sample of varying thickness placed on the top of microchannel containing Fe_3O_4@SiO_2@$NaYF_4$:Nd^{3+} NPs dispersed in aqueous solution, which can be rapidly confined by a magnet. b) Ex vivo imaging of chicken breast samples of different thickness (0, 2, 4, 6, 8, and 10 mm) under excitation of the 806 nm laser with a series of optical long-pass filters (830, 980, and 1200 nm) in the emission path. c) Normalized emitting intensity of Fe_3O_4@SiO_2@$NaYF_4$:Nd^{3+} NPs calculated from (b) as a function of penetration depth of chicken breast sample.

the thickness of the chicken breast sample reaches 4 mm, the signals from the UCNPs almost completely disappear. In this contrast experiment, we kept the same NP concentration as in the experiments with the Fe_3O_4@SiO_2@$NaYF_4$:Nd^{3+} sample in aqueous solution, but of course, used a 980 nm laser as the excitation source, whose power density is more than 27 times that of the 806 nm laser (300 vs 11 W cm^{-2}) used for NIR imaging. However, the penetration depth is only one third of that achieved by the Fe_3O_4@SiO_2@$NaYF_4$:Nd^{3+} NPs. It is clear that the NIR-to-NIR photoluminescent Fe_3O_4@SiO_2@$NaYF_4$:Nd^{3+} NPs are superior to the visible emitting, upconverting Fe_3O_4@SiO_2@$NaYF_4$:Er^{3+}, Yb^{3+} NPs, in terms of deep-tissue penetration capacity. This result strongly suggests that these Fe_3O_4@SiO_2@$NaYF_4$:Nd^{3+} NPs are excellent candidates for in vivo imaging and magnetic-driven applications.

Although these results point to the fact that the Fe_3O_4@SiO_2@$NaYF_4$:Nd^{3+} NPs are promising candidate agents for deep-tissue optical imaging, a thorough assessment of their cytotoxicity needs to be performed before further experiments in vivo. Aliquots of different concentrations of Fe_3O_4@SiO_2@$NaYF_4$:Nd^{3+} NPs cultured with HeLa cancer cells and human embryonic kidney (HEK 293T) cells were used to examine their cytotoxicity by using the 3-(4,5-dimethylthiazol-2-yl)-2,5-diphenyltetrazolium bromide (MTT) assay. As shown in Figure S10 (Supporting Information), the viability of both HeLa cancer cells and HEK 293T cells was higher than 90% in the presence of Fe_3O_4@SiO_2@$NaYF_4$:Nd^{3+} NPs even with their high concentration up to 250 μg mL^{-1}, suggesting that these NPs are biocompatible and do not possess significant toxic effects.

Owing to the superparamagnetic Fe_3O_4 core of this multifunctional nanoplatform, another important biomedical application of Fe_3O_4@SiO_2@$NaYF_4$:Nd^{3+} NPs is their use as a T_2 contrast agent for MR imaging. The T_2-weighted MR images of Fe_3O_4@SiO_2@$NaYF_4$:Nd^{3+} with varying Fe concentrations are shown in **Figure 4**a, which reveals the characteristic concentration-dependent darkening effect of negative T_2 MR contrast agent.[25] The T_2 relaxivity coefficient (r_2) of Fe_3O_4@SiO_2@$NaYF_4$:Nd^{3+}, calculated from the linear fitting of Figure 4b, was ≈61 mM^{-1} S^{-1}, which is close to that of Ferumoxsil (r_2 = 72 $mM^{-1}S^{-1}$, one of the clinically approved Fe-based contrast agents) at 3.0 T.[26] Subsequently, we explored their potential as a negative contrast agent for MR imaging in vivo. The mouse bearing a tumor injected with Fe_3O_4@SiO_2@$NaYF_4$:Nd^{3+} NPs (200 μL, 2 mg mL^{-1}, dose = 1.5 mg kg^{-1}) was imaged by a 3.0 T clinical MR scanner. The tumor shows a hyperintense area in the T_2-weighted MR images before injection while noticeable

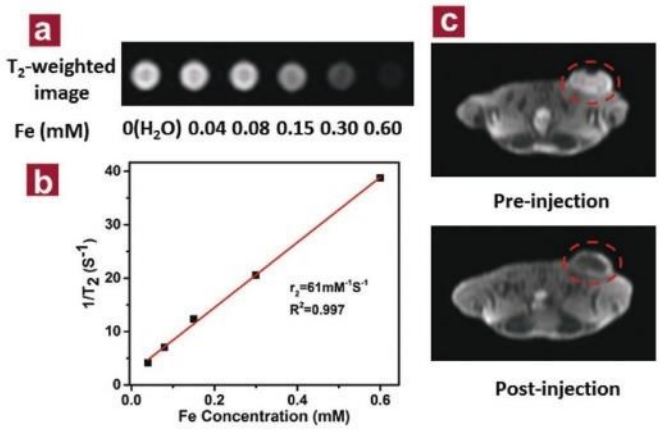

Figure 4. a) T_2-weighted MR images of Fe_3O_4@SiO_2@$NaYF_4$:Nd^{3+} NPs with various iron (Fe) concentrations. b) Plot of relaxation rate ($1/T_2$) versus different Fe concentrations of Fe_3O_4@SiO_2@$NaYF_4$:Nd^{3+} NPs. c) In vivo T_2-weighted transversal cross-section MR images of nude mouse bearing a tumor acquired at preinjection and 30 min intratumoral postinjection of Fe_3O_4@SiO_2@$NaYF_4$:Nd^{3+} NPs at 1.5 mg kg^{-1}. The position of the tumor is marked by red dash circles.

darkening appears in the tumor area at 30 min postinjection (red dash circles in Figure 4c). This remarkable T_2 negative effect makes the Fe_3O_4@SiO_2@$NaYF_4$:Nd^{3+} NPs ideal as the T_2 contrast agents for MR imaging in vivo.

3. Conclusions

In summary, we prepared a nanoplatform based on a Fe_3O_4 core coated by a middle SiO_2 shell and an outer layer of NIR-to-NIR photoluminescent $NaYF_4$:Nd^{3+} by a multistep synthetic procedure for the first time. The uniform Fe_3O_4@SiO_2@$NaYF_4$:Nd^{3+} NPs showed strong emission, excellent photostability, and impressive superparamagnetic properties. Meanwhile, under the excitation of using an 806 nm (NIR-I) laser, these NPs exhibited three emission bands, all lying within the biological windows (NIR-I and NIR-II). The ex vivo imaging testing indicates that the NIR-to-NIR photoluminescence property endows the Fe_3O_4@SiO_2@$NaYF_4$:Nd^{3+} NPs with the capability for the deep-tissue optical imaging and their superparamagnetic property ensures that they can be efficiently confined by a magnetic field, as well as act as ideal T_2 MR imaging contrast agents in vivo. With both suitable excitation and emission in the biological windows, these readily magnetically confinable NPs open up the new possibility of extending the use of multifunctional (superparamagnetic and photoluminescent) NPs from the currently used visible to the more attractive NIR spectral regions.

4. Experimental Section

Chemicals: Iron chloride hexahydrate ($FeCl_3·6H_2O$), sodium oleate, ammonium hydroxide solution ($NH_3·H_2O$, 28.0–30.0% ammonia content), Triton X-100, tetraethyl orthosilicate (TEOS, 99.999%), 1-hexanol (99%), rare earth nitrates [$Y(NO_3)_3·6H_2O$, $Yb(NO_3)_3·5H_2O$, $Er(NO_3)_3·5H_2O$ $Nd(NO_3)_3·6H_2O$, 99.9%], urea (99.0%), oleic acid (OA, technical grade 90%), 1-octadecene (ODE, technical grade 90%), branched PEI (M_w ≈ 25 000), phosphate buffered saline (PBS) were purchased from Sigma-Aldrich Inc. Hexane, cyclohexane, methanol, and ethanol were purchased from Fisher Scientific Company. All chemicals were used as purchased.

Synthesis of Fe_3O_4 Nanoparticles: Fe_3O_4 NPs were prepared by a modified thermal decomposition method.[17] $Fe(oleate)_3$ precursor was synthesized in the first step. Typically, 1.08 g (4 mmol) of $FeCl_3·6H_2O$ and 4.87 g (16 mmol) of sodium oleate were dissolved in a mixed solution of 8 mL of ethanol, 6 mL of distilled water, and 14 mL of hexane. The mixed solution was subsequently heated to 70 °C and refluxed for 6 h. After that, the formed $Fe(oleate)_3$ complex was washed several times with hot distilled water in a separatory funnel. At last, the $Fe(oleate)_3$ complex was kept in a vacuum oven at 70 °C for 8 h in order to remove excess hexane. In the second step of preparing Fe_3O_4 NPs, 0.9 g (1 mmol) of $Fe(oleate)_3$ and 142 mg (0.5 mmol) of OA were dissolved in 10 mL of ODE. The mixture was then transferred to a three-neck round bottom flask and heated to 320 °C under vigorous stirring for 1 h. After cooling to room temperature, the black Fe_3O_4 NPs were collected by centrifugation and washed several times with ethanol and hexane. Finally, the prepared Fe_3O_4 NPs were dispersed in cyclohexane as stock dispersion for the subsequent synthesis of Fe_3O_4@SiO_2 NPs.

Synthesis of Fe_3O_4@SiO_2 Core@Shell NPs: The Fe_3O_4@SiO_2 core@shell NPs were synthesized by a microemulsion method.[5c] Briefly, a 200 µL dispersion of Fe_3O_4 NPs in cyclohexane (5 mg mL^{-1}) was added into a microemulsion solution, which consisted of 5 mL of Triton X-100, 0.5 mL of distilled water, 4 mL of 1-hexanol, 15 mL of cyclohexane, and 125 µL of $NH_3·H_2O$. After the resulting mixture was stirred for 1 h, 40 µL of TEOS was added. The mixture solution was then stirred for 24 h at room temperature. After that, the Fe_3O_4@SiO_2 NPs were precipitated by adding methanol and washed several times with ethanol.

Synthesis of Fe_3O_4@SiO_2@$NaYF_4$:Nd^{3+} and Fe_3O_4@SiO_2@$NaYF_4$:Er^{3+}, Yb^{3+} NPs: Before the synthesis of an outer $NaYF_4$:Nd^{3+} layer, a $Y(OH)CO_3$:Nd^{3+} precursor layer was first synthesized by a urea-assisted homogeneous precipitation method.[20] In a typical synthesis, 0.364 g (0.95 mmol) of $Y(NO_3)_3·6H_2O$, 0.0219 g (0.05 mmol) of $Nd(NO_3)_3·6H_2O$, and 2 g of urea were dissolved in 25 mL of distilled water. Subsequently, 20 mg of Fe_3O_4@SiO_2 NPs were dispersed in the solution under continuous stirring for 1 h. The mixture was then heated to 90 °C and kept at that temperature for 2 h. Finally, Fe_3O_4@SiO_2@$Y(OH)CO_3$:Nd^{3+} NPs were collected by centrifugation and washed with water several times.

Fe_3O_4@SiO_2@$NaYF_4$:Nd^{3+} NPs were synthesized by a hydrothermal method.[20] Briefly, 0.042 g (1 mmol) of NaF, 0.025 g (1 mmol) of PEI, and 0.111 g (3 mmol) of NH_4F were dissolved in 10 mL of distilled water. Following this, the Fe_3O_4@SiO_2@$Y(OH)CO_3$:Nd^{3+} NPs were added into the mixture solution and stirred for 1 h. The mixed solution was then transferred to a 25 mL Teflon lined autoclave and kept at 110 °C for 3.5 h. The Fe_3O_4@SiO_2@$NaYF_4$:Nd^{3+} NPs were separated by centrifugation and washed with distilled water.

Fe_3O_4@SiO_2@$NaYF_4$:Er^{3+}, Yb^{3+} NPs were synthesized following the same procedure as the Fe_3O_4@SiO_2@$NaYF_4$:Nd^{3+} NPs, except for replacing 0.364 g (0.95 mmol) of $Y(NO_3)_3·6H_2O$ and 0.0219 g (0.05 mmol) of $Nd(NO_3)_3·6H_2O$ with 0.298 g (0.78 mmol) of $Y(NO_3)_3·6H_2O$, 0.0088 g (0.02 mmol) of $Er(NO_3)_3·5H_2O$, and 0.0898 g (0.20 mmol) of $Yb(NO_3)_3·5H_2O$.

Structural, Magnetic, and Optical Characterizations: The crystal structure of all the samples was characterized by XRD (Bruker D8 Advance) with Cu Kα (λ = 1.540598 Å) radiation at a 40 kV tube voltage and 40 mA tube current. The morphology of the samples was investigated by TEM (JEOL 2100F) at 200 kV equipped with a charge-coupled device (CCD) camera. EDX and selected area electron diffraction were taken on specific areas during TEM measurements. The chemical state of the elements in the products was studied using XPS (ESCALAB 220I-XL spectrometer) equipped with an Al Kα (1486.6 eV) monochromatic source. The magnetic hysteresis loop was measured by a vibrating sample magnetometer (VSM, Model 4 HF-VSM, ADE USA) at a working temperature of 300 K with magnetic fields up to 3 T. Temperature-dependent zero-field-cooled and field-cooled magnetization curves were taken under an applied field of 100 Oe between 5 and 300 K. FTIR spectrum was recorded by a ThermoFisher Scientific Nicolet 6700 FTIR spectrometer using KBr as a reference. Upconverted emission and NIR photoluminescence spectra were acquired under laser excitation of 980 and 806 nm, respectively. Both laser power densities were fixed at 140 W cm^{-2}. The upconversion emission in the visible range was focused by a lens in a 90° configuration and then detected by an Avaspec-ULS2048L spectrometer (Avantes) through an optical fiber. By keeping the same optical path configuration, the NIR emission was detected by a Shamrock 500i monochromator (Andor) equipped with an iDus InGaAs 1.7 NIR detector (Andor).

Cell Culture and Viability Assay: HeLa cancer cells and HEK 293T cells were cultured in Dulbecco's modified Eagle's medium (DMEM) containing 10% fetal bovine serum, 50 units per mL penicillin, and 50 units per mL streptomycin in 5% CO_2 at 37 °C. HEK 293T and HeLa cells were plated at 5×10^5 cells per well into a 96-well plate and incubated for 24 h in DMEM (100 µL). They were then incubated with various concentrations of Fe_3O_4@SiO_2@$NaYF_4$:Nd^{3+} NPs for 24 h. Blank controls without Fe_3O_4@SiO_2@$NaYF_4$:Nd^{3+} NPs (i.e., cells only) were run simultaneously. Cell viability was measured using CellTiter 96 nonradioactive cell proliferation assay kit (MTT, Promega) according to the manufacturer's protocol. Briefly, MTT solutions (15 µL) were added into each well. After 24 h incubation, the medium containing unreacted MTT was carefully removed. Dimethyl sulfoxide (100 µL) was added into each well in order to dissolve the formed formazan blue crystals, and then the absorbance at λ = 570 nm was recorded using a Powerwave HT Microplate Reader (Bio-Tek). Each concentration was 6-replicated (n = 6). Cell viability was calculated as the percent ratio of absorbance of mixtures containing Fe_3O_4@SiO_2@$NaYF_4$:Nd^{3+} NPs to control samples (i.e., cells only).

NIR and Visible Imaging Ex Vivo: NIR images were taken by an Xeva-1.7 infrared camera (Xenics Corp), in which the InGaAs array is used to detect the emitting signal ranging from 900 to 1700 nm. Three long-pass filters (830, 980, 1200 nm) were used to record images in the specific spectral range and block the scattered excitation light of the 806 nm laser. The visible images of Fe_3O_4@SiO_2@$NaYF_4$:Er^{3+}, Yb^{3+} NPs were taken by a silicon chip camera (Point Grey) equipped with a 980 nm short-pass filter to remove all wavelengths beyond 980 nm. The NIR and visible images were taken under laser diode excitation of 806 nm (power density of 11 W cm^{-2}) and 980 nm (power density of 300 W cm^{-2}), respectively.

Animal Model: 4T1 murine breast cancer cells were cultured in standard cell media recommended by American type culture collection (ATCC). Female Balb/C mice were purchased from Nanjing Peng Sheng Biological Technology Co. Ltd. and used under protocols approved by Soochow University Laboratory Animal Center.

T_2 Relaxivity Study In Vitro and MR Imaging In Vivo: T_2-weighted MR images were acquired by a 3T clinical MRI scanner (Bruker Biospin Corporation, Billerica, MA, USA) at room temperature. Fe_3O_4@SiO_2@$NaYF_4$:Nd^{3+} NPs dispersed in PBS buffer at different concentrations were placed in tubes for T_2-weighted MR imaging. The concentration of iron was determined by inductively coupled plasma-optical emission spectrometry. Relaxivity (r_2) values were calculated by fitting the curve of $1/T_2$ relaxation time (s^{-1}) versus the concentration of Fe ($\times 10^{-3}$ M).

Fe_3O_4@SiO_2@$NaYF_4$:Nd^{3+} NPs dispersed in PBS buffer (200 µL, 2 mg mL^{-1}) were injected into mice bearing 4T1 tumors. The MR imaging of the mouse was conducted on the same scanner equipped with a special coil designed for small animal imaging. The mouse was scanned before and after injection of the contrast agent.

Supporting Information

Supporting Information is available from the Wiley Online Library or from the author.

Acknowledgements

F.Y. and F.R. greatly appreciate the financial support from the Merit Scholarship Program for Foreign Students from the Ministère de l'Éducation, du Loisir et du Sport du Québec. The authors would like to thank J. Xu from Soochow University for the help with MR imaging. The authors acknowledge Z. Yang from Peking University for the magnetic characterization. D.M. and F.V. are grateful to the Natural Sciences and Engineering Research Council of Canada (NSERC) and the Fonds de Recherche du Québec – Nature et technologies (FRQNT) for funding. D.M. also appreciates the financial support of the strategic network "Le Centre québécois sur les matériaux fonctionnels."

Conflict of Interest

The authors declare no conflict of interest.

Keywords

deep-tissue optical imaging, dual-mode imaging, magnetic resonance imaging, multifunctional nanoparticles, near-infrared to near-infrared

Received: October 26, 2017
Revised: December 26, 2017
Published online: January 22, 2018

[1] a) Z. Ali, A. Z. Abbasi, F. Zhang, P. Arosio, A. Lascialfari, M. F. Casula, A. Wenk, W. Kreyling, R. Plapper, M. Seidel, R. Niessner, J. Knöll, A. Seubert, W. J. Parak, *Anal. Chem.* **2011**, *83*, 2877; b) T. Pellegrino, S. Kudera, T. Liedl, A. Muñoz Javier, L. Manna, W. Parak, *Small* **2005**, *1*, 48; c) J. Gao, W. Zhang, P. Huang, B. Zhang, X. Zhang, B. Xu, *J. Am. Chem. Soc.* **2008**, *130*, 3710.
[2] Wahajuddin, Arora, *Int. J. Nanomed.* **2012**, *7*, 3445.
[3] U. Jeong, X. Teng, Y. Wang, H. Yang, Y. Xia, *Adv. Mater.* **2007**, *19*, 33.
[4] K. Licha, C. Olbrich, *Adv. Drug Delivery Rev.* **2005**, *57*, 1087.
[5] a) L. Cheng, C. Wang, X. Ma, Q. Wang, Y. Cheng, H. Wang, Y. Li, Z. Liu, *Adv. Funct. Mater.* **2013**, *23*, 272; b) D. Shi, H. S. Cho, Y. Chen, H. Xu, H. Gu, J. Lian, W. Wang, G. Liu, C. Huth, L. Wang, R. C. Ewing, S. Budko, G. M. Pauletti, Z. Dong, *Adv. Mater.* **2009**, *21*, 2170; c) F. Zhang, G. B. Braun, A. Pallaoro, Y. Zhang, Y. Shi, D. Cui, M. Moskovits, D. Zhao, G. D. Stucky, *Nano Lett.* **2012**, *12*, 61.
[6] C. Liu, Z. Gao, J. Zeng, Y. Hou, F. Fang, Y. Li, R. Qiao, L. Shen, H. Lei, W. Yang, M. Gao, *ACS Nano* **2013**, *7*, 7227.
[7] J.-H. Lee, Y.-W. Jun, S.-I. Yeon, J.-S. Shin, J. Cheon, *Angew. Chem., Int. Ed.* **2006**, *45*, 8160.
[8] O. Chen, L. Riedemann, F. Etoc, H. Herrmann, M. Coppey, M. Barch, C. T. Farrar, J. Zhao, O. T. Bruns, H. Wei, P. Guo, J. Cui, R. Jensen, Y. Chen, D. K. Harris, J. M. Cordero, Z. Wang, A. Jasanoff,

D. Fukumura, R. Reimer, M. Dahan, R. K. Jain, M. G. Bawendi, *Nat. Commun.* **2014**, *5*, 5093.
[9] D. Ma, J. Guan, S. Dénommée, G. Enright, T. Veres, B. Simard, *Chem. Mater.* **2006**, *18*, 1920.
[10] I. Villa, A. Vedda, I. X. Cantarelli, M. Pedroni, F. Piccinelli, M. Bettinelli, A. Speghini, M. Quintanilla, F. Vetrone, U. Rocha, C. Jacinto, E. Carrasco, F. S. Rodríguez, Á. Juarranz, B. del Rosal, D. H. Ortgies, P. H. Gonzalez, J. G. Solé, D. J. García, *Nano Res.* **2015**, *8*, 649.
[11] a) E. Hemmer, A. Benayas, F. Légaré, F. Vetrone, *Nanoscale Horiz.* **2016**, *1*, 168; b) P. Vijayaraghavan, C. H. Liu, R. Vankayala, C. S. Chiang, K. C. Hwang, *Adv. Mater.* **2014**, *26*, 6689.
[12] A. B. Chinen, C. M. Guan, J. R. Ferrer, S. N. Barnaby, T. J. Merkel, C. A. Mirkin, *Chem. Rev.* **2015**, *115*, 10530.
[13] a) A. Benayas, F. Ren, E. Carrasco, V. Marzal, B. del Rosal, B. A. Gonfa, Á. Juarranz, F. Sanz-Rodríguez, D. Jaque, J. García-Solé, D. Ma, F. Vetrone, *Adv. Funct. Mater.* **2015**, *25*, 6650; b) F. Ren, B. del Rosal, S. Y. An, F. Yang, E. Carrasco, A. Benayas, J. K. Oh, D. Jaque, Á. J. de la Fuente, F. Vetrone, D. Ma, *Part. Part. Syst. Charact.* **2017**, *34*, 1600242; c) E. N. Cerón, D. H. Ortgies, B. del Rosal, F. Ren, A. Benayas, F. Vetrone, D. Ma, F. Sanz-Rodríguez, J. G. Solé, D. Jaque, E. M. Rodríguez, *Adv. Mater.* **2015**, *27*, 4781.
[14] a) D. Yang, P. Ma, Z. Hou, Z. Cheng, C. Li, J. Lin, *Chem. Soc. Rev.* **2015**, *44*, 1416; b) X. Xie, N. Gao, R. Deng, Q. Sun, Q. H. Xu, X. Liu, *J. Am. Chem. Soc.* **2013**, *135*, 12608; c) A. Skripka, R. Marin, A. Benayas, P. Canton, E. Hemmer, F. Vetrone, *Phys. Chem. Chem. Phys.* **2017**, *19*, 11825; d) A. Skripka, A. Benayas, R. Marin, P. Canton, E. Hemmer, F. Vetrone, *Nanoscale* **2017**, *9*, 3079.
[15] S. Diao, G. Hong, A. L. Antaris, J. L. Blackburn, K. Cheng, Z. Cheng, H. Dai, *Nano Res.* **2015**, *8*, 3027.
[16] U. Rocha, K. U. Kumar, C. Jacinto, I. Villa, F. Sanz-Rodríguez, M. del Carmen Iglesias de la Cruz, A. Juarranz, E. Carrasco, F. C. J. M. van Veggel, E. Bovero, J. G. Solé, D. Jaque, *Small* **2014**, *10*, 1141.
[17] J. Park, K. An, Y. Hwang, J. G. Park, H. J. Noh, J. Y. Kim, J. H. Park, N. M. Hwang, T. Hyeon, *Nat. Mater.* **2004**, *3*, 891.
[18] F. Erogbogbo, K. T. Yong, R. Hu, W. C. Law, H. Ding, C. W. Chang, P. N. Prasad, M. T. Swihart, *ACS Nano* **2010**, *4*, 5131.
[19] A. E. Nel, L. Mädler, D. Velegol, T. Xia, E. M. V. Hoek, P. Somasundaran, F. Klaessig, V. Castranova, M. Thompson, *Nat. Mater.* **2009**, *8*, 543.
[20] D. Yang, X. Kang, P. Ma, Y. Dai, Z. Hou, Z. Cheng, C. Li, J. Lin, *Biomaterials* **2013**, *34*, 1601.
[21] J. W. Yoo, E. Chambers, S. Mitragotri, *Curr. Pharm. Des.* **2010**, *16*, 2298.
[22] G. Chen, T. Y. Ohulchanskyy, S. Liu, W. C. Law, F. Wu, M. T. Swihart, H. Ågren, P. N. Prasad, *ACS Nano* **2012**, *6*, 2969.
[23] a) M. F. Hansen, S. Mørup, *J. Magn. Magn. Mater.* **1999**, *203*, 214; b) C. Cannas, M. F. Casula, G. Concas, A. Corrias, D. Gatteschi, A. Falqui, A. Musinu, C. Sangregorio, G. Spano, *J. Mater. Chem.* **2001**, *11*, 3180.
[24] J. S. Lee, J. M. Cha, H. Y. Yoon, J. K. Lee, Y. K. Kim, *Sci. Rep.* **2015**, *5*, 12135.
[25] K. Yang, G. Yang, L. Chen, L. Cheng, L. Wang, C. Ge, Z. Liu, *Biomaterials* **2015**, *38*, 1.
[26] H. X. Zhao, Q. Zou, S. K. Sun, C. Yu, X. Zhang, R. J. Li, Y. Y. Fu, *Chem. Sci.* **2016**, *7*, 5294.

ADVANCED FUNCTIONAL MATERIALS

Supporting Information

for *Adv. Funct. Mater.*, DOI: 10.1002/adfm.201706235

An Integrated Multifunctional Nanoplatform for Deep-Tissue Dual-Mode Imaging

Fan Yang, Artiom Skripka, Antonio Benayas, Xianke Dong, Sung Hwa Hong, Fuqiang Ren, Jung Kwon Oh, Xinyu Liu, Fiorenzo Vetrone, and Dongling Ma**

Supporting Information

An Integrated Multifunctional Nanoplatform for Deep-tissue Dual-mode Imaging

Fan Yang, Artiom Skripka, Antonio Benayas, Xianke Dong, Sung Hwa Hong, Fuqiang Ren, Jung Kwon Oh, Xinyu Liu, Fiorenzo Vetrone, Dongling Ma**

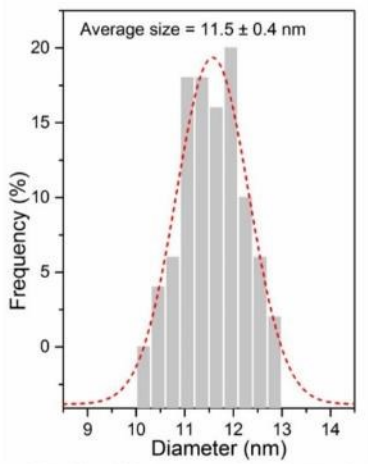

Figure S1. Size histogram of cubic Fe_3O_4 NPs.

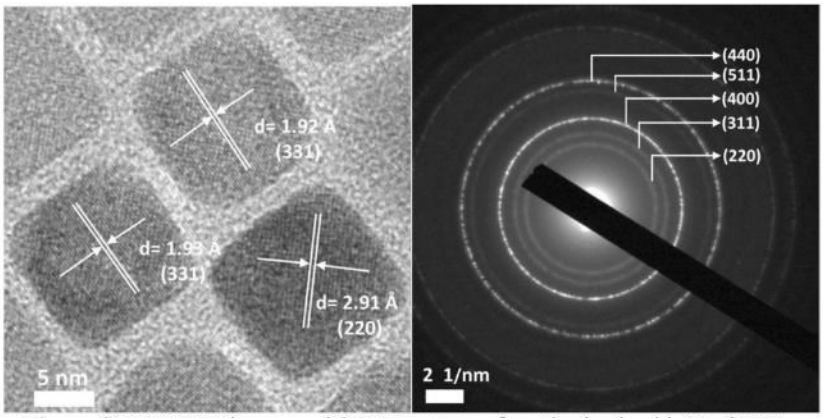

Figure S2. HRTEM image and SAED pattern of synthesized cubic Fe_3O_4 NPs.

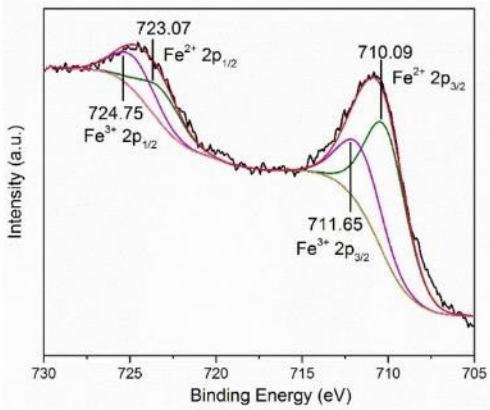

Figure S3. High-resolution XPS spectrum of Fe 2p of synthesized cubic Fe_3O_4 NPs.The binding energy of Fe 2p is about 710.43 eV (Fe $2p_{3/2}$) and 723.33 eV (Fe $2p_{1/2}$). The peak of Fe $2p_{3/2}$ can be deconvoluted into two peaks at 710.09 eV (Fe^{2+} $2p_{3/2}$) and 711.65 eV (Fe^{3+} $2p_{3/2}$) and the peak of Fe $2p_{1/2}$ can be deconvoluted into two peaks 723.07 eV (Fe^{2+} $2p_{1/2}$) and 724.75 eV (Fe^{3+} $2p_{1/2}$), which indicate that both Fe^{2+} and Fe^{3+} exist in the same sample.[1] Besides, the characteristic satellite peak of γ-Fe_2O_3 at around 719 eV is absent, which further confirms the formation of Fe_3O_4.

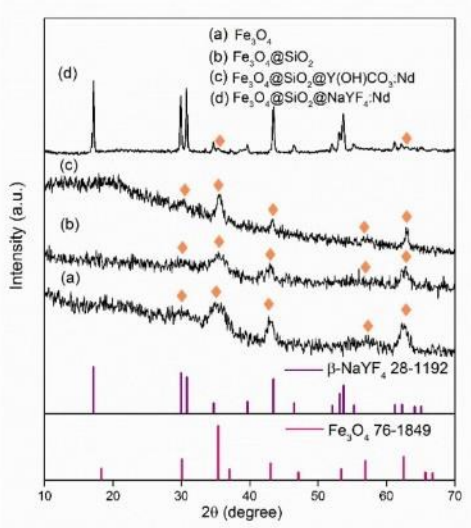

Figure S4. XRD patterns of Fe_3O_4 (a), Fe_3O_4@SiO_2 (b), Fe_3O_4@SiO_2@$Y(OH)CO_3$:Nd^{3+} (c), Fe_3O_4@SiO_2@$NaYF_4$:Nd^{3+} (d) and the standard patterns of Fe_3O_4 (76-1849) and β-$NaYF_4$ (28-1192). The orange diamond labels denote the main diffraction peaks of Fe_3O_4.

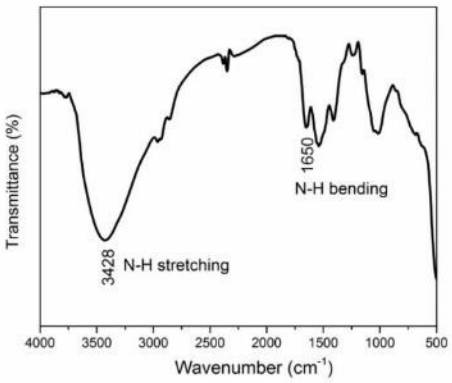

Figure S5. FTIR spectrum of Fe_3O_4@SiO_2@$NaYF_4$:Nd^{3+} NPs. The peaks at 3428 cm^{-1} and 1650 cm^{-1} originate from the stretching and bending vibration of N-H groups of PEI, respectively.[2] This result indicates that PEI was coated on the surface of Fe_3O_4@SiO_2@$NaYF_4$:Nd^{3+} NPs, endowing these NPs water dispersity for potential biomedical application.

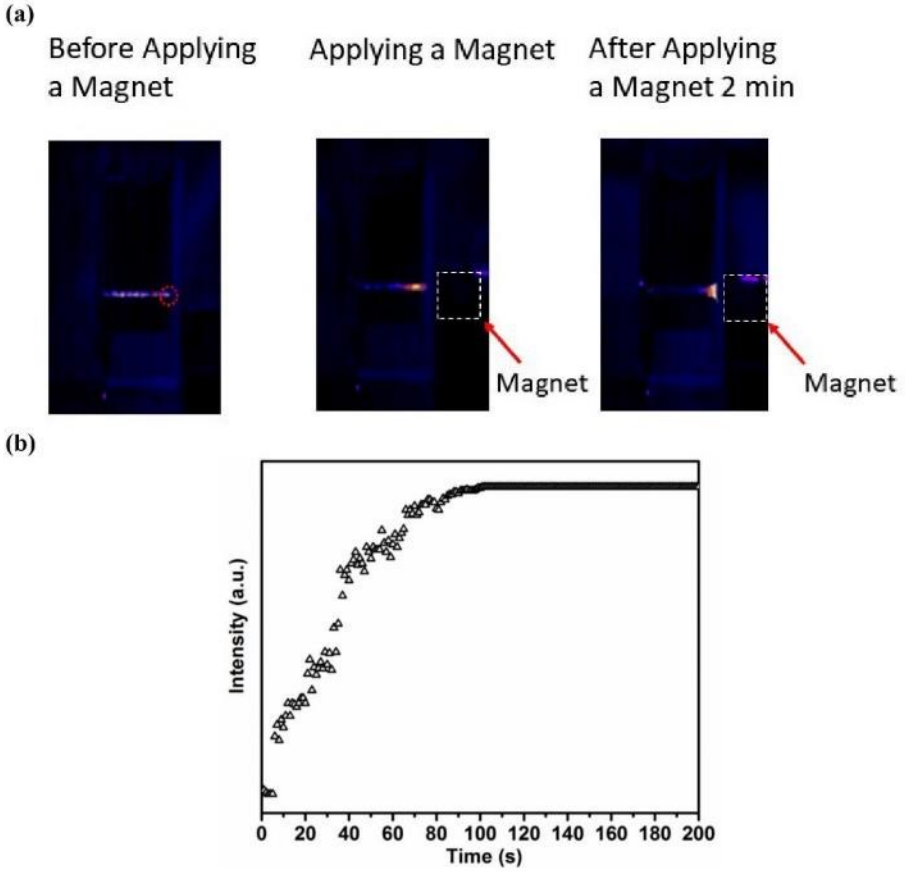

Figure S6 (a) Under excitation of an 806 nm laser, NIR images of Fe_3O_4@SiO_2@$NaYF_4$:Nd^{3+} NPs dispersed in aqueous solution (left), immediately (middle) and 2 min (right) after a magnet was applied. (b) Time evolution of emission intensity of Fe_3O_4@SiO_2@$NaYF_4$:Nd^{3+} NPs confined by the magnet. The emission intensity was obtained from the region of interest (as denoted by a red circle) on the cuvette.

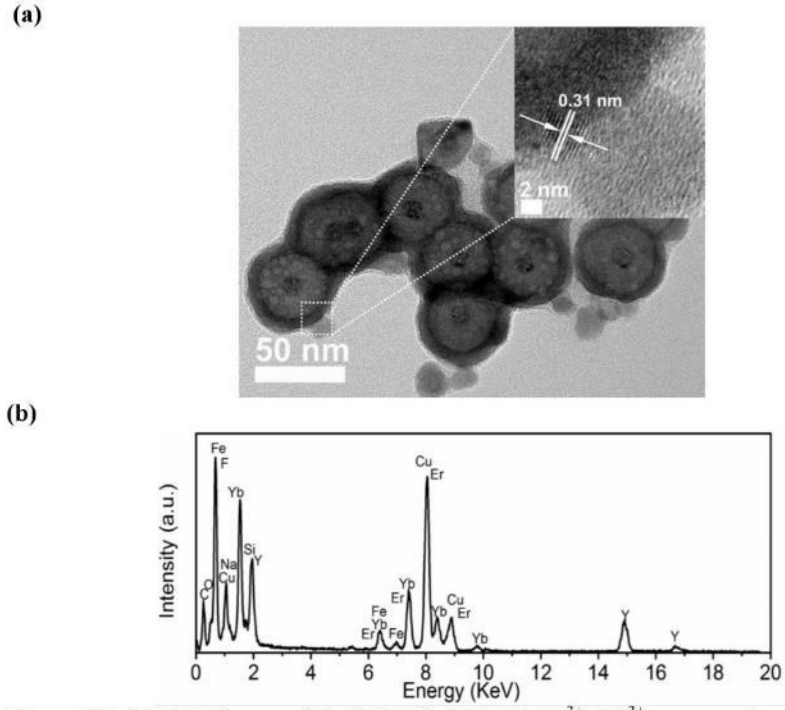

Figure S7. (a) TEM image of Fe_3O_4@SiO_2@$NaYF_4$:Er^{3+}, Yb^{3+} upconverting NPs. The inset is the HRTEM image of $NaYF_4$:Er^{3+}, Yb^{3+} with labelled *d* spacing of 0.31 nm, which corresponds to the (110) plane of hexagonal β-$NaYF_4$:Er^{3-}, Yb^{3-}. (b) EDX pattern of Fe_3O_4@SiO_2@$NaYF_4$:Er^{3+}, Yb^{3+} upconverting NPs. All the elements of Fe_3O_4@SiO_2@ $NaYF_4$:Er^{3+}, Yb^{3+} were detected.

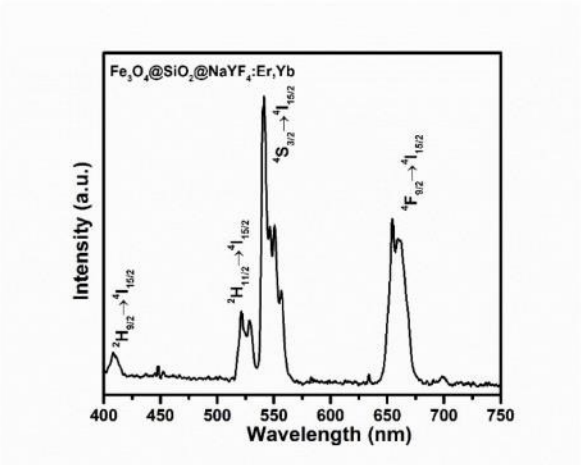

Figure S8. Upconversion spectrum of $Fe_3O_4@SiO_2@NaYF_4:Er^{3+}$, Yb^{3+} NPs. Under excitation of a 980 nm NIR laser, the emission spectrum showed four emission peaks in the visible range centred at 409 nm, 521 nm, 542 nm and 654 nm, which can be attributed to the $^2H_{9/2}\rightarrow{}^4I_{15/2}$, $^2H_{11/2}\rightarrow{}^4I_{15/2}$, $^4S_{3/2}\rightarrow{}^4I_{15/2}$ and $^4F_{9/2}\rightarrow{}^4I_{15/2}$ transitions of Er^{3+}, respectively.

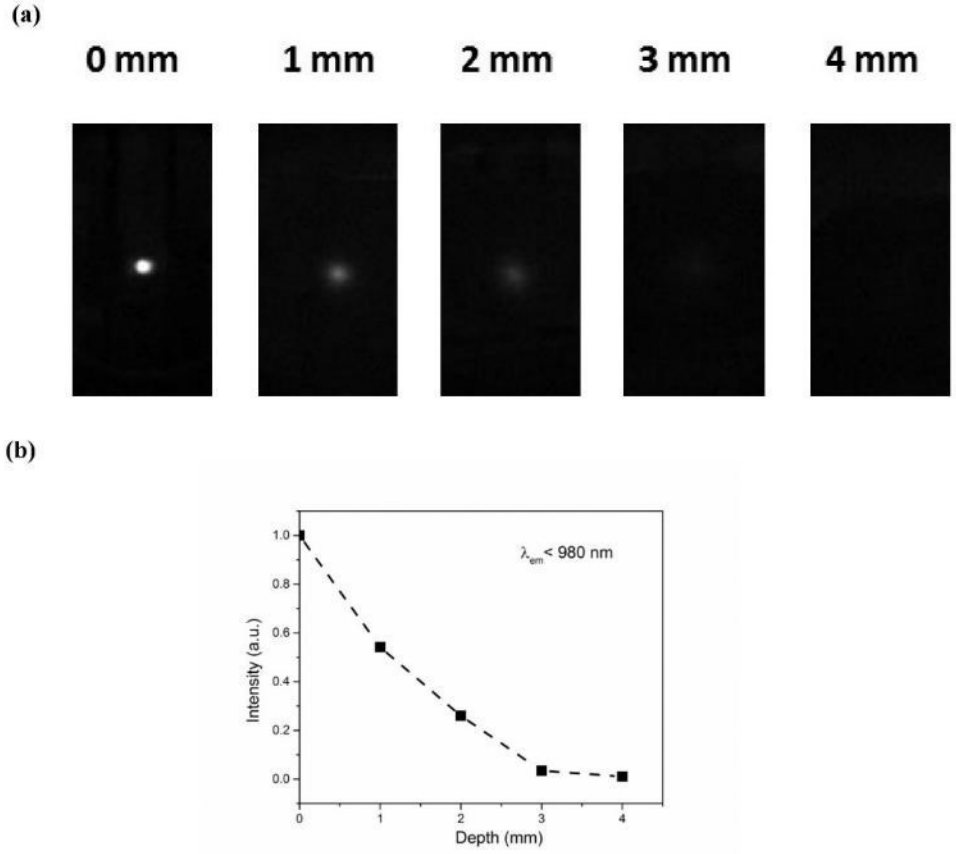

Figure S9. (a) *Ex vivo* imaging of chicken breast samples of different thickness under excitation of a 980 nm laser with an optical 980 nm short-pass filter by using Fe_3O_4@SiO_2@ $NaYF_4$:Er^{3+}, Yb^{3+} upconverting NPs. When the thickness of chicken breast reached 4 mm, the signals from the upconverting NPs almost completely disappeared. (b) Normalized emission intensity of Fe_3O_4@SiO_2@$NaYF_4$:Er^{3+}, Yb^{3+} upconverting NPs as a function of penetration depth of chicken breast.

(a)

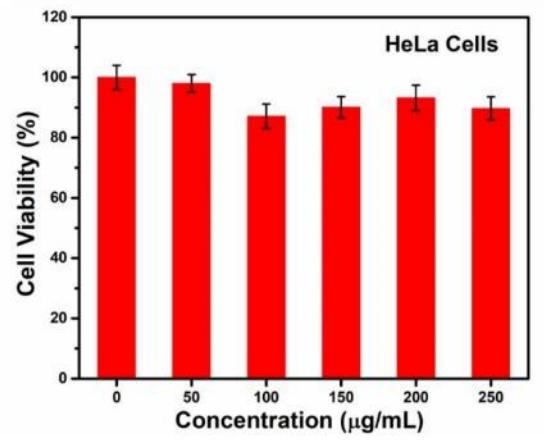

(b)

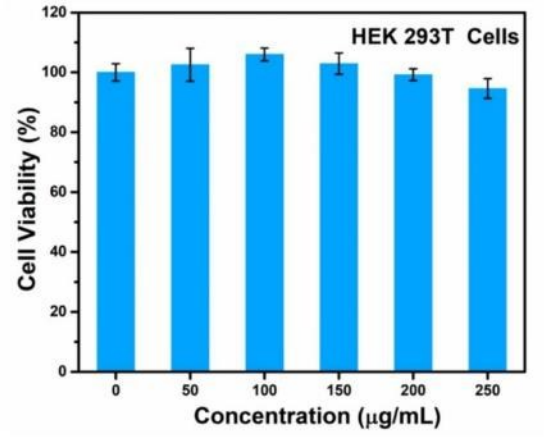

Figure S10. Viability of HeLa (a) and HEK 293T (b) cells cultured with various concentrations of Fe_3O_4@SiO_2@$NaYF_4$:Nd^{3+} NPs.

Reference:

1. Wu, H.; Gao, G.; Zhou, X.; Zhang, Y.; Guo, S. *Crystengcomm* **2012,** 14, (2), 499-504.

2. Fang, X.; Ma, H.; Xiao, S.; Shen, M.; Guo, R.; Cao, X.; Shi, X. *Journal of Materials Chemistry* **2011,** 21, (12), 4493-4501.

4.2 Multifunctional Self-Assembled Supernanoparticles for Deep-Tissue Bimodal Imaging and Amplified Dual-Mode Heating Treatment

Fan Yang, Artiom Skripka, Maryam Sadat Tabatabaei, Sung Hwa Hong, Fuqiang Ren, Antonio Benayas, Jung Kwon Oh, Sylvain Martel, Xinyu Liu, Fiorenzo Vetrone, and Dongling Ma

ACS Nano, 13 (2019) 408-420.

Although above mentioned core/shell/shell Fe_3O_4@SiO_2@$NaYF_4$:Nd^{3+} nanoplatform can be potentially used for high-resolution and deep-tissue bimodal imaging *in vivo*, the single magnetic core feature induced low magnetism restricts its use for magnetic-driven bioapplications and magnetothermal therapy. The development of multifunctional theranostic nanoplatform containing multiple magnetic NPs is highly desirable. On the other hand, despite the great potential for cancer therapy, magnetothermal therapy suffers from relatively poor thermal energy transfer efficiency of currently studied magnetic NPs, while photothermal therapy is not applicable to deep-lying subcutaneous cancer cells due to the limitation of light penetration. The integration of magnetothermal and photothermal therapy into a single nanoplatform can solve therapeutic issue above, providing a dual-mode therapeutic approach to realize high-efficiency and deep-tissue cancer treatment.

In this paper, we developed a multifunctional nanoplatform consisting of multiple superparamagnetic Fe_3O_4 NPs and photoluminescent PbS/CdS QDs with their emission in NIR-II by self-assembly method, aiming at synergistic bimodal imaging and amplified heating treatment. Our *ex vivo* photoluminescence imaging experiments revealed the outstanding deep-tissue penetrating capabilities of self-assembled Fe_3O_4 and PbS/CdS (NIR-II) supernanoparticles [SASNs (NIR-II)], which is beneficial for optical bioimaging. Meanwhile, the self-assembly-induced clustering characteristic of SASNs (NIR-II)] endowed them enhanced T_2 relaxivity property for MR imaging. Subsequently, the prepared SASNs (NIR-II) exhibited the dual capacity to act as both magnetothermal and photothermal agents with extremely efficient heating output at the local site, overcoming the main drawbacks of each type of heating individually. This work represents the first study realizing the highly promising multifunctional theranostic nanoplatforms, *i.e.* NIR-excited deep-tissue bimodal imaging and dual-mode heating agents, by self-assembly of NIR-II PbS/CdS QDs with superparamagnetic Fe_3O_4 NPs.

ACS NANO
Cite This: ACS Nano 2019, 13, 408−420
www.acsnano.org

ARTICLE

Multifunctional Self-Assembled Supernanoparticles for Deep-Tissue Bimodal Imaging and Amplified Dual-Mode Heating Treatment

Fan Yang,[†] Artiom Skripka,[†] Maryam Sadat Tabatabaei,[‡] Sung Hwa Hong,[∥] Fuqiang Ren,[†] Antonio Benayas,[†,§] Jung Kwon Oh,[∥] Sylvain Martel,[‡] Xinyu Liu,[⊥] Fiorenzo Vetrone,*[,†] and Dongling Ma*[,†]

[†]Institut National de la Recherche Scientifique, Centre Énergie, Matériaux et Télécommunications, Université du Québec, 1650 Boulevard Lionel-Boulet, Varennes, Quebec J3X 1S2, Canada

[‡]NanoRobotics Laboratory, Department of Computer and Software Engineering, Institute of Biomedical Engineering, Polytechnique Montréal, Montreal, Quebec H3T 1J4, Canada

[∥]Department of Chemistry and Biochemistry, Concordia University, Montreal, Quebec H4B 1R6, Canada

[§]Department of Physics and CICECO−Aveiro Institute of Materials, University of Aveiro, 3810-193, Aveiro, Portugal

[⊥]Department of Mechanical and Industrial Engineering, University of Toronto, 5 King's College Road, Toronto, Ontario M5S 3G8, Canada

Supporting Information

ABSTRACT: **Developing multifunctional therapeutic and diagnostic (theranostic) nanoplatforms is critical for addressing challenging issues associated with cancers. Here, self-assembled supernanoparticles consisting of superparamagnetic Fe_3O_4 nanoparticles and photoluminescent PbS/CdS quantum dots whose emission lies within the second biological window (II-BW) are developed. The proposed self-assembled Fe_3O_4 and PbS/CdS (II-BW) supernanoparticles [SASNs (II-BW)] exhibit outstanding photoluminescence detectable through a tissue as thick as 14 mm, by overcoming severe light extinction and concomitant autofluorescence in II-BW, and significantly enhanced T_2 relaxivity (282 mM^{-1} s^{-1}, *ca.* 4 times higher than free Fe_3O_4 nanoparticles) due to largely enhanced magnetic field inhomogeneity. On the other hand, SASNs (II-BW) possess the dual capacity to act as both magnetothermal and photothermal agents, overcoming the main drawbacks of each type of heating separately. When SASNs (II-BW) are exposed to the dual-mode (magnetothermal and photothermal) heating, the thermal energy transfer efficiency is amplified 7-fold compared with magnetic heating alone. These results, in hand with the excellent photo- and colloidal stability, and negligible cytotoxicity, demonstrate the potential use of SASNs (II-BW) for deep-tissue bimodal (magnetic resonance and photoluminescence) *in vivo* imaging, while simultaneously providing the possibility of SASNs (II-BW)-mediated amplified dual-mode heating treatment for cancer therapy.**

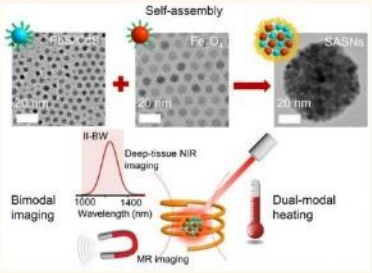

KEYWORDS: *self-assembly, multifunctional supernanoparticles, second biological window, bimodal imaging, dual-modal heating*

Emerging nanotechnologies have driven the development of multifunctional (superparamagnetic and photoluminescent) nanoparticles (NPs) to fulfill the increasing needs of contrast agents suited for a bimodal [magnetic resonance (MR) and photoluminescence] imaging approach.[1−3] Various bimodal contrast agents have been fabricated, including dye-incorporated iron oxide nanocomposites, hybrid nanomaterials composed of magnetic NPs and upconversion nanoparticles, magnetically doped quantum dots (QDs), and clusters of Fe_3O_4 NPs and visible QDs.[2−4] Nevertheless, the photoluminescent component of these NPs in most studies operates within the visible range, which results in shallow penetration depth and ambiguous photolumines-

Received: August 28, 2018
Accepted: December 31, 2018
Published: January 3, 2019

DOI: 10.1021/acsnano.8b06563
ACS Nano 2019, 13, 408−420

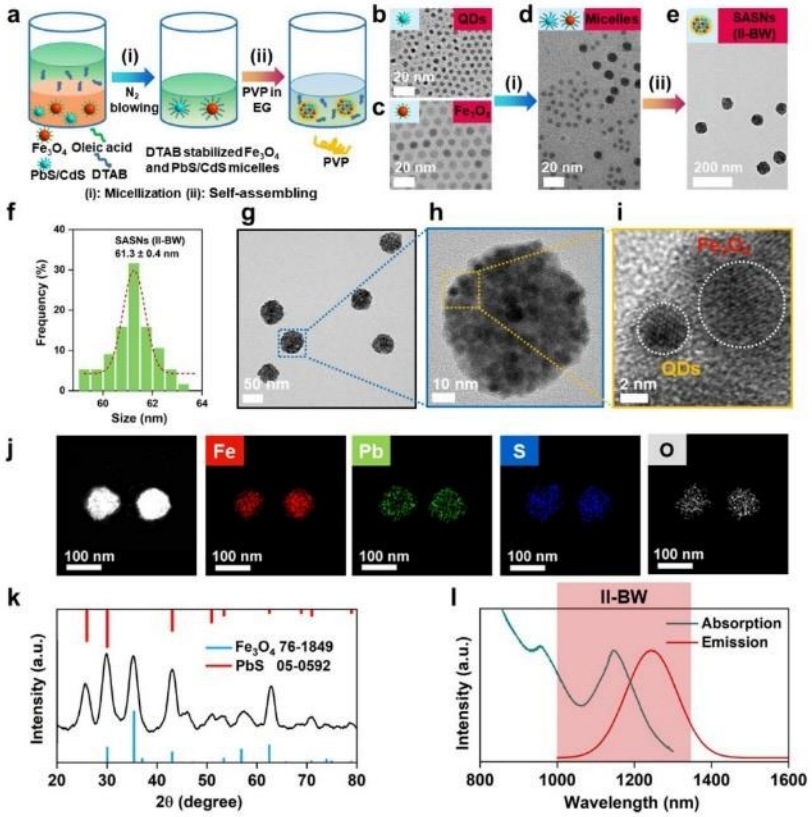

Figure 1. (a) Schematic illustration of the formation process of SASNs (II-BW). (b, c) TEM images of PbS/CdS (II-BW) QDs and Fe_3O_4 dispersed in chloroform. (d) DTAB-stabilized PbS/CdS (II-BW) and Fe_3O_4 micelles. (e) SASNs (II-BW). (f) Size distribution of SASNs (II-BW). (g–i) TEM images of SASNs (II-BW) at different magnifications. (j) HAADF-STEM image and EDX-elemental maps of SASNs (II-BW). (k) XRD pattern of SASNs (II-BW). Standard peaks of Fe_3O_4 (blue, JCPDS 76-1849) and PbS (red, JCPDS 05-0592) are shown. (l) Absorption and photoluminescence emission spectra of SASNs (II-BW).

cence signals due to the tissue-induced light extinction and autofluorescence, thus limiting their use as deep-tissue *in vivo* photoluminescence probes.[5] By introducing NPs with absorption and emission wavelengths in the biological windows (BW) located in the near-infrared (NIR) range (I-BW: 700–950 nm; II-BW: 1000–1350 nm),[6–8] these challenges can be overcome, enabling deep-tissue photoluminescent imaging with high signal-to-noise ratio. Biological tissues in BWs are considered to be optically transparent because the optical extinction (absorption and scattering) of NIR photons can be largely avoided and the autofluorescence background greatly diminished.[5,9–11] Thus, it is substantially beneficial to engineer new multifunctional (superparamagnetic and photoluminescent) NPs, employing NIR-modulated probes for deep-tissue *in vivo* bimodal imaging. Recently Dai *et al.* reported a bright non-toxic photoluminescence probe based on PbS/CdS (II-BW) QDs, which allows for non-invasive deep-tissue photoluminescence imaging with high spatial resolution in 2D/3D confocal modes and real-time photoluminescence imaging of vascular regeneration with dynamic tissue perfusion.[12,13] Also, our group has worked on a series of Pb-based QDs such as PbS, PbS/CdS, and PbS/CdS/ZnS, which exhibit excellent NIR photoluminescence properties.[14–22] However, research regarding hybrid bimodal contrast agents, which combine Fe_3O_4 NPs and promising Pb-based NIR QDs, has not been reported thus far.

Magnetothermal therapy is a well-known thermal cancer treatment technique in which heat is induced by Néel and Brownian relaxation of magnetic NPs when exposed to an alternating magnetic field (AMF).[23] Jordan *et al.* reported the first clinical application of magnetothermal therapy in locally recurrent prostate cancer in 2005.[24] Subsequently, a variety of clinical trials were carried out worldwide,[25,26] paving the way for NanoTherm Therapy (MagForce AG) in commercial clinical settings.[27] Similarly, photothermal therapy employing NIR light absorbing agents to generate heat from NIR laser irradiation to burn cancer cells has received considerable attention because of its advantages including non-invasiveness, high specificity, and precise spatiotemporal selectivity.[28–31] In addition, our previous collaborative work demonstrated Pb-

DOI: 10.1021/acsnano.8b06563
ACS Nano 2019, 13, 408–420

based NIR QDs can act as efficient temperature self-monitored photothermal agents.[32]

There are still drawbacks that must be addressed in both magnetothermal and photothermal therapeutics. For example, magnetothermal therapy agents are used at quite high concentrations ([Fe] = 1−2 M, several orders of magnitude higher than the concentration used for MR imaging), which remains a strong concern in the clinical setting. Because of the relatively poor thermal energy transfer efficiency of magnetic NPs [defined as specific loss power (SLP), the power dissipation per unit of mass of the magnetic material], large amounts are required to efficiently convert magnetic energy into heat.[33] For diagnostic purposes, such high concentration cannot be used for MR imaging because of the signal void in the areas containing high concentrations of magnetic NPs.[34] On the other hand, photothermal therapy is not applicable to malignancies in distant organs due to the limited penetration depth of NIR light into the tissue.[28] In this regard, magnetothermal therapy can ignore problems associated with light tissue penetration as radiofrequency electromagnetic waves are exploited for the magnetic heating.[33] Given these issues, integrating magnetothermal and photothermal therapy into a single nanoplatform may provide a dual-mode therapeutic approach to realize high-efficiency and deep-tissue cancer treatment. Claire *et al.* have demonstrated that the simultaneous stimulation of iron oxide nanocubes under both AMF and NIR laser irradiation offers remarkable heating efficiency, addressing the individual challenges of any monomagnetic and mono-optical heating modality for iron oxide.[35] Although overwhelming heating can be achieved by this nanoplatform, their biomedical applications are restricted due to lack of appropriate diagnostic modality.

Self-assembled supernanoparticles (SASNs) can be regarded as the collections of individual colloidal NPs by self-assembly, which allow for the rational control of the optical, plasmonic, electronic, and/or magnetic phenomena pairing between distinct NPs. In this way, supernanoparticles (SNs) possess not only the intrinsic physical and chemical characteristics of their individual NPs but also the collective properties of these NPs due to coupling effects.[36] For example, self-assembled binary magnetic superlattice membranes exhibit collective interparticle dipolar interactions,[37] and iron oxide clusters cause remarkably enhanced T_2 relaxivity in MR imaging.[38] Notably, the self-assembly approach is a simple, reproducible, and inexpensive way to synthesize multifunctional SNs by combing two or more types of independently tailored NPs. For instance, Bawendi *et al.* demonstrated the preparation of magneto-photoluminescent SNs based on coassembling CdSe/CdS QDs and Fe_3O_4 NPs and their application for *in vivo* bimodal imaging of mice bearing murine mammary carcinoma.[39]

Here, we present multifunctional self-assembled Fe_3O_4 and PbS/CdS (II-BW) supernanoparticles [SASNs (II-BW)] aimed at synergistic bimodal imaging and heating treatment, based on their outstanding superparamagnetic and NIR photoluminescence properties. Our *ex vivo* deep-tissue imaging experiments revealed that the NIR emission, lying within II-BW, endows the SASNs (II-BW) with deep-tissue penetrating capabilities beneficial for optical bioimaging, superior to their counterpart operating within I-BW [SASNs (I-BW)]. Meanwhile, owing to the synergistic effect of their clustering characteristic, SASNs (II-BW) exhibit a significantly enhanced T_2 relaxivity for MR imaging compared with that of free Fe_3O_4 NPs. In addition, the SASNs (II-BW) allow us to perform photoluminescence tracking by magnetic confinement, enabling potential application for high-sensitivity detection of cancer cells. Subsequently, we demonstrate that SASNs (II-BW) can be stimulated by dual-mode heating, which provides an unrivaled SLP, overcoming the main drawbacks of magnetothermal or photothermal therapy individually. The multifunctional SASNs (II-BW) developed here could be suitable not only for deep-tissue bimodal imaging but also for dual-mode heating treatment, rendering them an excellent candidate for realizing future multipronged cancer theranostics.

RESULTS AND DISCUSSION

Schematics of the self-assembling procedures for preparing superparamagnetic and photoluminescent SASNs (II-BW) are shown in Figure 1a. Core/shell PbS/CdS QDs (Figure 1b and Figure S1b) synthesized by microwave-assisted cation exchange of PbS QDs (Figure S1a), with their emission band at *ca.* 1260 nm (II-BW) (Figure S2), were chosen as the photoluminescent component.[40] The average diameter of PbS/CdS QDs was about 4.7 ± 0.3 nm (Figure S3). Meanwhile, high-quality Fe_3O_4 NPs (Figure 1c) with an average size about 8.3 ± 0.7 nm in diameter (Figure S3) were used as the superparamagnetic part. In the first step, by using dodecyltrimethylammonium bromide (DTAB) as a surfactant, oleic acid capped PbS/CdS QDs and Fe_3O_4 NPs dispersed in chloroform were transferred into water by micellar encapsulation, due to hydrophobic van der Waals interactions between the hydrocarbon chains of oleic acid and DTAB. After water transfer, it can be observed that the PbS/CdS and Fe_3O_4 NPs trapped in the micelles retain their monodispersity and size (Figure 1d). In the second step, the aqueous dispersion of PbS/CdS and Fe_3O_4 micelles was quickly injected into the ethylene glycol (EG) solution of polyvinylpyrrolidone (PVP), in which the van der Waals interactions between oleic acid ligands and DTAB surfactants were gradually weakened.[41] This resulted in the loss of DTAB molecules from the PbS/CdS QDs and Fe_3O_4 NPs, engulfing micelles, and eventually led to the decomposition of these micelles. As a consequence, the self-assembling process occurred, aggregating the PbS/CdS QDs and Fe_3O_4 NPs, owing to the introduced solvophobic interaction between the oleic acid ligands on the surface of NPs and the EG solution. Meanwhile, PVP acted as a capping agent, coating the SASNs (II-BW) and stabilizing them against further aggregation of individual SNs through repulsive steric interactions.[42] The principal infrared vibrations of C=O, C−N, and CH_2 functional groups in the Fourier-transform infrared (FTIR) spectrum (Figure S4) confirm the PVP capping on the SASNs (II-BW). The resulting 3D spherical SASNs (II-BW) with an average size of 61.3 ± 0.4 nm in diameter (Figure 1f) are shown in Figure 1e.

In order to verify the morphology and distribution of the Fe_3O_4 NPs and PbS/CdS QDs inside the SASNs (II-BW), transmission electron microscopy (TEM) images at different magnifications, high-angle annular dark-field scanning transmission electron microscopy (HAADF-STEM), and energy dispersive X-ray (EDX)-elemental mapping were acquired (Figure 1g−j). The higher magnification TEM images demonstrate that each SASN (II-BW) is composed of multiple randomly distributed Fe_3O_4 NPs and PbS/CdS QDs. The molar ratio of Fe/Pb was found to be 1:1.2 as measured by inductively coupled plasma-optical emission spectrometry (ICP-OES), which is in agreement with the initially employed

DOI: 10.1021/acsnano.8b06563
ACS Nano 2019, 13, 408−420

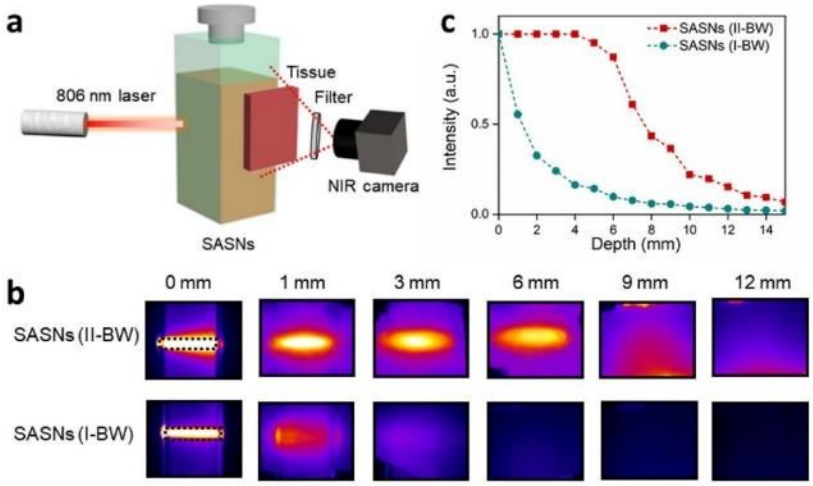

Figure 2. (a) Scheme of the experiment setup for demonstrating *ex vivo* NIR imaging through pork tissue of various thicknesses, placed on one side of the cuvette filled with an aqueous solution containing SASNs. (b) *Ex vivo* NIR images through pork tissue of different thicknesses (0, 1, 3, 6, 9, and 12 mm) for SASNs (I-BW) and SASNs (II-BW) under 806 nm laser excitation. The power density of the 806 nm laser was adjusted to 10 W/cm^2 in both cases. (c) Normalized emission intensity of SASNs (I-BW) and SASNs (II-BW) as a function of penetration depth in pork tissue. Emitted intensity was calculated from the region of interest denoted by a dashed black rectangle.

ratio of Fe_3O_4 NPs and PbS/CdS QDs. Meanwhile, this ratio is anticipated to be an optimal value for photoluminescent imaging (Figure S5). Owing to their different sizes (Figure S2), it is easy to distinguish the Fe_3O_4 NPs and PbS/CdS QDs (Figure 1h,i). Through the corresponding HAADF-STEM and EDX-elemental maps, it can be observed that Fe, Pb, S, and O elements are homogeneously distributed over the entire SASNs' volume. In addition, the X-ray diffraction (XRD) pattern (Figure 1k) verifies the coexistence of Fe_3O_4 NPs and PbS/CdS QDs in the SASNs (II-BW). Figure 1l shows the absorption and emission spectra of SASNs (II-BW). The first-order excitonic absorption and emission bands of SASNs (II-BW) are located at around 1150 and 1240 nm, respectively, covering most of the II-BW's spectral range. Interestingly, compared with the bare PbS/CdS (II-BW) QDs (absorption: 1185 nm, emission: 1260 nm) (Figure S1), the absorption and emission peaks of SASNs (II-BW) show a blue shift, which can be attributed to the change of electronic density in the surface states of immobilized QDs under passivation by the PVP coating.[43,44]

In the meantime, we have adopted the same self-assembling protocol to prepare similar superparamagnetic and photoluminescent SASNs (I-BW) by using smaller PbS/CdS (I-BW) QDs (Figure S6a) with an average size about 2.9 ± 0.3 nm in diameter (Figure S6b) and possessing an emission band centered at *ca.* 915 nm (Figure S6c). The same Fe_3O_4 NPs (Figure 1c) were employed as the superparamagnetic component to prepare SASNs (I-BW). After self-assembling with Fe_3O_4 NPs, the prepared SASNs (I-BW) (Figure S7a) show similar morphology to previously observed SASNs (II-BW) and have an average size about 59.7 ± 0.9 nm (Figure S7b). Due to the larger size difference between the Fe_3O_4 and smaller PbS/CdS (I-BW) QDs with respect to the PbS/CdS (II-BW) QDs, it is easier to identify the Fe_3O_4 and PbS/CdS QDs in the SASNs (I-BW). After self-assembly, the absorption and emission peaks of SASNs (I-BW) show a slight blue shift (Figure S7c), which can be easily understood following the same reasoning as in the case of SASNs (II-BW).

In order to assess and compare the deep-tissue bioimaging capabilities of SASNs (I-BW) and SASNs (II-BW), we have implemented an experimental setup (Figure 2a) in which pork tissue of different thickness was placed on one side of the cuvette filled with an aqueous solution containing the SASNs. Subsequently, NIR images were acquired by an NIR camera placed above the pork tissue. It is worth mentioning that the pork tissue herein was chosen to mimic human soft tissue, since it is photophysically closest to human soft tissue among commonly used animal tissue models.[45] Excitation of the SASNs was achieved by an 806 nm laser diode, which has been shown to be particularly well suited for optical bioimaging.[46,47] Foremost, NIR excitation at wavelengths such as 806 nm is superior to those on the visible spectral side due to the lower photo-induced cytotoxicity.[48] Moreover, the water absorption of 806 nm is significantly reduced compared to that of 980 nm (another commonly used wavelength for exciting NIR optical probes), which helps to reduce the undesired overheating effect of biological tissues. Here, the power density of the 806 nm laser (10 W/cm^2) spot on target and the concentration of both types of SASNs (0.8 mg/mL) were identical in both cases, to fairly compare the penetration depth of the photoluminescence signal from the SASNs (I-BW) and SASNs (II-BW). Figure 2b shows *ex vivo* NIR images through pork tissue with different thickness (0, 1, 3, 6, 9, and 12 mm) for SASNs (I-BW) and SASNs (II-BW). The corresponding collected light intensity, calculated from the region of interest (and normalized to 1.0 at 0 mm), as a function of pork tissue thickness is plotted in Figure 2c. We observed that SASNs (II-BW) showed a strong photoluminescence signal in the NIR

DOI: 10.1021/acsnano.8b06563
ACS Nano 2019, 13, 408−420

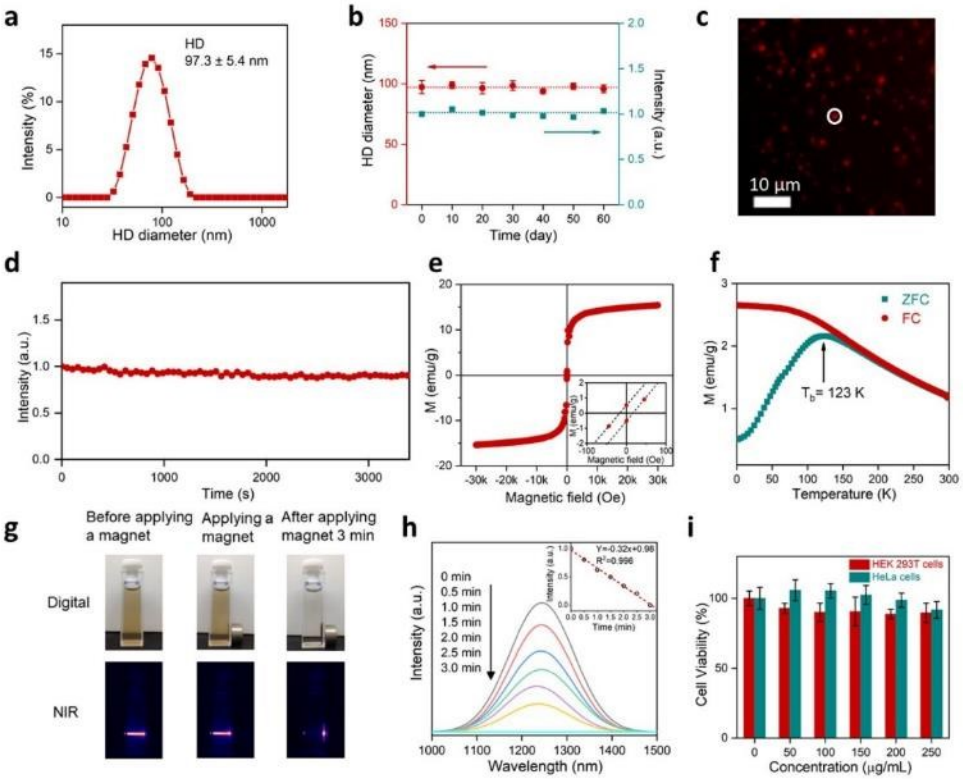

Figure 3. (a) Hydrodynamic diameter, denoted as HD, of the SASNs (II-BW). (b) Hydrodynamic diameter and normalized photoluminescence emission intensity of the SASNs (II-BW) as a function of storage time. (c) Photoluminescence imaging of the SASNs (II-BW) on a coverslip. (d) Photoluminescence intensity change with time for a single aggregate of SASNs (II-BW) denoted in (c). (e) Magnetization of SASNs (II-BW) as a function of magnetic field at 300 K. The inset shows the magnified view of the magnetization curve under low magnetic field. (f) Temperature-dependent ZFC and FC magnetization curves at 100 Oe for SASNs (II-BW). (g) Digital and NIR photographs of SASNs (II-BW) in aqueous solution before applying a magnet (left), applying a magnet (middle) at 0 min, and after applying the magnet for 3 min (right). The NIR images were taken by a NIR camera upon excitation of the SASNs (II-BW) with an 806 nm laser. (h) Photoluminescence emission spectra of the supernatant in SASNs (II-BW) solution measured every 30 s after applying a magnet shown in the middle of (g). The insert in (h) shows corresponding integrated intensity of supernatant (d) as a function of time. (i) Cytotoxicity study of SASNs (II-BW) on HeLa and HEK 293T cells cultured with various concentrations of SASNs (II-BW).

images and their emission intensity saturated the detector of the NIR camera for the ≤4 mm thick pork tissue; most importantly, the NIR signal could still be detected even when the pork tissue thickness reached 14 mm. However, regarding the SASNs (I-BW), the photoluminescence signal rapidly diminished with the increasing thickness of the pork tissue and dropped to ≤20% of the initial intensity by the 4 mm mark. These results indicate that the capability of deep-tissue penetration of SASNs (II-BW) is superior to that of SASNs (I-BW), since the optical extinction of tissue in the II-BW is reduced compared to that in the I-BWs, which is also in a good agreement with our previous report.[17] Therefore, the SASNs (II-BW) are expected to be better imaging probes for deep-tissue imaging, as their NIR emission is guaranteed to penetrate further in biological tissues. In the following text, we focus on studying the greater optical property of SASNs (II-BW) and further exploiting them for MR imaging and magnetothermal and photothermal experiments.

When NPs circulate in biological media such as blood, colloidal stability is a key parameter entangled with their physicochemical properties and strongly influences the NPs' interaction with biological media.[49] In order to better investigate the colloidal stability of SASNs (II-BW), long-term average size distribution as a criterion for evaluating colloidal stability was carried out by dynamic light scattering (DLS) measurements. The hydrodynamic diameter of SASNs (II-BW) was found to be 97.3 ± 5.4 nm (Figure 3a), and, most importantly, it was retained through a 60-day period (Figure 3b), revealing the superior colloidal stability of SASNs (II-BW). Alternatively, we also monitored the colloidal stability of SASNs (II-BW) by tracking their photoluminescence intensity against storage time (Figure 3b). No significant changes were observed throughout the 60-day period, once again confirming

DOI: 10.1021/acsnano.8b06563
ACS Nano 2019, 13, 408−420

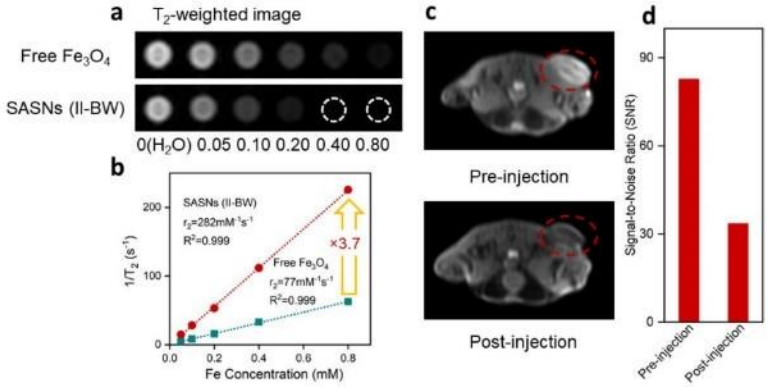

Figure 4. (a) T_2-weighted MR images of various Fe concentrations of SASNs (II-BW) and free Fe_3O_4 NPs, respectively. (b) Relaxation rate r_2 ($1/T_2$) *vs* different Fe concentrations of SASNs (II-BW) and free Fe_3O_4 NPs. (c) *In vivo* T_2-weighted MR images of a nude mouse bearing a tumor with transverse section taken at pre-injection and at 12 h intravenous post-injection of SASNs (II-BW). The position of the tumor is marked by a red dashed circle in (c). (d) Corresponding SNR in the tumor (c) at pre-injection and 12 h post-injection of the SASNs (II-BW).

the excellent colloidal stability of the developed SASNs. We attribute the long-term colloidal stability mainly to the PVP coating, which endows the SASNs (II-BW) with remarkable dispersibility in an aqueous milieu. It also shields the Fe_3O_4 NPs and PbS/CdS QDs from direct contact with water molecules, avoiding the quenching of PbS/CdS QDs with time. To testify whether SASNs (II-BW) show any photoluminescence photobleaching, SASNs (II-BW) were adsorbed and immobilized on a coverslip and imaged by a custom-built multiphoton hyperspectral microscope (Figure 3c). The plot of the photoluminescence intensity against time of a singled-out aggregate of multiple SASNs (II-BW) is shown in Figure 3d. Under illumination by an 808 nm laser for 3600 s, no evidence of photobleaching of the SASNs (II-BW) was observed, suggesting that SASNs (II-BW) possess remarkable photostability for deep-tissue photoluminescence imaging.

The magnetic properties of SASNs (II-BW) were characterized by field-dependent magnetization measurements, as shown in Figure 3e. The magnetization curve of SASNs (II-BW) shows the characteristic superparamagnetic behavior (near-zero coercivity and remanence) with a saturation magnetization of 15.4 emu/g at 300 K. This value is lower than that of free Fe_3O_4 (61.5 emu/g) (Figure S8) since the presence of the non-magnetic component of PbS/CdS (II-BW) QDs inside the SASNs (II-BW) reduces the relative mass ratio of the magnetic component, thus decreasing the value of the saturation magnetization per gram of SASNs (II-BW). The temperature-dependent zero-field-cooled (ZFC) and field-cooled (FC) magnetization measurements were performed under an applied field of 100 Oe between 5 and 300 K (Figure 3f). The ZFC and FC curves coincide at relatively high temperature but separate gradually with decreasing temperature since different sized particles in the same sample progressively block with decreasing temperature, which is a characteristic behavior of superparamagnetism.[50,51] The blocking temperature (T_b) is ~123 K, significantly lower than room temperature, suggesting the superparamagnetic properties of SASNs (II-BW) at room temperature. Furthermore, a relatively small external magnetic field was used to check whether the superparamagnetism of the SASNs (II-BW) can fulfill the requirement of easy and fast manipulation for future biomedical application (Figure 3g). From the digital images, it can be observed that the SASNs (II-BW) are well dispersed in solution prior to complete confinement by an externally placed magnet within about 3 min. Since the movement of the SASNs (II-BW) can be easily tracked by their photoluminescence, the NIR images of SASNs (II-BW) were acquired by a NIR camera under excitation of an 806 nm laser, further confirming the observed superparamagnetism and its effect on the rapid SASNs' confinement to the desired area. NIR images clearly show that the SASNs (II-BW) are sensitive to the magnetic field and can quickly accumulate in the direction of the applied magnetic field. It should be pointed out that the photoluminescence signal was only detected in the confined area under the magnetic field, indicating no free SASNs (II-BW), at a detectable level, were dispersed in the solution. In addition, the photoluminescence spectra of the supernatant in the SASNs (II-BW) solution were measured every 30 s with the applied external magnetic field (Figure 3h). The photoluminescence emission intensity decreased gradually with time, reaching almost zero by 3 min, which can be easily seen from the integrated emission intensity against time (inset of Figure 3h). This trend was consistent with the phenomenon observed in the NIR images, which indicates the rapid response of SASNs (II-BW) to the magnetic field. Interestingly, the integrated photoluminescence emission intensity shows a linear behavior, suggesting the homogeneous confinement of the SASNs (II-BW).

The cytotoxicity of SASNs (II-BW) at different concentrations was evaluated on HeLa cervical cancer cells and human embryonic kidney (HEK 293T) cells by the MTT assay (Figure 3i). Both HeLa cancer cells and HEK 293T cells showed no obvious toxicity (>90% cell viability), even at a significantly high concentration of 250 μg/mL, indicating the non-toxicity and good biocompatibility of SASNs (II-BW). The non-toxicity of SASNs (II-BW) mainly stems from the presence of the PVP coating, which effectively prevents the heavy metals (Pb and Cd) of the QDs from direct exposure to

DOI: 10.1021/acsnano.8b06563
ACS Nano 2019, 13, 408−420

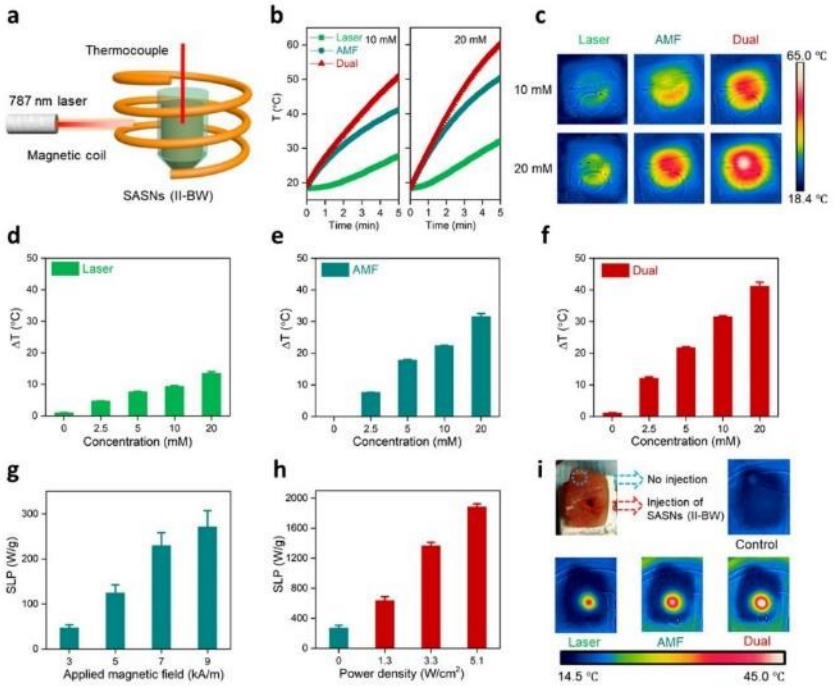

Figure 5. (a) Scheme of the setup for the combined magnetothermal and photothermal experiments. (b) Time-dependent temperature curves of solutions containing SASNs (II-BW) of 10 and 20 mM concentration under three types of modulation (laser at 3.3 W/cm², AMF at 7 kA/m, dual-mode). (c) Corresponding thermal images of SASNs (II-BW) solution after 5 min of each modulation. Thermal images are taken from the top of the tube with a cross-sectional view. Temperature increase of SASNs (II-BW) solutions at different concentrations after 5 min of each modulation: (d) laser at 3.3 W/cm², (e) AMF at 7 kA/m, and (f) dual-mode heating (laser at 3.3 W/cm² and AMF at 7 kA/m). SLP value of SASNs (II-BW) as a function of applied magnetic field (3, 5, 7, and 9 kA/m) (g) with a fixed frequency of 150 kHz and (h) 787 nm laser (1.3, 3.3, and 5.1 W/cm²) in the dual-mode (9 kA/m, 150 kHz). (i) Optical image of pork tissue used for *ex vivo* dual-modal heating and their thermal images at 3 min post-injection of SASNs (II-BW) under three types of modulations (laser at 3.3 W/cm², AMF at 7 kA/m, and dual-mode). The injection point of the SASNs (II-BW) is denoted by a red circle. The blue circle indicates a location free of SASNs (II-BW) (non-injection spot), and the laser was focused on that spot without AMF in the control experiment.

the biological medium, and further, avoids their leakage to the exterior of the SASNs (II-BW). The biocompatibility of PVP has been proven to enhance the application of numerous PVP-capped NPs in the biomedical field.[52−54]

Understanding the biodistribution and clearance of SASNs (II-BW) is directly related to the safety issue and is of great importance for the biomedical application of SASNs *in vivo*. By collecting blood samples at desired time points from 0.5 to 24 h and measuring the Fe concentration in blood (Figure S9a), the blood circulation half-life of the SASNs (II-BW) in a mouse model was calculated to be 1.7 h. The relatively long blood circulation half-life is suitable for the effective accumulation of SASNs (II-BW) in the tumor site by the enhanced permeability and retention (EPR) effect.[55] In the meantime, the biodistribution of the SASNs (II-BW) in different organs of mice shows that the accumulation of SASNs (II-BW) in the liver and spleen becomes dominant at 24 h post-injection, as shown in Figure S9b. This observation of clearance of SASNs (II-BW) is similar to some previously reported studies, suggesting that the SASNs are mainly excreted through the reticuloendothelial system.[56,57]

To pursue high-performance MR imaging contrast agents, *i.e.*, high T_2 contrast relaxivity (r_2), many efforts have been undertaken to rationally engineer magnetic NPs by tuning their composition, size, shape, crystal structure, and surface properties.[58−66] In addition to the above strategies, another intriguing design is to form clusters of magnetic NPs from single magnetic NPs, which can lead to an obvious decrease of the T_2 relaxation time and thus an increase of the r_2 value. The reason for the enhanced relaxivity within NP clusters may be the cluster-induced increase of magnetic field inhomogeneity, which largely enhances the perturbation of proton phase coherence when water molecules diffuse around adjacent magnetic NPs.[38,67] Given a large number of Fe_3O_4 NPs in each SASN (II-BW), combined with their excellent superparamagnetic properties, SASNs (II-BW) were expected to be an ideal T_2 contrast agent with high relaxivity for MR imaging. To evaluate the T_2 MR imaging performance of SASNs (II-BW), the T_2-weighted MR images of various Fe concentrations of SASNs (II-BW) were acquired by a 3T clinical MR scanner, as shown in Figure 4a. At the same time, the free Fe_3O_4 NPs were also examined as a control (Figure 4a). Both SASNs (II-BW)

DOI: 10.1021/acsnano.8b06563
ACS Nano 2019, 13, 408−420

and free Fe_3O_4 NPs exhibit a concentration-dependent darkening effect of the negative T_2 MR contrast agent. However, the darkening effect of SASNs (II-BW) is significantly more pronounced than that of free Fe_3O_4 NPs. The relaxivity (r_2) of the SASNs (II-BW) was calculated to be approximately 282 mM^{-1} s^{-1}, which is more than ~3.7 times that of free Fe_3O_4 NPs (77 mM^{-1} s^{-1}) (Figure 4b), as well as several types of clinically approved Fe-based contrast agents (72 mM^{-1} s^{-1} for Ferumoxsil, 98.3 mM^{-1} s^{-1} for Ferumoxide, and 150 mM^{-1} s^{-1} for Resovist).[68] Such high relaxivity for the SASNs (II-BW) can be attributed to the synergistic MR enhancement effect of multiple Fe_3O_4 NPs aggregated inside the SASNs (II-BW), which is in agreement with previous reports.[38,67] This result strongly suggests the potential of SASNs (II-BW) as T_2 contrast agents for *in vivo* MR imaging, which was further explored. SASNs (II-BW) (200 μL, 2 mg/mL, dose = 10 mg/kg) were administered to a mouse bearing 4T1 tumors intravenously and imaged by a 3T clinical MR scanner. A noticeable darkening effect in the tumor area can be observed 12 h after post-injection (red dashed circles in Figure 4c), and the corresponding signal-to-noise ratio (SNR) value of the tumor region (Figure 4d) decreases significantly, which indicated passive accumulation of the SASNs (II-BW) in the tumors. Therefore, this remarkable T_2 negative effect makes the SASNs (II-BW) ideal as T_2 contrast agents for *in vivo* MR imaging. All together, these results suggest that SASNs (II-BW) possess excellent superparamagnetic properties, which renders them suitable for MR imaging and magnetic-driven applications.

In order to study the combined magnetothermal and photothermal capabilities of the SASNs (II-BW), we designed an experimental setup in which an Eppendorf tube containing a solution of SASNs (II-BW) was placed in the center of a magnetic coil and irradiated by a 787 nm laser (787 nm is an equally convenient excitation wavelength for bioimaging, located within the I-BW), and the temperature increase was recorded by a thermocouple, as shown in Figure 5a. By switching the laser and AMF on and off, we can realize three types of heating: photothermal (only by laser, at power densities of 1.3–5.1 W/cm^2), magnetothermal (only by AMF with a fixed frequency of 150 kHz and magnetic field amplitude from 3 to 9 kA/m), and combined magnetothermal and photothermal (dual-mode, simultaneously with the laser and AMF). Time-dependent temperature curves of SASNs (II-BW) solution at concentrations of 10 and 20 mM under 5 min of each modulation (laser at 3.3 W/cm^2, AMF at 7 kA/m, and dual-mode) were recorded and are presented in Figure 5b. The temperature of the two samples under three heating modalities increases monotonically with time, while the rate of temperature increase varies with different modalities (dual-mode > AMF > laser). We found that the temperature increase after 5 min of dual-mode heating (31 and 43 °C at 10 and 20 mM, respectively) is approximately equal to the sum of magnetothermal heating (22 and 31 °C for 10 and 20 mM samples under AMF, respectively) and photothermal heating (9 and 13 °C for 10 and 20 mM under laser irradiation, respectively). It is worth noting that differences in absolute temperatures and increase rates, when either of the heating modalities is used alone, stem from the fact that during the AMF modulation the SASNs (II-BW) solution is being heated homogeneously throughout the whole volume, whereas heating by laser irradiation is highly localized to the incident beam spot. Figure 5c shows the corresponding thermal images of SASNs (II-BW) solutions of 10 and 20 mM after 5 min of magnetic or optical modulation. It can be seen that dual-mode heating surpasses either photothermal or magnetothermal heating alone, while the magnetothermal heating is dominant in the dual-mode heating at the present experimental conditions. The temperature increase at different concentrations of SASNs (II-BW) after 5 min of each modulation (laser, AMF, and dual-mode) was investigated and is presented in Figure 5d, e, and f, respectively. Remarkably, the temperature increase of all the samples under dual-mode heating matches with the sum of the heating for laser or AMF conditions alone, which confirms the cumulative effect of dual-mode heating. It is important to note that pure water as a control shows only a very low temperature increase under laser irradiation and near zero increase under AMF. Hence, our technique can help to avoid damage to the surrounding biological tissues, which are in the absence of dual-mode thermal agents, during the treatments. We also compared PbS/CdS QDs and Fe_3O_4 NPs alone with the same concentration of SASNs (II-BW) under the three heating modalities (Figure S10). Of all the samples, SASNs (II-BW) exhibit much more promising heating capabilities than PbS/CdS QDs or Fe_3O_4 NPs individually, especially when dual-mode heating is considered.

The heat output of both photothermal and magnetothermal modalities can be tuned by varying the laser power density and the magnetic field (frequency and amplitude), respectively (Figures S11, S12). The efficiency of magnetothermal heating is usually expressed as SLP, and the values under AMF are plotted in Figure 5g. It can be seen that the SLP values increase with the increasing amplitude of the applied magnetic field. Moreover, photothermal heating increases with the laser's power density, expressed in W/cm^2, as shown in Figure S12. After combining laser irradiation with AMF (dual-mode) (Figure 5h), the SLP value surged up to 1883 W/g at a laser power density of 5.1 W/cm^2, which is almost 7 times higher than that of the maximum value under AMF (271 W/g). This result indicated that the SLP value was strongly enhanced by combining the laser irradiation. Although this value seems not very high, it can be easily understood since the magnetic field used in our work is several orders of magnitude lower than for the other reported studies in terms of frequency (150 kHz) and amplitude (from 3 to 9 kA/m) (Table S1). The conclusion was further supported by using a commercial ferrofluid (fluidMAG-PMO) solution as a control sample under dual-mode modulation (Figure S13, Table S1) and by comparing data obtained herein with their previously reported data. Given the SLP value of commercial ferrofluids is only one-third that of SASNs (II-BW), we believe that SASNs (II-BW) possess excellent heating capability with an excellent SLP value if comparable AMF was employed in combination with photothermal heating. Furthermore, we sought to evaluate the potential application of SASNs (II-BW) for dual-mode heating treatments in biological systems by *ex vivo* experiments. Briefly, a pork tissue sample was injected at *ca.* 2 mm in depth with 100 μL of an aqueous solution of SASNs (II-BW) (2 mg/mL). The pork tissue was then subjected to laser irradiation, AMF, and dual-mode, respectively, and the thermal images in each case were collected in order to determine the temperature increase at the surface of the tissue, as shown in Figure 5i. The average temperature at the injection site increased to 27 °C under the laser irradiation, while the temperature also slightly increased to 18 °C at the non-injection laser irradiated site in the control experiment (the initial temperature of pork tissue

DOI: 10.1021/acsnano.8b06563
ACS Nano 2019, 13, 408–420

was 17 °C), which indicates that significant heating occurs only at the injection site. In addition, it should be noted that the laser spot of 3.3 W/cm^2 power density, used in this experiment, did not cause any tissue damage (at the non-injection site) after irradiation for several minutes. The power density is comparable to that used in *in vivo* photothermal therapy based on gold nanorods and carbon nanotubes.[69,70] The temperature under AMF and dual-mode modulation increased to 38 and 45 °C after 3 min, respectively, and the temperature increase in the dual-mode manipulation exhibited the cumulative effect of individual modalities. At this point, we should note that the AMF for magnetothermal therapy *in vivo* is subject to a strict limitation of magnetic field frequency (f) and amplitude (H): $H \times f < 5 \times 10^9$ Am^{-1} s^{-1}, so as to avoid Eddy currents, which have been shown to induce non-selective heating and cardiac stimulation.[71] In our work, the fixed frequency (150 kHz) and magnetic field amplitude from 3 to 9 kA/m were within this safe application range. Therefore, notable *ex vivo* results suggest that SASNs (II-BW) could be potentially used as highly efficient nanoheaters for *in vivo* combined dual-mode thermal treatment.

CONCLUSIONS

In summary, multifunctional (superparamagnetic and NIR photoluminescent) SASNs (II-BW) were prepared by the self-assembly method, and their formation mechanism during the self-assembling process was studied. Under excitation with an 806 nm laser (I-BW), the SASNs (II-BW) allowed us to obtain NIR photoluminescence imaging with enhanced tissue penetration depth compared to that of SASNs (I-BW) due to minimized light extinction in biological tissues. In addition to their excellent NIR photoluminescence, the SASNs (II-BW) exhibit remarkable superparamagnetism, impressive photostability, and colloidal stability. Moreover, the MR imaging results indicate that SASNs (II-BW) can be used as promising T_2 contrast agents for *in vivo* MR imaging due to the significantly enhanced T_2 relaxivity arising from the clustered Fe_3O_4 NPs. The dual-mode heating studies with SASNs (II-BW) as heating agents showed an extremely efficient heating output at the local site. Overall this work opens a new avenue toward the use of SASNs (II-BW) for multifunctional theranostic applications, specifically, as NIR-excited deep-tissue bimodal imaging and dual-mode heating agents.

MATERIALS AND METHODS

Materials. Iron chloride hexahydrate ($FeCl_3 \cdot 6H_2O$), sodium oleate, oleic acid (OA, technical grade 90%), 1-octadecene (ODE, technical grade 90%), lead chloride ($PbCl_2$, 98%), lead acetate trihydrate ($Pb(OAc)_2 \cdot 3H_2O$, 99.9%), sulfur (S, 100%), bis-(trimethylsilyl) sulfide ($(TMS)_2S$, synthesis grade), trioctylphosphine (TOP, 90%), oleylamine (OLA, technical grade, 70%), cadmium oxide (CdO, 99%), dimethyl sulfoxide (DMSO, ≥99.9%), polyvinylpyrrolidone (PVP, MW ~55 000), ethylene glycol (EG, 99.8%), and dodecyltrimethylammonium bromide (DTAB, 99%) were purchased from Sigma-Aldrich Inc. Commercial ferrofluids (fluidMAG-PMO, 25 mg/mL) with a size of 20 nm were purchased from Chemicell GmbH (Berlin, Germany). Hexane, toluene, methanol, and ethanol were purchased from Fisher Scientific Company. All chemicals were used as purchased.

Synthesis of Fe_3O_4 Magnetic Nanoparticles. The Fe_3O_4 NPs were synthesized by thermal decomposition of iron oleate precursor according to a previous report.[72] Typically, the iron oleate complex was prepared by refluxing of $FeCl_3 \cdot 6H_2O$ (1.08 g, 4 mmol) and sodium oleate (4.87 g, 16 mmol) in a mixture solution of ethanol (8 mL), distilled water (6 mL), and hexane (14 mL) at 70 °C for 6 h. After that, the iron oleate precursor was washed several times with hot distilled water in a separation funnel. The iron oleate precursor (0.9 g, 1 mmol) was then dissolved in a mixture of OA (142 mg, 0.5 mmol) and ODE (10 mL) and heated to 320 °C with the protection of N_2 for 1 h. The black Fe_3O_4 NPs were precipitated by centrifugation and washed with ethanol and hexane. The unreacted precursors were completely removed by repeating the centrifugation and washing several times. Finally, the Fe_3O_4 NPs were dispersed in chloroform as stock solution.

Synthesis of Smaller PbS (I-BW) QDs (Size: ~2.9 nm in Diameter). Smaller PbS (I-BW) QDs were synthesized by a hot-injection method.[73,74] Typically, $Pb(OAc)_2 \cdot 3H_2O$ (760 mg), OA (2.4 mL), and ODE (15 mL) were added into a three-neck flask and heated to 150 °C for 1 h with stirring and N_2 flow. Then the mixture was cooled to 130 °C under vacuum for 30 min. Subsequently, a 2 mL mixture of $(TMS)_2S$ and TOP (1:10 ratio by volume) was quickly injected into the flask, and the temperature was kept at 100 °C for 5 min under N_2 flow. Finally, the reaction was quenched by cold water. The PbS (I-BW) QDs dispersed in hexane were stored at 4 °C for 2 days, then centrifuged at 8000 rpm for 30 min to remove the sediment. Following the addition of methanol, the QDs were precipitated and redispersed in toluene. This purification was repeated one more time, and finally the QDs were dispersed in toluene for the growth of the CdS shell.

Synthesis of Larger PbS (II-BW) QDs (Size: ~4.7 nm in Diameter). Larger PbS (II-BW) QDs were synthesized by using OLA as capping ligands instead of OA for smaller PbS (I-BW) QDs.[40] Briefly, $PbCl_2$ (10 g) and OLA (24 mL) in a 50 mL flask were heated to 160 °C and degassed under vacuum for 1 h. The N_2 flow was then opened, and the $PbCl_2$–OLA solution was cooled to 120 °C. After that, sulfur (115 mg) in OLA (4 mL) was quickly injected into the above $PbCl_2$–OLA solution. The growth reaction of PbS QDs was kept at 100 °C for several minutes. When the PbS (II-BW) QDs reached the desired size, the reaction was quenched by cold water. The PbS (II-BW) QDs were purified by adding ethanol and toluene, followed by centrifugation to separate the PbS (II-BW) QDs. Last, the PbS (II-BW) QDs were dispersed in toluene for the further growth of the CdS shell.

Synthesis of Core/Shell PbS/CdS (I-BW and II-BW) QDs. PbS/CdS (I-BW) and PbS/CdS (II-BW) QDs were synthesized by a microwave-assisted cation exchange method.[40] In a typical reaction, CdO (3 g), OA (15 mL), and ODE (20 mL) were heated to 200 °C to form a colorless solution. The Cd oleate solution was then cooled to 100 °C and degassed under vacuum for 30 min. After this step, 8 mL of Cd oleate solution and 12 mL of PbS (I-BW)/PbS (II-BW) QDs in toluene were introduced into a 35 mL microwave reaction tube and heated to 100 °C under microwave radiation for several minutes. Finally, PbS/CdS QDs were purified by ethanol–toluene several times and dispersed in chloroform.

Synthesis of Self-Assembled Fe_3O_4 and PbS/CdS (II-BW) Supernanoparticles [SASNs (II-BW)] and Self-Assembled Fe_3O_4 and PbS/CdS (I-BW) Supernanoparticles [SASNs (I-BW)]. For a typical synthesis of SASNs (II-BW), 1 mL of Fe_3O_4 (4 mg) NPs and 1 mL of PbS/CdS (II-BW) QDs (6 mg) chloroform solution (molar ratio of Fe/Pb = 1:1.2) were injected into 1 mL of DTAB (20 mg/mL) aqueous solution. The solution was thoroughly mixed by vortex, following chloroform evaporation under N_2 flow. After that, the aqueous mixture of PbS/CdS (II-BW) QDs and Fe_3O_4 NPs was swiftly injected into a PVP-in-EG solution (20 mg/mL) and left under vigorous stirring for 4 h. The resulting SASNs (II-BW) were isolated by centrifugation, washed with ethanol, and finally dispersed in water.

SASNs (I-BW) were synthesized following the same procedure as the SASNs (II-BW), except for replacing PbS/CdS (II-BW) QDs (6 mg) with PbS/CdS (I-BW) QDs (6 mg).

Characterization. The crystal structure of all the samples was characterized by using a Bruker D8 ADVANCE X-ray diffractometer, equipped with a Cu anode X-ray source (Cu Kα, λ = 1.540 598 Å). The TEM images, HAADF-STEM images, and EDX-elemental

DOI: 10.1021/acsnano.8b06563
ACS Nano 2019, 13, 408–420

mapping were obtained using a JEOL 2100F microscope at 200 kV equipped with a charge-coupled device camera. The hydrodynamic size of the SASNs (II-BW) was characterized by a Malvern Zetasizer Nano-S90 DLS instrument. Content of Pb and Fe elements in the SASNs (II-BW) was assessed by ICP-OES (Agilent Technologies, 5100). FTIR spectra were collected in the range of 4000−500 cm^{-1} by using a ThermoFisher Scientific Nicolet 6700 FTIR spectrometer. The magnetic hysteresis loop was measured by a vibrating sample magnetometer (VSM, model 4 HF-VSM, ADE USA) at 300 K with a magnetic field up to 3 T. Temperature-dependent ZFC and FC magnetization curves were taken under an applied field of 100 Oe between 5 and 300 K. Absorption spectra of all the samples were measured by a UV−visible−NIR spectrophotometer (Cary 5000) with a scan speed of 600 nm/min. NIR photoluminescence spectra were acquired on a Fluorolog-3 system (Horiba Jobin Yvon) using an excitation wavelength of 600 nm.

Photoluminescence Time Trace Measurements for a Singled-out Aggregate of SASNs (II-BW). The NIR photoluminescence image of SASNs (II-BW) on a glass coverslip was taken using a multiphoton/NIR hyperspectral microscope (Photon Etc., Canada) with detection limits from 400 to 1750 nm, equipped with a pulsed femtosecond Ti:Sapphire Mai Tai laser as excitation source (Spectra Physics, USA) and an excitation wavelength fixed at 808 nm. The platform is based on the inverted epifluorescent microscope body (Nikon Eclipse Ti-S, Japan), equipped with a 20× 0.40 NA objective (Nikon, Japan). The collected photoluminescence signal is spectrally separated from the excitation beam by utilizing an appropriate NIR filter cube and passed onto the dispersive element from which the spectral information at a single excitation spot is registered with an InGaAs camera (Nunavut, BaySpec, USA). The fluorescence intensity trace was obtained from the NIR spectra of SASNs (II-BW) measurement every 52 s.

Cell Culture and Viability Assay. HeLa cervical cancer cells and human embryonic kidney (HEK 293T) cells were cultured in Dulbecco's modified Eagle's medium (DMEM), 10% fetal bovine serum (FBS), 50 units/mL penicillin, and 50 units/mL streptomycin in 5% CO_2 at 37 °C. HEK 293T and HeLa cells were plated at 5 × 10^5 cells/well into a 96-well plate and incubated for 24 h in DMEM (100 μL). Cells were then treated with SASNs (II-BW) at various concentration. Blank controls without SASNs (II-BW) (cells only) were run simultaneously. Cell viability was measured by using a CellTiter 96 Non-Radioactive cell proliferation assay kit (MTT, Promega) according to the manufacturer's protocol. Briefly, 3-(4,5-dimethylthiazol-2-yl)-2,5-diphenyltetrazolium bromide (MTT) solutions (15 μL) were added into each well. The medium containing unreacted MTT was carefully removed after 24 h of incubation. Then DMSO (100 μL) was added into each well in order to dissolve the formed formazan blue crystals, and the absorbance at λ = 570 nm was recorded using a Powerwave HT microplate reader (Bio-Tek). Each concentration was 6-replicated (n = 6). Cell viability was calculated as the percent ratio of mixtures with SASNs (II-BW) to control (cells only).

NIR Imaging *ex Vivo*. NIR images were taken by an Xeva-1.7 infrared camera (Xenics Corp) equipped with a 830 nm filter to record images in the specific spectral range and to block the scattered excitation light. The 806 nm laser diode was used as a fixed excitation source ((Lumics, power density of 10 W/cm^2).

Animal Model. 4T1 murine breast cancer cells were cultured in standard cell media recommended by American Type Culture Collection (ATCC). Female Balb/c mice were purchased from Nanjing Peng Sheng Biological Technology Co. Ltd. and used under protocols approved by Soochow University Laboratory Animal Center.

T_2 Relaxivity Measurements *in Vitro* and MR Imaging *in Vivo*. T_2-weighted MR images were acquired by a 3T clinic MRI scanner (Bruker Biospin Corporation, Billerica, MA, USA) at room temperature. SASNs (II-BW) in PBS buffer with different concentrations were placed in a series of tubes for T_2-weighted MR imaging. The concentration of Fe was determined by ICP-OES (Agilent Technologies, 5100). The relaxivity value (r_2) was calculated based on the fitting curve of $1/T_2$ relaxation time (s^{-1}) *vs* the concentration of Fe (mM).

A mouse bearing one 4T1 tumor was administered with SASNs (II-BW) in PBS buffer (200 μL, 2 mg/mL, dose = 10 mg/kg) by an intravenous injection *via* its tail vein. The MR imaging of the mouse was conducted on the same scanner equipped with a special coil designed for small animal imaging. The mouse was scanned before and after injection of the contrast agent.

Biodistribution Study. SASNs (II-BW) in PBS buffer (200 μL, 2 mg/mL, dose = 10 mg/kg) were injected into the mice intravenously. Blood samples were collected from the facial vein at the desired time points (30 min and 1, 2, 4, 6, 12, and 24 h). The Fe content in blood was determined by ICP-OES after the red blood cells were removed by centrifugation. The following organs including liver, heart, spleen, kidneys, and lungs were collected, weighed, completely lysed in aqua regia, and examined by ICP-OES at 24 h post-injection. The biodistribution results were expressed as the percentage of injected dose per gram of organ (% ID/g)

Photothermal, Magnetic Hyperthermia and Dual-Mode Measurements *in Vitro*. For magnetic hyperthermia experiment, the alternating magnetic field was generated by a magnetothermal equipment (Ameritherm Inc., New York), consisting of a coil (3 turns of loops of Cu pipe, 6 cm in diameter), which was cooled by a water circulation system. The magnetic field frequency was fixed at 150 kHz, and the magnetic field amplitude could be tuned by the current from 0 to 180 A. Magnetic field amplitude (H) was calculated by the equation

$$H = n\frac{\mu_0 I}{2R}$$

where $\mu_0 = 4\pi \times 10^{-7}$ T·m/A, n is the number of turns, R is the loop radius, and I is the applied current.

Typically, a solution (0.6 mL) of SASNs (II-BW) in an Eppendorf tube, surrounded by Styrofoam to minimize possible external temperature fluctuations, was placed at the center of the coil, and the temperature increase was recorded by a computer-attached optical fiber based thermocouple (Reflex, SN:T18 217A, Neoptix Inc., Canada).

For laser photothermal experiments, a continuous wave portable 787 nm NIR laser (Ningbo Lasever Inc., China) was used as an irradiation source. An Eppendorf tube containing the SASNs (II-BW) solution was irradiated by the laser placed on the same holder at the center of coil as for the magnetic hyperthermia experiment (the magnetic field was switched off). The distance between laser and sample was fixed at 13 cm. The temperature increase was recorded by the same sensor above.

For the dual-mode heating experiment, the same configuration for laser photothermal experiment was adopted while keeping the magnetic field on.

Thermal images were recorded by an infrared thermal imaging camera (FLIR E4, FLIR Systems AB, Sweden) from the top of the sample.

Specific loss power is defined as the power dissipation per unit mass of magnetic material (W/g) in order to evaluate the heating effect. The SLP values of different samples were calculated based on the following equation:

$$\mathrm{SLP} = C\frac{\Delta T V}{\Delta t m}$$

where C is the specific heat capacity of the medium (C_{water} = 4185 J/L/K), $\Delta T/\Delta t$ is the initial slope of the time-dependent temperature curve ($t \approx 30$ s), V is the volume of the sample, and m is the total mass of magnetic material in the sample.[75]

A discussion regarding the use of three different wavelength NIR lasers (787, 806, 808 nm) and the excitation spectrum of SASNs (II-BW) are provided in Figure S14 to avoid confusion and to clarify that the difference in these wavelengths does not have any significant effect on relevant experiments.

DOI: 10.1021/acsnano.8b06563
ACS Nano 2019, 13, 408−420

ASSOCIATED CONTENT

Supporting Information

The Supporting Information is available free of charge on the ACS Publications website at DOI: 10.1021/acsnano.8b06563.

Additional explanations about data and Figures S1−S14 (PDF)

AUTHOR INFORMATION

Corresponding Authors

*E-mail: vetrone@emt.inrs.ca.

*E-mail: ma@emt.inrs.ca.

ORCID

Fan Yang: 0000-0001-6306-4501

Artiom Skripka: 0000-0003-4060-4290

Jung Kwon Oh: 0000-0002-4220-308X

Fiorenzo Vetrone: 0000-0002-3222-3052

Dongling Ma: 0000-0001-8558-3150

Notes

The authors declare no competing financial interest.

ACKNOWLEDGMENTS

D.M. and F.V. are grateful to the Natural Sciences and Engineering Research Council of Canada (NSERC: RGPIN-2015-06756) and the Fonds de Recherche du Québec−Nature et Technologies (FRQNT: 2014-PR-174462) for funding. F.Y., F.R., and A.S. greatly appreciate the financial support from the Merit Scholarship Program for Foreign Students from the Ministère de l'Éducation, du Loisir et du Sport du Québec (No. 193353, No. 255072, and No. 257149). We would like to thank J.X. from Soochow University for the help with *in vivo* experiments. We acknowledge Z.Y. from Peking University for the magnetic characterization.

REFERENCES

(1) Yang, F.; Skripka, A.; Benayas, A.; Dong, X.; Hong, S. H.; Ren, F.; Oh, J. K.; Liu, X.; Vetrone, F.; Ma, D. An Integrated Multifunctional Nanoplatform for Deep-Tissue Dual-Mode Imaging. *Adv. Funct. Mater.* **2018**, *28*, 1706235.

(2) Kim, J.; Lee, J. E.; Lee, S. H.; Yu, J. H.; Lee, J. H.; Park, T. G.; Hyeon, T. Designed Fabrication of a Multifunctional Polymer Nanomedical Platform for Simultaneous Cancer- Targeted Imaging and Magnetically Guided Drug Delivery. *Adv. Mater.* **2008**, *20*, 478−483.

(3) Corr, S. A.; Rakovich, Y. P.; Gun'ko, Y. K. Multifunctional Magnetic-Fluorescent Nanocomposites for Biomedical Applications. *Nanoscale Res. Lett.* **2008**, *3*, 87.

(4) Xia, A.; Gao, Y.; Zhou, J.; Li, C.; Yang, T.; Wu, D.; Wu, L.; Li, F. Core-Shell $NaYF_4$:Yb^{3+},Tm^{3+}@Fe_xO_y Nanocrystals for Dual-Modality T_2-Enhanced Magnetic Resonance and NIR-to-NIR Upconversion Luminescent Imaging of Small-Animal Lymphatic Node. *Biomaterials* **2011**, *32*, 7200−7208.

(5) Villa, I.; Vedda, A.; Cantarelli, I. X.; Pedroni, M.; Piccinelli, F.; Bettinelli, M.; Speghini, A.; Quintanilla, M.; Vetrone, F.; Rocha, U.; Jacinto, C.; Carrasco, E.; Rodríguez, F. S.; Juarranz, Á.; Rosal, B.; Ortgies, D. H.; Gonzalez, P. H.; Solé, J. G.; García, D. J. 1.3 μm Emitting SrF_2:Nd^{3+} Nanoparticles for High Contrast *In Vivo* Imaging in the Second Biological Window. *Nano Res.* **2015**, *8*, 649−665.

(6) Hemmer, E.; Benayas, A.; Legare, F.; Vetrone, F. Exploiting the Biological Windows: Current Perspectives on Fluorescent Bioprobes Emitting above 1000 nm. *Nanoscale Horiz.* **2016**, *1*, 168−184.

(7) Vijayaraghavan, P.; Liu, C. H.; Vankayala, R.; Chiang, C. S.; Hwang, K. C. Designing Multi-Branched Gold Nanoechinus for NIR Light Activated Dual Modal Photodynamic and Photothermal Therapy in the Second Biological Window. *Adv. Mater.* **2014**, *26*, 6689−6695.

(8) Jiang, Y.; Pu, K. Multimodal Biophotonics of Semiconducting Polymer Nanoparticles. *Acc. Chem. Res.* **2018**, *51*, 1840−1849.

(9) Chinen, A. B.; Guan, C. M.; Ferrer, J. R.; Barnaby, S. N.; Merkel, T. J.; Mirkin, C. A. Nanoparticle Probes for the Detection of Cancer Biomarkers, Cells, and Tissues by Fluorescence. *Chem. Rev.* **2015**, *115*, 10530−10574.

(10) Miao, Q.; Pu, K. Organic Semiconducting Agents for Deep-Tissue Molecular Imaging: Second Near-Infrared Fluorescence, Self-Luminescence, and Photoacoustics. *Adv. Mater.* **2018**, *30*, 1801778.

(11) Jiang, Y.; Li, J.; Zhen, X.; Xie, C.; Pu, K. Dual-Peak Absorbing Semiconducting Copolymer Nanoparticles for First and Second Near-Infrared Window Photothermal Therapy: A Comparative Study. *Adv. Mater.* **2018**, *30*, 1705980.

(12) Zhang, M.; Yue, J.; Cui, R.; Ma, Z.; Wan, H.; Wang, F.; Zhu, S.; Zhou, Y.; Kuang, Y.; Zhong, Y.; Pang, D.; Dai, H. Bright Quantum Dots Emitting at ~ 1,600 nm in the NIR-IIb Window for Deep Tissue Fluorescence Imaging. *Proc. Natl. Acad. Sci. U. S. A.* **2018**, *115*, 6590.

(13) Ma, Z.; Zhang, M.; Yue, J.; Alcazar, C.; Zhong, Y.; Doyle, T. C.; Dai, H.; Huang, N. F. Near-Infrared IIb Fluorescence Imaging of Vascular Regeneration with Dynamic Tissue Perfusion Measurement and High Spatial Resolution. *Adv. Funct. Mater.* **2018**, *28*, 1803417.

(14) Zhao, H.; Chaker, M.; Ma, D. Bimodal Photoluminescence During the Growth of PbS Quantum Dots. *J. Phys. Chem. C* **2009**, *113*, 6497−6504.

(15) Zhao, H.; Wang, D.; Zhang, T.; Chaker, M.; Ma, D. Two-Step Synthesis of High-Quality Water-Soluble Near-Infrared Emitting Quantum Dots *via* Amphiphilic Polymers. *Chem. Commun.* **2010**, *46*, 5301−3.

(16) Zhao, H.; Chaker, M.; Wu, N.; Ma, D. Towards Controlled Synthesis and Better Understanding of Highly Luminescent PbS/CdS Core/Shell Quantum Dots. *J. Mater. Chem.* **2011**, *21*, 8898−8904.

(17) Benayas, A.; Ren, F.; Carrasco, E.; Marzal, V.; Rosal, B.; Gonfa, B. A.; Juarranz, Á.; Sanz-Rodríguez, F.; Jaque, D.; García-Solé, J.; Ma, D.; Vetrone, F. PbS/CdS/ZnS Quantum Dots: A Multifunctional Platform for *In Vivo* Near-Infrared Low-Dose Fluorescence Imaging. *Adv. Funct. Mater.* **2015**, *25*, 6650−6659.

(18) Ren, F.; Rosal, B.; An, S. Y.; Yang, F.; Carrasco, E.; Benayas, A.; Oh, J. K.; Jaque, D.; de la Fuente, Á. J.; Vetrone, F. Development and Investigation of Ultrastable PbS/CdS/ZnS Quantum Dots for Near-Infrared Tumor Imaging. *Part. Part. Syst. Charact.* **2017**, *34*, 1600242.

(19) Tan, L.; Zhou, Y.; Ren, F.; Benetti, D.; Yang, F.; Zhao, H.; Rosei, F.; Chaker, M.; Ma, D. Ultrasmall PbS Quantum Dots: A Facile and Greener Synthetic Route and Their High Performance in Luminescent Solar Concentrators. *J. Mater. Chem. A* **2017**, *5*, 10250−10260.

(20) Ren, F.; Lindley, S. A.; Zhao, H.; Tan, L.; Gonfa, B. A.; Pu, Y. C.; Yang, F.; Liu, X.; Vidal, F.; Zhang, J. Z.; Vetrone, F.; Ma, D. Towards Understanding the Unusual Photoluminescence Intensity Variation of Ultrasmall Colloidal PbS Quantum Dots with the Formation of a Thin CdS Shell. *Phys. Chem. Chem. Phys.* **2016**, *18*, 31828−31835.

(21) Tan, L.; Yang, F.; Kim, M. R.; Li, P.; Gangadharan, D. T.; Margot, J.; Izquierdo, R.; Chaker, M.; Ma, D. Enhanced Long-Term and Thermal Stability of Polymer Solar Cells in Air at High Humidity with the Formation of Unusual Quantum Dot Networks. *ACS Appl. Mater. Interfaces* **2017**, *9*, 26257−26267.

(22) Xu, Z.; Liu, Y.; Ren, F.; Yang, F.; Ma, D. Development of Functional Nanostructures and Their Applications in Catalysis and Solar Cells. *Coord. Chem. Rev.* **2016**, *320*, 153−180.

(23) Fortin, J. P.; Wilhelm, C.; Servais, J.; Ménager, C.; Bacri, J. C.; Gazeau, F. Size-Sorted Anionic Iron Oxide Nanomagnets as Colloidal Mediators for Magnetic Hyperthermia. *J. Am. Chem. Soc.* **2007**, *129*, 2628−2635.

(24) Johannsen, M.; Gneveckow, U.; Eckelt, L.; Feussner, A.; Waldöfner, N.; Scholz, R.; Deger, S.; Wust, P.; Loening, S.; Jordan, A. Clinical Hyperthermia of Prostate Cancer Using Magnetic Nano-

particles: Presentation of a New Interstitial Technique. *Int. J. Hyperthermia* **2005**, *21*, 637−647.
(25) Akiyama, S.; Kawasaki, S.; Kodera, Y.; Hibi, K.; Kato, S.; Ito, K.; Nakao, A. A New Method of Thermo-Chemotherapy Using a Stent for Patients with Esophageal Cancer. *Surg. Today* **2005**, *36*, 19−24.
(26) Maier-Hauff, K.; Ulrich, F.; Nestler, D.; Niehoff, H.; Wust, P.; Thiesen, B.; Orawa, H.; Budach, V.; Jordan, A. Efficacy and Safety of Intratumoral Thermotherapy Using Magnetic Iron-Oxide Nanoparticles Combined with External Beam Radiotherapy on Patients with Recurrent Glioblastoma Multiforme. *J. Neuro-Oncol.* **2011**, *103*, 317−324.
(27) MagForce AG. MagForce AG Corporate News. https://www.magforce.com/en/presse-investoren/news-events/corporate-news/corporate-news-archiv/browse/1/select_category/23.html (accessed Dec 28, 2018).
(28) Zou, L.; Wang, H.; He, B.; Zeng, L.; Tan, T.; Cao, H.; He, X.; Zhang, Z.; Guo, S.; Li, Y. Current Approaches of Photothermal Therapy in Treating Cancer Metastasis with Nanotherapeutics. *Theranostics* **2016**, *6*, 762.
(29) Li, J.; Zhen, X.; Lyu, Y.; Jiang, Y.; Huang, J.; Pu, K. Cell Membrane Coated Semiconducting Polymer Nanoparticles for Enhanced Multimodal Cancer Phototheranostics. *ACS Nano* **2018**, *12*, 8520−8530.
(30) Zhen, X.; Zhang, J.; Huang, J.; Xie, C.; Miao, Q.; Pu, K. Macrotheranostic Probe with Disease-Activated Near-Infrared Fluorescence, Photoacoustic, and Photothermal Signals for Imaging-Guided Therapy. *Angew. Chem., Int. Ed.* **2018**, *57*, 7804−7808.
(31) Lyu, Y.; Cui, D.; Sun, H.; Miao, Y.; Duan, H.; Pu, K. Dendronized Semiconducting Polymer as Photothermal Nanocarrier for Remote Activation of Gene Expression. *Angew. Chem.* **2017**, *129*, 9283−9287.
(32) Rosal, B.; Carrasco, E.; Ren, F.; Benayas, A.; Vetrone, F.; Sanz-Rodríguez, F.; Ma, D.; Juarranz, Á.; Jaque, D. Infrared-Emitting QDs for Thermal Therapy with Real-Time Subcutaneous Temperature Feedback. *Adv. Funct. Mater.* **2016**, *26*, 6060.
(33) Lee, J.-H.; Jang, J.-t.; Choi, J.-s.; Moon, S. H.; Noh, S.-h.; Kim, J.-w.; Kim, J.-G.; Kim, I.-S.; Park, K. I.; Cheon, J. Exchange-Coupled Magnetic Nanoparticles for Efficient Heat Induction. *Nat. Nanotechnol.* **2011**, *6*, 418−422.
(34) Johannsen, M.; Gneveckow, U.; Thiesen, B.; Taymoorian, K.; Cho, C. H.; Waldöfner, N.; Scholz, R.; Jordan, A.; Loening, S. A.; Wust, P. Thermotherapy of Prostate Cancer Using Magnetic Nanoparticles: Feasibility, Imaging, and Three-Dimensional Temperature Distribution. *Eur. Urol.* **2007**, *52*, 1653−1662.
(35) Espinosa, A.; Di Corato, R.; Kolosnjaj-Tabi, J.; Flaud, P.; Pellegrino, T.; Wilhelm, C. Duality of Iron Oxide Nanoparticles in Cancer Therapy: Amplification of Heating Efficiency by Magnetic Hyperthermia and Photothermal Bimodal Treatment. *ACS Nano* **2016**, *10*, 2436−2446.
(36) Wang, T.; LaMontagne, D.; Lynch, J.; Zhuang, J.; Cao, Y. C. Colloidal Superparticles from Nanoparticle Assembly. *Chem. Soc. Rev.* **2013**, *42*, 2804−2823.
(37) Chen, J.; Dong, A.; Cai, J.; Ye, X.; Kang, Y.; Kikkawa, J. M.; Murray, C. B. Collective Dipolar Interactions in Self-Assembled Magnetic Binary Nanocrystal Superlattice Membranes. *Nano Lett.* **2010**, *10*, 5103−5108.
(38) Zhou, Z.; Tian, R.; Wang, Z.; Yang, Z.; Liu, Y.; Liu, G.; Wang, R.; Gao, J.; Song, J.; Nie, L. Artificial Local Magnetic Field Inhomogeneity Enhances T_2 Relaxivity. *Nat. Commun.* **2017**, *8*, 15468.
(39) Chen, O.; Riedemann, L.; Etoc, F.; Herrmann, H.; Coppey, M.; Barch, M.; Farrar, C. T.; Zhao, J.; Bruns, O. T.; Wei, H.; Guo, P.; Cui, J.; Jensen, R.; Chen, Y.; Harris, D. K.; Cordero, J. M.; Wang, Z.; Jasanoff, A.; Fukumura, D.; Reimer, R.; Dahan, M.; Jain, R. K.; Bawendi, M. G. Magneto-Fluorescent Core-Shell Supernanoparticles. *Nat. Commun.* **2014**, *5*, 5093.
(40) Ren, F.; Zhao, H.; Vetrone, F.; Ma, D. Microwave-Assisted Cation Exchange Toward Synthesis of Near-Infrared Emitting PbS/CdS Core/Shell Quantum Dots with Significantly Improved Quantum Yields Through a Uniform Growth Path. *Nanoscale* **2013**, *5*, 7800.
(41) Zhuang, J.; Wu, H.; Yang, Y.; Cao, Y. C. Controlling Colloidal Superparticle Growth Through Solvophobic Interactions. *Angew. Chem., Int. Ed.* **2008**, *47*, 2208−2212.
(42) Zhuang, J.; Wu, H.; Yang, Y.; Cao, Y. C. Supercrystalline Colloidal Particles from Artificial Atoms. *J. Am. Chem. Soc.* **2007**, *129*, 14166−14167.
(43) Wang, D.; He, J.; Rosenzweig, N.; Rosenzweig, Z. Superparamagnetic Fe_2O_3 Beads-CdSe/ZnS Quantum Dots Core-Shell Nanocomposite Particles for Cell Separation. *Nano Lett.* **2004**, *4*, 409−413.
(44) Li, M.; You, G.; Wang, A. Y.; Hu, W.; Wang, J.; Sun, F.; Zhu, Y.; Henderson, R.; Xu, J. Lasing and Magnetic Microbeads Loaded with Colloidal Quantum Dots and Iron Oxide Nanocrystals. *Nanoscale* **2013**, *5*, 9598−9603.
(45) Jafari, D.; Cody, K.; Dean, A.; Shofer, F.; Jenq, K.; Fischer, J.; Panebianco, N. Human or Animal? Finding the Best Ultrasound Soft Tissue Model for Foreign Body Evaluation. *Crit Ultrasound J.* **2012**, *4*, A18.
(46) Wang, Y. F.; Liu, G. Y.; Sun, L. D.; Xiao, J. W.; Zhou, J. C.; Yan, C. H. Nd^{3+}-Sensitized Upconversion Nanophosphors: Efficient *In Vivo* Bioimaging Probes with Minimized Heating Effect. *ACS Nano* **2013**, *7*, 7200−7206.
(47) Skripka, A.; Marin, R.; Benayas, A.; Canton, P.; Hemmer, E.; Vetrone, F. Covering the Optical Spectrum Through Collective Rare-Earth Doping of $NaGdF_4$ Nanoparticles: 806 and 980 nm Excitation Routes. *Phys. Chem. Chem. Phys.* **2017**, *19*, 11825−11834.
(48) Liang, H.; Vu, K. T.; Krishnan, P.; Trang, T. C.; Shin, D.; Kimel, S.; Berns, M. W. Wavelength Dependence of Cell Cloning Efficiency After Optical Trapping. *Biophys. J.* **1996**, *70*, 1529−1533.
(49) Johnston, B. D.; Kreyling, W. G.; Pfeiffer, C.; Schäffler, M.; Sarioglu, H.; Ristig, S.; Hirn, S.; Haberl, N.; Thalhammer, S.; Hauck, S. M. Colloidal Stability and Surface Chemistry Are Key Factors for the Composition of the Protein Corona of Inorganic Gold Nanoparticles. *Adv. Funct. Mater.* **2017**, *27*, 1701956.
(50) Hansen, M. F.; Mørup, S. Estimation of Blocking Temperatures from ZFC/FC Curves. *J. Magn. Magn. Mater.* **1999**, *203*, 214−216.
(51) Cannas, C.; Casula, M. F.; Concas, G.; Corrias, A.; Gatteschi, D.; Falqui, A.; Musinu, A.; Sangregorio, C.; Spano, G. Magnetic Properties of γ-Fe_2O_3-SiO_2 Aerogel and Xerogel Nanocomposite Materials. *J. Mater. Chem.* **2001**, *11*, 3180−3187.
(52) Koczkur, K. M.; Mourdikoudis, S.; Polavarapu, L.; Skrabalak, S. E. Polyvinylpyrrolidone (PVP) in Nanoparticle Synthesis. *Dalton Trans.* **2015**, *44*, 17883−17905.
(53) Tang, F.; Li, L.; Chen, D. Mesoporous Silica Nanoparticles: Synthesis, Biocompatibility and Drug Delivery. *Adv. Mater.* **2012**, *24*, 1504−1534.
(54) Xiao, L.; Li, J.; Brougham, D. F.; Fox, E. K.; Feliu, N.; Bushmelev, A.; Schmidt, A.; Mertens, N.; Kiessling, F.; Valldor, M. Water-Soluble Superparamagnetic Magnetite Nanoparticles with Biocompatible Coating for Enhanced Magnetic Resonance Imaging. *ACS Nano* **2011**, *5*, 6315−6324.
(55) Matsumura, Y.; Maeda, H. A New Concept for Macromolecular Therapeutics in Cancer Chemotherapy: Mechanism of Tumoritropic Accumulation of Proteins and the Antitumor Agent Smancs. *Cancer Res.* **1986**, *46*, 6387−6392.
(56) Duan, X.; Li, Y. Physicochemical Characteristics of Nanoparticles Affect Circulation, Biodistribution, Cellular Internalization, and Trafficking. *Small* **2013**, *9*, 1521−1532.
(57) Wang, Z.; Qiao, R.; Tang, N.; Lu, Z.; Wang, H.; Zhang, Z.; Xue, X.; Huang, Z.; Zhang, S.; Zhang, G. Active Targeting Theranostic Iron Oxide Nanoparticles for MRI and Magnetic Resonance-Guided Focused Ultrasound Ablation of Lung Cancer. *Biomaterials* **2017**, *127*, 25−35.
(58) Jun, Y.-w.; Huh, Y.-M.; Choi, J.-s.; Lee, J.-H.; Song, H.-T.; Yoon, S.; Kim, K.-S.; Shin, J.-S; Suh, J.-S.; Cheon, J. Nanoscale Size Effect of Magnetic Nanocrystals and Their Utilization for Cancer

DOI: 10.1021/acsnano.8b06563
ACS Nano 2019, 13, 408−420

Diagnosis *via* Magnetic Resonance Imaging. *J. Am. Chem. Soc.* **2005**, *127*, 5732−5733.
(59) Tromsdorf, U. I.; Bigall, N. C.; Kaul, M. G.; Bruns, O. T.; Nikolic, M. S.; Mollwitz, B.; Sperling, R. A.; Reimer, R.; Hohenberg, H.; Parak, W. J. Size and Surface Effects on the MRI Relaxivity of Manganese Ferrite Nanoparticle Contrast Agents. *Nano Lett.* **2007**, *7*, 2422−2427.
(60) Zhao, Z.; Zhou, Z.; Bao, J.; Wang, Z.; Hu, J.; Chi, X.; Ni, K.; Wang, R.; Chen, X.; Chen, Z.; Gao, J. Octapod Iron Oxide Nanoparticles as High-Performance T_2 Contrast Agents for Magnetic Resonance Imaging. *Nat. Commun.* **2013**, *4*, 2266.
(61) Pöselt, E.; Kloust, H.; Tromsdorf, U.; Janschel, M.; Hahn, C.; Maßlo, C.; Weller, H. Relaxivity Optimization of a PEGylated Iron-Oxide-Based Negative Magnetic Resonance Contrast Agent for T_2-Weighted Spin-Echo Imaging. *ACS Nano* **2012**, *6*, 1619−1624.
(62) Zhou, Z.; Zhao, Z.; Zhang, H.; Wang, Z.; Chen, X.; Wang, R.; Chen, Z.; Gao, J. Interplay Between Longitudinal and Transverse Contrasts in Fe_3O_4 Nanoplates with (111) Exposed Surfaces. *ACS Nano* **2014**, *8*, 7976−7985.
(63) Jang, J.-t.; Nah, H.; Lee, J.-H.; Moon, S. H.; Kim, M. G.; Cheon, J. Critical Enhancements of MRI Contrast and Hyperthermic Effects by Dopant-Controlled Magnetic Nanoparticles. *Angew. Chem.* **2009**, *121*, 1260−1264.
(64) Yang, D.; Yang, G.; Yang, P.; Lv, R.; Gai, S.; Li, C.; He, F.; Lin, J. Assembly of Au Plasmonic Photothermal Agent and Iron Oxide Nanoparticles on Ultrathin Black Phosphorus for Targeted Photothermal and Photodynamic Cancer Therapy. *Adv. Funct. Mater.* **2017**, *27*, 1700371.
(65) Xu, J.; Han, W.; Yang, P.; Jia, T.; Dong, S.; Bi, H.; Gulzar, A.; Yang, D.; Gai, S.; He, F. Tumor Microenvironment-Responsive Mesoporous MnO_2-Coated Upconversion Nanoplatform for Self-Enhanced Tumor Theranostics. *Adv. Funct. Mater.* **2018**, *28*, 1803804.
(66) Xu, J.; He, F.; Cheng, Z.; Lv, R.; Dai, Y.; Gulzar, A.; Liu, B.; Bi, H.; Yang, D.; Gai, S. Yolk-Structured Upconversion Nanoparticles with Biodegradable Silica Shell for FRET Sensing of Drug Release and Imaging-Guided Chemotherapy. *Chem. Mater.* **2017**, *29*, 7615−7628.
(67) Paquet, C.; de Haan, H. W.; Leek, D. M.; Lin, H.-Y.; Xiang, B.; Tian, G.; Kell, A.; Simard, B. Clusters of Superparamagnetic Iron Oxide Nanoparticles Encapsulated in a Hydrogel: A Particle Architecture Generating a Synergistic Enhancement of the T_2 Relaxation. *ACS Nano* **2011**, *5*, 3104−3112.
(68) Zhao, H. X.; Zou, Q.; Sun, S. K.; Yu, C.; Zhang, X.; Li, R. J.; Fu, Y. Y. Theranostic Metal-Organic Framework Core-Shell Composites for Magnetic Resonance Imaging and Drug Delivery. *Chem. Sci.* **2016**, *7*, 5294−5301.
(69) Maestro, L. M.; Haro-González, P.; Rosal, B.; Ramiro, J.; Caamano, A.; Carrasco, E.; Juarranz, A.; Sanz-Rodríguez, F.; Solé, J. G.; Jaque, D. Heating Efficiency of Multi-Walled Carbon Nanotubes in the First and Second Biological Windows. *Nanoscale* **2013**, *5*, 7882−7889.
(70) Robinson, J. T.; Welsher, K.; Tabakman, S. M.; Sherlock, S. P.; Wang, H.; Luong, R.; Dai, H. High Performance *In Vivo* Near-IR (> 1 μm) Imaging and Photothermal Cancer Therapy with Carbon Nanotubes. *Nano Res.* **2010**, *3*, 779−793.
(71) Hergt, R.; Dutz, S. Magnetic Particle Hyperthermia-Biophysical Limitations of a Visionary Tumour Therapy. *J. Magn. Magn. Mater.* **2007**, *311*, 187−192.
(72) Park, J.; An, K.; Hwang, Y.; Park, J.-G.; Noh, H.-J.; Kim, J.-Y.; Park, J.-H.; Hwang, N.-M.; Hyeon, T. Ultra-Large-Scale Syntheses of Monodisperse Nanocrystals. *Nat. Mater.* **2004**, *3*, 891−5.
(73) Hines, M. A.; Scholes, G. D. Colloidal PbS Nanocrystals with Size-Tunable Near-Infrared Emission: Observation of Post-Synthesis Self-Narrowing of the Particle Size Distribution. *Adv. Mater.* **2003**, *15*, 1844−1849.
(74) Zhang, T.; Zhao, H.; Riabinina, D.; Chaker, M.; Ma, D. Concentration-Dependent Photoinduced Photoluminescence Enhancement in Colloidal PbS Quantum Dot Solution. *J. Phys. Chem. C* **2010**, *114*, 10153−10159.
(75) Soetaert, F.; Kandala, S. K.; Bakuzis, A.; Ivkov, R. Experimental Estimation and Analysis of Variance of the Measured Loss Power of Magnetic Nanoparticles. *Sci. Rep.* **2017**, *7*, 6661.

DOI: 10.1021/acsnano.8b06563
ACS Nano 2019, 13, 408−420

Multifunctional Self-Assembled Supernanoparticles for Deep-Tissue Bimodal Imaging and Amplified Dual-Mode Heating Treatment

Fan Yang[†], *Artiom Skripka*[†], *Maryam Sadat Tabatabaei*[‡], *Sung Hwa Hong*[¶], *Fuqiang Ren*[†], *Antonio Benayas*[†,§], *Jung Kwon Oh*[¶], *Sylvain Martel*[‡], *Xinyu Liu*[⊥], *Fiorenzo Vetrone*[*,†], *Dongling Ma*[*,†]

[†] Institut National de la Recherche Scientifique, Centre Énergie, Matériaux et Télécommunications, Université du Québec, 1650 Boul. Lionel-Boulet, Varennes, Québec J3X 1S2, Canada

[‡] NanoRobotics Laboratory, Department of Computer and Software Engineering, Institute of Biomedical Engineering, Polytechnique Montréal, Montréal, QC H3T 1J4, Canada

[¶] Department of Chemistry and Biochemistry, Concordia University, Montreal, Quebec H4B 1R6, Canada

[§] Department of Physics and CICECO – Aveiro Institute of Materials, University of Aveiro, 3810-193, Aveiro, Portugal

[⊥] Department of Mechanical and Industrial Engineering, University of Toronto, 5 King's College Road, Toronto, Ontario, M5S 3G8, Canada

Supporting information

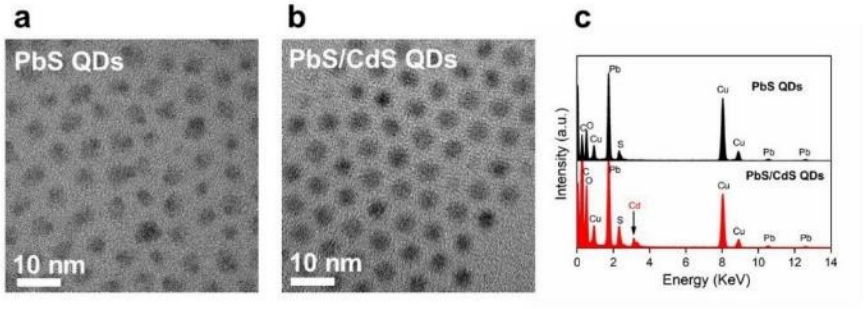

Figure S1 TEM images of larger PbS (II-BW) QDs (a), core/shell PbS/CdS (II-BW) QDs (b) and corresponding EDX spectra taken from the whole area of (a) and (b). The presence of Cd (indicated by an arrow) in the PbS/CdS QDs is clearly shown in the EDX spectrum, confirming the formation of CdS shell.

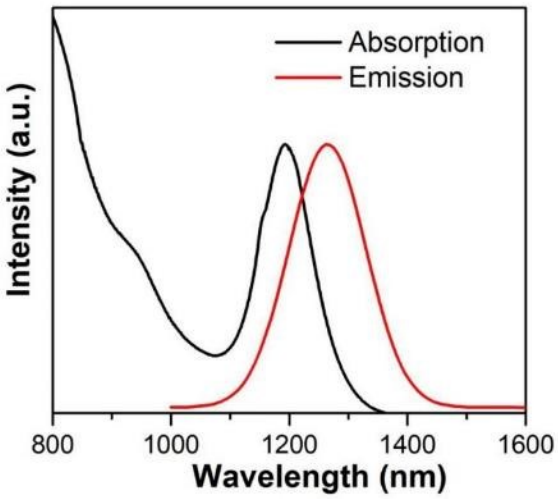

Figure S2 Absorption and photoluminescence spectra of PbS/CdS (II-BW) QDs synthesized by the microwave method. The PbS/CdS (II-BW) QDs show an emission peak at 1260 nm in the second biological optical transparency window.

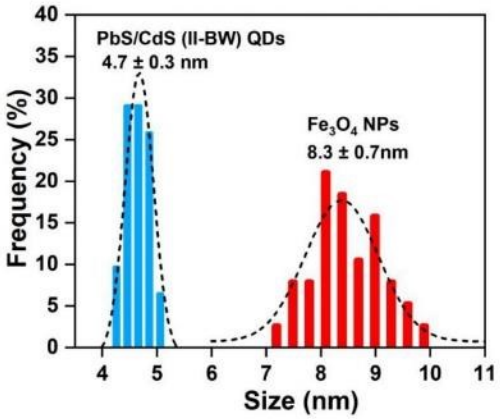

Figure S3 Size distribution of the larger PbS/CdS (II-BW) QDs and Fe_3O_4 NPs.

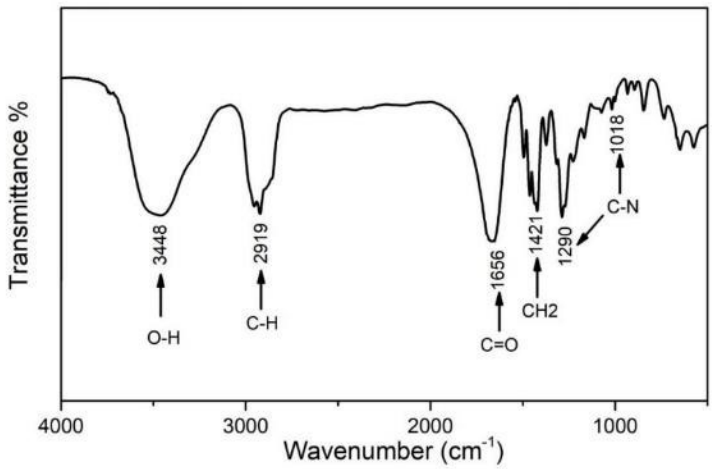

Figure S4 FTIR spectrum of SASNs (II-BW). The broad peaks at 3448 cm^{-1} and 2919 cm^{-1} correspond to O-H stretching and C-H stretching vibration, respectively. The peak at 1656 cm^{-1} is assigned to the C=O stretching in the PVP. CH_2 groups in the alkyl chain in PVP show asymmetric stretching at 1421 cm^{-1}. Other important peaks at 1290 cm^{-1} and 1018 cm^{-1} are assigned to the stretching vibration of C-N in the pyrrole ring of PVP. These results suggest that PVP is bound onto the surface of the SASNs (II-BW).[1-2]

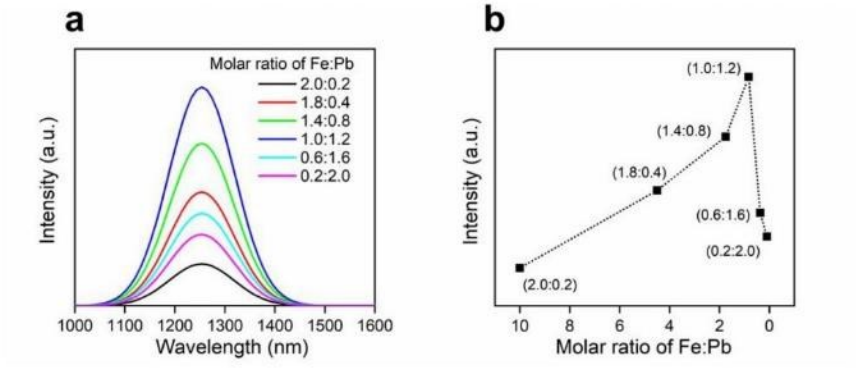

Figure S5 (a) Photoluminescence emission spectra of SASNs (II-BW) with various molar ratios of Fe:Pb (2.0:0.2, 1.8:0.4, 1.4:0.8, 1.0:1.2, 0.6:1.6, 0.2:2.0). (b) The corresponding integrated emission intensity of SASNs (II-BW) as a function of molar ratios of Fe:Pb (2.0:0.2, 1.8:0.4, 1.4:0.8, 1.0:1.2, 0.6:1.6, 0.2:2.0). The variation of emission intensity with the molar ratio is a result of the interplay between the quenching caused by Fe_3O_4 NPs and the self-quenching among PbS/CdS QDs themselves. The molar ratio of Fe:Pb = 1:1.2 was found to be optimal for photoluminescence imaging.

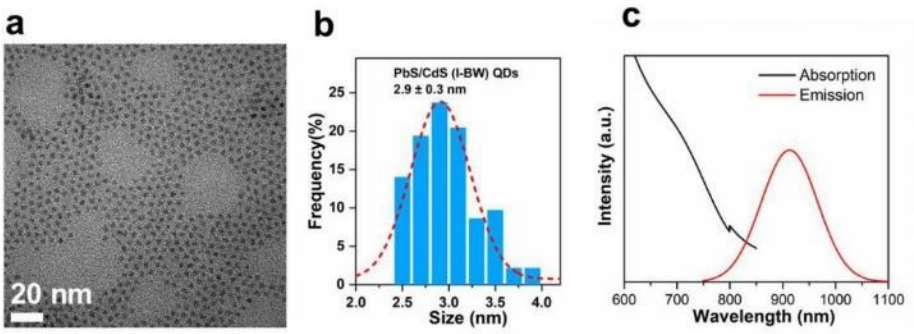

Figure S6 (a) TEM image of smaller PbS/CdS (I-BW) QDs. (b) Size distribution of PbS/CdS (I-BW) QDs. (c) Absorption and photoluminescence emission spectra of PbS/CdS (I-BW) QDs synthesized by the microwave method. The smaller PbS/CdS (I-BW) QDs show an emission peak at 915 nm in the first biological optical transparency window.

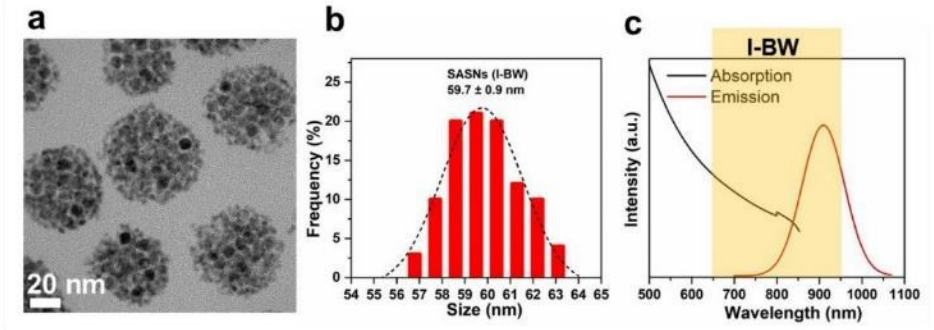

Figure S7 (a) TEM image and (b) size distribution of the SASNs (I-BW). (c) Absorption and photoluminescence emission spectra of SASNs (I-BW).

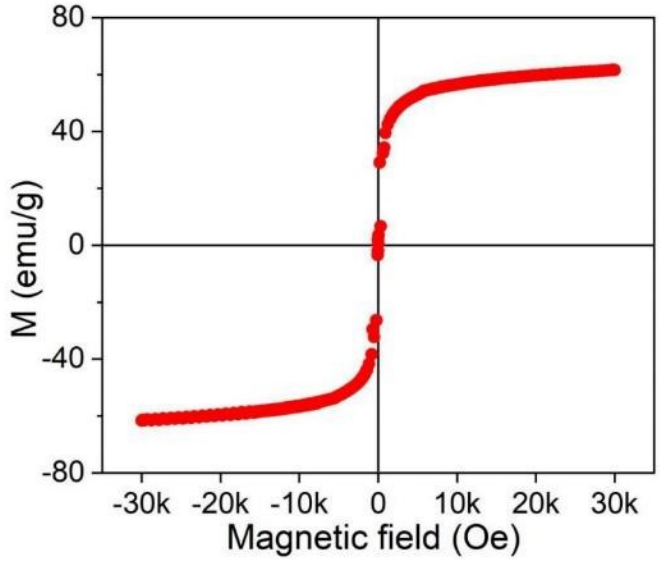

Figure S8 The magnetization of free Fe_3O_4 NPs as a function of magnetic field at 300 K.

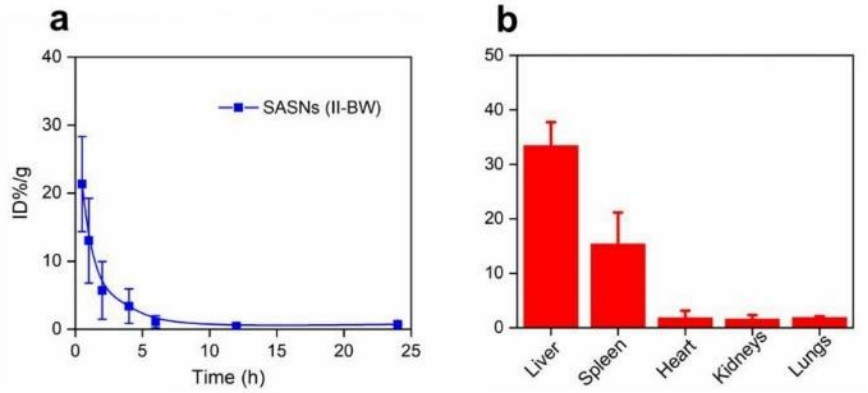

Figure S9 (a) Blood circulation profile of SASNs (II-BW) in mice by measuring the Fe concentration in blood at different time points. (b) Biodistribution of SASNs (II-BW) in different organs of mice by measuring the concentrations of Fe based on ICP-AES analysis at 24 h post-injection.

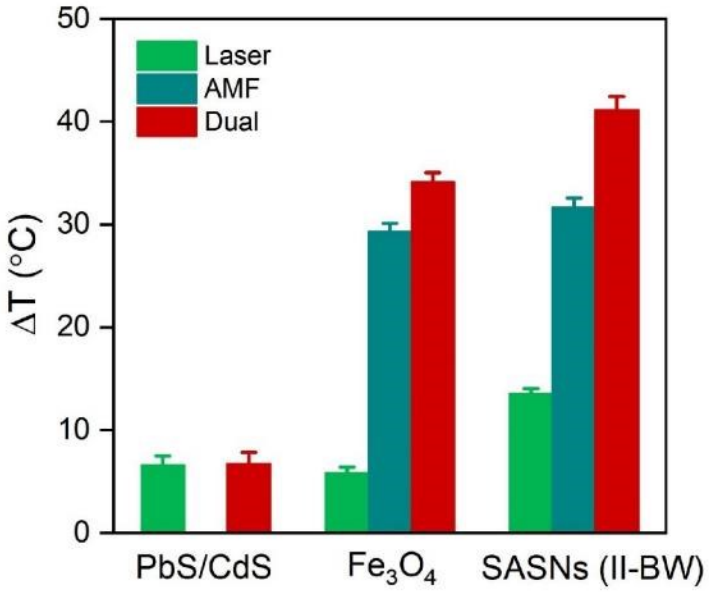

Figure S10 Temperature change of PbS/CdS, Fe_3O_4 and SASNs (II-BW) after 5 min of each treatment (laser at 3.3 W/cm^2, AMF at 7 kA/m, dual-mode). The concentration of PbS/CdS, Fe_3O_4 and SASNs (II-BW) were kept the same.

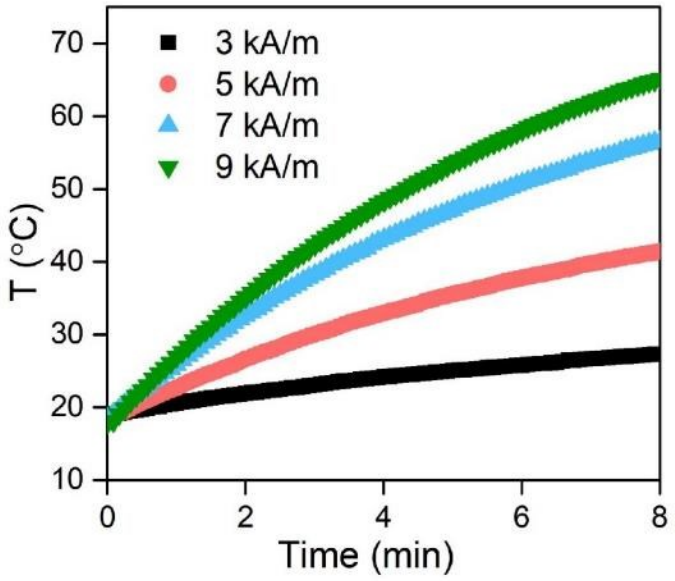

Figure S11 Temperature increase of the SASNs (II-BW) as a function of time under different magnetic fields with a fixed frequency of 150 kHz.

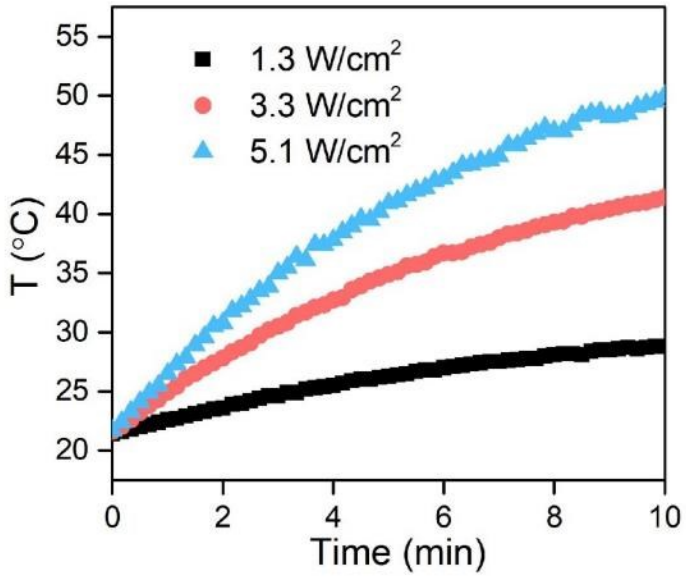

Figure S12 Temperature increase of the SASNs (II-BW) as a function of time under different power density of the 787 nm laser (1.3, 3.3 and 5.1 W/cm^2).

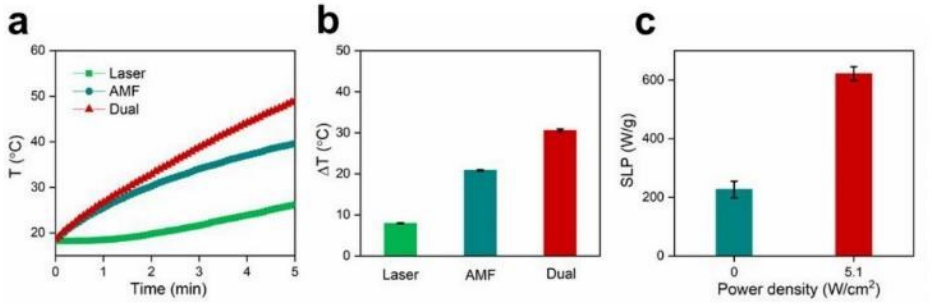

Figure S13 (a) The time-dependent temperature curves of a commercial ferrofluid (fluidMAG-PMO) solution with 20 mM concentration under three types of modulation (laser at 3.3 W/cm^2, AMF at 7 kA/m, dual-mode). (b) Temperature increase of fluidMAG-PMO solution after 5 min of each modulation (laser at 3.3 W/cm^2, AMF at 7 kA/m, dual-mode). (c) The SLP values of fluidMAG-PMO solution under AMF and dual-mode modulation. It should be noted that the magnetic field in both modulations are fixed (9 kA/m, 150 kHz) and 787 nm laser with maximum power density of 5.1 W/cm^2 are adopted in the dual-mode modulation in order to compare the SLP value with SASNs (II-BW). The SLP value of ferrofluids is lower than SASNs (II-BW) because the PbS/CdS (II -BW) QDs inside SNs contribute to photothermal heating.

Table S1. SLP values reported in published studies of magnetothermal heating

Nanoparticles	[C](mg /mL)	Size (nm)	Magnetic field frequency (f) (kHz)	Amplitude (H) (kA/m)	Heating modality(single/ dual)	SLP (W/g)	Ref.
$CoFe_2O_4$	5	9	500	37.3	single	100~450	[3]
$CoFe_2O_4$@ XFe_2O_4 (X=Mn, Co, Fe, Zn)	5	15	500	37.3	single	1000~4000	[3]
$MnFe_2O_4$ decorated graphene oxide	0.1	80~90	240	41.98~59.99	single	480~1588	[4]
Fe_3O_4 /$Zn_{0.4}Fe_{2.6}O_4$ cube	~	15.5~19.2	380	16	single	189.6~1019.2	[5]
BNF(Partikeltechnologie)	22	126	150	5~48	single	0~550	[6]
JHU	64	117	150	5~48	single	30~450	[6]
Nanomag-D-spio (Partikeltechnologie)	96	106	150	5~48	single	0~160	[6]
$MnFe_2O_4$	11.3 ± 1.5	12 ± 3	150~375	4~44	single	108	[7]
Hexagonal Fe_3O_4 nanoplatelets	1	85~100	366	5	single	26~765	[8]
MFe_2O_4 (M = Fe, Co and Mn)	1	3.8~16	276	9.8	single	10~92	[9]
Flower-shaped maghemite	8	6~55	300~ 900	6.4~21.5	single	48~1944	[10]
Mn-Zn ferrite	1	30~40	390~780	~	single	201.1~513.2	[11]
$CoFe_2O_4$/γ-Fe_2O_3	~	5~16.5	700	24.8	single	4~1650	[12]
γ-Fe_2O_3	3.5	10.2~19.7	100~1000	3~17	single	5~120	[13]

Fe_3O_4	~	9.3~34.5	341	36.5	single	60~500	[14]
Fe_3O_4 sphere and octopod	2	17~47	310	15.9~63.8	single	10~415	[15]
Fe_3O_4	1~4	40	765	23.9	single	400~550	[16]
Iron oxide(Fe_3O_4+γ-Fe_2O_3)	10.01	15±10	2100	20	single	415	[17]
FeO/Fe_3O_4	1	20±2	310	31.9~63.8	single	50~270	[18]
Fe_3O_4 nanorod	1~3	41~65	310	31.9~63.8	single	140~862	[19]
Iron oxide cube	0.7	20	320~900	20	dual	800~4850	[20]
Commercial ferrofluids (fluidMAG-PMO)	0.8	20	150	9	dual	621	This work
SASNs (II-BW)	0.8	61	150	9	dual	1883	This work

The SLP value is not only determined by the magnetic materials (size, concentration, composition), but also strongly depends on the magnetic field [magnetic field frequency (*f*) and amplitude (*H*)] provided by the magnetothermal equipment.[3] In our case, the magnetic field frequency of the equipment is fixed and only the amplitude can be tuned from 3 to 9 kA/m. Compared with the reported studies above, the magnetic field frequency (150 kHz) and amplitude (9 kA/m) is significantly lower. It can be seen that the SLP value is almost linear against the applied magnetic field and dual-mode heating in Fig 5g and 5h of the main text. For example, if we keep the same frequency of 150 kHz and increase the amplitude from 9 to 20 kA/m, the SLP will increase to 5084 W/g under dual-mode treatment (laser at 5.1 W/cm^2). In addition, the heating capability of a commercial ferrofluid (fluidMAG-PMO) solution are also examined as a control. The SLP value of fluidMAG-PMO solution is lower compared to the cited works above, which can further confirm the low magnetic field used in our experiment. Thus, SASNs (II-BW) can achieve a high SLP value of *ca.* three times that of fluidMAG-PMO even under such a weak magnetic field. Overall there is no doubt that an unprecedented SLP value of SASNs (II-BW) can be realized under considerable AMF and laser dual-mode modulation.

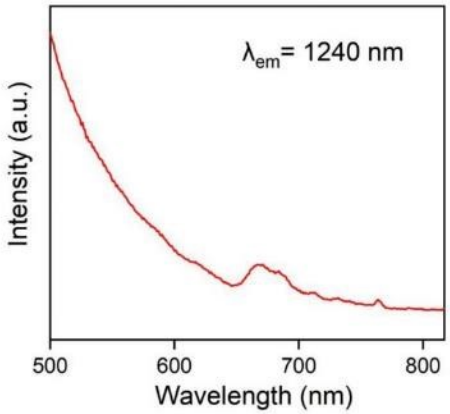

Figure S14 Excitation spectrum of SASNs (II-BW). Emission intensity was monitored at the emission peak wavelength of 1240 nm. Ideally, a single excitation wavelength would be preferable across various experiments presented. However, due to the technical constrains in certain cases, we had to vary the excitation sources in order to conduct these experiments. Nonetheless, from the excitation spectrum above, it can be seen that different excitation wavelengths (787 nm, 806 nm, 808 nm) used are in close proximity to each other, all yielding the similar level of photoluminescence. It indicates that the use of these three NIR lasers of different wavelengths did not have any significant effect on the conducted experiments.

References:

1. Koczkur, K. M.; Mourdikoudis, S.; Polavarapu, L.; Skrabalak, S. E. Polyvinylpyrrolidone (PVP) In Nanoparticle Synthesis. *Dalton Trans.* **2015,** *44*, 17883-17905.

2. Selvam, S.; Sundrarajan, M. Functionalization of Cotton Fabric with PVP/ZnO Nanoparticles for Improved Reactive Dyeability and Antibacterial Activity. *Carbohydr. Polym.* **2012,** *87*, 1419-1424.

3. Lee, J. H.; Jang, J. t.; Choi, J. s.; Moon, S. H.; Noh, S. h.; Kim, J. w.; Kim, J. G.; Kim, I. S.; Park, K. I.; Cheon, J. Exchange-Coupled Magnetic Nanoparticles for Efficient Heat Induction. *Nat. Nanotechnol.* **2011,** *6*, 418-422.

4. Peng, E.; Choo, E. S. G.; Chandrasekharan, P.; Yang, C. T.; Ding, J.; Chuang, K. H.; Xue, J. M. Synthesis of Manganese Ferrite/Graphene Oxide Nanocomposites for Biomedical Applications. *Small* **2012,** *8*, 3620-3630.

5. Bauer, L. M.; Situ, S. F.; Griswold, M. A.; Samia, A. C. S. High-Performance Iron Oxide Nanoparticles for Magnetic Particle Imaging-Guided Hyperthermia (hMPI). *Nanoscale* **2016,** *8*, 12162-12169.

6. Dennis, C. L.; Krycka, K. L.; Borchers, J. A.; Desautels, R. D.; Van Lierop, J.; Huls, N. F.; Jackson, A. J.; Gruettner, C.; Ivkov, R. Internal Magnetic Structure of Nanoparticles Dominates Time-Dependent Relaxation Processes in a Magnetic Field. *Adv. Funct. Mater.* **2015,** *25*, 4300-4311.

7. Soetaert, F.; Kandala, S. K.; Bakuzis, A.; Ivkov, R. Experimental Estimation and Analysis of Variance of the Measured Loss Power of Magnetic Nanoparticles. *Sci. Rep.* **2017,** *7*, 6661.

8. Wang, H.; Shrestha, T. B.; Basel, M. T.; Pyle, M.; Toledo, Y.; Konecny, A.; Thapa, P.; Ikenberry, M.; Hohn, K. L.; Chikan, V. Hexagonal Magnetite Nanoprisms: Preparation, Characterization and Cellular Uptake. *J. Mater. Chem. B* **2015,** *3*, 4647-4653.

9. Mendo, S. G.; Alves, A. F.; Ferreira, L. P.; Cruz, M. M.; Mendonça, M. H.; Godinho, M.; Carvalho, M. D. Hyperthermia Studies of Ferrite Nanoparticles Synthesized in the Presence of Cotton. *New J. Chem.* **2015,** *39*, 7182-7193.

10. Hugounenq, P.; Levy, M.; Alloyeau, D.; Lartigue, L.; Dubois, E.; Cabuil, V. r.; Ricolleau, C.; Roux, S. p.; Wilhelm, C.; Gazeau, F. Iron Oxide Monocrystalline Nanoflowers for Highly Efficient Magnetic Hyperthermia. *J. Phys. Chem. C* **2012,** *116*, 15702-15712.

11. Xie, J.; Yan, C.; Zhang, Y.; Gu, N. Shape Evolution of "Multibranched" Mn-Zn Ferrite Nanostructures with High Performance: a Transformation of Nanocrystals into Nanoclusters. *Chem. Mater.* **2013,** *25*, 3702-3709.

12. Fortin, J. P.; Wilhelm, C.; Servais, J.; Ménager, C.; Bacri, J. C.; Gazeau, F. Size-Sorted Anionic Iron Oxide Nanomagnets as Colloidal Mediators for Magnetic Hyperthermia. *J. Am. Chem. Soc* **2007,** *129*, 2628-2635.

13. Cobianchi, M.; Guerrini, A.; Avolio, M.; Innocenti, C.; Corti, M.; Arosio, P.; Orsini, F.; Sangregorio, C.; Lascialfari, A. Experimental Determination of the Frequency and Field Dependence of Specific Loss Power in Magnetic Fluid Hyperthermia. *J. Magn. Magn. Mater.* **2017,** *444*, 154-160.

14. Vreeland, E. C.; Watt, J.; Schober, G. B.; Hance, B. G.; Austin, M. J.; Price, A. D.; Fellows, B. D.; Monson, T. C.; Hudak, N. S.; Maldonado-Camargo, L. Enhanced Nanoparticle Size Control by Extending LaMer's Mechanism. *Chem. Mater.* **2015,** *27*, 6059-6066.

15. Nemati, Z.; Alonso, J.; Martinez, L.; Khurshid, H.; Garaio, E.; Garcia, J.; Phan, M.; Srikanth, H. Enhanced Magnetic Hyperthermia in Iron Oxide Nano-Octopods: Size and Anisotropy Effects. *J. Mater. Chem. C* **2016,** *120*, 8370-8379.

16. Myrovali, E.; Maniotis, N.; Makridis, A.; Terzopoulou, A.; Ntomprougkidis, V.; Simeonidis, K.; Sakellari, D.; Kalogirou, O.; Samaras, T.; Salikhov, R. Arrangement at the Nanoscale: Effect on Magnetic Particle Hyperthermia. *Sci. Rep.* **2016,** *6*, 37934.

17. Worden, M.; Bruckman, M. A.; Kim, M. H.; Steinmetz, N. F.; Kikkawa, J. M.; LaSpina, C.; Hegmann, T. Aqueous Synthesis of Polyhedral "Brick-Like" Iron Oxide Nanoparticles for Hyperthermia and T_2 MRI Contrast Enhancement. *J. Mater. Chem. B* **2015,** *3*, 6877-6884.

18. Khurshid, H.; Alonso, J.; Nemati, Z.; Phan, M.; Mukherjee, P.; Fdez-Gubieda, M.; Barandiarán, J.; Srikanth, H. Anisotropy Effects in Magnetic Hyperthermia: A Comparison Between Spherical and Cubic Exchange-Coupled FeO/Fe_3O_4 Nanoparticles. *J. Appl. Phys.* **2015,** *117*, 17A337.

19. Das, R.; Alonso, J.; Nemati Porshokouh, Z.; Kalappattil, V.; Torres, D.; Phan, M. H.; Garaio, E.; García, J. A. n.; Sanchez Llamazares, J. L.; Srikanth, H. Tunable High Aspect Ratio Iron Oxide Nanorods for Enhanced Hyperthermia. *J. Phys. Chem. C* **2016,** *120*, 10086-10093.

20. Espinosa, A.; Di Corato, R.; Kolosnjaj-Tabi, J.; Flaud, P.; Pellegrino, T.; Wilhelm, C. Duality of Iron Oxide Nanoparticles in Cancer Therapy: Amplification of Heating Efficiency by Magnetic Hyperthermia and Photothermal Bimodal Treatment. *ACS Nano* **2016,** *10*, 2436-2446.

4.3 Magnetic-Photoluminescent Nanoplatform Built from Large-Pore Mesoporous Silica

Fan Yang, Artiom Skripka, Maryam Sadat Tabatabaei, Sung Hwa Hong, Fuqiang Ren, Yue Huang, Jung Kwon Oh, Sylvain Martel, Xinyu Liu, Fiorenzo Vetrone, and Dongling Ma

Chem. Mater., 31 (2019) 3201-3210.

Mesoporous silica ($mSiO_2$) NPs are widely implemented as multifunctional nanoplatforms for drug delivery due to their unique characteristics, including biocompatibility, high stability and ease of surface modification of linking drug molecules. Unfortunately, $mSiO_2$ NPs normally prepared by CTAB or other soft templates show small pore size (< 2 nm), which greatly restricts their use for encapsulation of macromolecular drugs (> 2 nm) and multifunctional NPs (QDs, iron oxide, gold NPs, *etc.*). Therefore, it is highly desired to fabricate uniform $mSiO_2$ with large pore size (> 5 nm) for *in vivo* biomedical applications.

In this paper, we synthesized a relatively-large-pore (>10 nm) $mSiO_2$ by a biphase stratification continuous growth approach. After simple silane coupling reaction, owing to its unique relatively-large-pore structure with high loading capacity, the thiol-modified $mSiO_2$ can be used as matrix to incorporate superparamagnetic Fe_3O_4 NPs and PbS/CdS QDs by coordination-driven reaction. This theranostic nanoplatform ($mSiO_2$@PbS/CdS-Fe_3O_4) exhibited excellent NIR-excitation and NIR-emission photoluminescence features for deep-tissue bioimaging, which was demonstrated *ex vivo* with tissue as thick as 14 mm. Meanwhile, $mSiO_2$@PbS/CdS-Fe_3O_4 can be rapidly confined under an external magnetic field (MF) and possess a significantly high T_2 relaxivity resulting from the synergistic effect induced by superparamagnetic NPs coupling. On the other hand, this nanoplatform can produce strong local heating as a highly efficient magnetic hyperthermia therapy (MHT)/ photothermal therapy (PTT) agent under external physical stimuli of MF and/or a NIR laser. After being loaded with DOX, the release rate of DOX under multi-stimuli (pH/MF/NIR) was significantly enhanced at lower pH and higher temperatures, caused by magnetothermal/photothermal effects. Our results pave the avenue towards developing a promising multifunctional theranostic nanoplatform for bimodal imaging, and simultaneously for integrating synergistic and highly localized treatment capabilities of MHT/PTT and pH/MF/NIR-responsive drug release.

CHEMISTRY OF MATERIALS
Cite This: Chem. Mater. 2019, 31, 3201−3210
Article
pubs.acs.org/cm

Magnetic Photoluminescent Nanoplatform Built from Large-Pore Mesoporous Silica

Fan Yang,[†] Artiom Skripka,[†] Maryam Sadat Tabatabaei,[‡] Sung Hwa Hong,[§] Fuqiang Ren,[†] Yue Huang,[†] Jung Kwon Oh,[§] Sylvain Martel,[‡] Xinyu Liu,[∥] Fiorenzo Vetrone,*[,†] and Dongling Ma*[,†]

[†]Institut National de la Recherche Scientifique, Centre Énergie, Matériaux et Télécommunications, Université du Québec, 1650 Boul. Lionel-Boulet, Varennes, Quebec J3X 1S2, Canada

[‡]NanoRobotics Laboratory, Department of Computer and Software Engineering, Institute of Biomedical Engineering, Polytechnique Montréal, Montreal, Quebec H3T 1J4, Canada

[§]Department of Chemistry and Biochemistry, Concordia University, Montreal, Quebec H4B 1R6, Canada

[∥]Department of Mechanical and Industrial Engineering, University of Toronto, 5 King's College Road, Toronto, Ontario M5S 3G8, Canada

Supporting Information

ABSTRACT: Integrating multiple components to realize cancer diagnosis and therapy in a single theranostic nanoplatform has drawn considerable attention. Herein, a multifunctional theranostic nanoplatform ($mSiO_2$@PbS/CdS-Fe_3O_4) was successfully fabricated by carefully designing thiol-modified large-pore mesoporous silica nanospheres ($mSiO_2$), followed by coordination-driven embedding of Fe_3O_4 nanoparticles (NPs) and PbS/CdS quantum dots (QDs) inside. The excellent feature of near-infrared (NIR) excitation and NIR emission of PbS/CdS QDs enables deep-tissue photoluminescence imaging, which was demonstrated ex vivo with tissue as thick as 14 mm. Meanwhile, owing to the presence of superparamagnetic Fe_3O_4 NPs, $mSiO_2$@PbS/CdS-Fe_3O_4 can be rapidly confined under an external magnetic field (MF), and exhibit a significantly high T_2 relaxivity in T_2-weighted magnetic resonance (MR) images in vivo. When $mSiO_2$@PbS/CdS-Fe_3O_4 was exposed to external physical stimuli of MF and/or NIR laser, they produced strong local heating through magnetothermal/photothermal effects. Owing to the unique mesoporous structure of $mSiO_2$@PbS/CdS-Fe_3O_4, doxorubicin (DOX) was readily loaded into them and the drug-release profile was subsequently evaluated under multistimuli (pH/MF/NIR). The release of DOX was significantly enhanced at lower pH, and higher temperatures caused by magnetothermal/photothermal effects. Our results pave the road toward developing a highly powerful nanoplatform for bimodal imaging (NIR deep-tissue photoluminescence and MR imaging), and simultaneously for integrating synergistic treatment capabilities of hyperthermia and pH/MF/NIR-responsive drug release.

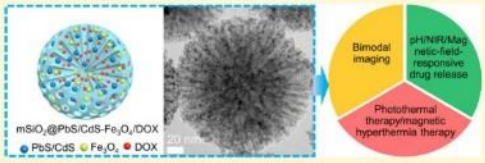

INTRODUCTION

Over the last few decades, various imaging techniques have been developed to study dynamic physiological changes in biological environments, especially for early cancer diagnosis. Magnetic resonance (MR) imaging, one of the most advanced imaging techniques, has become a staple in the clinic and is extensively applied for cancer diagnosis.[1] However, retrieving detailed subcellular information from MR imaging is difficult due to the limited spatial resolution and low contrast agent sensitivity.[2] Photoluminescence imaging, on the other hand, can potentially overcome these issues due to its high sensitivity at the subcellular level, which also has an additional advantage of relatively low cost of related imaging facilities. The combination of both, MR and photoluminescence imaging, into a single bimodal imaging platform is thus highly desired in the fight against cancer because it integrates acquisition of macroscopic and subcellular information, in turn increasing the reliability and accuracy of diagnosis. Motivated by the unprecedented efficacy of cancer diagnosis, studies that combine MR and photoluminescence imaging probes have been emerging gradually.[1,3−9] Nonetheless, among these previous studies, most of them focused on the use of visible-emitting organic dyes, upconverting nanoparticles (NPs) and quantum dots (QDs), which suffer from limited tissue penetration and whose signal can be also obscured by tissue autofluorescence in the visible range.[2−4,8−12] To solve this problem, an ideal photoluminescent component, with its absorption and emission wavelengths both located in the so-called biological windows with high optical transparency in the near-infrared (NIR) range (NIR-I: 700−950 nm; NIR-II:

Received: January 4, 2019
Revised: April 22, 2019
Published: April 24, 2019

DOI: 10.1021/acs.chemmater.9b00028
Chem. Mater. 2019, 31, 3201−3210

Scheme 1. Schematic of Fe_3O_4- and PbS/CdS-Loaded Large-Pore $mSiO_2$ ($mSiO_2$@PbS/CdS-Fe_3O_4) Nanospheres for Application in Bimodal (NIR Photoluminescence and MR) Imaging, PTT/MHT, and Simultaneous pH/NIR/MF Multiresponsive Drug Release

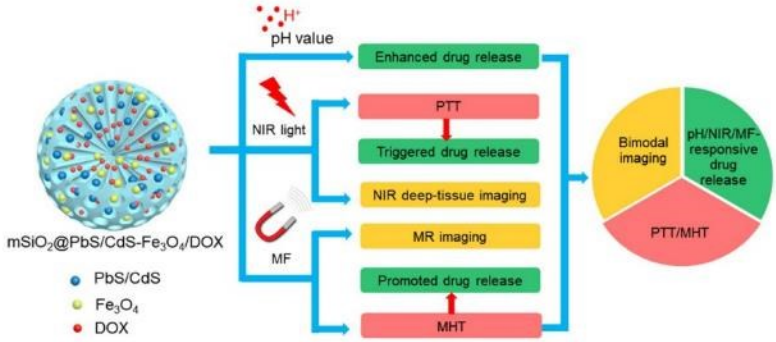

1000−1350 nm), should be specifically developed.[13,14] With the introduction of NIR-operable emitters, the bimodal imaging probe can efficiently circumvent absorption and scattering of both incident and emitted photons by endogenous tissue constituents, thus achieving deep-tissue penetrated photoluminescence imaging with a high signal-to-noise ratio.[15] Therefore, it is highly desirable to engineer new multifunctional (superparamagnetic and photoluminescent) NPs with integrated MR and NIR optical imaging for in vivo deep-tissue bimodal diagnostics.

Once the early diagnosis of cancer has been established, the survival rate for cancer can be largely increased if appropriate therapeutic strategies are timely implemented. Designing external stimulus-responsive nanoplatforms for remotely controlled cancer treatment has aroused widespread interest, as a means to potentially avoid drug overdose and reduce side effects.[16] To date, a variety of external physical stimuli, such as light, pH, temperature, and magnetic field (MF), have been used to trigger/control functional NPs-based cancer therapy.[17−20] Among these, magnetic hyperthermia therapy (MHT) using superparamagnetic NPs has been translated into the commercial clinical setting for the treatment of cancers.[21] Meanwhile, the NIR light-stimulated photothermal therapy (PTT) has become one of the research focuses rapidly approaching the clinical setting, owing to its easy operation, noninvasiveness, high specificity, and reasonable penetration.[19] Besides using heat to directly kill the cancer cells in both MHT and PTT, the thermal effect can be used to trigger the release of therapeutic drugs highly locally at specific tumor sites, thus providing a synergistically improved therapeutic efficiency compared to a single mode of MHT/PTT. A number of studies based on gold NPs, carbon nanotubes, graphene oxide, and iron oxide hybrid NPs for MHT/PTT and multiresponsive drug release have been reported.[21−24] Nonetheless, there are few research studies integrating bimodal imaging (not to mention NIR imaging), MHT/PTT, and multiresponsive drug release into one nanoplatform, which can result in a largely enhanced theranostic potential allowing for the simultaneous diagnosis and treatment of the disease.[25]

Mesoporous silica ($mSiO_2$) NPs are extensively investigated in the application of drug delivery as an alternative to traditional organic emulsions/liposomes because they generally possess a rigid mesostructured framework, high stability against various temperatures, and ease of surface modification for linking drug molecules.[16,26,27] Unfortunately, $mSiO_2$ NPs prepared by employing cetyltrimethylammonium bromide or other alkylammonium surfactants as a template usually show small pore size (<2 nm), which greatly hinders their use for encapsulation of macromolecular drugs (>2 nm) and functional NPs (iron oxide, gold, QDs, etc.).[28] Therefore, it is of paramount importance to fabricate uniform $mSiO_2$ with large pore size (>5 nm) for in vivo biomedical applications. Very recently, Zhao and co-workers have reported a novel type of three-dimensional dendritic biodegradable $mSiO_2$ nanospheres using a biphase stratification approach.[27] The average pore size of $mSiO_2$ nanospheres could be adjusted to 13 nm by adopting appropriate experimental reaction parameters. Owing to their unique large pores, these $mSiO_2$ nanospheres acted as effective nanocarriers, exhibiting high protein (bovine β-lactoglobulin)-loading capacity.

Inspired by the previously published work of Zhao and co-workers,[27] herein, we successfully realized a multifunctional nanoplatform based on the deliberately modified large-pore $mSiO_2$ for bimodal imaging, PTT/MHT, and pH/MF/NIR-responsive drug release, as illustrated in Scheme 1. Specifically, Fe_3O_4 NPs of suitable size and PbS/CdS QDs with desired NIR photoluminescence were loaded into the thiol-modified large-pore $mSiO_2$ to form a multifunctional photoluminescent and superparamagnetic nanoplatform ($mSiO_2$@PbS/CdS-Fe_3O_4). Doxorubicin (DOX), a widely used clinical anticancer drug, was used as a model to study their multiresponsive drug-release behavior.[29] The $mSiO_2$@PbS/CdS-Fe_3O_4 as a nanocarrier/host with high loading capacity allows to integrate the unique properties of each component in a single nanoarchitecture. When this nanoplatform was exposed to an acidic tumor microenvironment, pH-responsive drug release was promoted. Under irradiation of NIR light, the PbS/CdS QDs incorporated into the $mSiO_2$@PbS/CdS-Fe_3O_4 not only generated NIR photoluminescence for deep-tissue bioimaging but also converted NIR light to heat for PTT and further triggered or accelerated drug release. Meanwhile, $mSiO_2$@PbS/CdS-Fe_3O_4 consisting of a large number of superparamagnetic Fe_3O_4 NPs were expected to serve as potential MR imaging probes, MHT agents, and effective vehicles for targeted delivery of drugs to cancer sites and to realize promoted MF-responsive drug release.

DOI: 10.1021/acs.chemmater.9b00028
Chem. Mater. 2019, 31, 3201−3210

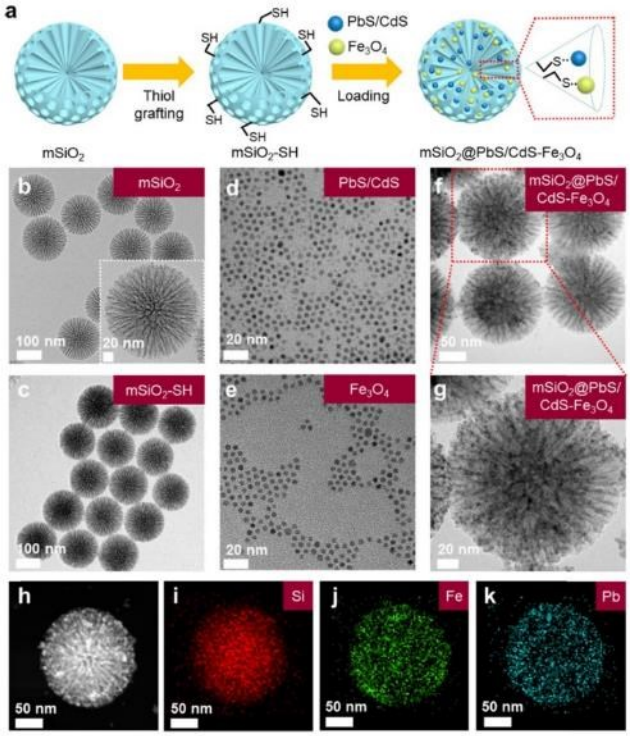

Figure 1. (a) Schematic of the synthetic procedure for $mSiO_2$@PbS/CdS-Fe_3O_4. (b) Transmission electron microscopy (TEM) image of $mSiO_2$. The inset shows the corresponding TEM image of $mSiO_2$ at a higher magnification. (c) TEM images of thiol-modified $mSiO_2$ (denoted as $mSiO_2$-SH herein), (d) PbS/CdS QDs, and (e) Fe_3O_4 NPs. (f, g) TEM images of $mSiO_2$@PbS/CdS-Fe_3O_4 at different magnifications. (h) High-angle annular dark-field scanning transmission electron microscopy (HAADF-STEM) image and (i–k) energy-dispersive X-ray (EDX) elemental mapping images of an individual $mSiO_2$@PbS/CdS-Fe_3O_4.

To the best of our knowledge, this is the first report to simultaneously combine bimodal imaging (NIR deep-tissue photoluminescence and MR imaging), PTT/MHT, and pH/MF/NIR-responsive drug release in one system. This system exhibits three remarkable advantages: (1) multimodal imaging featuring combined preferred NIR deep-tissue photoluminescence and MR imaging; (2) synergistic and highly localized hyperthermia and multiresponsive drug release; and (3) remotely controlled drug release due to the MF/NIR-responsive character. It is expected that such a nanoplatform can be simultaneously used for high efficacy imaging, diagnostics, and therapeutics. The thiol modification, the relatively large pore size, and the rational synthesis of loaded NPs with appropriate sizes are all critical in achieving this complex, highly functional nanostructure.

■ RESULTS AND DISCUSSION

The synthetic strategy for $mSiO_2$@PbS/CdS-Fe_3O_4 is outlined in Figure 1a, which involves the functionalization of large-pore $mSiO_2$ first with thiol groups using (3-mercaptopropyl)-trimethoxysilane as a coupling agent and subsequent immobilization of Fe_3O_4 NPs and PbS/CdS QDs into thiol-modified nanocarriers ($mSiO_2$). The large-pore $mSiO_2$ was synthesized by a biphase stratification continuous growth approach, i.e., a heterogeneous oil-water biphase stratification reaction system containing tetraethyl orthosilicate in hydrophobic organic solvent of the upper oil phase as well as cationic cetyltrimethylammonium chloride as the template and triethanolamine as the catalyst in the lower aqueous phase.[27] The mesopore size of the nanospheres highly depends on the swelling behavior of the hydrophobic organic solvent in oil-water biphase stratification system. According to the previously published work, $mSiO_2$ with the largest mesopore size of ~13 nm could be obtained when 5% v/v tetraethyl orthosilicate-in-cyclohexane solution was selected as the upper oil phase due to its more effective swelling behavior compared to other organic solvents.[27] Here, since $mSiO_2$ was used as a host for Fe_3O_4 NPs and PbS/CdS QDs, relatively large pore sizes (>10 nm) are in principle preferred for loading more Fe_3O_4 NPs and PbS/CdS QDs. We thus took the same strategy to prepare the $mSiO_2$ with mesopore size >10 nm, as shown in Figure 1b. The resultant large-pore $mSiO_2$ is highly uniform and has a three-dimensional dendritic mesoporous structure with an average size of ca. 170 nm (Figure S1c). Their center-radial mesopore channels can be clearly observed in the inset of Figure 1b. To evaluate the surface area and pore size distribution of $mSiO_2$,

DOI: 10.1021/acs.chemmater.9b00028
Chem. Mater. 2019, 31, 3201−3210

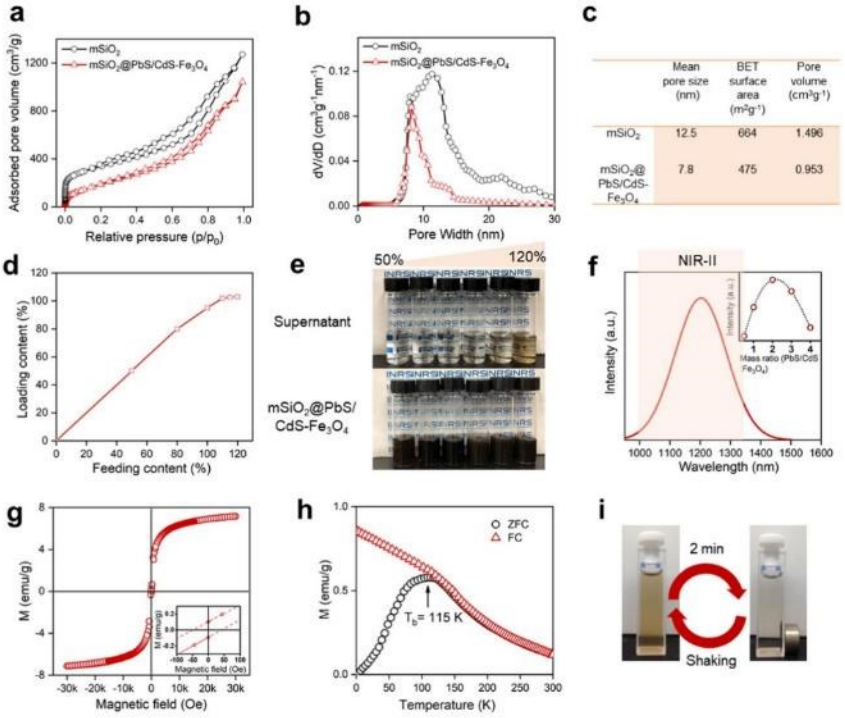

Figure 2. (a) Nitrogen adsorption−desorption isotherms and (b) pore size distribution of $mSiO_2$ and $mSiO_2$@PbS/CdS-Fe_3O_4. (c) Textural properties of $mSiO_2$ and $mSiO_2$@PbS/CdS-Fe_3O_4. (d) Relationship between the measured loading level and feeding content of Fe_3O_4 NPs and PbS/CdS QDs. (e) Photographs of the supernatant (top) and redispersed $mSiO_2$@PbS/CdS-Fe_3O_4 (bottom) after loading Fe_3O_4 NPs and PbS/CdS QDs into thiol-modified $mSiO_2$ with feeding content varied from 50 to 120%. (f) Photoluminescence spectrum of $mSiO_2$@PbS/CdS-Fe_3O_4 in the NIR-II window. The inset shows the corresponding integrated NIR photoluminescence intensity as a function of mass ratio of PbS/CdS QDs to Fe_3O_4 NPs. (g) Field-dependent magnetization of $mSiO_2$@PbS/CdS-Fe_3O_4 at 300 K. The inset shows the enlarged view of field-dependent magnetization curve under low magnetic fields. (h) Temperature-dependent zero-field-cooled (ZFC) and field-cooled (FC) magnetization curves at 100 Oe for $mSiO_2$@PbS/CdS-Fe_3O_4. (i) Photographs of an aqueous dispersion of $mSiO_2$@PbS/CdS-Fe_3O_4 in a cuvette (left) before and (right) after applying a magnet for 2 min. $mSiO_2$@PbS/CdS-Fe_3O_4 can be well redispersed in aqueous solution again after shaking. Logo in (e): used with permission from INRS.

nitrogen adsorption−desorption isotherms (Figure 2a) were acquired by measuring Brunauer−Emmett−Teller (BET) surface adsorption. The isotherms of large-pore $mSiO_2$ can be classified as the type IV isotherm with H4 hysteresis loop, which demonstrates the typical ordered mesoporous structure with a narrow pore size distribution.[30] The BET surface area of $mSiO_2$ was measured to be ~664 m^2/g and the total pore volume ~1.496 cm^3/g (Figure 2c). The derived pore size distribution of the $mSiO_2$ is shown in Figure 2b, from which the mean pore size was estimated to be ~12.5 nm (Figure 2c). It is anticipated that the large pore volume and size of the $mSiO_2$ can provide sufficient space for embedding both Fe_3O_4 NPs and PbS/CdS QDs. The large-pore $mSiO_2$ was subsequently grafted with thiol groups using (3-mercaptopropyl)trimethoxysilane for anchoring Fe_3O_4 NPs and PbS/CdS QDs.[31] The thiol-modified $mSiO_2$ retains the same morphology of $mSiO_2$ (Figure 1c), while the C−H and S−H stretching modes at 2940 and 2560 cm^{-1} in the Fourier transform infrared (FTIR) spectrum (Figure S2) confirm the successful thiol modification of $mSiO_2$.[31]

To easily and efficiently embed Fe_3O_4 NPs and PbS/CdS QDs into the mesoporous channels of the $mSiO_2$, the size of Fe_3O_4 NPs and PbS/CdS QDs should be small enough for loading. Otherwise, these NPs may only be anchored onto the surface of the $mSiO_2$ instead of inside the mesoporous channels and the loading level will be largely restricted. Since PbS/CdS QDs can be synthesized such as to operate in the NIR-II (including both excitation and emission), which is well suited for high-contrast deep-tissue imaging,[32] they have been chosen as the photoluminescent component. Generally, PbS QDs synthesized from the most commonly used sulfur-oleylamine injection method (also used herein) possess sizes in the range of 4.2−6.4 nm.[33−35] After the cation-exchange process, the resultant PbS/CdS QDs maintain a similar size to the initial PbS QDs.[36,37] Their TEM image (Figure 1d) and size distribution histogram (Figure S1a) indicate that the prepared PbS/CdS QDs are 4.3 ± 0.6 nm in diameter and are suitable for loading into the mesopore channels of thiol-modified $mSiO_2$. The emission peak of PbS/CdS QDs is located at 1200 nm in the NIR-II window (Figure S3).

DOI: 10.1021/acs.chemmater.9b00028
Chem. Mater. 2019, 31, 3201−3210

Regarding Fe_3O_4 NPs, high-quality, uniform ones synthesized by the typical thermal decomposition method in 1-octadecene (ODE, boiling point: 320 °C) are usually larger than 10 nm in diameter, which hinders their loading into $mSiO_2$. To circumvent this issue, herein, we have synthesized ultrasmall Fe_3O_4 NPs by a slightly modified thermal decomposition method, in which a mixture of 1-tetradecene/ODE, instead of pure ODE, was employed to lower the boiling point of the solvent (290 °C).[38] The diameter of resulting Fe_3O_4 NPs decreases to ca. 5 nm, which is much smaller than that of Fe_3O_4 NPs synthesized in pure ODE.[38] From their TEM image (Figure 1e) and size distribution histogram (Figure S1b), it can be seen that the ultrasmall Fe_3O_4 NPs have uniform morphology, a narrow size distribution (4.9 ± 0.5 nm), and good dispersity (i.e., no agglomeration), all pertinent for efficient loading inside the thiol-modified $mSiO_2$.

The loading procedure was performed by mixing Fe_3O_4 NPs, PbS/CdS QDs, and the thiol-modified $mSiO_2$ particles in chloroform. The strong coordination between the thiol groups and metal cations resulted in the efficient loading and immobilization of Fe_3O_4 NPs and PbS/CdS QDs inside the mesoporous channels of $mSiO_2$.[31,39] Corresponding TEM images (Figure 1f,g), high-angle annular dark-field scanning transmission electron microscopy (HAADF-STEM) image (Figure 1h), and energy-dispersive X-ray (EDX) elemental mapping images (Figure 1i–k) confirm the loading of Fe_3O_4 NPs and PbS/CdS QDs into thiol-modified $mSiO_2$, and the overall size of $mSiO_2$@PbS/CdS-Fe_3O_4 remains the same as that of the initial $mSiO_2$ (Figure S1d), suggesting that most of the particles are indeed uniformly situated inside the mesoporous channels, instead of residing on the external surface of thiol-modified $mSiO_2$, which is favorable for targeted biomedical applications herein. This conclusion was also supported by BET measurements, to be described in the text later. Meanwhile, the EDX spectra and X-ray diffraction (XRD) patterns (Figure S4a,b) verify that the $mSiO_2$@PbS/CdS-Fe_3O_4 consists of Fe_3O_4 NPs and PbS/CdS QDs. In addition, it should be mentioned that Fe_3O_4 NPs and PbS/CdS QDs cannot be immobilized inside the as-prepared $mSiO_2$ without any surface modification due to the lack of strong interactions between metal cations and SiO_2 (Figure S5). It underlines the critical role of thiol modification, applied herein, in the construction of the multifunctional nanoplatforms of our interest.

We further explored the loading capacity of the mesoporous channels of the $mSiO_2$ matrix. We mixed the Fe_3O_4 NPs and PbS/CdS QDs at a mass ratio of 1:1 and then added them into the thiol-modified $mSiO_2$-in-chloroform dispersion at varying quantities. The loading content (mass ratio of loaded Fe_3O_4 NPs and PbS/CdS QDs to thiol-modified $mSiO_2$ matrix), measured by inductively coupled plasma-optical emission spectrometry, reached 95% (Figure 2d), very close to the nominal feeding content of 100% (mass ratio of added Fe_3O_4 NPs and PbS/CdS QDs to thiol-modified $mSiO_2$). This excellent result was in line with our observation that the supernatant after centrifuging the mixed dispersion was nearly colorless, straightforwardly supporting that not many free, unloaded Fe_3O_4 NPs and PbS/CdS QDs remained in the dispersion (Figure 2e). With a highly porous structure, it is clear that the thiol-modified $mSiO_2$ exhibits a high loading capacity and widely tunable loading levels, which can be adjusted in the range of 0–103% (Figure 2d) by varying the feeding content from 0 to 120%.

It is known that Fe_3O_4 NPs have the photoluminescence quenching effect on QDs, namely, the photoluminescence of QDs decreases in the presence of Fe_3O_4 NPs in a mixed system.[40,41] The details of the photoluminescence quenching mechanism are beyond the scope of the present work. Herein, we fixed the concentration of Fe_3O_4 NPs and then gradually increased the loading concentration of PbS/CdS QDs for the purpose of obtaining the maximum photoluminescence of $mSiO_2$@PbS/CdS-Fe_3O_4 for NIR deep-tissue imaging. It can be observed from TEM images (Figure S6a–c) that significantly more PbS/CdS QDs can be found in the channels of $mSiO_2$@PbS/CdS-Fe_3O_4 with the increased loading of PbS/CdS QDs. The NIR photoluminescence spectrum of $mSiO_2$@PbS/CdS-Fe_3O_4 shows a peak centered at around 1200 nm in the NIR-II window (Figure 2f), which is almost the same as that of the initial PbS/CdS QDs (Figure S3). The NIR photoluminescence intensity of $mSiO_2$@PbS/CdS-Fe_3O_4 first increases with the mass ratio and then decreases mainly due to the self-quenching effect of PbS/CdS QDs at higher concentrations, with the maximum intensity achieved at the mass ratio of 2:1 (Figure 2f). We thus fixed the mass ratio of PbS/CdS QDs to Fe_3O_4 NPs at 2:1 as an optimal value for NIR deep-tissue imaging and used it for the subsequent investigations of this work. After loading with PbS/CdS QDs and Fe_3O_4 NPs, the nitrogen adsorption–desorption isotherms shrink (Figure 2a), which can be easily understood since the mesopores of $mSiO_2$ are now occupied by PbS/CdS QDs and Fe_3O_4 NPs. Similarly, the average pore size becomes smaller and the pore size distribution becomes narrower (Figure 2b), as expected. The average pore size, BET surface area, and pore volume of $mSiO_2$@PbS/CdS-Fe_3O_4 were measured to be ~7.8 nm, ~475 m^2/g, and ~0.953 cm^3/g (Figure 2c), respectively. Although they are all smaller than those of pure $mSiO_2$, as expected, $mSiO_2$@PbS/CdS-Fe_3O_4 still has sufficient space for loading drug molecules because of their unique three-dimensional dendritic mesoporous structure.

Since the ultrasmall Fe_3O_4 NPs are embedded into the mesopores of $mSiO_2$, the $mSiO_2$@PbS/CdS-Fe_3O_4 possesses interesting superparamagnetic properties. The magnetic characterization was performed using a vibrating sample magnetometer. The field-dependent magnetization plot with negligible remanence and coercivity shown in Figure 2g illustrates that $mSiO_2$@PbS/CdS-Fe_3O_4 is superparamagnetic with a saturation magnetization (M_s) of ~7.1 emu/g at 300 K. This value is lower than those reported for plain Fe_3O_4 NPs in the literature because the presence of nonmagnetic components of thiol-modified $mSiO_2$ and PbS/CdS QDs inside $mSiO_2$@PbS/CdS-Fe_3O_4 reduces the "magnetically effective" weight, and thus decreases the value of Ms per gram of $mSiO_2$@PbS/CdS-Fe_3O_4. The temperature-dependent zero-field-cooled (ZFC) and field-cooled (FC) magnetization curves of $mSiO_2$@PbS/CdS-Fe_3O_4 (Figure 2h) were measured under a magnetic field of 100 Oe between 5 and 300 K. The ZFC and FC curves coincide at high temperatures but diverge at low temperatures due to progressive blocking of particles as the temperature decreases, which is consistent with the characteristic superparamagnetic behavior.[42,43] The blocking temperature (T_b) was estimated to be ~115 K, lower than room temperature, suggesting the superparamagnetic behavior of $mSiO_2$@PbS/CdS-Fe_3O_4 at room temperature and further ensuring its easy manipulation by an external MF at room temperature. As a consequence, the complex $mSiO_2$@PbS/CdS-Fe_3O_4 particles well dispersed in an aqueous solution

DOI: 10.1021/acs.chemmater.9b00028
Chem. Mater. 2019, 31, 3201–3210

(Figure 2i, left) can be rapidly confined toward a magnet in 2 min after it is applied (Figure 2i, right). Slight shaking of the cuvette will redisperse the $mSiO_2$@PbS/CdS-Fe_3O_4 back into the original solution after removing the magnet. The easy confinement and redispersion of the $mSiO_2$@PbS/CdS-Fe_3O_4 is reversible and can be repeated many times. Unlike classic ferromagnetic NPs that will form nonseparable agglomerates after initial magnetic confinement, the superparamagnetic, redispersible behavior of these $mSiO_2$@PbS/CdS-Fe_3O_4 particles is undoubtedly very important for magnetically driven biomedical applications, such as bioseparation and site-specific targeting.[44]

As mentioned above, $mSiO_2$@PbS/CdS-Fe_3O_4 exhibits strong photoluminescence in the NIR-II window, which is a merit for deep-tissue bioimaging. To demonstrate the use of $mSiO_2$@PbS/CdS-Fe_3O_4 particles as a bioprobe for deep-tissue imaging, we designed an ex vivo setup to examine their NIR photoluminescence penetration capability (Figure 3a).

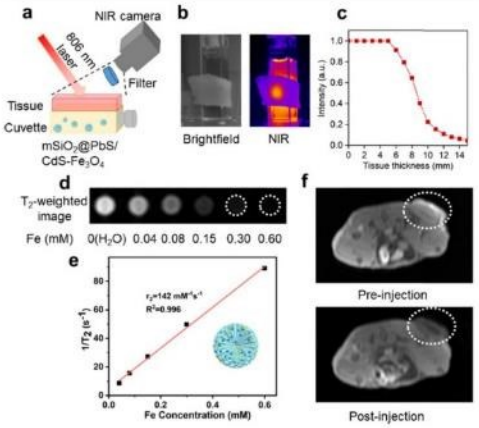

Figure 3. (a) Scheme of the experimental setup for the deep-tissue NIR photoluminescence imaging of $mSiO_2$@PbS/CdS-Fe_3O_4. (b) The corresponding bright-field and NIR photoluminescence images of $mSiO_2$@PbS/CdS-Fe_3O_4 in the cuvette covered with tissue. The bright-field image was acquired under indoor light without any filters in the optical path. The NIR photoluminescence image was recorded upon excitation with an 806 nm laser, along with an 830 nm long-pass filter. (c) Normalized photoluminescence intensity of the $mSiO_2$@PbS/CdS-Fe_3O_4 measured from the NIR images as a function of tissue thickness. (d) T_2-weighted MR images of $mSiO_2$@PbS/CdS-Fe_3O_4 with various Fe concentrations. (e) Relaxation rate r_2 ($1/T_2$) vs different molar Fe concentrations of $mSiO_2$@PbS/CdS-Fe_3O_4. (f) In vivo T_2-weighted transversal cross-sectional MR imaging of nude mouse bearing a tumor acquired at pre-injection and 30 min intratumoral post-injection of $mSiO_2$@PbS/CdS-Fe_3O_4 at 1.5 mg/kg. The position of the tumor was marked by white dashed circles.

Briefly, an 806 nm laser with power density of 10 W/cm^2 was used to excite the $mSiO_2$@PbS/CdS-Fe_3O_4 aqueous dispersion in a cuvette through a piece of pork tissue, while the NIR camera equipped with an 830 nm optical long-pass filter was fixed above the tissue to collect the emitted NIR signal. The use of the 806 nm laser as an excitation source not only provides enhanced penetration depth, compared to excitation wavelengths around 1000 nm, but also reduces the thermal load in the area of interest and thus minimizes potential damage to healthy biological tissues.[13,45] Figure 3b shows the bright-field and NIR photoluminescence images of $mSiO_2$@PbS/CdS-Fe_3O_4 in the cuvette covered with the pork tissue. Intense NIR photoluminescence can be seen in the center of pork tissue, which is larger than the size of the excitation beam due to the scattering of both the excitation and emitted lights as they pass through the tissue. By changing the thickness of the pork tissue, we can evaluate the NIR photoluminescence penetration depth from the normalized photoluminescence intensity of the $mSiO_2$@PbS/CdS-Fe_3O_4 in the aqueous solution, as illustrated in Figure 3c. The intensity of the photoluminescence signal saturates the detector of the NIR camera when the thickness of the pork tissue is $\lesssim$5 mm. After that, with increasing thickness of the pork tissue (>5 mm), the signal gradually diminishes. With this setup, a maximum penetration depth of approximately 14 mm was obtained using $mSiO_2$@PbS/CdS-Fe_3O_4.

Prior to performing in vivo MR imaging studies, we assessed the biocompatibility of $mSiO_2$@PbS/CdS-Fe_3O_4 in vitro using HeLa cancer cells and human embryonic kidney (HEK 293T) cells. As shown in Figure S7, after being incubated with $mSiO_2$@PbS/CdS-Fe_3O_4 for 24 h, both HeLa and HEK 293T cells retained more than 70% viability even at the high particle concentration up to 250 μg/mL. Inspired by their excellent superparamagnetic properties, we next examined their use as T_2 contrast agents for MR imaging. The in vitro T_2-weighted MR images of $mSiO_2$@PbS/CdS-Fe_3O_4 with various Fe concentrations are shown in Figure 3d, which clearly demonstrates the characteristic concentration-dependent negative enhancement effect on T_2 MR imaging. That is, the images of $mSiO_2$@PbS/CdS-Fe_3O_4 dispersions are gradually getting darker with increasing Fe concentration in dispersions, whereas the particle-free sample remains bright. The T_2 relaxivity coefficient (r_2) of $mSiO_2$@PbS/CdS-Fe_3O_4 could be calculated from the fitting curve of T_2 versus Fe concentration (Figure 3e), and was determined to be approximately 142 mM^{-1} s^{-1}, which is almost twice that of Ferumoxsil (r_2 = 72 mM^{-1} s^{-1}, one of the clinically approved Fe-based MR imaging contrast agents).[46] The short distance between Fe_3O_4 NPs located in the mesoporous channel of the $mSiO_2$ might permit magnetic coupling between the magnetic NPs, resulting in a synergistic increase in r_2.[47] This value is not only higher than that (61 mM^{-1} s^{-1}) of our previously reported single-core Fe_3O_4@SiO_2@$NaYF_4$:Nd^{3+} nanoplatform, but also comparable to those of multi-magnetic-core NPs for MR imaging reported in the literature.[7,48−50] Considering the excellent in vitro MR imaging capability of $mSiO_2$@PbS/CdS-Fe_3O_4 particles, we further explored their potential as a negative contrast agent for in vivo MR imaging. A mouse bearing a tumor was imaged by a 3.0 T clinical MR scanner at pre-injection and 30 min after intratumoral injection of $mSiO_2$@PbS/CdS-Fe_3O_4 (200 μL, 2 mg/mL, dose = 1.5 mg/kg), as shown in Figure 3f. The tumor area of the mouse appears bright before the injection of $mSiO_2$@PbS/CdS-Fe_3O_4, while a remarkable darkening effect in the tumor site can be observed at 30 min post-injection (white dashed circles in Figure 3f). This significant T_2 negative effect makes $mSiO_2$@PbS/CdS-Fe_3O_4 ideal as a highly efficient T_2 contrast agent for MR imaging. Combined with excellent deep-tissue NIR photoluminescence penetration capacity, these experimental results reveal that $mSiO_2$@PbS/CdS-Fe_3O_4 can serve

DOI: 10.1021/acs.chemmater.9b00028
Chem. Mater. 2019, 31, 3201−3210

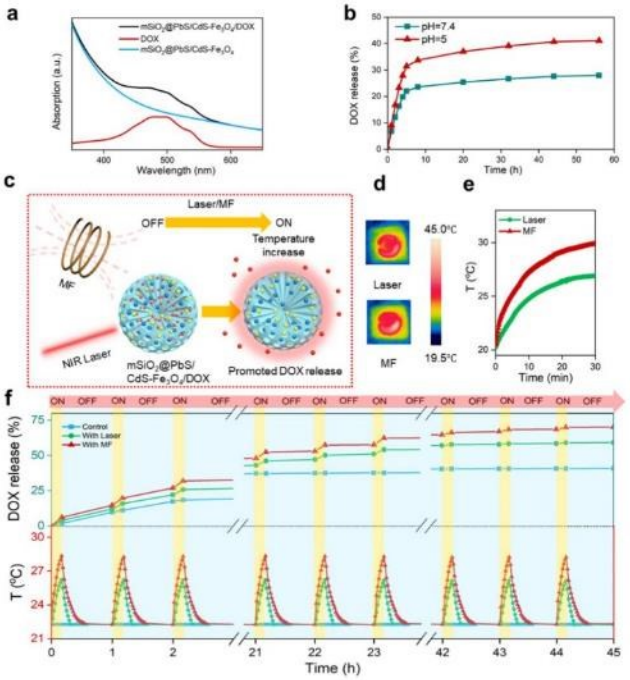

Figure 4. (a) Absorption spectra of free DOX, $mSiO_2$@PbS/CdS-Fe_3O_4, and DOX-loaded $mSiO_2$@PbS/CdS-Fe_3O_4 ($mSiO_2$@PbS/CdS-Fe_3O_4/DOX). (b) DOX release profile of $mSiO_2$@PbS/CdS-Fe_3O_4/DOX at pH = 7.4 and 5. (c) Schematic illustration of PTT/MHT and heat-induced DOX release in response to the external laser and MF. (d) Thermal images of $mSiO_2$@PbS/CdS-Fe_3O_4 solution after 30 min of two types of modulation (laser at 1.3 W/cm^2, MF at 5 kA/m). (e) Corresponding time-dependent temperature curves of $mSiO_2$@PbS/CdS-Fe_3O_4 (0.4 mg in a total volume of 2 mL) solution. (f) DOX release profiles of $mSiO_2$@PbS/CdS-Fe_3O_4/DOX dispersion (0.2 mg/mL, 2 mL) stimulated by laser/MF (top) and the time evolution of the corresponding temperature of the solution (bottom); the $mSiO_2$@PbS/CdS-Fe_3O_4/DOX dispersion under no stimulation, i.e., without the use of the laser or MF, is shown as a control. The laser and MF were switched between "ON" and "OFF" modes.

as a promising and powerful bimodal (photoluminescence and MR) imaging probe in vivo.

To investigate their potential as drug-delivery carriers, DOX was selected as a model drug to load into $mSiO_2$@PbS/CdS-Fe_3O_4. There are not any obvious peaks in the absorption spectrum of $mSiO_2$@PbS/CdS-Fe_3O_4 before drug loading, while an absorption peak located at ~480 nm can be clearly found after DOX loading, which is the characteristic absorption peak of DOX (Figure 4a). Hence, the loading efficiency of DOX can be calculated by monitoring the absorption intensity at 480 nm (the details of calibration of DOX loading are shown in Figure S8). In our case, the loading efficiency of DOX for $mSiO_2$@PbS/CdS-Fe_3O_4 was calculated to be about 36.4%, lower than that (71%) of plain $mSiO_2$, which is due to the fact that the integrated Fe_3O_4 NPs and PbS/CdS QDs occupy considerable space in the mesoporous channels of the $mSiO_2$ (as supported by BET measurements) and block the DOX molecules from easily accessing the mesopores. It has been known that the extracellular pH value of normal cells is close to neutral, but the presence of cancer cells increases the acidity of their microenvironments due to the excess metabolic products in the rapid proliferation of cancer cells.[51,52] The different pH values between normal tissues and cancer cellular environment may provide an additional safe and efficient physiological stimulus for pH-responsive and target-specific drug delivery. In this way, the drug release can be inhibited during systemic circulation of drug carriers at a physiological pH value of 7.4, while it is enhanced in the acidic environment at tumor sites. Thus, pH-sensitive nanoplatform, like $mSiO_2$@PbS/CdS-Fe_3O_4/DOX, is appealing and highly desirable to reduce overdose-induced side effects of traditional nonspecific chemotherapy. Considering this factor, we studied the DOX release behavior from $mSiO_2$@PbS/CdS-Fe_3O_4/DOX in phosphate-buffered saline (PBS) at two different pH values (pH = 7.4 and 5), as illustrated in Figure 4b. Both profiles show fast release of DOX in the first 4 h, followed by a slow release over 8 h. These different release rates can be reasonably explained by the different loading locations of DOX inside $mSiO_2$@PbS/CdS-Fe_3O_4. To be more specific, the DOX molecules situated in the outer mesoporous channels or on the external silica surface are easily released at the beginning, while the DOX molecules loaded into the inner channels require longer time to diffuse from inside to outside. This behavior is beneficial for targeted drug release since the initially fast release can efficiently inhibit the growth of cancer cells and then the slow release of the rest of drugs can further curb the surviving cancer cells.[53] In addition, the DOX release profile of $mSiO_2$@PbS/CdS-Fe_3O_4/

DOI: 10.1021/acs.chemmater.9b00028
Chem. Mater. 2019, 31, 3201−3210

DOX shows pH-dependent behavior: the DOX release reaches 41% after 56 h at pH = 5, while it only increases to 28% at pH = 7.4. The higher drug release can be ascribed to the enhanced hydrophilicity and higher solubility of DOX by increased protonation of NH_2 groups of DOX at lower pH values. This clear pH-sensitive drug release behavior is advantageous for localized cancer chemotherapy.

We then further studied the PTT and MHT of $mSiO_2$@PbS/CdS-Fe_3O_4 under external stimuli of the NIR laser and MF, respectively, and their effect on the DOX release behavior (Figure 4c). The thermal images of $mSiO_2$@PbS/CdS-Fe_3O_4 dispersion (0.2 mg/mL) after 30 min of two types of modulation (laser at 1.3 W/cm^2, MF at 5 kA/m) and time-dependent temperature curves of $mSiO_2$@PbS/CdS-Fe_3O_4 solution are shown in Figure 4d,e, respectively. The temperature of $mSiO_2$@PbS/CdS-Fe_3O_4 dispersion after 30 min heating by the NIR laser and MF increases by 6.7 and 9.5 °C, respectively, while the PBS solution alone shows negligible temperature increase under the same modulation (Figure S9). This result clearly confirms that the temperature increase is attributed to the response of $mSiO_2$@PbS/CdS-Fe_3O_4 to the external laser/MF and suggests their high potential as PTT/MHT agents. Subsequently, the MF/NIR-responsive drug release of DOX from the $mSiO_2$@PbS/CdS-Fe_3O_4/DOX particles was examined (Figure 4f). The dispersion was stimulated with the MF or NIR laser (ON) for 10 min, followed by a 50 min interval with MF/NIR being switched OFF. The "ON/OFF" cycles were performed in a 45 h period, and the time evolution of the temperature of the dispersion was recorded at the same time. Meanwhile, an $mSiO_2$@PbS/CdS-Fe_3O_4/DOX dispersion without being stimulated by the laser/MF was shown as a control. The release of DOX is increased when the NIR/MF is ON. When the NIR/MF is switched OFF, the drug-release rate returns back to the regular value, similar to that of the control. The temperature curves under the ON/OFF mode show the similar trend to the drug-release profile, which means that the surge of DOX release is ascribed to the local heating effect produced by the external stimuli of NIR/MF (Figure 4c). The total release amount of DOX reached 59 and 70% after 45 h under NIR/MF, respectively, compared to 40% in the control experiment. Given their excellent magnetothermal and photothermal conversion effect of $mSiO_2$@PbS/CdS-Fe_3O_4, this nanoplatform should be an ideal candidate for PTT/MHT and a new efficient drug carrier for MF/NIR-responsive drug release.

■ CONCLUSIONS

In summary, we have successfully prepared a multifunctional nanoplatform ($mSiO_2$@PbS/CdS-Fe_3O_4), which integrated NIR photoluminescent PbS/CdS QDs and superparamagnetic Fe_3O_4 NPs into a large-pore silica matrix enabled by simple thiol modification. The $mSiO_2$@PbS/CdS-Fe_3O_4 exhibited excellent photoluminescence in the NIR-II window, enabling its use for deep-tissue imaging, as well as excellent superparamagnetic properties that make it easily confined by an external MF and ideal as a highly efficient T_2 contrast agent for MR imaging in vivo. In particular, it showed an extremely high r_2 value due to the synergistic magnetic coupling effect induced by close distance of Fe_3O_4 NPs embedded in the mesoporous channel. This nanoplatform also demonstrated a great potential as a drug-delivery carrier for cancer therapy. After being loaded with DOX, in addition to showing pH-responsive drug-release behavior, $mSiO_2$@PbS/CdS-Fe_3O_4 can produce local heat via the magnetothermal effect, thanks to the presence of superparamagnetic NPs, and accelerate the drug release. Furthermore, benefitting from the presence of the NIR-absorbing QDs, $mSiO_2$@PbS/CdS-Fe_3O_4 can not only serve as a highly efficient PTT agent but also increase the drug-release rate under NIR irradiation. This nanoplatform thus yields a synergistic effect from the integrated heating mode and multiresponsive drug release to achieve a high therapeutic efficacy. Such specifically designed multifunctional nanoplatform combining bimodal imaging (NIR deep-tissue photoluminescence and MR imaging), PTT/MHT, and pH/MF/NIR-responsive drug release has a great potential for cancer imaging diagnostics and therapeutics.

■ ASSOCIATED CONTENT

Supporting Information

The Supporting Information is available free of charge on the ACS Publications website at DOI: 10.1021/acs.chemmater.9b00028.

Experimental section; size distribution of PbS/CdS QDs, Fe_3O_4 NPs, $mSiO_2$, and $mSiO_2$@PbS/CdS-Fe_3O_4; FTIR spectra of $mSiO_2$ and $mSiO_2$-SH; photoluminescence spectrum of PbS/CdS QDs; EDX spectra and XRD patterns of $mSiO_2$ and $mSiO_2$@PbS/CdS-Fe_3O_4; TEM images of pure $mSiO_2$ loaded with Fe_3O_4 NPs and PbS/CdS QDs; TEM images of $mSiO_2$@PbS/CdS-Fe_3O_4 with various loading ratios of PbS/CdS QDs and Fe_3O_4 NPs; cytotoxicity study of $mSiO_2$@PbS/CdS-Fe_3O_4; DOX calibration; and temperature curves of PBS solution under laser/MF (PDF)

■ AUTHOR INFORMATION

Corresponding Authors

*E-mail: vetrone@emt.inrs.ca (F.V.).
*E-mail: ma@emt.inrs.ca (D.M.).

ORCID

Fan Yang: 0000-0001-6306-4501
Artiom Skripka: 0000-0003-4060-4290
Jung Kwon Oh: 0000-0002-4220-308X
Xinyu Liu: 0000-0001-5705-9765
Fiorenzo Vetrone: 0000-0002-3222-3052
Dongling Ma: 0000-0001-8558-3150

Notes

The authors declare no competing financial interest.

■ ACKNOWLEDGMENTS

D.M. and F.V. are grateful to the Natural Sciences and Engineering Research Council of Canada (NSERC: RGPIN-2015-06756) and the Fonds de Recherche du Québec—Nature et technologies (FRQNT: 2014-PR-174462) for funding. F.Y., F.R., and A.S. greatly appreciate the financial support from the Merit Scholarship Program for Foreign Students from the Ministère de l'Éducation, du Loisir et du Sport du Québec (Nos. 193353, 255072, and 257149).

■ REFERENCES

(1) Liu, C.; Gao, Z.; Zeng, J.; Hou, Y.; Fang, F.; Li, Y.; Qiao, R.; Shen, L.; Lei, H.; Yang, W.; Gao, M. Magnetic/Upconversion Fluorescent $NaGdF_4$:Yb,Er Nanoparticle-Based Dual-Modal Molecular Probes for Imaging Tiny Tumors *In Vivo*. *ACS Nano* **2013**, *7*, 7227−7240.

DOI: 10.1021/acs.chemmater.9b00028
Chem. Mater. 2019, 31, 3201−3210

(2) Lee, J.; Jun, Y.; Yeon, S.; Shin, J.; Cheon, J. Dual-Mode Nanoparticle Probes for High-Performance Magnetic Resonance and Fluorescence Imaging of Neuroblastoma. *Angew. Chem., Int. Ed.* **2006**, *45*, 8160−8162.
(3) Chen, O.; Riedemann, L.; Etoc, F.; Herrmann, H.; Coppey, M.; Barch, M.; Farrar, C. T.; Zhao, J.; Bruns, O. T.; Wei, H.; Guo, P.; Cui, J.; Jensen, R.; Chen, Y.; Harris, D. K.; Cordero, J. M.; Wang, Z.; Jasanoff, A.; Fukumura, D.; Reimer, R.; Dahan, M.; Jain, R. K.; Bawendi, M. G. Magneto-Fluorescent Core-Shell Supernanoparticles. *Nat. Commun.* **2014**, *5*, No. 5093.
(4) Cheng, L.; Wang, C.; Ma, X.; Wang, Q.; Cheng, Y.; Wang, H.; Li, Y.; Liu, Z. Multifunctional Upconversion Nanoparticles for Dual-Modal Imaging-Guided Stem Cell Therapy under Remote Magnetic Control. *Adv. Funct. Mater.* **2013**, *23*, 272−280.
(5) Zhang, L.; Wang, Y.; Yang, Y.; Zhang, F.; Dong, W.; Zhou, S.; Pei, W.; Chen, H.; Sun, H. Magnetic/Upconversion Luminescent Mesoparticles of Fe_3O_4@LaF_3:Yb^{3+}, Er^{3+} for Dual-Modal Bioimaging. *Chem. Commun.* **2012**, *48*, 11238−11240.
(6) Zhu, X.; Zhou, J.; Chen, M.; Shi, M.; Feng, W.; Li, F. Core-Shell Fe_3O_4@$NaLuF_4$:Yb,Er/Tm Nanostructure for MRI, CT and Upconversion Luminescence Tri-Modality Imaging. *Biomaterials* **2012**, *33*, 4618−4627.
(7) Yang, F.; Skripka, A.; Benayas, A.; Dong, X.; Hong, S. H.; Ren, F.; Oh, J. K.; Liu, X.; Vetrone, F.; Ma, D. An Integrated Multifunctional Nanoplatform for Deep-Tissue Dual-Mode Imaging. *Adv. Funct. Mater.* **2018**, *28*, No. 1706235.
(8) Part, F.; Zaba, C.; Bixner, O.; Grünewald, T. A.; Michor, H.; Küpcü, S.; Debreczeny, M.; De Vito Francesco, E.; Lassenberger, A.; Schrittwieser, S.; et al. The Doping Method Determines Para-or Superparamagnetic Properties of Photostable and Surface Modifiable Quantum Dots for Multimodal Bioimaging. *Chem. Mater.* **2018**, *30*, 4233−4241.
(9) Pahari, S. K.; Olszakier, S.; Kahn, I.; Amirav, L. Magneto-Fluorescent Yolk-Shell Nanoparticles. *Chem. Mater.* **2018**, *30*, 775−780.
(10) Ma, D.; Guan, J.; Dénommée, S.; Enright, G.; Veres, T.; Simard, B. Multifunctional Nano-Architecture for Biomedical Applications. *Chem. Mater.* **2006**, *18*, 1920−1927.
(11) Zhang, F.; Braun, G. B.; Pallaoro, A.; Zhang, Y.; Shi, Y.; Cui, D.; Moskovits, M.; Zhao, D.; Stucky, G. D. Mesoporous Multifunctional Upconversion Luminescent and Magnetic "Nanorattle" Materials for Targeted Chemotherapy. *Nano Lett.* **2012**, *12*, 61−67.
(12) Shi, D.; Cho, H. S.; Chen, Y.; Xu, H.; Gu, H.; Lian, J.; Wang, W.; Liu, G.; Huth, C.; Wang, L.; Ewing, R. C.; Budko, S.; Pauletti, G. M.; Dong, Z. Fluorescent Polystyrene-Fe_3O_4 Composite Nanospheres for *In Vivo* Imaging and Hyperthermia. *Adv. Mater.* **2009**, *21*, 2170−2173.
(13) Hemmer, E.; Benayas, A.; Legare, F.; Vetrone, F. Exploiting the Biological Windows: Current Perspectives on Fluorescent Bioprobes Emitting above 1000 nm. *Nanoscale Horiz.* **2016**, *1*, 168−184.
(14) Skripka, A.; Karabanovas, V.; Jarockyte, G.; Marin, R.; Tam, V.; Cerruti, M.; Rotomskis, R.; Vetrone, F. Decoupling Theranostics with Rare Earth Doped Nanoparticles. *Adv. Funct. Mater.* **2019**, *29*, No. 1807105.
(15) Chinen, A. B.; Guan, C. M.; Ferrer, J. R.; Barnaby, S. N.; Merkel, T. J.; Mirkin, C. A. Nanoparticle Probes for the Detection of Cancer Biomarkers, Cells, and Tissues by Fluorescence. *Chem. Rev.* **2015**, *115*, 10530−10574.
(16) Liu, B.; Li, C.; Ma, P.; Chen, Y.; Zhang, Y.; Hou, Z.; Huang, S.; Lin, J. Multifunctional $NaYF_4$:Yb,Er@$mSiO_2$@Fe_3O_4-PEG nanoparticles for UCL/MR bioimaging and magnetically targeted drug delivery. *Nanoscale* **2015**, *7*, 1839−1848.
(17) Cheng, R.; Meng, F.; Deng, C.; Klok, H.; Zhong, Z. Dual and Multi-Stimuli Responsive Polymeric Nanoparticles for Programmed Site-Specific Drug Delivery. *Biomaterials* **2013**, *34*, 3647−3657.
(18) Wang, C.; Xu, H.; Liang, C.; Liu, Y.; Li, Z.; Yang, G.; Cheng, L.; Li, Y.; Liu, Z. Iron Oxide@Polypyrrole Nanoparticles as a Multifunctional Drug Carrier for Remotely Controlled Cancer Therapy with Synergistic Antitumor Effect. *ACS Nano* **2013**, *7*, 6782−6795.
(19) Jing, L.; Liang, X.; Li, X.; Lin, L.; Yang, Y.; Yue, X.; Dai, Z. Mn-Porphyrin Conjugated Au Nanoshells Encapsulating Doxorubicin for Potential Magnetic Resonance Imaging and Light Triggered Synergistic Therapy of Cancer. *Theranostics* **2014**, *4*, 858.
(20) Kang, X.; Cheng, Z.; Yang, D.; Ma, P.; Shang, M.; Peng, C.; Dai, Y.; Lin, J. Design and Synthesis of Multifunctional Drug Carriers Based on Luminescent Rattle-Type Mesoporous Silica Microspheres with a Thermosensitive Hydrogel as a Controlled Switch. *Adv. Funct. Mater.* **2012**, *22*, 1470−1481.
(21) Chiang, W. L.; Ke, C. J.; Liao, Z. X.; Chen, S. Y.; Chen, F. R.; Tsai, C. Y.; Xia, Y.; Sung, H. W. Pulsatile Drug Release from PLGA Hollow Microspheres by Controlling the Permeability of Their Walls with a Magnetic Field. *Small* **2012**, *8*, 3584−3588.
(22) Liu, J.; Wang, C.; Wang, X.; Wang, X.; Cheng, L.; Li, Y.; Liu, Z. Mesoporous Silica Coated Single-Walled Carbon Nanotubes as a Multifunctional Light-Responsive Platform for Cancer Combination Therapy. *Adv. Funct. Mater.* **2015**, *25*, 384−392.
(23) Wang, H.; Cao, G.; Gai, Z.; Hong, K.; Banerjee, P.; Zhou, S. Magnetic/NIR-Responsive Drug Carrier, Multicolor Cell Imaging, and Enhanced Photothermal Therapy of Gold Capped Magnetite-Fluorescent Carbon Hybrid Nanoparticles. *Nanoscale* **2015**, *7*, 7885−7895.
(24) Kurapati, R.; Raichur, A. M. Near-Infrared Light-Responsive Graphene Oxide Composite Multilayer Capsules: A Novel Route for Remote Controlled Drug Delivery. *Chem. Commun.* **2013**, *49*, 734−736.
(25) Sumer, B.; Gao, J. Theranostic Nanomedicine for Cancer. *Nanomedicine* **2008**, *3*, 137−140.
(26) Chen, Y.; Gao, Y.; Chen, H.; Zeng, D.; Li, Y.; Zheng, Y.; Li, F.; Ji, X.; Wang, X.; Chen, F.; et al. Engineering Inorganic Nanoemulsions/Nanoliposomes by Fluoride-Silica Chemistry for Efficient Delivery/Co-Delivery of Hydrophobic Agents. *Adv. Funct. Mater.* **2012**, *22*, 1586−1597.
(27) Shen, D.; Yang, J.; Li, X.; Zhou, L.; Zhang, R.; Li, W.; Chen, L.; Wang, R.; Zhang, F.; Zhao, D. Biphase Stratification Approach to Three-Dimensional Dendritic Biodegradable Mesoporous Silica Nanospheres. *Nano Lett.* **2014**, *14*, 923−932.
(28) Niu, D.; Liu, Z.; Li, Y.; Luo, X.; Zhang, J.; Gong, J.; Shi, J. Monodispersed and Ordered Large-Pore Mesoporous Silica Nanospheres with Tunable Pore Structure for Magnetic Functionalization and Gene Delivery. *Adv. Mater.* **2014**, *26*, 4947−4953.
(29) Cheng, Z.; Ma, P.; Hou, Z.; Wang, W.; Dai, Y.; Zhai, X.; Lin, J. YVO_4:Eu^{3+} Functionalized Porous Silica Submicrospheres as Delivery Carriers of Doxorubicin. *Dalton Trans.* **2012**, *41*, 1481−1489.
(30) Sangwichien, C.; Aranovich, G.; Donohue, M. Density Functional Theory Predictions of Adsorption Isotherms with Hysteresis Loops. *Colloids Surf., A* **2002**, *206*, 313−320.
(31) Lu, Z.; Gao, C.; Zhang, Q.; Chi, M.; Howe, J. Y.; Yin, Y. Direct Assembly of Hydrophobic Nanoparticles to Multifunctional Structures. *Nano Lett.* **2011**, *11*, 3404−3412.
(32) Benayas, A.; Ren, F.; Carrasco, E.; Marzal, V.; del Rosal, B.; Gonfa, B. A.; Juarranz, Á.; Sanz-Rodríguez, F.; Jaque, D.; García-Solé, J.; Ma, D.; Vetrone, F. PbS/CdS/ZnS Quantum Dots: A Multifunctional Platform for *In Vivo* Near-Infrared Low-Dose Fluorescence Imaging. *Adv. Funct. Mater.* **2015**, *25*, 6650−6659.
(33) Tan, L.; Zhou, Y.; Ren, F.; Benetti, D.; Yang, F.; Zhao, H.; Rosei, F.; Chaker, M.; Ma, D. Ultrasmall PbS Quantum Dots: a Facile and Greener Synthetic Route and Their High Performance in Luminescent Solar Concentrators. *J. Mater. Chem. A* **2017**, *5*, 10250−10260.
(34) Ren, F.; del Rosal, B.; An, S. Y.; Yang, F.; Carrasco, E.; Benayas, A.; Oh, J. K.; Jaque, D.; de la Fuente, ÁJ.; Vetrone, F.; Ma, D. Development and Investigation of Ultrastable PbS/CdS/ZnS Quantum Dots for Near-Infrared Tumor Imaging. *Part. Part. Syst. Charact.* **2017**, *34*, No. 1600242.

DOI: 10.1021/acs.chemmater.9b00028
Chem. Mater. 2019, 31, 3201−3210

(35) Xu, Z.; Liu, Y.; Ren, F.; Yang, F.; Ma, D. Development of Functional Nanostructures and Their Applications in Catalysis and Solar Cells. *Coord. Chem. Rev.* **2016**, *320–321*, 153–180.
(36) Ren, F.; Lindley, S. A.; Zhao, H.; Tan, L.; Gonfa, B.; Pu, Y.; Yang, F.; Liu, X.; Vidal, F.; Zhang, J.; Vetrone, F.; Ma, D. Towards Understanding the Unusual Photoluminescence Intensity Variation of Ultrasmall Colloidal PbS Quantum Dots with the Formation of a Thin CdS Shell. *Phys. Chem. Chem. Phys.* **2016**, *18*, 31828–31835.
(37) Tan, L.; Yang, F.; Kim, M. R.; Li, P.; Gangadharan, D. T.; Margot, J.; Izquierdo, R.; Chaker, M.; Ma, D. Enhanced Long-term and Thermal Stability of Polymer Solar Cells in Air at High Humidity with the Formation of Unusual Quantum Dot Networks. *ACS Appl. Mater. Interfaces* **2017**, *9*, 26257–26267.
(38) Lynch, J.; Zhuang, J.; Wang, T.; LaMontagne, D.; Wu, H.; Cao, Y. C. Gas-Bubble Effects on the Formation of Colloidal Iron Oxide Nanocrystals. *J. Am. Chem. Soc.* **2011**, *133*, 12664–12674.
(39) Huang, L.; Liao, T.; Wang, J.; Ao, L.; Su, W.; Hu, J. Brilliant Pitaya-Type Silica Colloids with Central-Radial and High-Density Quantum Dots Incorporation for Ultrasensitive Fluorescence Immunoassays. *Adv. Funct. Mater.* **2018**, *28*, No. 1705380.
(40) Erogbogbo, F.; Yong, K.; Hu, R.; Law, W.; Ding, H.; Chang, C.; Prasad, P. N.; Swihart, M. T. Biocompatible Magnetofluorescent Probes: Luminescent Silicon Quantum Dots Coupled with Superparamagnetic Iron (III) Oxide. *ACS Nano* **2010**, *4*, 5131–5138.
(41) Sathe, T. R.; Agrawal, A.; Nie, S. Mesoporous Silica Beads Embedded with Semiconductor Quantum Dots and Iron Oxide Nanocrystals: Dual-Function Microcarriers for Optical Encoding and Magnetic Separation. *Anal. Chem.* **2006**, *78*, 5627–5632.
(42) Hansen, M. F.; Mørup, S. Estimation of Blocking Temperatures from ZFC/FC Curves. *J. Magn. Magn. Mater.* **1999**, *203*, 214–216.
(43) Cannas, C.; Casula, M. F.; Concas, G.; Corrias, A.; Gatteschi, D.; Falqui, A.; Musinu, A.; Sangregorio, C.; Spano, G. Magnetic Properties of γ-Fe_2O_3-SiO_2 Aerogel and Xerogel Nanocomposite Materials. *J. Mater. Chem.* **2001**, *11*, 3180–3187.
(44) Sung Lee, J.; Myung Cha, J.; Young Yoon, H.; Lee, J.; Keun Kim, Y. Magnetic Multi-Granule Nanoclusters: A Model System That Exhibits Universal Size Effect of Magnetic Coercivity. *Sci. Rep.* **2015**, *5*, No. 12135.
(45) Yang, F.; Skripka, A.; Tabatabaei, M. S.; Hong, S. H.; Ren, F.; Benayas, A.; Oh, J. K.; Martel, S.; Liu, X.; Vetrone, F.; Ma, D. Multifunctional Self-Assembled Supernanoparticles for Deep-Tissue Bimodal Imaging and Amplified Dual-Mode Heating Treatment. *ACS Nano* **2019**, *13*, 408–420.
(46) Zhao, H.; Zou, Q.; Sun, S.; Yu, C.; Zhang, X.; Li, R.; Fu, Y. Theranostic Metal-Organic Framework Core-Shell Composites for Magnetic Resonance Imaging and Drug Delivery. *Chem. Sci.* **2016**, *7*, 5294–5301.
(47) Yang, X.; Grailer, J. J.; Rowland, I. J.; Javadi, A.; Hurley, S. A.; Matson, V. Z.; Steeber, D. A.; Gong, S. Multifunctional Stable and pH-Responsive Polymer Vesicles Formed by Heterofunctional Triblock Copolymer for Targeted Anticancer Drug Delivery and Ultrasensitive MR Imaging. *ACS Nano* **2010**, *4*, 6805–6817.
(48) Hickey, R. J.; Meng, X.; Zhang, P.; Park, S. Low-Dimensional Nanoparticle Clustering in Polymer Micelles and Their Transverse Relaxivity Rates. *ACS Nano* **2013**, *7*, 5824–5833.
(49) Pöselt, E.; Kloust, H.; Tromsdorf, U.; Janschel, M.; Hahn, C.; Maßlo, C.; Weller, H. Relaxivity Optimization of a PEGylated Iron-Oxide-Based Negative Magnetic Resonance Contrast Agent for T_2-Weighted Spin-Echo Imaging. *ACS Nano* **2012**, *6*, 1619–1624.
(50) Zhou, Z.; Tian, R.; Wang, Z.; Yang, Z.; Liu, Y.; Liu, G.; Wang, R.; Gao, J.; Song, J.; Nie, L.; Chen, X. Artificial Local Magnetic Field Inhomogeneity Enhances T_2 Relaxivity. *Nat. Commun.* **2017**, *8*, No. 15468.
(51) Kato, Y.; Ozawa, S.; Miyamoto, C.; Maehata, Y.; Suzuki, A.; Maeda, T.; Baba, Y. Acidic Extracellular Microenvironment and Cancer. *Cancer Cell Int.* **2013**, *13*, No. 89.
(52) Zhang, G.; Li, X.; Liao, Q.; Liu, Y.; Xi, K.; Huang, W.; Jia, X. Water-Dispersible PEG-Curcumin/Amine-Functionalized Covalent Organic Framework Nanocomposites as Smart Carriers for *In Vivo* Drug Delivery. *Nat. Commun.* **2018**, *9*, No. 2785.
(53) Lv, R.; Gai, S.; Dai, Y.; Niu, N.; He, F.; Yang, P. Highly Uniform Hollow GdF_3 Spheres: Controllable Synthesis, Tuned Luminescence, and Drug-Release Properties. *ACS Appl. Mater. Interfaces* **2013**, *5*, 10806–10818.

DOI: 10.1021/acs.chemmater.9b00028
Chem. Mater. 2019, 31, 3201–3210

Magnetic-Photoluminescent Nanoplatform Built from Large-Pore Mesoporous Silica

Fan Yang[†], Artiom Skripka[†], Maryam Sadat Tabatabaei[‡], Sung Hwa Hong[¶], Fuqiang Ren[†], Yue Huang[†], Jung Kwon Oh[¶], Sylvain Martel[‡], Xinyu Liu[§], Fiorenzo Vetrone[*,†], Dongling Ma[*,†]

[†] Institut National de la Recherche Scientifique, Centre Énergie, Matériaux et Télécommunications, Université du Québec, 1650 Boul. Lionel-Boulet, Varennes, Québec J3X 1S2, Canada

[‡] NanoRobotics Laboratory, Department of Computer and Software Engineering, Institute of Biomedical Engineering, Polytechnique Montréal, Montréal, QC H3T 1J4, Canada

[¶] Department of Chemistry and Biochemistry, Concordia University, Montreal, Quebec H4B 1R6, Canada

[§] Department of Mechanical and Industrial Engineering, University of Toronto, 5 King's College Road, Toronto, Ontario, M5S 3G8, Canada

Supporting information

Experimental section

Chemicals

Iron chloride hexahydrate ($FeCl_3.6H_2O$), sodium oleate, oleic acid (OA, technical grade 90%), 1-Tetradecene (TDE, technical grade 92%), 1-Octadecene (ODE, technical grade 90%), ammonium hydroxide solution ($NH_3.H_2O$, 28.0~30.0% ammonia content), tetraethyl orthosilicate (TEOS, 99.999%), (3-mercaptopropyl)trimethoxysilane (MPTS, 95%), triethanolamine (TEA), cetyltrimethylammonium chloride solution (CTAC, 25 wt% in H_2O), lead chloride ($PbCl_2$, 98%), sulfur (S, 100%), oleylamine (OLA, technical grade, 70%), cadmium oxide (CdO, 99%), ammonium nitrate (NH_4NO_3), branched polyethylenimine (PEI, Mw $\approx$ 25 000), doxorubicin hydrochloride (DOX) and phosphate buffered saline (PBS) were purchased from Sigma-Aldrich Inc. Hexane, toluene, chloroform, cyclohexane and ethanol were purchased from Fisher Scientific Company. All chemicals were used as purchased.

Synthesis of ultrasmall Fe_3O_4 magnetic nanoparticles (NPs)

Fe_3O_4 NPs were synthesized by a modified thermal decomposition method according to a previous report.[1] Typically, iron oleate precursor was prepared by refluxing $FeCl_3.6H_2O$ (1.08 g, 4 mmol) and sodium oleate (4.87 g, 16 mmol) in a mixture solution of ethanol (8 mL), distilled water (6 mL) and hexane (14 mL) at 70 °C for 6 h. The iron oleate precursor was then separated by a funnel and washed several times. After that, the iron oleate precursor (0.9 g, 1 mmol) was dissolved in a mixture of OA (142 mg, 0.5 mmol), TDE (1.75 g, 9 mmol) and ODE (3.25 g, 13 mmol), then heated to 290 °C under N_2 flow for 1 h. Finally, the Fe_3O_4 NPs were precipitated by adding ethanol and dispersed in chloroform as stock solution.

Synthesis of PbS quantum dots (QDs)

PbS QDs were synthesized by a hot-injection method.[2, 3] In a typical reaction, $PbCl_2$ (10 g) and OLA (24 mL) were added into a 50 mL flask and heated to 160 °C for 1 h. The $PbCl_2$-OLA solution was then cooled to 120 °C under vacuum for 30 min. Subsequently, sulfur (115 mg) in OLA (4

mL) was quickly injected into the above $PbCl_2$-OLA solution under N_2 flow. The growth reaction of PbS QDs was kept at 100 °C for several min to reach the desired size. The reaction was quenched by cold water, followed by adding ethanol and toluene to purify the PbS QDs. Finally, the PbS QDs were dispersed in toluene for the further growth of CdS shell.

Synthesis of PbS/CdS core/shell QDs

PbS/CdS QDs were synthesized by a microwave-assisted cation exchange method.[3] Briefly, CdO (3 g), OA (15 mL) and ODE (20 mL) were heated to 200 °C to prepare the Cd precursor solution. The solution was then cooled to 100 °C and degassed under vacuum for 30 min. The temperature was further decreased to 30 °C and 12 mL of PbS QDs in toluene was added via a syringe. Then 20 mL of the mixed solution was introduced into a 35 mL microwave reaction tube and heated at 100 °C under microwave radiation for several min. Finally, PbS/CdS QDs were purified by repeated precipitation and re-dispersion.

Synthesis of large-pore mesoporous silica nanospheres ($mSiO_2$)

The 3-demensional dendritic $mSiO_2$ particles were prepared by a one-pot biphase stratification method.[4] Typically, CTAC solution (12 mL 25 wt%) and TEA (0.09 g) were added into distilled water (18 mL) and stirred at 60 °C in an oil bath for 1 h. Then TEOS (0.5 mL) in cyclohexane (9.5 mL) was gently added to the above mixed solution. The reaction was kept at 60 °C for 60 h. The resulting products were collected by centrifugation and washed several times with ethanol. At last, the products were extracted with 0.6 wt% NH_4NO_3 ethanol solution at 60 °C for 6 h twice to remove the CTAC template completely, and dispersed in ethanol.

Synthesis of thiol-modified mesoporous silica nanospheres ($mSiO_2$-SH)

For surface modification with thiol groups, $mSiO_2$ (300 mg) in 15 mL of ethanol was added with 150 μL of MPTS and 375 μL of $NH_3.H_2O$, followed by vigorous stirring for 12 h at room temperature. The final products of $mSiO_2$-SH were washed with ethanol several times and dispersed in chloroform.

Synthesis of Fe_3O_4 and PbS/CdS loaded $mSiO_2$ ($mSiO_2$@PbS/CdS-Fe_3O_4)

Briefly, 1mL of Fe_3O_4 and PbS/CdS (4 mg/mL)-in-chloroform solution was added into 4 mL of $mSiO_2$-SH chloroform solution (2 mg/mL) and stirred at room temperature for 30 min. The loading ratio can be simply controlled by varying the volume of Fe_3O_4 and PbS/CdS chloroform solution. The $mSiO_2$@PbS/CdS-Fe_3O_4 particles were then retrieved by centrifugation and washed by chloroform once to remove free, not-loaded Fe_3O_4 NPs and PbS/CdS QDs. Subsequently, 1 mL of $mSiO_2$@PbS/CdS-Fe_3O_4 in chloroform dispersion (5 mg/mL) was mixed with 20 mg of PEI and stirred for 2 h to transfer the $mSiO_2$@PbS/CdS-Fe_3O_4 into water by forming a PEI coating. Finally, the PEI-coated $mSiO_2$@PbS/CdS-Fe_3O_4 particles were precipitated by adding cyclohexane and re-dispersed in water.

Structural, magnetic and optical characterizations

X-Ray Diffraction (XRD) pattern was acquired using a Bruker D8 ADVANCE X-ray diffractometer equipped with Cu anode X-ray source (Cu-kα, λ=1.540598 Å). The morphology of

as-prepared NPs was investigated by transmission electron microscopy (TEM, JEOL 2100F) at 200 kV equipped with a charge-coupled device (CCD) camera. Energy Dispersive X-ray Spectroscopy (EDX) was taken on specific areas during TEM measurements. Absorption spectra were taken by a UV-visible-NIR spectrophotometer (Cary 5000) with a scan speed of 600 nm/min. Photoluminescence (PL) spectra were acquired on a Fluorolog®-3 system (Horiba Jobin Yvon) using an excitation wavelength of 600 nm. Fourier-transform infrared (FTIR) spectra were recorded by a ThermoFisher Scientific Nicolet 6700 FTIR spectrometer using KBr as a reference. The nitrogen adsorption-desorption isotherms were measured using Quantachrome Autosorb-1 Automated Gas Sorption System Analyzer. Specific surface areas and pore size distributions were calculated based on BET (Brunauer-Emmett-Teller) measurements and density functional theory (DFT) method. The loading content of Fe_3O_4 NPs and PbS/CdS QDs was determined by inductively coupled plasma-optical emission spectrometry (ICP-OES) (Agilent Technologies, 5100). Magnetic hysteresis loop was measured by a vibrating sample magnetometer (VSM, Model 4 HF-VSM, ADE USA) at 300 K with magnetic field up to 3 T. Temperature-dependence ZFC and FC magnetization curves were taken under an applied field of 100 Oe between 5 K and 300 K.

Cell culture and viability assay of $mSiO_2$@PbS/CdS-Fe_3O_4

HeLa cancer cells and human embryonic kidney (HEK 293T) cells were cultured in Dulbecco's modified Eagle's medium (DMEM) containing 10% fetal bovine serum (FBS), 50 units/mL penicillin and 50 units/mL streptomycin in 5% CO_2 at 37 °C. HEK 293T and HeLa cells were plated into a 96-well plate with a density of 5×10^5 cells/well and incubated for 24 h in DMEM (100 μL). Various concentrations of $mSiO_2$@PbS/CdS-Fe_3O_4 were then added into the plate. Blank controls without $mSiO_2$@PbS/CdS-Fe_3O_4 (*i.e.*, cells only) were run simultaneously. Cell viability was measured using CellTiter 96 Non-Radioactive Cell Proliferation Assay kit (MTT, Promega) according to the manufacturer's protocol. Briefly, 3-(4,5-dimethylthiazol-2-yl)-2,5-diphenyltetrazolium bromide (MTT) solution (15 μL) was added into each well. After 24 h incubation, the medium containing unreacted MTT was carefully removed. Dimethyl sulfoxide (DMSO, 100 μL) was added into each well in order to dissolve the formed formazan blue crystals, and then the absorbance at $\lambda = 570$ nm was recorded using a Powerwave HT Microplate Reader (Bio-Tek). Each concentration was 6-replicated ($n = 6$). Cell viability was calculated as the ratio of absorbance of mixtures containing $mSiO_2$@PbS/CdS-Fe_3O_4 to control cells.

DOX loading and pH/MF/NIR-responsive drug release

DOX loading: 5 mL of $mSiO_2$@PbS/CdS-Fe_3O_4 samples (2 mg/mL) were mixed with 2 mL of DOX solution in PBS buffer (1mg/mL) under magnetic stirring for 24 h. Then the $mSiO_2$@PbS/CdS-Fe_3O_4/DOX particles were separated by centrifugation and washed with PBS buffer. To evaluate the DOX loading efficiency, the supernatant and washed solutions were collected and the residual DOX content was measured by a UV-Vis absorption spectrophotometer at wavelength of 480 nm. The loading efficiency (LE) can be calculated as following:

$$\mathrm{LE} = \frac{O_{DOX} - R_{DOX}}{O_{DOX}}$$

Where O_{DOX} is original DOX content, R_{DOX} is residual DOX content in collected supernatant and washed solution by centrifugation.

pH-responsive DOX release: $mSiO_2$@PbS/CdS-Fe_3O_4/DOX particles were immersed in 2 mL of PBS in a flask (pH= 7.4/5.0) with gentle stirring. At certain time intervals, the supernatant was taken out by centrifugation to measure the concentration of released DOX and fresh PBS was added again for further drug release experiments.

Magnetic field-responsive DOX release: The same procedure as pH-responsive DOX release was adopted except for putting the flask containing $mSiO_2$@PbS/CdS-Fe_3O_4/DOX under magnetic field (MF). The MF was generated by magnetothermal equipment (Ameritherm Inc., New York) consisting of 3 turns of copper coil (6 cm in diameter) with a water-cooling circuit. The MF frequency of the equipment is 150 kHz as default setting and MF amplitude could be tuned by the current in the range of 0~180 A. MF (H) was calculated by the following equation:

$$H = n\frac{\mu_0 I}{2R},$$

where μ_0 = $4\pi\times10^{-7}$ T.m/A, n is the number of turns, R is the loop radius and I is the applied current. In our experiment, the current was set as 100 A and H was estimated to be 5 kA/m.

NIR-responsive DOX release: The stimulus of pH was replaced by an 806 nm continuous NIR laser (power density of 1.3 W/cm^2) while other setups were kept the same.

The temperature increase during the drug release was recorded by a computer attached optical fibre based thermocouple (Reflex, SN:T18 217A, Neoptix Inc, Canada).

Thermal images were recorded by an infrared thermal imaging camera (FLIR E4, FLIR systems AB, Sweden).

NIR imaging *ex vivo* and photoluminescence signal penetration depth

We designed an experimental setup to acquire NIR images *ex vivo* and estimate the photoluminescence penetration depth, in which the $mSiO_2$@PbS/CdS-Fe_3O_4 aqueous solution was filled in a cuvette underneath a piece of pork tissue of different thickness. NIR images were recorded by a Xeva-1.7 infrared camera (Xenics Corp, Belgium) equipped with a 830 nm long-pass optical filter to block the light below 830 nm and the scattered excitation light of the 806 nm laser. The laser diode of 806 nm with power density of 10 W/cm^2 was used as excitation source.

Animal model

4T1 murine breast cancer cells were cultured in standard cell media recommended by American type culture collection (ATCC). Female Balb/C mice were purchased from Nanjing Peng Sheng Biological Technology Co Ltd and used under approved protocols approved by Soochow University Laboratory Animal Center.

T_2 relaxivity study *in vitro* and MR imaging *in vivo*

T_2-weighted MR images were acquired by a 3T clinical MRI scanner (Bruker Biospin Corporation, Billerica, MA, USA) at room temperature. The $mSiO_2$@PbS/CdS-Fe_3O_4 particles dispersed in PBS buffer at different concentrations were placed in tubes for T_2-weighted MR imaging. The concentration of Fe was determined by inductively coupled plasma-optical emission spectrometry (ICP-OES). Relaxivity (r_2) values were calculated by fitting the curve of $1/T_2$ relaxation time (s^{-1}) vs the concentration of Fe (mM).

For *in vivo* MR imaging, $mSiO_2$@PbS/CdS-Fe_3O_4 dispersed in PBS buffer (200 μL, 2 mg/mL) were injected into mice bearing 4T1 tumors. MR imaging of the mouse was conducted on the same scanner equipped with a special coil designed for small animal imaging. The mouse was scanned before and after injection of the contrast agent.

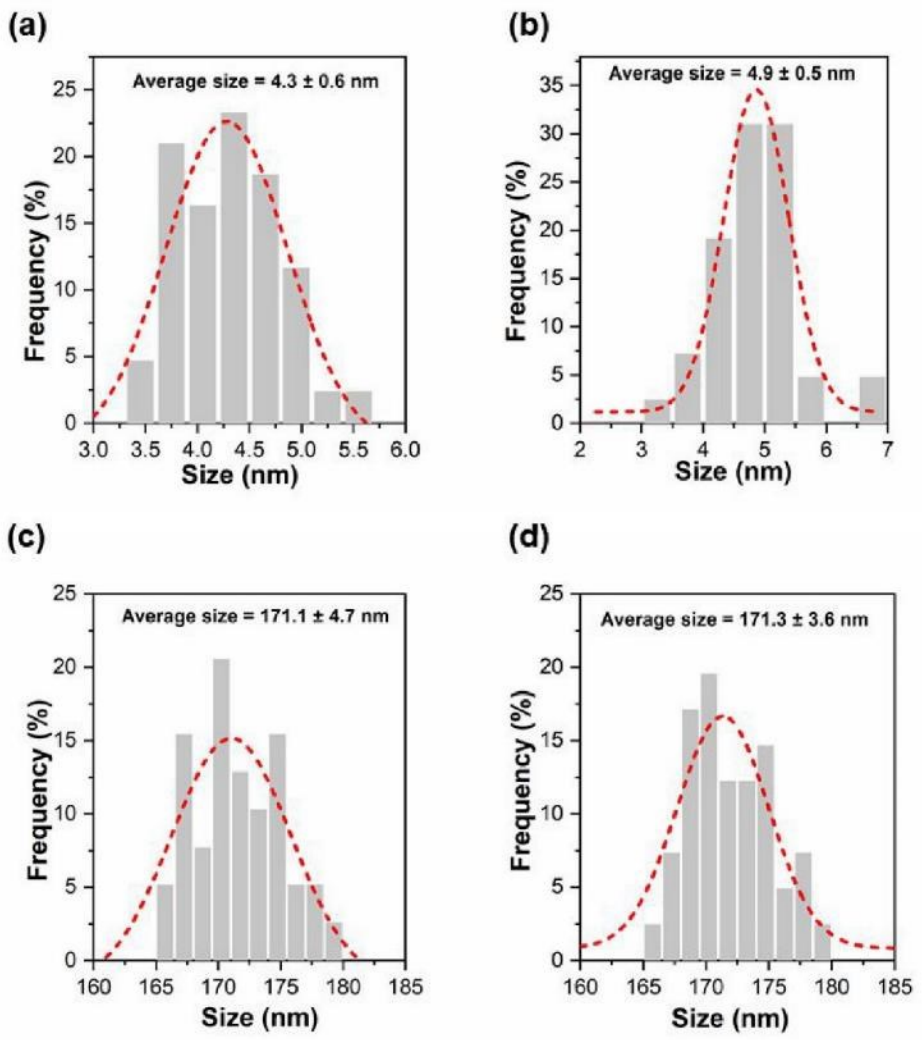

Figure S1 Size distribution histogram of (a) PbS/CdS QDs, (b) Fe_3O_4 NPs, (c) $mSiO_2$ and (d) $mSiO_2$@PbS/CdS-Fe_3O_4.

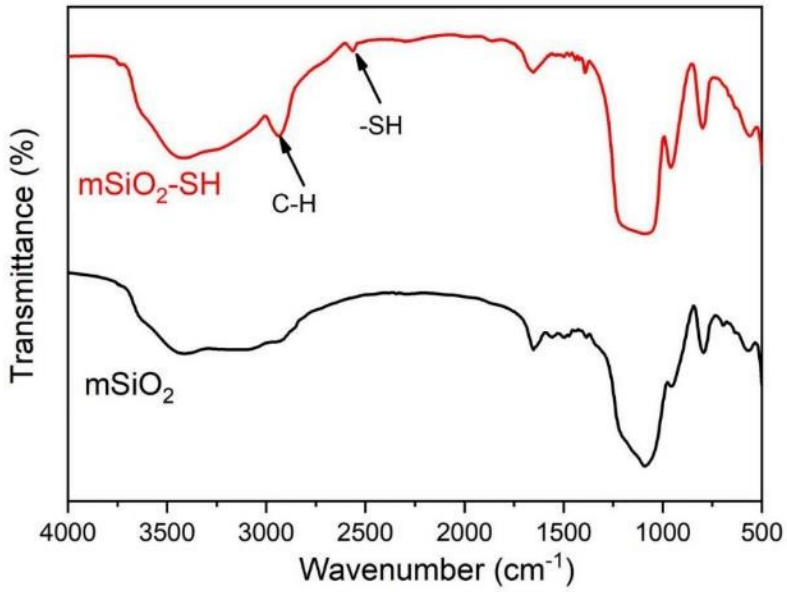

Figure S2 FTIR spectra of $mSiO_2$ and thiol-modified $mSiO_2$ (denoted as $mSiO_2$-SH herein). The peaks at 2940 and 2560 cm^{-1} are assigned to the C-H and -SH stretching modes,[5] which indicates the grafting of thiol groups onto $mSiO_2$ after MPTS modification.

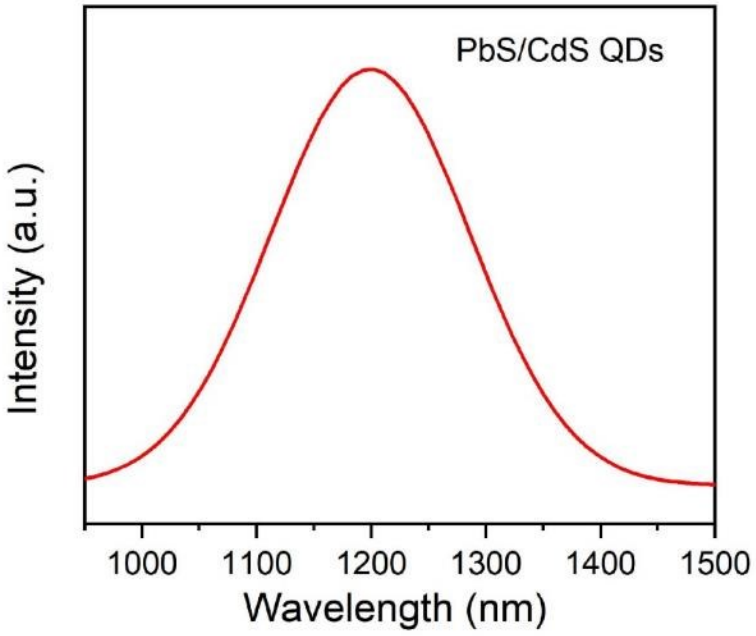

Figure S3 NIR photoluminescence spectrum of PbS/CdS QDs.

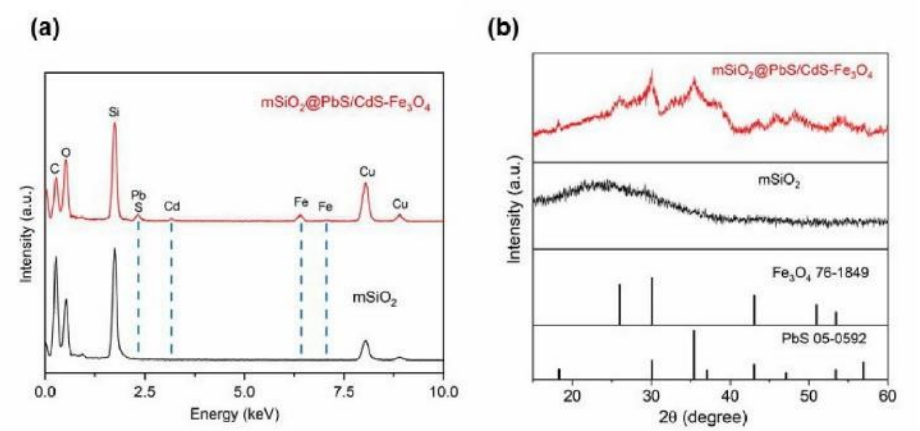

Figure S4 EDX spectra (a) and XRD patterns (b) of $mSiO_2$ and $mSiO_2$@PbS/CdS-Fe_3O_4. The EDX spectrum of $mSiO_2$@PbS/CdS-Fe_3O_4 shows the co-existence of Si, O, Fe, Pb, Cd and S elements whereas that of $mSiO_2$ only shows the composition of Si and O elements. It should be noted that Cu/C elements are from carbon film-covered-copper TEM grids. In addition, the XRD pattern of $mSiO_2$@PbS/CdS-Fe_3O_4 exhibits the characteristic diffraction peaks of PbS and Fe_3O_4 while that of $mSiO_2$ only exhibits the broad peak of amorphous silica. These results indicate that $mSiO_2$@PbS/CdS-Fe_3O_4 consist of Fe_3O_4 NPs and PbS/CdS QDs.

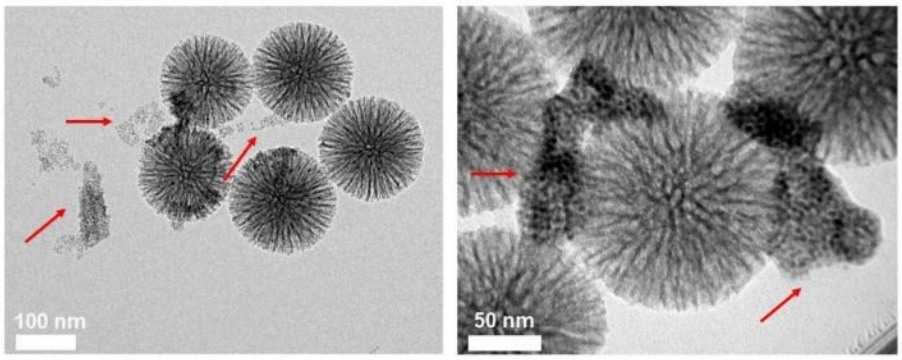

Figure S5 TEM images of the sample after the loading experiment of Fe_3O_4 NPs and PbS/CdS QDs into pure (not thiol-modified) $mSiO_2$. The red arrows indicate the unloaded Fe_3O_4 NPs and PbS/CdS QDs. It can be seen that the Fe_3O_4 NPs and PbS/CdS QDs cannot be efficiently immobilized into mesoporous channels of pure $mSiO_2$ without thiol modification.

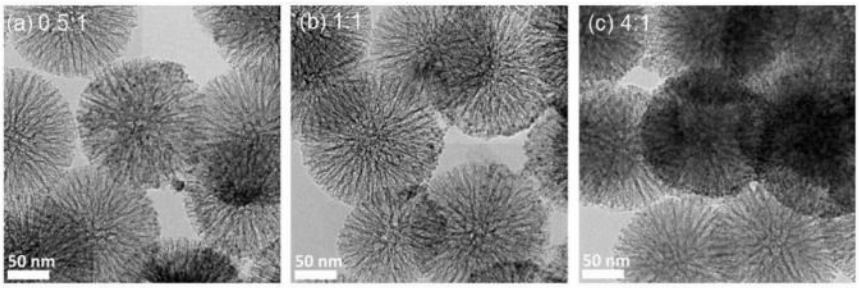

Figure S6 TEM images (a-c) of $mSiO_2$@PbS/CdS-Fe_3O_4 with various mass ratio of PbS/CdS QDs and Fe_3O_4 NPs (PbS/CdS: Fe_3O_4 = 0.5:1, 1:1 and 4:1).

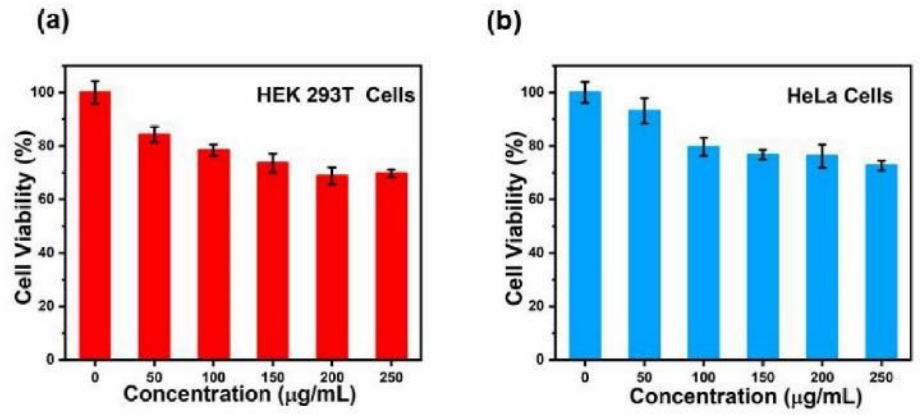

Figure S7 *In vitro* cytotoxicity study of HEK 293T (a) and HeLa (b) cells cultured with various concentrations of $mSiO_2$@PbS/CdS-Fe_3O_4 particles.

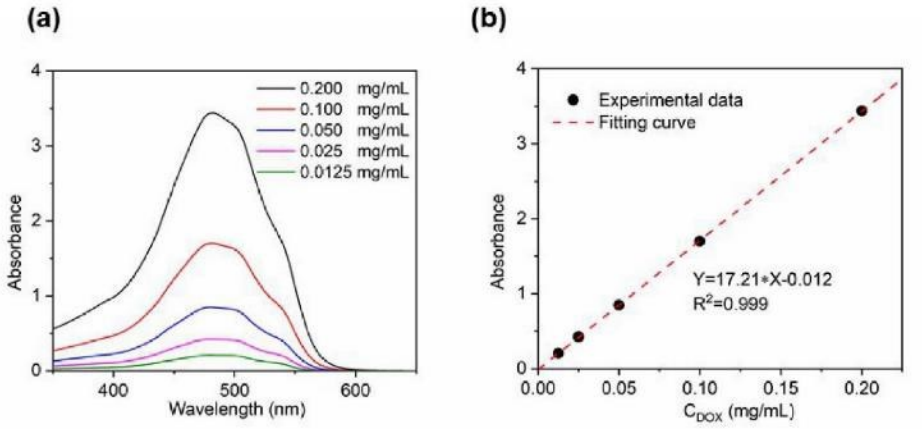

Figure S8 (a) Absorption spectra of aqueous DOX solutions at various known concentrations. (b) The linear fitting curve of absorption as a function of DOX concentration based on experimental data in (a).

Linear fitting of experimental data: $Y=17.21*X-0.012$, $R^2=0.999$.

Calculation of the concentration of DOX: $C_{DOX}= (Y+0.012)/17.21$, where Y is the absorption value at 480 nm determined by a UV-vis spectrometer.

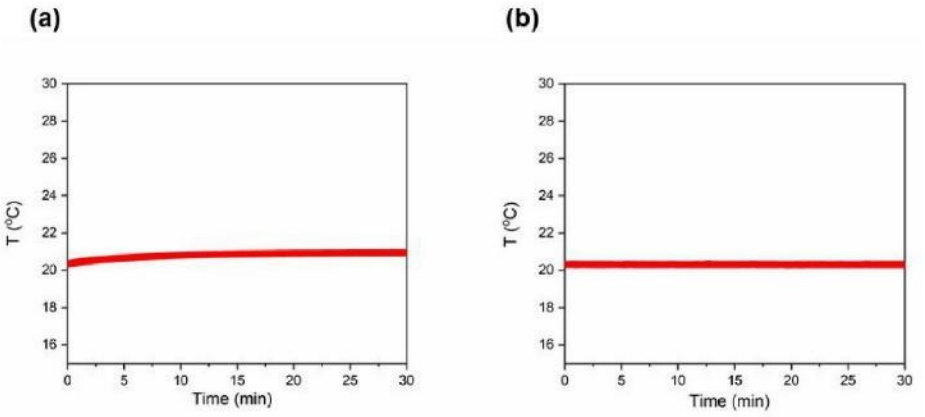

Figure S9 (a) Time-dependent temperature curves of PBS solution under two types of modulation: (a) Laser at 1.3 W/cm^2 and (b) MF at 5 kA/m.

References:

1. Park, J.; An, K.; Hwang, Y.; Park, J. G.; Noh, H. J.; Kim, J. Y.; Park, J. H.; Hwang, N. M.; Hyeon, T., Ultra-Large-Scale Syntheses of Monodisperse Nanocrystals. *Nat. Mater.* **2004,** 3, 891-5.

2. Cademartiri, L.; Bertolotti, J.; Sapienza, R.; Wiersma, D. S.; Freymann, G.; Ozin, G. A., Multigram Scale, Solventless, and Diffusion-Controlled Route to Highly Monodisperse PbS Nanocrystals. *J. Phys. Chem. B* **2006,** 110, (2), 671-673.

3. Ren, F.; Zhao, H.; Vetrone, F.; Ma, D., Microwave-Assisted Cation Exchange toward Synthesis of Near-Infrared Emitting PbS/CdS Core/Shell Quantum Dots with Significantly Improved Quantum Yields through a Uniform Growth Path. *Nanoscale* **2013,** 5, 7800-4.

4. Shen, D.; Yang, J.; Li, X.; Zhou, L.; Zhang, R.; Li, W.; Chen, L.; Wang, R.; Zhang, F.; Zhao, D., Biphase Stratification Approach to Three-Dimensional Dendritic Biodegradable Mesoporous Silica Nanospheres. *Nano Lett.* **2014,** 14, 923-932.

5. Lu, Z.; Gao, C.; Zhang, Q.; Chi, M.; Howe, J. Y.; Yin, Y., Direct Assembly of Hydrophobic Nanoparticles to Multifunctional Structures. *Nano Lett.* **2011,** 11, 3404-3412.

CHAPTER 5 CONCLUSIONS AND PERSPECTIVES

5.1 Conclusions

Multifunctional (superparamagnetic and photoluminescent) NPs are intensively studied as highly promising tools (magnetic confinement and targeting, imaging, therapeutic, *etc.*) for biomedical applications. However, most of these multifunctional NPs show low tissue penetration properties for optical imaging due to tissue-induced optical extinction and autofluorescence as the photoluminescent components in many cases emit in the visible range. To overcome this issue, in this thesis, we focus on the designing and synthesis of multifunctional (superparamagnetic and photoluminescent) NPs in the so-called biological windows (NIR-I/II) with modalities for bioimaging and therapeutics. So, the results of this thesis project are divided into three parts based on the structure of nanocomposites and their potential biomedical applications.

Part I is mainly focused on the development of multifunctional core/shell/shell nanoplatform (Fe_3O_4@SiO_2@$NaYF_4$:Nd^{3+}) by a multistep synthetic procedure. The uniform Fe_3O_4@SiO_2@$NaYF_4$:Nd^{3+} NPs exhibit excellent photostability, impressive superparamagnetic properties and strong photoluminescence emission. Under the excitation of an 806 nm (NIR-I) laser, these NPs present three emission wavelengths (900 nm, 1060 nm and 1340 nm), all lying within the biological windows (NIR-I and NIR-II). The *ex vivo* imaging testing indicates that the unique NIR-to-NIR photoluminescence property endows Fe_3O_4@SiO_2@$NaYF_4$:Nd^{3+} NPs with capability for deep-tissue optical imaging. The superparamagnetic Fe_3O_4 core inside these multifunctional nanoplatform results in rapid magnetic response to an external magnetic field. *In vivo* MR imaging exhibits a significant darkening effect in T_2-weighted images with the use of Fe_3O_4@SiO_2@$NaYF_4$:Nd^{3+} NPs as a contrast agent. Another important advantage of the developed nanoplatform is that they are much less toxic than semiconductor QDs, which usually contain Pb and/or Cd. Therefore, this nanoplatform can be considered as potential bioprobe for deep-tissue dual-mode (optical and MR) imaging *in vivo* and magnetic-driven applications.

In part II, we prepared novel multifunctional (superparamagnetic and photoluminescent) self-assembled Fe_3O_4 and PbS/CdS (NIR-II) supernanoparticles [SASNs (NIR-II)] and their formation mechanism during the self-assembly was studied. Due to their unique NIR photoluminescence feature, the SASNs (NIR-II) are allowed to obtain NIR optical imaging with enhanced tissue penetration depth compared with that of SASNs (NIR-I) due to minimized light extinction in biological tissues. In addition to their excellent NIR photoluminescence properties, the SASNs (NIR-II) exhibit remarkable photostability and colloidal stability. Subsequently, owing to the synergistic effect of their clustering characteristic inside SASNs (NIR-II), the significantly enhanced T_2 relaxivity is proved by MR imaging experiment. At last, the prepared SASNs

(NIR-II) can be served as both magnetothermal and photothermal agents, which can overcome the main drawbacks of each type of heating separately. The overwhelming thermal conversion efficiency at the local site with the use of SASNs (NIR-II) can be achieved under dual-mode (magnetothermal and photothermal) heating modality. Overall these results, in hand with their excellent photo and colloidal stability, make SASNs (NIR-II) extremely promising for use in deep-tissue bimodal (optical and MR) imaging *in vivo* and amplified dual-mode heating treatment associated with cancers.

Part III is mainly focused on another multifunctional nanoplatform ($mSiO_2$@PbS/CdS-Fe_3O_4), which integrated superparamagnetic Fe_3O_4 NPs and NIR photoluminescent PbS/CdS QDs into a large pore mesoporous silica nanospheres ($mSiO_2$). The relatively-large-pore (>10 nm) $mSiO_2$ was deliberately synthesized by a biphase stratification continuous growth approach and the final $mSiO_2$@PbS/CdS-Fe_3O_4 was prepared by coordination-driven embedding of Fe_3O_4 NPs and PbS/CdS QDs into the mesoporous channels of $mSiO_2$. The $mSiO_2$@PbS/CdS-Fe_3O_4 nanoplatform exhibits excellent photoluminescence in the NIR-II window enabling its use for deep-tissue imaging as well as superb superparamagnetic properties that make it easily confined by an external MF and ideal as a highly efficient T_2 contrast agent for MR imaging *in vivo.* Due to large-pore characteristics, the nanoplatform also demonstrates great potential as a drug delivery carrier for cancer therapy. After being loaded with DOX, in addition to showing pH-responsive drug release behavior, $mSiO_2$@PbS/CdS-Fe_3O_4 can produce local heat and accelerate the drug release *via* the magnetothermal effect. In addition, benefitting from the presence of the NIR-absorbing QDs, $mSiO_2$@PbS/CdS-Fe_3O_4 can not only serve as a highly efficient PTT agent, but also promote the drug release rate under NIR irradiation. Thus, such multifunctional nanoplatform has a great potential for bimodal imaging and highly efficient therapeutic effect from the integrated heating mode (PTT/MHT) and multi-stimuli (pH/MF/NIR) responsive drug release.

5.2 Perspectives

We have developed several multifunctional (superparamagnetic and photoluminescent) nanoplatforms and studied their bioimaging and therapeutic modalities. However, despite of certain progress we made, the research area of multifunctional (superparamagnetic and photoluminescent) NPs is still in its infant stage and significant efforts are still needed for further development of these kinds of NPs and their utilization for biomedical application. There are several interesting research directions in this highly promising field.

5.2.1 Synthetic procedures optimization

Even though the multifunctional (superparamagnetic and photoluminescent) NPs have tremendous applications in the field of biomedicine, this research field is still far from sufficient because of the complexity in the synthetic procedures and intricacies associated with the combination of quite different

materials presenting diverse properties. For example, it is hard to precisely control the synthesis to get uniform and size-tunable NPs with both desired superparamagnetic and fluorescent properties; it is difficult to obtain small size multifunctional NPs, which however is very important since the size of NPs decides the uptake mechanism of cells and affects cellular uptake efficiency and subcellular distribution for bioimaging of intracellular environment; long-term colloidal stability and versatile surface modifications for meeting the specific requirements of different biological applications are important for designing multifunctional NPs. Therefore, in the future, more simple and versatile synthetic strategies should be developed to fulfill the following design criteria of multifunctional (superparamagnetic and fluorescent) NPs: uniform and tunable sizes, optimal magnetic component loading for synergistic magnetic properties, appropriate fluorescence component loading for optimized fluorescence signal, long-term colloidal stability, versatile surface functionality and effective bioconjugation/specific-targeting capability for bioapplications.

5.2.2 Photoluminescence efficiency optimization

One major challenge in the synthesis of such multifunctional NPs is to avoid the quenching effect of the photoluminescent NPs by the superparamagnetic iron oxide NPs due to the energy transfer. In other words, it is highly desired to construct multifunctional NPs with optimal photoluminescence to ensure their use as an effective optical imaging probe. With respect to Fe_3O_4@SiO_2@$NaYF_4$:Nd^{3+} NPs in chapter 4.1, the intermediate silica shell can effectively minimize the photoluminescence quenching by the Fe_3O_4 core. While regarding SASNs (NIR-II) in chapter 4.2 and mSiO_2@PbS/CdS-Fe_3O_4 in chapter 4.3, the random distribution of PbS/CdS QDs and Fe_3O_4 NPs inside multifunctional particles and the possible close distance between PbS/CdS QDs themselves and between PbS/CdS QDs and Fe_3O_4 NPs causes photoluminescence quenching by Fe_3O_4 and/or the self-quenching of the QDs. So, the optimal photoluminescence in both cases can be regarded as the interplay between quenching effect by Fe_3O_4 NPs and self-quenching. It may be improved by controlling the distribution of the QDs and Fe_3O_4 NPs. Although out of the scope of this thesis, the optimization of their photoluminescence efficiency will be investigated in the future.

5.2.3 Toxicity investigation

Although these multifunctional (superparamagnetic and photoluminescent) NPs are very stable in aqueous solution and our cell viability MTT tests studies show that these multifunctional NPs are not toxic in the cell level, more systematic toxicity study needs to be done at different levels and for the lone term before any clinic trials. The toxicity of NPs to the normal tissues *in vivo* is largely depend on their intrinsic physicochemical properties, such as size, chemical composition and surface functionalization. However, such information of these multifunctional NPs is lacking. Further systematic and thorough investigation on the toxic effects of these hybrid NPs at organ level, and whole organism level is still required. Particularly, the toxicity of QDs-based multifunctional (superparamagnetic and photoluminescent) NPs which contain

heavy metals of Pb and Cd remains a strong concern. To be specific, the systematic biosafety evaluations of QDs-based multifunctional NPs *in vivo*, including physical appearance and body weight every day, H&E staining images of major organs and tumors, and complete blood panel test of treated mice and control group, are still necessary before further exploring their bioapplications, such as human cancer imaging.

5.2.4 Surface modification

It is well known that the surface modification of multifunctional NPs plays a crucial role in determining their toxicity and effectivity when they are introduced into biological media. Specifically, the surface modification is important for 1) prohibiting the agglomeration of NPs due to interparticle interactions and eventually providing their colloidal stability; 2) enhancing biocompatibility of NPs by preventing the leakage of toxic ions to the exterior environment; 3) serving as a base for further anchoring of functional groups such as antibodies, peptides and biomarkers. However, the main focus of the multifunctional nanoplatforms in this thesis is still on their magnetic and optical properties, but not on their bioengineering for *in vivo* applications. The non-modified characteristic makes these NPs more visible to the immune system, which results in the fast elimination from the bloodstream.

To improve the biocompatibility and circulation time of multifunctional NPs for future *in vivo* experiments, it is of great importance to extend PEG modification on these NPs. Previously reported studies have proved that PEG coating reveals excellent stability in aqueous dispersions and physiological media and dramatically increases the blood circulation time of NPs by enhancing their hindrance from the body's defence system. Additionally, after surface coating of PEG to provide suitable base, we propose to conjugate functional groups with PEG to the multifunctional NPs. In this case, the new formed nanoplatforms are expected to target NPs to specific tissue or cells by specific recognition, thus improving therapeutic efficiency and minimizing the toxicity to normal tissue/cells.

REFERENCES

1. Lu, A. H.; Salabas, E. e. L.; Schüth, F., Magnetic nanoparticles: synthesis, protection, functionalization, and application. *Angew. Chem. Int. Ed.* **2007,** *46* (8), 1222-1244.

2. Jun, Y.-w.; Seo, J.-w.; Cheon, J., Nanoscaling laws of magnetic nanoparticles and their applicabilities in biomedical sciences. *Acc. Chem. Res.* **2008,** *41* (2), 179-189.

3. Jeong, U.; Teng, X.; Wang, Y.; Yang, H.; Xia, Y., Superparamagnetic Colloids: Controlled Synthesis and Niche Applications. *Adv. Mater.* **2007,** *19* (1), 33-60.

4. Ma, D.; Guan, J.; Dénommée, S.; Enright, G.; Veres, T.; Simard, B., Multifunctional Nano-Architecture for Biomedical Applications. *Chem. Mater.* **2006,** *18* (7), 1920-1927.

5. Li, K.; Pan, J.; Feng, S. S.; Wu, A. W.; Pu, K. Y.; Liu, Y.; Liu, B., Generic strategy of preparing fluorescent conjugated-polymer-loaded poly (dl-lactide-co-glycolide) nanoparticles for targeted cell imaging. *Adv. Funct. Mater.* **2009,** *19* (22), 3535-3542.

6. Huang, C. C.; Yang, Z.; Lee, K. H.; Chang, H. T., Synthesis of highly fluorescent gold nanoparticles for sensing mercury (II). *Angew. Chem. Int. Ed.* **2007,** *119* (36), 6948-6952.

7. Smith, A. M.; Mancini, M. C.; Nie, S., Second window for *in vivo* imaging. *Nat. Nanotechnol.* **2009,** *4*, 710.

8. Cao, L.; Wang, X.; Meziani, M. J.; Lu, F.; Wang, H.; Luo, P. G.; Lin, Y.; Harruff, B. A.; Veca, L. M.; Murray, D., Carbon dots for multiphoton bioimaging. *J. Am. Chem. Soc.* **2007,** *129* (37), 11318-11319.

9. Zrazhevskiy, P.; Sena, M.; Gao, X., Designing multifunctional quantum dots for bioimaging, detection, and drug delivery. *Chem. Soc. Rev.* **2010,** *39* (11), 4326-4354.

10. Hemmer, E.; Venkatachalam, N.; Hyodo, H.; Hattori, A.; Ebina, Y.; Kishimoto, H.; Soga, K., Upconverting and NIR emitting rare earth based nanostructures for NIR-bioimaging. *Nanoscale* **2013,** *5* (23), 11339-11361.

11. Medintz, I. L.; Uyeda, H. T.; Goldman, E. R.; Mattoussi, H., Quantum dot bioconjugates for imaging, labelling and sensing. *Nat. Mater.* **2005,** *4* (6), 435-446.

12. Yu, D.; Baird, M. A.; Allen, J. R.; Howe, E. S.; Klassen, M. P.; Reade, A.; Makhijani, K.; Song, Y.; Liu, S.; Murthy, Z., A naturally monomeric infrared fluorescent protein for protein labeling *in vivo*. *Nat. Meth.* **2015,** *12* (8), 763.

13. Villa, I.; Vedda, A.; Cantarelli, I. X.; Pedroni, M.; Piccinelli, F.; Bettinelli, M.; Speghini, A.; Quintanilla, M.; Vetrone, F.; Rocha, U.; Jacinto, C.; Carrasco, E.; Rodríguez, F. S.; Juarranz, Á.; Rosal, B.;

Ortgies, D. H.; Gonzalez, P. H.; Solé, J. G.; García, D. J., 1.3 μm emitting $SrF_2:Nd^{3+}$ nanoparticles for high contrast *in vivo* imaging in the second biological window. *Nano Res.* **2014,** *8* (2), 649-665.

14. Pansare, V. J.; Hejazi, S.; Faenza, W. J.; Prud'homme, R. K., Review of long-wavelength optical and NIR imaging materials: contrast agents, fluorophores, and multifunctional nano carriers. *Chem. Mater.* **2012,** *24* (5), 812-827.

15. Hemmer, E.; Benayas, A.; Legare, F.; Vetrone, F., Exploiting the biological windows: current perspectives on fluorescent bioprobes emitting above 1000 nm. *Nanoscale Horiz.* **2016**, *1*, 168-184.

16. Alivisatos, A. P., Semiconductor clusters, nanocrystals, and quantum dots. *Science* **1996,** *271* (5251), 933-937.

17. Smith, A. M.; Nie, S., Semiconductor Nanocrystals: Structure, Properties, and Band Gap Engineering. *Acc. Chem. Res.* **2010,** *43* (2), 190-200.

18. Donega, C. d. M., Synthesis and properties of colloidal heteronanocrystals. *Chem. Soc. Rev.* **2011,** *40* (3), 1512-1546.

19. Pichaandi, J.; van Veggel, F. C., Near-infrared emitting quantum dots: Recent progress on their synthesis and characterization. *Coord. Chem. Rev.* **2014,** *263*, 138-150.

20. Fan, G.; Wang, C.; Fang, J., Solution-based synthesis of III–V quantum dots and their applications in gas sensing and bio-imaging. *Nano Today* **2014,** *9* (1), 69-84.

21. Bharali, D. J.; Lucey, D. W.; Jayakumar, H.; Pudavar, H. E.; Prasad, P. N., Folate-receptor-mediated delivery of InP quantum dots for bioimaging using confocal and two-photon microscopy. *J. Am. Chem. Soc.* **2005,** *127* (32), 11364-11371.

22. Zebibula, A.; Alifu, N.; Xia, L.; Sun, C.; Yu, X.; Xue, D.; Liu, L.; Li, G.; Qian, J., Ultrastable and Biocompatible NIR-II Quantum Dots for Functional Bioimaging. *Adv. Funct. Mater.* **2018,** *28* (9), 1703451.

23. Benayas, A.; Ren, F.; Carrasco, E.; Marzal, V.; del Rosal, B.; Gonfa, B. A.; Juarranz, Á.; Sanz-Rodríguez, F.; Jaque, D.; García-Solé, J.; Ma, D.; Vetrone, F., PbS/CdS/ZnS Quantum Dots: A Multifunctional Platform for *In Vivo* Near-Infrared Low-Dose Fluorescence Imaging. *Adv. Funct. Mater.* **2015,** *25* (42), 6650-6659.

24. Cerón, E. N.; Ortgies, D. H.; del Rosal, B.; Ren, F.; Benayas, A.; Vetrone, F.; Ma, D.; Sanz-Rodríguez, F.; Solé, J. G.; Jaque, D.; Rodríguez, E. M., Hybrid Nanostructures for High-Sensitivity Luminescence Nanothermometry in the Second Biological Window. *Adv. Mater.* **2015,** *27* (32), 4781-4787.

25. Zhang, Y.; Hong, G.; Zhang, Y.; Chen, G.; Li, F.; Dai, H.; Wang, Q., Ag_2S quantum dot: a bright and biocompatible fluorescent nanoprobe in the second near-infrared window. *ACS Nano* **2012,** *6* (5), 3695-3702.

26. Chen, G.; Tian, F.; Zhang, Y.; Zhang, Y.; Li, C.; Wang, Q., Tracking of transplanted human mesenchymal stem cells in living mice using near-infrared Ag_2S quantum dots. *Adv. Funct. Mater.* **2014,** *24* (17), 2481-2488.

27. Guo, W.; Sun, X.; Jacobson, O.; Yan, X.; Min, K.; Srivatsan, A.; Niu, G.; Kiesewetter, D. O.; Chang, J.; Chen, X., Intrinsically radioactive [^{64}Cu] CuInS/ZnS quantum dots for PET and optical imaging: improved radiochemical stability and controllable Cerenkov luminescence. *ACS Nano* **2015,** *9* (1), 488-495.

28. Lv, G.; Guo, W.; Zhang, W.; Zhang, T.; Li, S.; Chen, S.; Eltahan, A. S.; Wang, D.; Wang, Y.; Zhang, J., Near-infrared emission CuInS/ZnS quantum dots: all-in-one theranostic nanomedicines with intrinsic fluorescence/photoacoustic imaging for tumor phototherapy. *ACS Nano* **2016,** *10* (10), 9637-9645.

29. Hines, M. A.; Scholes, G. D., Colloidal PbS Nanocrystals with Size-Tunable Near-Infrared Emission: Observation of Post-Synthesis Self-Narrowing of the Particle Size Distribution. *Adv. Mater.* **2003,** *15* (21), 1844-1849.

30. Cademartiri, L.; Bertolotti, J.; Sapienza, R.; Wiersma, D. S.; von Freymann, G.; Ozin, G. A., Multigram Scale, Solventless, and Diffusion-Controlled Route to Highly Monodisperse PbS Nanocrystals. *J. Phys. Chem. B* **2006,** *110* (2), 671-673.

31. Hendricks, M. P.; Campos, M. P.; Cleveland, G. T.; Jen-La Plante, I.; Owen, J. S., A tunable library of substituted thiourea precursors to metal sulfide nanocrystals. *Science* **2015,** *348* (6240), 1226-1230.

32. Li, J. J.; Wang, Y. A.; Guo, W.; Keay, J. C.; Mishima, T. D.; Johnson, M. B.; Peng, X., Large-scale synthesis of nearly monodisperse CdSe/CdS core/shell nanocrystals using air-stable reagents via successive ion layer adsorption and reaction. *J. Am. Chem. Soc.* **2003,** *125* (41), 12567-12575.

33. Pietryga, J. M.; Werder, D. J.; Williams, D. J.; Casson, J. L.; Schaller, R. D.; Klimov, V. I.; Hollingsworth, J. A., Utilizing the lability of lead selenide to produce heterostructured nanocrystals with bright, stable infrared emission. *J. Am. Chem. Soc.* **2008,** *130* (14), 4879-4885.

34. Brumer, M.; Kigel, A.; Amirav, L.; Sashchiuk, A.; Solomesch, O.; Tessler, N.; Lifshitz, E., PbSe/PbS and PbSe/$PbSe_xS_{1-x}$ core/shell nanocrystals. *Adv. Funct. Mater.* **2005,** *15* (7), 1111-1116.

35. Dong, H.; Sun, L.-D.; Yan, C.-H., Basic understanding of the lanthanide related upconversion emissions. *Nanoscale* **2013,** *5* (13), 5703-5714.

36. Suyver, J. F.; Grimm, J.; Van Veen, M.; Biner, D.; Krämer, K.; Güdel, H.-U., Upconversion spectroscopy and properties of $NaYF_4$ doped with Er^{3+}, Tm^{3+} and/or Yb^{3+}. *J. Lumin.* **2006,** *117* (1), 1-12.

37. Aebischer, A.; Hostettler, M.; Hauser, J.; Krämer, K.; Weber, T.; Güdel, H. U.; Bürgi, H. B., Structural and Spectroscopic Characterization of Active Sites in a Family of Light-Emitting Sodium Lanthanide Tetrafluorides. *Angew. Chem. Int. Ed.* **2006,** *45* (17), 2802-2806.

38. Hong, G.; Diao, S.; Antaris, A. L.; Dai, H., Carbon Nanomaterials for Biological Imaging and Nanomedicinal Therapy. *Chem. Rev.* **2015,** *115* (19), 10816-10906.

39. Chinen, A. B.; Guan, C. M.; Ferrer, J. R.; Barnaby, S. N.; Merkel, T. J.; Mirkin, C. A., Nanoparticle Probes for the Detection of Cancer Biomarkers, Cells, and Tissues by Fluorescence. *Chem. Rev.* **2015,** *115* (19), 10530-10574.

40. Chen, G.; Qiu, H.; Prasad, P. N.; Chen, X., Upconversion Nanoparticles: Design, Nanochemistry, and Applications in Theranostics. *Chem. Rev.* **2014,** *114* (10), 5161-5214.

41. Gai, S.; Li, C.; Yang, P.; Lin, J., Recent Progress in Rare Earth Micro/Nanocrystals: Soft Chemical Synthesis, Luminescent Properties, and Biomedical Applications. *Chem. Rev.* **2013,** *114* (4), 2343-2389.

42. Reddy, L. H.; Arias, J. L.; Nicolas, J.; Couvreur, P., Magnetic Nanoparticles: Design and Characterization, Toxicity and Biocompatibility, Pharmaceutical and Biomedical Applications. *Chem. Rev.* **2012,** *112* (11), 5818-5878.

43. Laurent, S.; Forge, D.; Port, M.; Roch, A.; Robic, C.; Vander Elst, L.; Muller, R. N., Magnetic iron oxide nanoparticles: synthesis, stabilization, vectorization, physicochemical characterizations, and biological applications. *Chem. Rev.* **2008,** *108* (6), 2064-2110.

44. Corr, S. A.; Rakovich, Y. P.; Gun'ko, Y. K., Multifunctional magnetic-fluorescent nanocomposites for biomedical applications. *Nanoscale Res. Lett.* **2008,** *3* (3), 87.

45. Huang, S.; Chen, G.; Chaker, M.; Ozaki, T.; Tijssen, P.; Ma, D., Fluorescent-magnetic multifunctional nanoparticles for imaging and drug delivery. *Reviews in Nanoscience and Nanotechnology* **2013,** *2* (5), 346-364.

46. Bigall, N. C.; Parak, W. J.; Dorfs, D., Fluorescent, magnetic and plasmonic-Hybrid multifunctional colloidal nano objects. *Nano Today* **2012,** *7* (4), 282-296.

47. Li, X.; Zhao, D.; Zhang, F., Multifunctional upconversion-magnetic hybrid nanostructured materials: Synthesis and bioapplications. *Theranostics* **2013,** *3* (5), 292.

48. Wang, G.; Su, X., The synthesis and bio-applications of magnetic and fluorescent bifunctional composite nanoparticles. *Analyst* **2011,** *136* (9), 1783-1798.

49. Guerrero-Martínez, A.; Pérez-Juste, J.; Liz-Marzán, L. M., Recent Progress on Silica Coating of Nanoparticles and Related Nanomaterials. *Adv. Mater.* **2010,** *22* (11), 1182-1195.

50. Wang, F.; Chen, X.; Zhao, Z.; Tang, S.; Huang, X.; Lin, C.; Cai, C.; Zheng, N., Synthesis of magnetic, fluorescent and mesoporous core-shell-structured nanoparticles for imaging, targeting and photodynamic therapy. *J. Mater. Chem.* **2011,** *21* (30), 11244-11252.

51. Badruddoza, A. Z. M.; Rahman, M. T.; Ghosh, S.; Hossain, M. Z.; Shi, J.; Hidajat, K.; Uddin, M. S., β-Cyclodextrin conjugated magnetic, fluorescent silica core-shell nanoparticles for biomedical applications. *Carbohydr. Polym.* **2013,** *95* (1), 449-457.

52. Chang, Z.-m.; Wang, Z.; Shao, D.; Yue, J.; Lu, M.-m.; Li, L.; Ge, M.; Yang, D.; Li, M.-q.; Yan, H., Fluorescent-magnetic Janus nanorods for selective capture and rapid identification of foodborne bacteria. *Sens. actuators. B: Chem.* **2018,** *260*, 1004-1011.

53. Wan, J.; Meng, X.; Liu, E.; Chen, K., Incorporation of magnetite nanoparticle clusters in fluorescent silica nanoparticles for high-performance brain tumor delineation. *Nanotechnology* **2010,** *21* (23), 235104.

54. Torkpur-Biglarianzadeh, M.; Salami-Kalajahi, M., Multilayer fluorescent magnetic nanoparticles with dual thermoresponsive and pH-sensitive polymeric nanolayers as anti-cancer drug carriers. *RSC Adv.* **2015,** *5* (38), 29653-29662.

55. Li, L.; Liu, C.; Zhang, L.; Wang, T.; Yu, H.; Wang, C.; Su, Z., Multifunctional magnetic-fluorescent eccentric-(concentric-Fe_3O_4@SiO_2)@polyacrylic acid core-shell nanocomposites for cell imaging and pH-responsive drug delivery. *Nanoscale* **2013,** *5* (6), 2249-2253.

56. Zhang, L.; Wang, T.; Li, L.; Wang, C.; Su, Z.; Li, J., Multifunctional fluorescent-magnetic polyethyleneimine functionalized Fe_3O_4-mesoporous silica yolk-shell nanocapsules for siRNA delivery. *Chem. Commun.* **2012,** *48* (69), 8706-8708.

57. Cho, Y.-S.; Yoon, T.-J.; Jang, E.-S.; Hong, K. S.; Lee, S. Y.; Kim, O. R.; Park, C.; Kim, Y.-J.; Yi, G.-C.; Chang, K., Cetuximab-conjugated magneto-fluorescent silica nanoparticles for *in vivo* colon cancer targeting and imaging. *Cancer Lett.* **2010,** *299* (1), 63-71.

58. Lee, J. E.; Lee, N.; Kim, H.; Kim, J.; Choi, S. H.; Kim, J. H.; Kim, T.; Song, I. C.; Park, S. P.; Moon, W. K., Uniform mesoporous dye-doped silica nanoparticles decorated with multiple magnetite

nanocrystals for simultaneous enhanced magnetic resonance imaging, fluorescence imaging, and drug delivery. *J. Am. Chem. Soc.* **2009,** *132* (2), 552-557.

59. Byoun, W.; Jang, M.; Yoo, H., Fabrication of highly fluorescent multiple Fe_3O_4 nanoparticles core-silica shell nanoparticles. *J Nanopart Res* **2019,** *21* (1), 1.

60. Rittikulsittichai, S.; Singhana, B.; Bryan, W. W.; Sarangi, S.; Jamison, A. C.; Brazdeikis, A.; Lee, T. R., Preparation, characterization, and utilization of multi-functional magnetic-fluorescent composites for bio-imaging and magnetic hyperthermia therapy. *RSC Adv.* **2013,** *3* (21), 7838-7849.

61. Chekina, N.; Horak, D.; Jendelova, P.; Trchova, M.; Benes, M. J.; Hruby, M.; Herynek, V.; Turnovcova, K.; Sykova, E., Fluorescent magnetic nanoparticles for biomedical applications. *J. Mater. Chem.* **2011,** *21* (21), 7630-7639.

62. Chekina, N.; Horák, D.; Jendelová, P.; Trchová, M.; Beneš, M. J.; Hrubý, M.; Herynek, V.; Turnovcová, K.; Syková, E., Fluorescent magnetic nanoparticles for biomedical applications. *J. Mater. Chem.* **2011,** *21* (21), 7630-7639.

63. Lu, Y.; He, B.; Shen, J.; Li, J.; Yang, W.; Yin, M., Multifunctional magnetic and fluorescent core-shell nanoparticles for bioimaging. *Nanoscale* **2015,** *7* (5), 1606-1609.

64. Fu, A.; Wilson, R. J.; Smith, B. R.; Mullenix, J.; Earhart, C.; Akin, D.; Guccione, S.; Wang, S. X.; Gambhir, S. S., Fluorescent magnetic nanoparticles for magnetically enhanced cancer imaging and targeting in living subjects. *ACS Nano* **2012,** *6* (8), 6862-6869.

65. Song, E.; Han, W.; Li, J.; Jiang, Y.; Cheng, D.; Song, Y.; Zhang, P.; Tan, W., Magnetic-encoded fluorescent multifunctional nanospheres for simultaneous multicomponent analysis. *Anal. Chem.* **2014,** *86* (19), 9434-9442.

66. Hu, D.; Chen, M.; Gao, Y.; Li, F.; Wu, L., A facile method to synthesize superparamagnetic and up-conversion luminescent $NaYF_4$:Yb,Er/Tm@SiO_2@Fe_3O_4 nanocomposite particles and their bioapplication. *J. Mater. Chem.* **2011,** *21* (30), 11276-11282.

67. Koc, K.; Karakus, B.; Rajar, K.; Alveroglu, E., Synthesis and characterization of ZnS@ Fe_3O_4 fluorescent-magnetic bifunctional nanospheres. *Superlattices Microstruct.* **2017,** *110*, 198-204.

68. Ding, H. L.; Zhang, Y. X.; Wang, S.; Xu, J. M.; Xu, S. C.; Li, G. H., Fe_3O_4@SiO_2 Core/Shell Nanoparticles: The Silica Coating Regulations with a Single Core for Different Core Sizes and Shell Thicknesses. *Chem. Mater.* **2012,** *24* (23), 4572-4580.

69. Wang, J.; Shah, Z. H.; Zhang, S.; Lu, R., Silica-based nanocomposites via reverse microemulsions: classifications, preparations, and applications. *Nanoscale* **2014,** *6* (9), 4418-4437.

70. Gao, Y.; Zou, X.; Zhao, J. X.; Li, Y.; Su, X., Graphene oxide-based magnetic fluorescent hybrids for drug delivery and cellular imaging. *Colloid Surf. B-Biointerfaces* **2013,** *112*, 128-133.

71. Wang, K.; Ruan, J.; Qian, Q.; Song, H.; Bao, C.; Zhang, X.; Kong, Y.; Zhang, C.; Hu, G.; Ni, J., BRCAA1 monoclonal antibody conjugated fluorescent magnetic nanoparticles for *in vivo* targeted magnetofluorescent imaging of gastric cancer. *J. Nanobiotechnol.* **2011,** *9* (1), 23.

72. Zhang, F.; Braun, G. B.; Pallaoro, A.; Zhang, Y.; Shi, Y.; Cui, D.; Moskovits, M.; Zhao, D.; Stucky, G. D., Mesoporous Multifunctional Upconversion Luminescent and Magnetic "Nanorattle" Materials for Targeted Chemotherapy. *Nano Lett.* **2011,** *12* (1), 61-67.

73. Yin, N.; Wu, P.; Liang, G.; Cheng, W., A multifunctional mesoporous Fe_3O_4/SiO_2/CdTe magnetic-fluorescent composite nanoprobe. *Appl. Phys. A.* **2016,** *122* (3), 243.

74. Liu, H.; Wang, T.; Zhang, L.; Li, L.; Wang, Y. A.; Wang, C.; Su, Z., Selected-Control Fabrication of Multifunctional Fluorescent-Magnetic Core-Shell and Yolk-Shell Hybrid Nanostructures. *Chem.-Eur. J* **2012,** *18* (12), 3745-3752.

75. Chen, H.; Colvin, D. C.; Qi, B.; Moore, T.; He, J.; Mefford, O. T.; Alexis, F.; Gore, J. C.; Anker, J. N., Magnetic and optical properties of multifunctional core–shell radioluminescence nanoparticles. *J. Mater. Chem.* **2012,** *22* (25), 12802-12809.

76. Zhu, X.; Zhou, J.; Chen, M.; Shi, M.; Feng, W.; Li, F., Core–shell Fe_3O_4@$NaLuF_4$:Yb,Er/Tm nanostructure for MRI, CT and upconversion luminescence tri-modality imaging. *Biomaterials* **2012,** *33* (18), 4618-4627.

77. Gai, S.; Yang, P.; Li, C.; Wang, W.; Dai, Y.; Niu, N.; Lin, J., Synthesis of Magnetic, Up-Conversion Luminescent, and Mesoporous Core–Shell-Structured Nanocomposites as Drug Carriers. *Adv. Funct. Mater.* **2010,** *20* (7), 1166-1172.

78. Zhang, P.-H.; Cao, J.-T.; Min, Q.-H.; Zhu, J.-J., Multi-shell structured fluorescent-magnetic nanoprobe for target cell imaging and on-chip sorting. *ACS Appl. Mater. Interfaces* **2013,** *5* (15), 7417-7424.

79. Xu, Y.; Karmakar, A.; Wang, D.; Mahmood, M. W.; Watanabe, F.; Zhang, Y.; Fejleh, A.; Fejleh, P.; Li, Z.; Kannarpady, G., Multifunctional Fe_3O_4 cored magnetic-quantum dot fluorescent nanocomposites for RF nanohyperthermia of cancer cells. *J. Phys. Chem. C* **2010,** *114* (11), 5020-5026.

80. Chen, S.; Zhang, J.; Song, S.; Xiong, C.; Dong, L., Hydrangea-like magneto-fluorescent nanoparticles through thiol-inducing assembly. *Mater. Res. Express.* **2017,** *4* (1), 015008.

81. Cho, H.-S.; Dong, Z.; Pauletti, G. M.; Zhang, J.; Xu, H.; Gu, H.; Wang, L.; Ewing, R. C.; Huth, C.; Wang, F., Fluorescent, superparamagnetic nanospheres for drug storage, targeting, and imaging: a multifunctional nanocarrier system for cancer diagnosis and treatment. *ACS Nano* **2010,** *4* (9), 5398-5404.

82. Koktysh, D.; Bright, V.; Pham, W., Fluorescent magnetic hybrid nanoprobe for multimodal bioimaging. *Nanotechnology* **2011,** *22* (27), 275606.

83. Lu, X.; Jiang, R.; Fan, Q.; Zhang, L.; Zhang, H.; Yang, M.; Ma, Y.; Wang, L.; Huang, W., Fluorescent-magnetic poly (poly (ethyleneglycol) monomethacrylate)-grafted Fe_3O_4 nanoparticles from post-atom-transfer-radical-polymerization modification: synthesis, characterization, cellular uptake and imaging. *J. Mater. Chem.* **2012,** *22* (14), 6965-6973.

84. Bhattacharya, D.; Das, M.; Mishra, D.; Banerjee, I.; Sahu, S. K.; Maiti, T. K.; Pramanik, P., Folate receptor targeted, carboxymethyl chitosan functionalized iron oxide nanoparticles: a novel ultradispersed nanoconjugates for bimodal imaging. *Nanoscale* **2011,** *3* (4), 1653-1662.

85. Kim, H. M.; Lee, H.; Hong, K. S.; Cho, M. Y.; Sung, M.-H.; Poo, H.; Lim, Y. T., Synthesis and high performance of magnetofluorescent polyelectrolyte nanocomposites as MR/near-infrared multimodal cellular imaging nanoprobes. *ACS Nano* **2011,** *5* (10), 8230-8240.

86. Fan, H.-M.; Olivo, M.; Shuter, B.; Yi, J.-B.; Bhuvaneswari, R.; Tan, H.-R.; Xing, G.-C.; Ng, C.-T.; Liu, L.; Lucky, S. S., Quantum dot capped magnetite nanorings as high performance nanoprobe for multiphoton fluorescence and magnetic resonance imaging. *J. Am. Chem. Soc.* **2010,** *132* (42), 14803-14811.

87. Lou, L.; Yu, K.; Zhang, Z.; Li, B.; Zhu, J.; Wang, Y.; Huang, R.; Zhu, Z., Functionalized magnetic-fluorescent hybrid nanoparticles for cell labelling. *Nanoscale* **2011,** *3* (5), 2315-2323.

88. Chen, S.; Zhang, J.; Song, S.; Feng, R.; Ju, Y.; Xiong, C.; Dong, L., Hydrophilic Magnetofluorescent Nanobowls: Rapid Magnetic Response and Efficient Photoluminescence. *Langmuir* **2016,** *32* (2), 611-618.

89. Feld, A.; Merkl, J. P.; Kloust, H.; Flessau, S.; Schmidtke, C.; Wolter, C.; Ostermann, J.; Kampferbeck, M.; Eggers, R.; Mews, A., A Universal Approach to Ultrasmall Magneto-Fluorescent Nanohybrids. *Angew. Chem. Int. Ed.* **2015,** *54* (42), 12468-12471.

90. Song, E.-Q.; Hu, J.; Wen, C.-Y.; Tian, Z.-Q.; Yu, X.; Zhang, Z.-L.; Shi, Y.-B.; Pang, D.-W., Fluorescent-magnetic-biotargeting multifunctional nanobioprobes for detecting and isolating multiple types of tumor cells. *ACS Nano* **2011,** *5* (2), 761-770.

91. Di Corato, R.; Bigall, N. C.; Ragusa, A.; Dorfs, D.; Genovese, A.; Marotta, R.; Manna, L.; Pellegrino, T., Multifunctional nanobeads based on quantum dots and magnetic nanoparticles: synthesis and cancer cell targeting and sorting. *ACS Nano* **2011,** *5* (2), 1109-1121.

92. Ruan, G.; Vieira, G.; Henighan, T.; Chen, A.; Thakur, D.; Sooryakumar, R.; Winter, J. O., Simultaneous magnetic manipulation and fluorescent tracking of multiple individual hybrid nanostructures. *Nano Lett.* **2010,** *10* (6), 2220-2224.

93. Ortgies, D. H.; De La Cueva, L.; Del Rosal, B.; Sanz-Rodríguez, F.; Fernández, N.; Iglesias-de la Cruz, M. C.; Salas, G.; Cabrera, D.; Teran, F. J.; Jaque, D., *In vivo* deep tissue fluorescence and magnetic imaging employing hybrid nanostructures. *ACS Appl. Mater. Interfaces* **2016,** *8* (2), 1406-1414.

94. Materia, M. E.; Pernia Leal, M.; Scotto, M.; Balakrishnan, P. B.; Kumar Avugadda, S.; García-Martín, M. L.; Cohen, B. E.; Chan, E. M.; Pellegrino, T., Multifunctional Magnetic and Upconverting Nanobeads as Dual Modal Imaging Tools. *Bioconjug. Chem.* **2017,** *28* (11), 2707-2714.

95. Xu, H.; Cheng, L.; Wang, C.; Ma, X.; Li, Y.; Liu, Z., Polymer encapsulated upconversion nanoparticle/iron oxide nanocomposites for multimodal imaging and magnetic targeted drug delivery. *Biomaterials* **2011,** *32* (35), 9364-9373.

96. Xia, A.; Gao, Y.; Zhou, J.; Li, C.; Yang, T.; Wu, D.; Wu, L.; Li, F., Core-shell $NaYF_4$:Yb^{3+}, Tm^{3+}@Fe_xO_y nanocrystals for dual-modality T_2-enhanced magnetic resonance and NIR-to-NIR upconversion luminescent imaging of small-animal lymphatic node. *Biomaterials* **2011,** *32* (29), 7200-7208.

97. Zhong, C.; Yang, P.; Li, X.; Li, C.; Wang, D.; Gai, S.; Lin, J., Monodisperse bifunctional Fe_3O_4@ $NaGdF_4$:Yb/Er@$NaGdF_4$:Yb/Er core–shell nanoparticles. *RSC Adv.* **2012,** *2* (8), 3194-3197.

98. Cui, X.; Mathe, D.; Kovács, N. m.; Horváth, I.; Jauregui-Osoro, M.; Torres Martin de Rosales, R.; Mullen, G. E.; Wong, W.; Yan, Y.; Krüger, D., Synthesis, characterization, and application of core-shell $Co_{0.16}Fe_{2.84}O_4$@$NaYF_4$(Yb, Er) and Fe_3O_4@$NaYF_4$(Yb, Tm) nanoparticle as Trimodal (MRI, PET/SPECT, and optical) imaging agents. *Bioconjug. Chem.* **2015,** *27* (2), 319-328.

99. Zhang, L.; Wang, Y.-S.; Yang, Y.; Zhang, F.; Dong, W.-F.; Zhou, S.-Y.; Pei, W.-H.; Chen, H.-D.; Sun, H.-B., Magnetic/upconversion luminescent mesoparticles of Fe_3O_4@LaF_3:Yb^{3+}, Er^{3+} for dual-modal bioimaging. *Chem. Commun.* **2012,** *48* (91), 11238-11240.

100. Shen, J.; Sun, L.-D.; Zhang, Y.-W.; Yan, C.-H., Superparamagnetic and upconversion emitting Fe_3O_4/$NaYF_4$:Yb, Er hetero-nanoparticles via a crosslinker anchoring strategy. *Chem. Commun.* **2010,** *46* (31), 5731-5733.

101. Xia, A.; Gao, Y.; Zhou, J.; Li, C.; Yang, T.; Wu, D.; Wu, L.; Li, F., Core-shell $NaYF_4$:Yb^{3+},Tm^{3+}@Fe_xO_y nanocrystals for dual-modality T_2-enhanced magnetic resonance and NIR-to-NIR upconversion luminescent imaging of small-animal lymphatic node. *Biomaterials* **2011,** *32* (29), 7200-7208.

102. Pahari, S. K.; Olszakier, S.; Kahn, I.; Amirav, L., Magneto-Fluorescent Yolk-Shell Nanoparticles. *Chem. Mater.* **2018,** *30* (3), 775-780.

103. Jha, D. K.; Saikia, K.; Chakrabarti, S.; Bhattacharya, K.; Varadarajan, K. S.; Patel, A. B.; Goyary, D.; Chattopadhyay, P.; Deb, P., Direct one-pot synthesis of glutathione capped hydrophilic FePt-CdS nanoprobe for efficient bimodal imaging application. *Mater. Sci. Eng. C* **2017,** *72*, 415-424.

104. Part, F.; Zaba, C.; Bixner, O.; Grünewald, T. A.; Michor, H.; Küpcü, S.; Debreczeny, M.; De Vito Francesco, E.; Lassenberger, A.; Schrittwieser, S., Doping Method Determines Para-or Superparamagnetic Properties of Photostable and Surface-Modifiable Quantum Dots for Multimodal Bioimaging. *Chem. Mater.* **2018,** *30* (13), 4233-4241.

105. Norris, D. J.; Yao, N.; Charnock, F. T.; Kennedy, T. A., High-quality manganese-doped ZnSe nanocrystals. *Nano Lett.* **2001,** *1* (1), 3-7.

106. Heer, S.; Kömpe, K.; Güdel, H. U.; Haase, M., Highly efficient multicolour upconversion emission in transparent colloids of lanthanide-doped $NaYF_4$ nanocrystals. *Adv. Mater.* **2004,** *16* (23-24), 2102-2105.

107. Sivakumar, S.; van Veggel, F. C. M.; Raudsepp, M., Bright White light through up-conversion of a single NIR source from Sol-Gel-Derived thin film made with Ln^{3+}-doped LaF_3 nanoparticles. *J. Am. Chem. Soc.* **2005,** *127* (36), 12464-12465.

108. Wernsdorfer, W.; Orozco, E. B.; Hasselbach, K.; Benoit, A.; Mailly, D.; Kubo, O.; Nakano, H.; Barbara, B., Macroscopic quantum tunneling of magnetization of single ferrimagnetic nanoparticles of barium ferrite. *Phys. Rev. Lett.* **1997,** *79* (20), 4014.

109. Gedda, G.; Chen, G.-R.; Yao, Y.-Y.; Girma, W. M.; Li, J.-D.; Yen, C.-L.; Ling, Y.-C.; Chang, J.-Y., Aqueous synthesis of dual-targeting Gd-doped $CuInS_2$/ZnS quantum dots for cancer-specific bi-modal imaging. *New J Chem* **2017,** *41* (23), 14161-14170.

110. Guo, W.; Yang, W.; Wang, Y.; Sun, X.; Liu, Z.; Zhang, B.; Chang, J.; Chen, X., Color-tunable Gd-Zn-Cu-In-S/ZnS quantum dots for dual modality magnetic resonance and fluorescence imaging. *Nano res.* **2014,** *7* (11), 1581-1591.

111. Yang, W.; Guo, W.; Gong, X.; Zhang, B.; Wang, S.; Chen, N.; Yang, W.; Tu, Y.; Fang, X.; Chang, J., Facile synthesis of Gd-Cu-In-S/ZnS bimodal quantum dots with optimized properties for tumor targeted fluorescence/MR *in vivo* imaging. *ACS Appl. Mater. Interfaces* **2015,** *7* (33), 18759-18768.

112. Li, Z.; Dergham, A.; McCulloch, H.; Qin, Y.; Yang, X.; Zhang, J.; Cao, X., Facile synthesis of Gd-doped CdTe quantum dots with optimized properties for optical/MR multimodal imaging. *JBIC J. Biol. Inorg. Chem.* **2017,** *22* (8), 1151-1163.

113. Zheng, Y.; Zou, Y.; Jiang, J., Synthesis of Gd-doped $CuInS_2$ quantum dots exhibiting photoluminescence and high longitudinal relaxivity. *Mater. Lett.* **2016,** *168*, 86-89.

114. Venkatesha, N.; Poojar, P.; Qurishi, Y.; Geethanath, S.; Srivastava, C., $Zn_{1-x}Gd_xS$ (x= 0.1, 0.2 and 0.3) nanoparticles for magnetic resonance imaging and optical fluorescence imaging. *Mater. Res. Express.* **2017,** *4* (3), 035030.

115. Zhou, R.; Sun, S.; Li, C.; Wu, L.; Hou, X.; Wu, P., Enriching Mn-Doped ZnSe Quantum Dots onto Mesoporous Silica Nanoparticles for Enhanced Fluorescence/Magnetic Resonance Imaging Dual-Modal Bio-Imaging. *ACS Appl. Mater. Interfaces* **2018,** *10* (40), 34060-34067.

116. Law, W.-C.; Xu, Z.; Yong, K.-T.; Liu, X.; Swihart, M. T.; Seshadri, M.; Prasad, P. N., Manganese-doped near-infrared emitting nanocrystals for *in vivo* biomedical imaging. *Opt. Express* **2016,** *24* (16), 17553-17561.

117. Cheng, L.; Yang, K.; Li, Y.; Chen, J.; Wang, C.; Shao, M.; Lee, S. T.; Liu, Z., Facile preparation of multifunctional upconversion nanoprobes for multimodal imaging and dual-targeted photothermal therapy. *Angew. Chem. Int. Ed.* **2011,** *123* (32), 7523-7528.

118. Zhang, L.; Wang, Y.; Tang, Y.; Jiao, Z.; Xie, C.; Zhang, H.; Gu, P.; Wei, X.; Yang, G.-Y.; Gu, H., High MRI performance fluorescent mesoporous silica-coated magnetic nanoparticles for tracking neural progenitor cells in an ischemic mouse model. *Nanoscale* **2013,** *5* (10), 4506-4516.

119. Cho, H.-S.; Dong, Z.; Pauletti, G. M.; Zhang, J.; Xu, H.; Gu, H.; Wang, L.; Ewing, R. C.; Huth, C.; Wang, F.; Shi, D., Fluorescent, Superparamagnetic Nanospheres for Drug Storage, Targeting, and Imaging: A Multifunctional Nanocarrier System for Cancer Diagnosis and Treatment. *ACS Nano* **2010,** *4* (9), 5398-5404.

120. Kim, K. S.; Kim, J.; Lee, J. Y.; Matsuda, S.; Hideshima, S.; Mori, Y.; Osaka, T.; Na, K., Stimuli-responsive magnetic nanoparticles for tumor-targeted bimodal imaging and photodynamic/hyperthermia combination therapy. *Nanoscale* **2016,** *8* (22), 11625-11634.

121. Gilchrist, R.; Medal, R.; Shorey, W. D.; Hanselman, R. C.; Parrott, J. C.; Taylor, C. B., Selective inductive heating of lymph nodes. *Ann. Surg.* **1957,** *146* (4), 596.

122. Jaque, D.; Martínez Maestro, L.; del Rosal, B.; Haro-Gonzalez, P.; Benayas, A.; Plaza, J. L.; Martín Rodríguez, E.; García Solé, J., Nanoparticles for photothermal therapies. *Nanoscale* **2014,** *6* (16), 9494-9530.

123. AG, M., MagForce AG Corporate News. *https://www.magforce.com/en/presse-investoren/news-events/corporate-news/corporate-news-archiv/browse/1/select_category/23.html (accessed Dec 28, 2018)*.

124. Ortgies, D. H.; Teran, F. J.; Rocha, U.; de la Cueva, L.; Salas, G.; Cabrera, D.; Vanetsev, A. S.; Rähn, M.; Sammelselg, V.; Orlovskii, Y. V., Optomagnetic nanoplatforms for in situ controlled hyperthermia. *Adv. Funct. Mater.* **2018,** *28* (11), 1704434.

125. De Paula, L.; Primo, F.; Pinto, M.; Morais, P.; Tedesco, A., Evaluation of a chloroaluminium phthalocyanine-loaded magnetic nanoemulsion as a drug delivery device to treat glioblastoma using hyperthermia and photodynamic therapy. *RSC Adv.* **2017,** *7* (15), 9115-9122.

Résumé

L'introduction

Les nanoparticules (NP) magnétiques ont été largement utilisées pour des applications biomédicales au cours des dernières décennies. Lorsque la taille des NP magnétiques diminue à une taille critique, chaque NP devient un seul domaine magnétique, ce qui donne lieu à la formation de NP superparamagnétiques. Les NPs superparamagnétiques sont rapidement saturés sous un champ magnétique (MF) externe et présentent une magnétisation et une coercivité résiduelles nulles lors de l'élimination du MF externe. [2,3] Par conséquent, les NPs superparamagnétiques peuvent être facilement manipulés par une MF externe et bien dispersés dans la solution après élimination de la MF externe, ce qui diffère nettement du comportement des NP ferromagnétiques classiques, qui forment des agglomérats non séparables après le confinement magnétique initial. Cette unique propriété super-paramagnétique leur confère d'énormes avantages pour diverses applications biologiques, notamment les agents de contraste pour imagerie par résonance magnétique (IRM), les diagnostics médicaux et le traitement de l'hyperthermie magnétique.

D'autre part, les NP fluorescents, qui présentent la fluorescence souhaitée sous une excitation optique appropriée, ont attiré une attention considérable pour les applications biologiques. Parmi ces NP fluorescents, les points quantiques (QD), également connus sous le nom de minuscules nanocristaux semi-conducteurs dont la taille est inférieure au rayon de l'exciton de Bohr, sont devenus des marqueurs fluorescents prometteurs. Contrairement à leurs matériaux massifs, les QD possèdent une bande interdite dépendante de la taille et résultant de l'effet de confinement quantique. Cela signifie que la bande interdite des QD diminue à mesure que la taille des QD augmente, car de plus en plus d'atomes sont liés les uns aux autres, ce qui fait que les niveaux d'énergie discrets se fondent progressivement en bandes d'énergie continuées. [17] La caractéristique unique de la bande interdite accordable résulte en les propriétés optiques des QD dépendantes de la taille, qui permettent éventuellement d'accorder leur photoluminescence sur une large plage spectrale en faisant varier leur taille. [18] Outre les QD, les NP à conversion ascendante dopées au lanthanide (UCNP) constituent une autre nouvelle classe de marque-bio fluorescent utilisé couramment pour les applications biologiques, en raison de plusieurs avantages, notamment de grands décalages de Stokes, une bonne stabilité chimique et physique et une faible toxicité. Fondamentalement, les UCNP sont constitués d'hôte cristallin inorganique et d'ions lanthanides dopés. Dans le processus fluorescent de conversion ascendante, les ions lanthanides dopés absorbent deux ou plusieurs photons d'excitation à basse énergie séquentiels dans la gamme NIR, puis se convertissent en un photon d'émission de haute énergie, généralement dans la gamme de UV/visible. [36, 37]

Cependant, les marqueurs fluorescents traditionnels sont basés sur des QD et des UCNP à émission visible, qui souffrent d'une faible profondeur de pénétration dans les tissus en raison de l'absorption considérable de lumière par les tissus et d'un faible rapport signal sur fond en raison d'une forte fluorescence du fond et aussi de diffusion de la lumière à partir de tissus biologiques. [7, 14] C'est une barrière majeure pour l'imagerie *in vivo*. Afin de résoudre ce problème, l'imagerie par fluorescence doit être réalisée avec une région de longueur d'onde supérieure à 650 nm. Des études précédemment rapportées ont prouvé que l'extinction globale pouvait être minimisée dans les deux gammes de longueurs d'onde (650-950 nm et 1000-1350 nm), appelées première et deuxième fenêtres biologiques (NIR-I et NIR-II). [15] De plus, le fond d'auto-fluorescence peut être minimisé car la lumière d'excitation absorbée par les tissus est négligeable dans NIR-I/II. Le développement de QD NIR et de NPs dopés au lanthanide est donc hautement souhaité pour les applications biologiques.

Au cours de la dernière décennie, les QD PbS émettant des signaux NIR avec une bande interdite directe de 0.41 eV à la température ambiante et un rayon de Bohr de 18 nm exciton large, fournissant une émission de fluorescence ajustable dans les régions NIR (825-1750 nm), suscitent une attention croissante pour les applications biologiques. [29] Normalement, les QD PbS étaient synthétisés selon la méthode d'injection à chaud, dans laquelle la source de soufre était directement injectée dans les précurseurs organométalliques de plomb. [29] En utilisant cette méthode, des QD PbS de haute qualité peuvent être obtenus, car les étapes de nucléation et de croissance des QD PbS sont efficacement séparées en contrôlant précisément la température pendant le processus d'injection à chaud. Cependant, le sulfure de bis (triméthylsilyle) toxique [$(TMS)_2S$] en tant que source de soufre dans la synthèse des QD et la manipulation obligatoire de la sensibilité à l'air et à l'humidité $(TMS)_2S$ dans la boîte à gants ont rendu cette synthèse compliquée et peu pratique pour la fabrication à grande échelle dans l'industrie. Dans notre travail, nous avons fait notre possible pour synthétiser les QD PbS en remplaçant $(TMS)_2S$ par du soufre élémentaire dans un système plus simple et plus vert de l'OLA « non visqueux». Récemment, les NP dopés au Nd^{3+} sont en train de devenir l'un des domaines de recherche qui se développent le plus rapidement en raison de leur section efficace d'absorption élevée et de leur faible phototoxicité par rapport aux UCNP dopés au Yb^{3+} couramment utilisés. Plus important encore, les nanoparticules dopées au Nd^{3+} peuvent être efficacement excitées par laser à environs 800 nm (NIR-I) et présentent trois pics d'émission à 900 (NIR-I), 1060 (NIR-II) et 1340 nm (NIR-II). Les longueurs d'onde d'excitation et d'émission des NP dopées au Nd^{3+} sont situées dans les fenêtres biologiques optiquement transparentes dans le proche infrarouge, ce qui leur permet d'avoir une propriété optique pénétrée dans le tissu profond avec un rapport signal sur bruit élevé.

Compte tenu de tous ces avantages des NP super-paramagnétiques et des Nd^{3+} fluorescents PbS fluorescents, combiner ces deux composants en une seule nano-architecture va sans aucun doute mener à une nouvelle gamme d'applications potentielles dans le domaine de la biomédecine. En bref, ces NP multifonctionnelles présentent au moins deux caractéristiques attrayantes, les propriétés de fluorescence (avec absorption et émission dans les régions NIR) et le super-paramagnétisme, qui leur permettent de jouer le rôle d'outils multidimensionnels (imagerie, confinement et traitement) dans les applications biomédicales. .

Les objectifs de la thèse

Cette thèse est divisée en deux parties avec deux objectifs étroitement liés. Spécifiquement, deux types principaux de nano-plateforme multifonctionnelles seront conçus sur la base d'un noyau magnétique. Le premier type est une structure noyau / coque avec une couche de fluorescence autour d'un seul noyau magnétique, tandis que l'autre nano-plateforme multifonctionnelle contient des NPS magnétiques et fluorescents qui se distribuent de façon aléatoire.

Partie I: Nano-composites multifonctionnels (super-paramagnétiques et photoluminescents NIR à NIR) avec un seul noyau magnétique pour la bio-imagerie bimodale.

Jusqu'ici, les NP multifonctionnels (superparamagnétiques et photoluminescents) se sont révélés être des outils extrêmement utiles pour les applications biologiques. L'une des applications biologiques les plus intéressantes est leur utilisation pour l'imagerie bimodale. Il est bien connu que l'imagerie optique présente un grand potentiel de traduction dans la clinique en raison de sa grande sensibilité au niveau subcellulaire et du coût relativement bas des installations d'imagerie; tandis que l'IRM est considérée comme une technique supérieure pour obtenir des images anatomiques, physiologiques et fonctionnelles avec une résolution spatiale 3D élevée. L'intégration de l'imagerie optique et IRM pour l'imagerie bimodale est clairement avantageuse dans la mesure où elle permettra de récupérer des informations macroscopiques et subcellulaires d'espèces biologiques, qui peut finalement améliorer la précision du diagnostic. Il est donc très important de concevoir de nouveaux NP multifonctionnels (super-paramagnétiques et photoluminescents) à haute sensibilité pour l'imagerie bimodale. Cependant, les NP multifonctionnelles (super-paramagnétiques et photoluminescentes) sont dans la plupart des cas basées sur des colorants organiques émetteurs visibles, des QD et des UCNPs, qui présentent une faible pénétration dans le tissu et une autofluorescence sévère à partir de tissu biologique, limitant ainsi leur utilisation comme bio-sonde pour l'imagerie *in vivo*. Pour résoudre ce problème, les composants photoluminescents idéaux avec leurs longueurs d'onde d'absorption et d'émission dans les fenêtres biologiques optiquement transparentes (NIR-

I/II) sont hautement souhaités. Cela peut garantir que les signaux d'excitation et d'émission sont moins atténués pour l'acquisition d'une imagerie des tissus profonds avec un rapport signal sur bruit plus élevé.

Par conséquent, les objectifs pour cette partie sont les suivants:

1. Préparation et caractérisation de nouveaux nano-composites multifonctionnels (superparamagnétiques et photoluminescents) noyau / coquille / coquille $Fe_3O_4/SiO_2/NaYF_4:Nd^{3+}$.

2. Recherche des propriétés de photoluminescence NIR à NIR de $Fe_3O_4/SiO_2/NaYF_4:Nd^{3+}$.

3. En comparant les propriétés de pénétration des tissus profonds de NIR-à-NIR $Fe_3O_4/SiO_2/NaYF_4:Nd^{3+}$ IP avec visible émettant de la conversion ascendante $Fe_3O_4/SiO_2/NaYF_4:Er^{3+}$, Yb^{3+} IP par imagerie optique *ex vivo*.

4. Exploitation de $Fe_3O_4/SiO_2/NaYF_4:Nd^{3+}$ comme agent de contraste T_2 pour l'IRM

Partie II: Nano-plateforme multifonctionnelles basées sur plusieurs NP magnétiques et QD NIR à modalité thérapeutique

Le développement de nano-plateforme théranostiques multifonctionnelles avancées est essentiel pour relever les défis du traitement du cancer, dans l'objectif de réaliser les objectifs ultimes de la médecine personnalisée. On s'attend à ce que ces systèmes assument simultanément des fonctions diagnostiques et thérapeutiques afin d'obtenir des images de haute qualité identifiant le site et la morphologie de la tumeur et d'atteindre le taux de guérison accru des cancers par le biais de stratégies thérapeutiques spécifiques. Le taux de survie peut être largement augmenté grâce à ces nano-plateforme théranostiques multifonctionnelles. Plus précisément, comparée avec l'imagerie optique et à l'imagerie par résonance magnétique uniquement, en tant qu'outil de diagnostic individuel, l'imagerie bimodale s'est révélée particulièrement intéressante, car elle peut fournir des informations complémentaires, comme indiqué dans la partie de l'introduction. En ce qui concerne les modalités thérapeutiques liées aux nano-plateforme, la thérapie magnétothermique est gênée par la faible efficacité de transfert d'énergie thermique des nanoparticules magnétiques, tandis que la thérapie photo-thermique ne convient pas aux cellules cancéreuses dans des organes distants en raison de la profondeur de pénétration de la lumière dans les tissus. Ainsi, l'intégration de la thérapie magnétothermique et photo-thermique dans une seule nano-plateforme peut constituer une approche thérapeutique à deux modes permettant d'obtenir un traitement du cancer des tissus profonds à haute efficacité. En outre, les chimiothérapies conventionnelles contre les cancers souffrent souvent de la faible efficacité thérapeutique (la monothérapie n'ayant pas la capacité de guérir le cancer de manière synergique

ou additive) et d'effets secondaires graves à cause des caractéristiques de libération incontrôlable du médicament. Une nano-plateforme multifonctionnelle (super-paramagnétique et photoluminescente) avec mode de délivrance de médicament peut améliorer les performances des agents chimiothérapeutiques, et réduire la toxicité globale en renforçant la spécificité de la délivrance de médicament par ciblage tumoral en présence d'un champ magnétique appliqué. En outre, la conception de nano-plateforme externes sensibles au stimulus pour un traitement du cancer contrôlé à distance peut potentiellement éviter une surdose de médicament et réduire les effets secondaires.

Par conséquent, les objectifs pour cette partie sont les suivants:

1. Préparer et caractériser les super-nanoparticules de Fe_3O_4 et PbS/CdS (NIR-II) auto-assemblées [SASN (NIR-II)], et étudier leur mécanisme de formation d'auto-assemblage.

2. Recherche de l'application des SASN (NIR-II) pour l'imagerie bimodale des tissus profonds (optique et IRM).

3. Étudier le traitement thermique bimodale (thérapie magnétothermique et photo-thermique) à l'aide de SASN (NIR-II).

4. Synthétiser et caractériser une nano-plateforme multifonctionnelle (super-paramagnétique et photoluminescente) à base de $mSiO_2$ et de $mSiO_2$ à grands pores ($mSiO_2$@PbS/CdS-Fe_3O_4).

5. Surveiller le comportement de libération du médicament en réponse aux multi-stimuli (pH / MF / NIR) de $mSiO_2$@PbS/CdS-Fe_3O_4 après avoir été chargé avec un médicament anticancéreux.

6. Étudier l'effet synergique du mode de chauffage intégré et de la libération de $mSiO_2$@PbS/CdS-Fe_3O_4 par un médicament sensible aux stimuli.

Dans la première section, nous avons spécifiquement développé une nano-plateforme multifonctionnelle cœur/coque /coque (Fe_3O_4@SiO_2@$NaYF_4$:Nd^{3+}), qui consiste en un noyau super-paramagnétique en Fe_3O_4 entouré d'une coque intermédiaire en SiO_2 et recouvert d'une couche de photoluminescence externe en $NaYF_4$:Nd^{3+}, comme le montre sur la Figure 1. Cette nano-plateforme multifonctionnelle peut être efficacement excitée par laser à environ. 800 nm (NIR-I) et présentent trois pics d'émission à 900 (NIR-I), 1060 (NIR-II) et 1340 nm (NIR-II). Les longueurs d'onde d'excitation et d'émission sont situées à l'intérieur des fenêtres biologiques optiquement transparentes dans le proche infrarouge (figure 2). En raison de cette caractéristique unique de photoluminescence NIR à NIR, les NPs Fe_3O_4@SiO_2@$NaYF_4$:Nd^{3+} préparées

présentent une propriété optique pénétrée dans le tissu profond avec un rapport signal sur bruit élevé. Notre expérience d'imagerie NIR a démontré que le signal de photoluminescence NIR de $Fe_3O_4@SiO_2@NaYF_4:Nd^{3+}$ peuvent être transmis à travers un tissu aussi épais que 13 mm (Figure 2), environ trois fois plus épais que celui obtenu par les similaire NPs de noyau/coquille/coquille contenant la coquille de $Fe_3O_4@SiO_2@NaYF_4:Er^{3+},Yb^{3+}$. D'autre part, $Fe_3O_4@SiO_2@NaYF_4:Nd^{3+}$ peut servir d'agent de contraste T2 négatif pour l'imagerie par résonance magnétique, comme en témoigne le remarquable effet

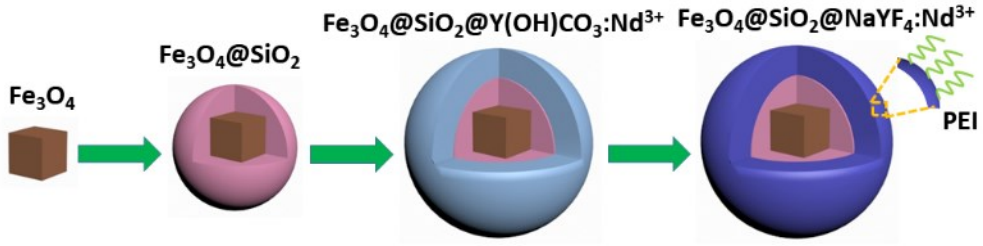

Figure 1. Illustration schématique de la procédure de synthèse de NPs $Fe_3O_4@SiO_2@NaYF_4:Nd^{3+}$.

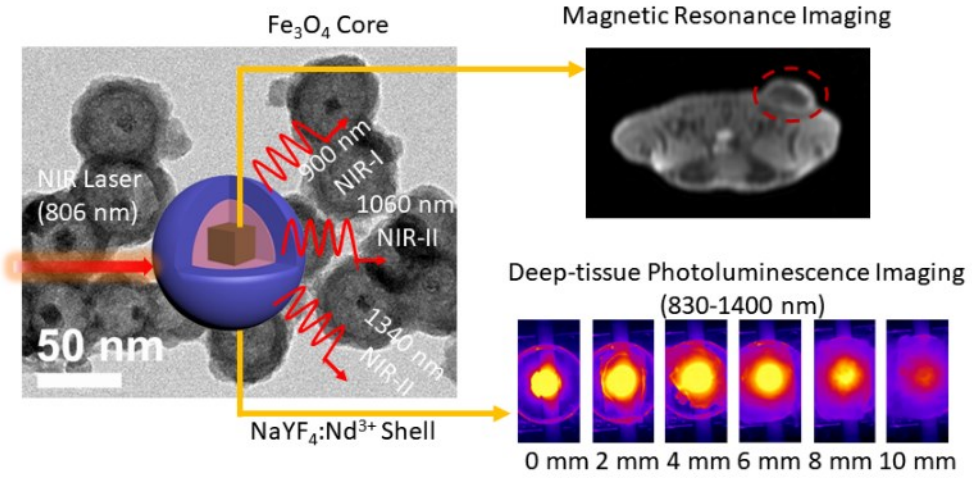

Figure 2. Imagerie en TEM de NPs $Fe_3O_4@SiO_2@NaYF_4:Nd^{3+}$ et leur caractéristique de photoluminescence NIR à NIR; Images IRM *in vivo* pondérées en T_2 de souris nue portant une tumeur acquise 30 minutes après l'injection intra-tumorale de $Fe_3O_4@SiO_2@NaYF_4:Nd^{3+}$; Imagerie photoluminescente d'échantillons de poitrines de poulet d'épaisseurs différentes (0, 2, 4, 6, 8 et 10 mm) placées au sommet d'un microcanal contenant du $Fe_3O_4@SiO_2@NaYF_4:Nd^{3+}$ dispersés dans une solution aqueuse sous excitation d'un laser à 806 nm.

d'assombrissement dans une expérience d'imagerie par résonance magnétique *in vivo* (Figure 2). Ces résultats suggèrent que les NP Fe_3O_4@SiO_2@$NaYF_4$:Nd^{3+} sont des candidats très prometteurs pour l'imagerie *in vivo* à haute résolution et en mode double dans les tissus profonds (optique et MR).

Les résultats correspondants dans cette section sont publiés dans l'article suivante:

Fan Yang, Artiom Skripka, Antonio Benayas, Xianke Dong, Sung Hwa Hong, Fuqiang Ren, Jung Kwon Oh, Xinyu Liu, Fiorenzo Vetrone, and Dongling Ma, An Integrated Multifunctional Nanoplatform for Deep-tissue Dual-Mode Imaging. *Adv. Funct. Mater.,* 28 (2018) 1706235.

La nano-plateforme multifonctionnelle de la partie I présente une faible aimantation en raison de sa caractéristique de noyau magnétique unique, qui ne convient pas aux applications biologiques par entraînement magnétique et à la thérapie magnétothermique. L'ingénierie d'une nano-plateforme multifonctionnelle contenant de multiples NP magnétiques est bénéfique pour réaliser des bio-applications de confinement rapides et pour obtenir une thérapie magnétothermique plus efficace. La partie II est donc centrée sur le développement de nouveaux NPs théranostiques multifonctionnels exploitant plusieurs NPs Fe_3O_4 super-paramagnétiques et d'intéressants QD PbS/CdS émetteurs de NIR, ainsi que leur intégration dans une nano-plateforme unique par auto-assemblage. Il est bien connu que les super-nanoparticules (SP) multifonctionnelles synthétisées par auto-assemblage possèdent non seulement les caractéristiques physiques et chimiques intrinsèques de leurs NP individuelles, mais également les propriétés collectives de ces NP dues aux effets de couplage. Par conséquent, cette nano-plateforme a été spécifiquement préparée par auto-assemblage de NPs Fe_3O_4 et de QD photoluminescents PbS/CdS avec leur émission dans NIR-II [SASN (NIR-II)] et son mécanisme de formation d'auto-assemblage a été systématiquement étudié dans la Figure 3a. Les SASN sphériques 3D résultants (NIR-II) sont composés de multiples NPs Fe_3O_4 et QD PbS/CdS distribués de manière aléatoire, avec une taille moyenne totale de 61.3 ± 0.4 nm de diamètre (Figure 3b-d). Les expériences d'imagerie par photoluminescence *ex vivo* ont révélé les remarquables capacités de pénétration des super-nanoparticules autoa-ssemblées de Fe_3O_4 et de PbS/CdS (NIR-II) [SASN (NIR-II)], qui sont bénéfiques pour la bio-imagerie optique. Pendant ce temps, la caractéristique de regroupement induite par l'auto-assemblage des SASN (NIR-II)] leur a conféré une propriété de relaxivité T_2 améliorée pour l'imagerie par résonance magnétique. En plus, les SASN préparés (NIR-II) dans notre travail possèdent la double capacité d'agir simultanément comme agents magnétothermiques et photo-thermiques, surmontant les principaux inconvénients de chaque type de chauffage séparément (Figure 4a, b). Lorsque les SASN (NIR-II) ont été exposés à la configuration de chauffage à double mode (magnétothermique et photothermique), l'efficacité du transfert d'énergie thermique (puissance de perte spécifique, SLP) a été multipliée par 7 par rapport au chauffage magnétique seul. Ces résultats, alliés à

l'excellente stabilité photo et colloïdale et à la cytotoxicité négligeable, démontrent l'utilisation potentielle des SASN (NIR-II) pour l'imagerie bimodale des tissus profonds (optique et IRM) *in vivo*, tout en permettant simultanément aux SASN (NIR-II)) traitement thermique bimodale par médiation pour le traitement du cancer.

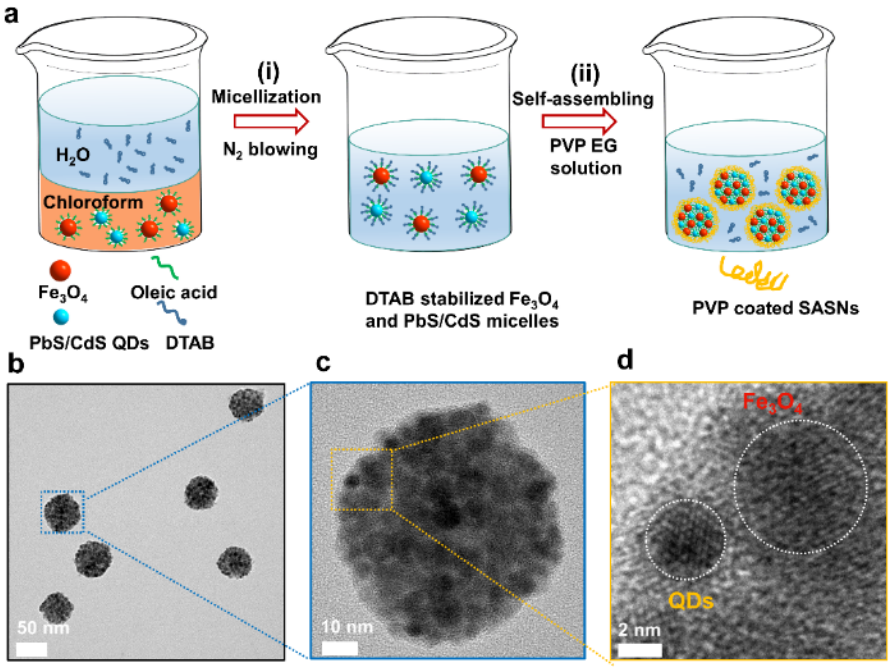

Figure 3. (a) Illustration schématique du processus de formation des SASN (NIR-II). (b-d) images TEM des SASN (NIR-II) à différents grossissements.

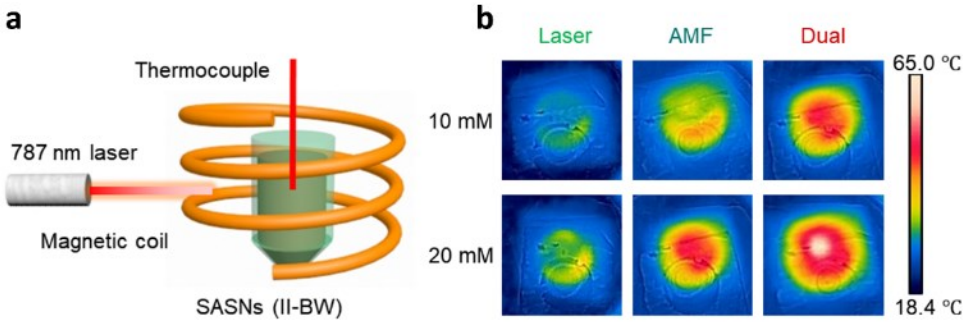

Figure 4. (a) Schéma de la configuration pour les expériences combinées magnétothermique et photo-thermique. (b) Les images thermiques de la solution SASN (NIR-II) après 5 min de chaque modulation (laser à 3,3 W / cm2, AMF à 7 kA / m, mode double). Les images thermiques sont prises à partir du haut du tube avec la vue en coupe.

Les résultats correspondants dans cette section sont publiés dans l'article suivant:

Fan Yang, Artiom Skripka, Maryam Sadat Tabatabaei, Sung Hwa Hong, Fuqiang Ren, Antonio Benayas, Jung Kwon Oh, Sylvain Martel, Xinyu Liu, Fiorenzo Vetrone, and Dongling Ma, Multifunctional self-assembled supernanoparticles for deep-tissue bimodal imaging and amplified dual-mode heating treatment. *ACS Nano,* 13 (2019) 408-420.

Bien que les SASN (NIR-II) possèdent une excellente modalité thérapeutique de chauffage à double mode, le revêtement de polyvinylpyrrolidone (PVP) utilisé en tant que stabilisateur de surface des NP montre une biocompatibilité correcte et une difficulté pour une fonctionnalisation plus poussée. De plus, nous proposons d'explorer les modalités d'administration des médicaments avec notre nano-plateforme multifonctionnelle. Des travaux publiés antérieurement ont indiqué que les matériaux mésoporeux conviennent parfaitement à la délivrance de médicaments. Avec cette considération, la silice mésoporeuse

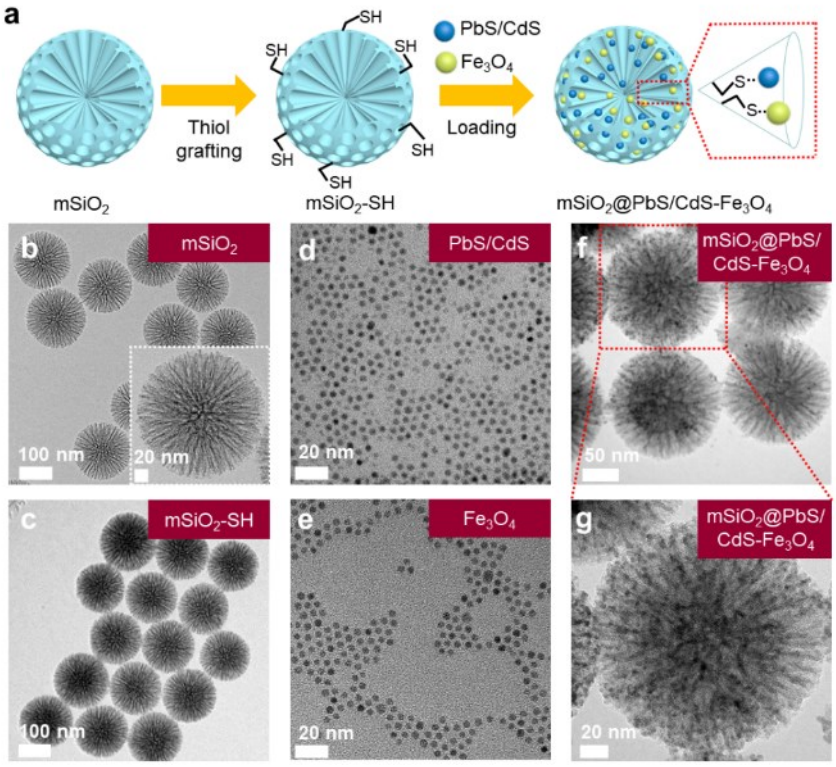

Figure 5. (a) Illustration schématique de la procédure de synthèse our $mSiO_2$@PbS/CdS-Fe_3O_4. (b) Image TEM de $mSiO_2$. L'encart montre l'image TEM correspondante de $mSiO_2$ à un grossissement supérieur. (c) Images TEM de $mSiO_2$ modifié par un thiol (désigné ici par $mSiO_2$-SH), (d) QD PbS/CdS et (e) NPs Fe_3O_4. (f, g) Images TEM de $mSiO_2$@PbS/CdS-Fe_3O_4 à différents grossissements.

($mSiO_2$) apparaît comme un support de médicament prometteur, car elle possède généralement un cadre mésostructuré rigide, qui offre une grande stabilité et une facilité de fonctionnalisation de surface pour la liaison des molécules de médicament. Dans la troisième section, nous avons synthétisé un $mSiO_2$ à pores relativement gros (> 10 nm) par une approche de croissance continue à stratification biphasique (Figure 5a-c). Après une simple réaction de couplage au silane, en raison de sa structure unique à pores relativement grands et à sa capacité de charge élevée, le $mSiO_2$ modifié par un thiol peut être utilisé comme matrice pour

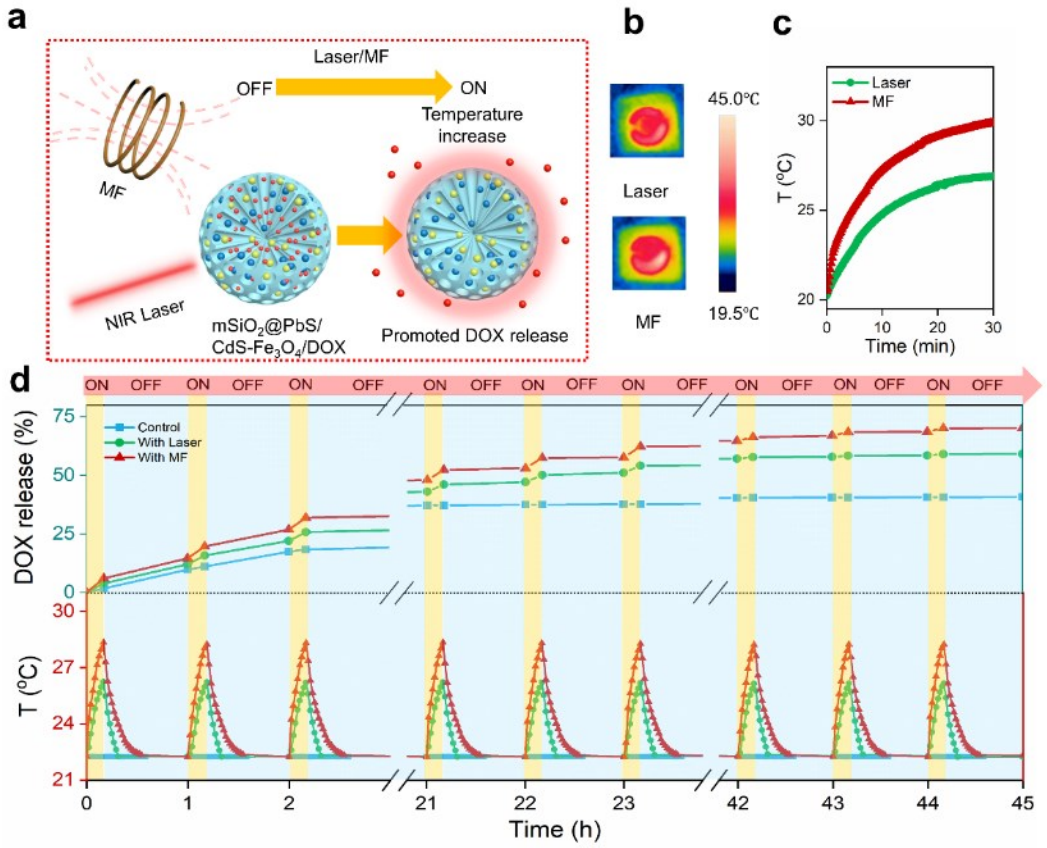

Figure 6. (a) Illustration schématique de la libération de DOX induite par la chaleur PTT / MHT et induite par la chaleur en réponse au laser externe et à la MF. (b) Images thermiques de la solution $mSiO_2$@PbS/CdS-Fe_3O_4 après 30 min de deux types de modulation (laser à 1,3 W/cm2, MF à 5 kA/m). (c) Courbes de température correspondantes dépendant du temps de la solution de $mSiO_2$@PbS/CdS-Fe_3O_4 (0,4 mg dans un volume total de 2 mL). (d) Profils de libération par DOX de la dispersion de $mSiO_2$@PbS/CdS-Fe_3O_4/DOX (0,2 mg/mL, 2 mL) stimulée par laser / MF (en hausse) et évolution dans le temps de la température correspondante de la solution (en bas); la dispersion de $mSiO_2$@PbS/CdS-Fe_3O_4/DOX sans stimulation, c'est-à-dire sans utilisation du laser ou de MF, est montrée à titre de témoin. Le laser et MF ont été commutés entre les modes «ON» et «OFF».

incorporer des QD PbS/CdS (Figure 5d) et des NPs Fe_3O_4 super-paramagnétiques (Figure 5e) de réaction axée sur la coordination. Cette nano-plateforme théranostique ($mSiO_2$@PbS/CdS-Fe_3O_4) (figure 5f, g) peut produire un fort chauffage local en tant qu'agent hautement efficace de traitement de l'hyperthermie magnétique (THP) / thérapie photo-thermique (PTT) sous l'effet d'un stimulus physique externe du champ magnétique (MF) et / ou un laser NIR (figure 6a-d). Après avoir été chargé de DOX, le taux de libération de DOX sous des stimuli multiples (pH/MF/NIR) a été significativement accru à un pH et à des températures plus élevés, provoqués par des effets magnétothermiques / photo-thermiques. Nos résultats ouvrent la voie au développement d'une nano-plateforme théranostique multifonctionnelle prometteuse pour l'imagerie bimodale et l'intégration simultanée de capacités de traitement synergiques et hautement localisées de la libération de médicaments sensibles au pH/MF/NIR.

Les résultats correspondants dans cette section sont publiés dans l'article suivant:

Fan Yang, Artiom Skripka, Maryam Sadat Tabatabaei, Sung Hwa Hong, Fuqiang Ren, Yue Huang, Jung Kwon Oh, Sylvain Martel, Xinyu Liu, Fiorenzo Vetrone, and Dongling Ma, Magnetic-Photoluminescent Nanoplatform Built from Large-Pore Mesoporous Silica. *Chem. Mater.,* 31 (2019) 3201-3210.